The Pennsylvania State University

The Graduate School

College of Engineering

NONLINEAR CONTROL OF MULTI-ACTUATOR ELECTROHYDRAULIC

SYSTEMS BASED ON FEEDBACK LINEARIZATION WITH APPLICATION

TO ROAD SIMULATORS

A Thesis in

Mechanical Engineering

by

Beshahwired Ayalew

Submitted in Partial Fulfillment
of the Requirements
for the Degree of

Doctor of Philosophy

August 2005

The thesis of Beshahwired Ayalew was reviewed and approved* by the following:

Bohdan T. Kulakowski
Professor of Mechanical Engineering
Thesis Advisor
Chair of Committee

Moustafa El-Gindy
Senior Research Associate, Applied Research Laboratory

Heath Hofmann
Associate Professor of Electrical Engineering

Kathryn W. Jablokow
Associate Professor of Mechanical Engineering

Christopher D. Rahn
Professor of Mechanical Engineering

H. Joseph Sommer III
Professor of Mechanical Engineering
Interim Head of the Department of Mechanical and Nuclear Engineering

*Signatures are on file in the Graduate School.

ABSTRACT

Electrohydraulic actuators constitute important force generation and positioning elements in various industrial and testing applications. Their high power-to-weight ratio and high load stiffness make them better choices than their rival electromechanical actuators in multi-actuator service load simulation testing applications such as road simulators, flight simulators and shaker tables. However, electrohydraulic actuators exhibit significant nonlinearities in their dynamics. In order to obtain satisfactory performance in the presence of these nonlinearities, more elaborate control techniques than the ubiquitous PID loops may be necessary.

In this thesis, nonlinear models of electrohydraulic systems are developed for a typical single actuator test system. This test system is such that detailed modeling of transmission line dynamics is found necessary. A useful result obtained from modal approximation of distributed transmission line dynamics is outlined for a specific causality case. Suitable system interconnection models are adopted and validated using experiments on the test system.

The validated system model is then used to derive nonlinear pressure/force and position controllers based on feedback linearization and its robust enhancements. Feedback linearization can be applied to certain model structures which allow the cancellation, in real-time, of the measured and modeled nonlinearities of the system. It is shown in this thesis that a model of an electrohydraulic system can be configured as input-output (IO) linearizable (or partial feedback linearizable) under some basic assumptions. In fact, these assumptions are necessary, and yet not unduly restrictive, that the term Near IO linearization is used with the controllers so derived.

A sliding mode controller is designed as a robust extension of the Near IO linearizing controller with pressure/force output. It is also shown that the Near IO linearizing controller with position output is equivalent to a cascade controller implementing the Near IO linearizing pressure/force controller as an inner-loop to a feedback plus feed forward outer-loop position controller. The cascade implementation has the convenient feature that the position control closed-loop error has a second-order

linear dynamics driven by the pressure/force control closed-loop error, which in itself has a first-order linear dynamics. A consequence of the equivalence is that it gives insight into the choice of the linear gains for the Near IO linearizing position controller. Furthermore, the cascade form allows one to view the robustness issues for position control from a Lyapunov backstepping perspective.

The performance of the nonlinear controller is compared against standard PID and linear state feedback with integral controllers using experiments and computer simulations of the nonlinear system model. It is shown that the nonlinear controllers have better tracking performance than the linear controllers, particularly in force control. It is demonstrated that there is more performance advantage for the nonlinear position controllers with suggested system layout changes and improved signal processing.

The nonlinear position controllers are further considered for a multi-actuator application in road simulation. A nonlinear full-bus model of a transit bus is developed for computer simulations of a four-post road simulation system. Time domain interaction measures are derived to look at interactions between decentralized PID+Δp and Near IO linearizing position control loops. It is shown that there is little interaction between either of the decentralized position control loops. However, a second cascaded decentralized controller considered for tracking a remote parameter like spindle vertical acceleration response faces significant and persistent interactions.

Finally, the performance of the multi-actuator road simulation system under a decentralized Near IO linearizing controller and a decentralized PID+Δp controller are compared for a typical rough road profile. The Near IO linearizing resulted in a more than 60% improvement in the tracking error metric across all four actuators and a more than 50% improvement in the response matching of the sprung mass acceleration power spectral density over that obtained with the PID+Δp controller.

TABLE OF CONTENTS

LIST OF FIGURES

LIST OF TABLES

NOMENCLATURE

A, B, C	feedback, input and output matrices for augmented model
A_b, A_t	piston areas for the bottom and top faces
A_r	line cross sectional area
A_i, B_i, C_i	feedback, input and output matrices in modal state equations
b_{lf}, b_{rf}, b_{lr}, b_{rr}	distances from each unsprung mass c.g. to the left and right tires
C_{arr}, C_{arf} and C_{ap}	auxiliary roll (rear and front) and pitch damping coefficients
C_L	leakage coefficient
$C_{t,i}$; $i=1,2,3,4$	tire damping coefficients
C_v	valve coefficient
$C_{v,i}$; $i=1,2,3,4$	valve coefficient referred to each port
c	speed of sound
$c_{d,i}$; $i=1,2,3,4$	discharge coefficients referred to each port
$c_s^{\pm}$	sign dependent friction parameter for Stribeck effect
D_n	dissipation number
d	diameter of line section
d_{lf}, d_{rf}, d_{lr}, d_{rr}	distances from the sprung mass c.g. to suspension attachment points
e	position tracking error
e_F	pressure force tracking error
$F_c^{\pm}$	sign-dependent Coulomb friction
F_{ext}	external force on piston not including gravity and friction
F_f	friction force on piston
F_L	load force or specimen reaction on piston
$F_{L,d}$	desired or reference load force trajectory
F_p	fluid pressure force on piston
$F_{p,d}$	desired or reference pressure force trajectory
F_{si}, $i=1, 2, 3, 4$	suspension forces
F_{ti}, $i=1, 2, 3, 4$	tire forces
$F_v^{\pm}$	sign-dependent viscous friction coefficient

$F_s^{\pm}$	sign-dependent static friction force
f_F	additive nonlinear function in pressure force dynamics
f_p	additive nonlinear function in position dynamics
f_{pL}	additive nonlinear function in load pressure dynamics
$f_{si}, i=1, 2, 3, 4$	interpolation function for air suspension stiffness
G	steady-state correction matrix
G_v	static gain of the valve
G_{XX}	input auto spectral density
G_{XY}	input-output cross spectral density
g	acceleration due to gravity
g_F	nonlinear input coefficient function in pressure force dynamics
g_p	nonlinear input coefficient function in position dynamics
g_{pL}	nonlinear input coefficient in load pressure dynamics
$\hat{g}$	time domain matrix for RGA computation
H	frequency response function
I	identity matrix
I_P	pitch moment of inertia for sprung mass
I_r, I_{uf}, I_{ur}	roll moments of inertia of sprung and front and rear unsprung masses
i, j, k, p	indexing integers
i_v	servovalve current
$\bar{i}_v$	net servovalve current
i_{voff}	offset current to account for abrasion wear and lap
i_{voff}	offset current to account for abrasion wear and lap conditions
K_{arr}, K_{arf}, K_{ap}	auxiliary roll (rear and front) and pitch stiffnesses
$K_P, K_I, K_D, K_{\Delta p}$	PID+Δp controller gains
K_s	linear specimen stiffness
$K_{ti}; i=1, 2, 3, 4$	tire stiffness
K_v	valve coefficient defined with spool position
$K_{v,i} ; i=1,2,3,4$	valve coefficients defined with spool position referred to each port

k_L	linear gain in load force tracking closed loop system
k_o	linear gain in pressure force tracking closed loop system
k_v, k_p	linear gain in outer-loop position control of the cascade controller
k_1, k_2, k_3	linear gains for the Near IO linearizing position controller
L	line hydraulic inertance
l	length of line section
l_f, l_r	distance from sprung mass c.g. to each axle
M_s, M_{uf}, M_{ur}	sprung and front and rear unsprung masses
m	polytropic exponent
m_p	lumped mass of piston, fixture and oil mass in cylinder
P_d, Q_d	Laplace domain downstream pressure and flow rate
P_u, P_d	Laplace domain upstream and downstream pressures
P_u, Q_u	Laplace domain upstream pressure and flow rate
P_u, P_d	Laplace domain upstream and downstream pressures
p_b, p_t	pressure in the bottom and top cylinder chambers
p_d, q_d	downstream pressure and flow rate for a line section
p_{di}, q_{ui}	downstream pressure and upstream flow rate as modal states
p_g	gas pressure in accumulator
p_{g0}	initial gas pressure
p_L	load or differential pressure ($p_L=\Delta p=p_b-p_t$)
p_R	return pressure at servovalve
p_S	supply pressure at servovalve
p_u, p_d	upstream and downstream pressures in time domain
p_u, q_u	upstream pressure and flow rate for a line section
Q_N	rated servovalve flow rate
Q_u, Q_d	Laplace domain upstream and downstream flow rates
q	flow rate variable
q_b, q_t	flow to the bottom and from the top cylinder chambers
$q_{e,b}, q_{e,t}$	external leakage from the bottom and top chambers
q_i	internal leakage in cylinder
q_u, q_d	upstream and downstream flow rates in time domain

R	line hydraulic resistance
R_{HSM}	linearized hydraulic resistance for the hydraulic service manifold
RGA	relative gain array
r_h	hydraulic radius
s	Laplace operator
$\bar{s}$	normalized Laplace operator $\bar{s} = s/\omega_c$
t	time
T, t_o	smoothing factor, and step time in smooth step generator
u	dummy variable for control input
u_1, u_2, u_3, u_4	underlap or overlap lengths for servovalve spool
V_b, V_t	bottom and top cylinder chamber volumes, respectively
V_g	instantaneous gas volume in accumulator
V_{g0}	initial gas volume in accumulator
v	intermediate linear control input in IO linearization
v_p	piston velocity
$w_i\ i=1, 2, 3, 4$	port widths
X	vector of input or drive signals
X_d	amplitude of desired reference magnitude in "smooth" step
$\boldsymbol{x}$	state vector for augmented model
x_d	desired or reference position trajectory
$\boldsymbol{x}_i$	modal state vector for i^{th} mode
x_p	piston position
x_v	servovalve spool position
x_{vmax}	maximum spool travel from null
x_{voff}	offset spool displacement
Y	vector of response signals
Y_d	vector of desired response signals
$\boldsymbol{y}$	output vector in state space description
$\boldsymbol{y}_i$	output vector for i^{th} mode
y_{ss}	steady state value of a response signal
Z_c	line characteristic impedance

Z_o	line impedance constant
z_s, z_{uf}, z_{ur}	position of c.g. of sprung mass, and front and rear unsprung mass
$z_{ui}, z_{si}\ i=1,\ 2,\ 3,\ 4$	positions of tire and suspension attachment points
$\alpha,\ \beta$	frequency-dependent viscosity effect correction factors
β_e	effective bulk modulus
θ	pitch angle of sprung mass
Δp	differential or load pressure $(\Delta p = p_L = p_b - p_t)$
Δp_{HSM}	pressure drop across hydraulic service manifold
Δp_N	rated pressure drop in servovalve specification
δ_{ui}	an input signals or it integral deviation from steady state
δ_{yi}	a response signal or its integral deviation from steady state
$\phi,\ \phi_{uf}, \phi_{ur}$	roll of body, and front and rear unsprung mass roll
Γ	propagation operator
$\lambda_{i,j}$	(i,j) th element of the RGA
λ_{si}	root indices defined in modal approximation of sinh T(s)
ν	kinematic viscosity of oil
ρ	density of hydraulic oil
ω	frequency in rad/s
ω_c	viscosity frequency, $\omega_c = \nu / r_h^2$
ω_{ci}	modal undamped natural frequencies of blocked line
$\omega_{n,v}$	natural frequency for valve model
ζ_v	damping ratio for valve model

ACKNOWLEDGEMENTS

My deepest gratitude is due to my advisor and mentor Dr Bohdan T.Kulakowski for his unwavering support, patience, and encouragement. I am thankful for the research, teaching and other professional opportunities I have been privileged to experience just by working with him.

I am indebted to Dr. Joel Anstrom for his expert opinion on many issues and also for giving me unrestricted access to his hardware and software tools for the experiments in this work. I would also like to thank Mr. Dave Klinikowski for facilitating access to the test actuator I used for experiments.

I would also like to thank Dr. Kathryn Jablokow, Dr. Heath Hoffmann, Dr. Moustafa El-Gindy and Dr. Christopher Rahn for serving on my Ph D committee and also for their very useful feedback on the contents of this thesis.

Finally, I would like to acknowledge the love and support I have received from family and friends throughout my graduate study.

I dedicate this thesis to the late Professor Donald A. Streit who motivated me to continue on this journey and whose exemplary life remains an inspiration.

Chapter 1

Introduction

Electrohydraulic actuators have a wide range of applications in machine tool drives, rolling mills, injection molding machines, materials handling equipment, aircraft control surfaces, construction, mining and agricultural equipment, aircraft control surfaces, vehicle active suspensions and motion and service load simulation systems. The latter are of particular interest in this thesis and include fatigue testing systems for material specimens, road simulators for vehicle structures, vibration or shaker test rigs for components, and flight simulators and aeronautical fatigue testers for aircraft structures.

In most of these applications, the demand on the actuators is on the controlled delivery of high output power (i.e., force and motion) with precision in the face of weight and space constraints. In addition to their high power-to-weight ratio, electrohydraulic actuators exhibit a better degree of self cooling and self lubrication (and hence less wear) than their rival counterparts in electromechanical actuators. Their high load stiffness is also another advantage. However, the dynamics of electrohydraulic actuators exhibit some dominant nonlinearities that pose control challenges for improved performance. In this thesis, nonlinear controllers are developed to address this issue for an experimental electrohydraulic actuation system typically employed in fatigue testing. The results are then extended to a multi-actuator service load simulation testing system.

1.1 Service Load Simulation Testing

Traditionally, service load testing used to involve dedicating such operating environments as test tracks and proving grounds designed to emulate expected in-service conditions and associated loads on the test (vehicle) structure. However, it has long been

argued that this practice is time-inefficient, expensive, and prone to inconsistencies due to environmental variables and test personnel error.

Since the early 70's, simulation testing, i.e. testing of components and assemblies using simulated loading systems, has been considered to complement, and in some cases serve as a convenient substitute to test track testing, thereby improving on the efficiency and consistency of testing efforts. Early on, successful applications of simulation testing were limited to simple loading patterns for component fatigue testing with the then available testing systems. With the advent of high speed digital computation, however, simulation testing systems have become capable of complex multi-axial loading of individual components and fully developed assemblies alike. Simulation testing now enables service load testing in a cost and time efficient manner and within a controlled and repeatable laboratory setting. In the rest of this work, we refer to this service load simulation testing systems for vehicles as road simulation systems or road simulators.

Generally speaking, a road simulation system is one which attempts to create a controlled and repeatable test environment that closely simulates the operating conditions for a significant portion of a vehicle or of the whole vehicle. This definition encompasses such testing rigs as chassis dynamometers, component shaker tables and vehicle shakers[1]. However, the most common use of the name 'road simulator' or 'road simulation system' is in reference to multi-post vehicle shakers employing actuators to provide excitation inputs to vehicle structures. We keep this use of the terms in this work.

A typical road simulation system aims at replicating road excited vehicle responses by providing simulated road excitation inputs to the vehicle system. The excitations are provided by controlled electrohydraulic or electromechanical actuators with their own dynamics. Therefore, a road simulation system is invariably a dynamic system. And if the road simulation system uses electrohydraulic actuators to provide the excitation to the vehicle, as is most often the case, then it is invariably a nonlinear dynamic system. It therefore poses challenges that may not be easily overcome using linear controllers on the electrohydraulic actuators.

Road induced inputs can be resolved into components that are longitudinal, vertical, lateral and rotational inputs with respect to the vehicle. The realistic road simulation system would therefore replicate this combined system of inputs with the correct phase relationship between each component [2]. In practice, however, some of the excitation input components are simplified or even ignored depending on the testing objective, cost and complexity of the road simulation system. There are therefore such classifications as uni-axial, bi-axial or tri-axial loading systems depending on the number of inputs to be applied at each wheel of the vehicle. As far as simulation testing of a whole vehicle structure goes, even a 'uni-axial' road simulation system applies the loads at the different wheels of a dynamically coupled structure: the vehicle. And it needs to maintain the correct magnitude and phase relationships at each wheel. This implies that even the simplest whole vehicle simulation testing system is a multi-axial nonlinear dynamic system.

It is natural to expect, at this point, that these nonlinear dynamics have a bearing on the effectiveness of service load simulation testing using road simulators. We briefly describe the existing solutions below and defer the detailed literature review to Chapter 2.

1.2 Improving the Performance of Road Simulators

The performance of road simulators, as gauged by the accuracy of replication of in-service response or of road profile tracking, has been improved by advances in practical control techniques and high performance electrohydraulics. The control techniques are heavily dependent on the PID controller and its linear enhancements, including differential pressure feedback, phase lead and/lag compensators, etc. To cope with the nonlinearities introduced by the electrohydraulic actuators' and the test vehicle's dynamics, iterative methods are employed to derive appropriate inputs that replicate on-road measured responses. However, these iterative approaches still keep the linear control scheme as an 'inner'-loop control on the nonlinear electrohydraulic hardware.

It is the overarching goal of this thesis to address the nonlinearity of the electrohydraulic system within the 'inner'-loop. It is felt that the use of nonlinear

controllers to obtain a better 'inner'-loop control of the electrohydraulic actuators may reduce the time and cost associated with setting up and executing the iterative loops. It is also possible that, depending on the test scenario and objective, these nonlinear controllers may eliminate the need for the iterative loops altogether.

To help in the evaluation of the effectiveness of the proposed nonlinear controllers as 'inner'-loops in a multi-actuator road simulation system, we make a distinction between decentralized and centralized controllers. By decentralized control we mean the control of each actuator independently of the others in an essentially single-input single-output (SISO) configuration. Centralized control refers to elaborate multiple-input multiple-output (MIMO) control systems. With decentralized control, which is primarily desirable for its simplicity, it is possible to evaluate the performance of the road simulator without completing iterative procedures. We only need to address the interaction or cross-coupling between the decentralized control loops due to the coupled dynamics of the test vehicle (and actuators).This is addressed separately in this thesis.

1.3 Main Contribution of the Thesis

The main contribution of this thesis is in the development and analysis of nonlinear controllers that cancel the dominant nonlinearities in the electrohydraulic system so that the 'inner'-loop decentralized control loop of an electrohydraulic actuator behaves linearly and the road simulation system performs better. These controllers are derived based on a Near-IO linearization approach. It is shown that cascade physical interpretations reveal a simple design procedure for the Near IO linearizing position controller. These cascade interpretations also lead to straightforward considerations of robust versions including sliding mode control.

Experiments are performed on a test system whole modeling led to a new modal approximation result for distributed parameter transmission line modeling. This is incorporated in the interconnected electrohydraulic system model to study the limitations of the basic assumptions made for controller derivation. The modal approximation result,

derived for one causality case here, gives better handling of steady state response, and also leads to a physically argued model order reduction for the interconnected system.

This work is different from related work in the literature on electrohydraulic actuator position and force control (reviewed in Section 2.2) in that, assumptions and limitations are clearly outlined, model validation results are presented and nearly all nonlinear controllers derived in this thesis are experimentally implemented. Furthermore, a physically intuitive design procedure is outlined for the Near IO linearizing position controller.

1.4 Thesis Outline

In Chapter 2, a thorough review of the existing techniques employed to obtain satisfactory performance with electrohydraulic road simulators is presented. A literature survey is also presented on advanced control techniques proposed for electrohydraulic actuators in general applications. A review of interaction (cross coupling) measures for use with multi-actuator systems in decentralized control is also included.

In Chapter 3, an experimental single actuator system is considered to gain insight into the modeling of various components in the electrohydraulic system and to validate the interconnected system model using closed-loop and open-loop experiments. Furthermore, during the course of the study, a detail model of the transmission hoses was found necessary. Some useful modal approximation models are derived and included.

The first part of Chapter 4 deals with the derivation of the nonlinear controllers based on the validated model from Chapter 3. The theoretical basis and robustness considerations are outlined. In the second part of Chapter 4, the performance of the nonlinear controllers is evaluated using both experiments and computer simulations of the full nonlinear system model.

In Chapter 5, the actuator modeling and controller development results of Chapter 4 are used in a model of a four-actuator road simulation system with a nonlinear full-bus model of a transit bus as a test vehicle for computer simulation studies. Interaction

measures are described, and decentralized control structures are evaluated. A performance comparison is also conducted between a decentralized linear PID+Δp controller and decentralized Near IO linearizing position tracking controller using a typical road profile.

Finally, Chapter 6 presents a summary of the main results and the conclusions of this work. Some recommendations for future research are also included in this final chapter.

Each of Chapters 3, 4, and 5 is organized with its own brief introductory notes and a chapter summary. The latter is particularly aimed at helping the reader identify specific sections within each chapter for easy reference of detailed discussions of a result.

Chapter 2

Literature Review

2.1 Road Simulators

2.1.1 Introduction to Road Simulation

Road simulators enable the laboratory assessment of vehicle structural durability, ride comfort and Noise and Vibration Harshness (NVH) without having to run the vehicle's drive train on an actual road surface. They can also be used in the assessment of pavement damage and the study of road-vehicle interaction [3, 4]. Perhaps the most significant of these applications is the evaluation of structural durability and integrity in which it is desired to establish how structural components and subassemblies fail from fatigue.

The simplest durability tests involve driving the vehicle over representative road surfaces and repeating the process while monitoring the level of degradation. While potentially realistic, such tests are expensive and time consuming. This is a major problem especially for heavy vehicles where the expected lifetime mileage may be over 500,000miles [1].

Some degree of accelerated mileage accumulation (and testing time compression) could be achieved by using test tracks. On test tracks common road features such as chuck holes, sine waves, chatter bumps, potholes, etc., are placed in series on a dedicated road section. The arrangement of these road features is carefully designed in such a way that the in-service fatigue failures are correlated well with the accelerated on-test track failures. A not overly severe test track for transit buses, like the one operated by the Pennsylvania Transportation Institute (PTI), achieves a mileage compression of 10:1 based on counts of axle acceleration reversals [5]. These two figures imply that durability

testing of heavy vehicles could last in the order of 50,000 miles. It can therefore be argued that even the use of test tracks alone could be expensive, time consuming, and prone to inconsistencies from driver and test personnel fatigue. Besides, runs on the test track require consistently favorable weather for an extended period of time.

The use of the test track for structural durability testing can be complemented and often replaced by the use of road simulators. Trial runs could be done on a validated test track and further response replication could be continued in the laboratory using road simulators. Aside from the possibility of full test automation, the ability to digitally edit less important road profile features and response elements in terms of structural failure is an added distinct advantage of computer controlled road simulators. Test accelerations of 5-10 times are possible using some of these systems [6].

There are two basic types of road simulators in general use for structural analysis of whole vehicle structures. These are tire coupled and spindle coupled. Tire coupled road simulators are vertical actuators on top of which the test vehicle is mounted and only single axis vertical inputs are simulated with the vehicle forward speed maintained essentially constant. Fore-aft forces and lateral forces generated at the tire-road contact patch from acceleration, braking and cornering maneuvers are not intended to be simulated using these simulators [7]. Spindle coupled systems, on the other hand, can be configured to simulate vertical, lateral, longitudinal and braking inputs to the test vehicle.

Tire coupled simulators have certain advantages over spindle-coupled simulators. The inputs to the vehicle on a tire coupled system are applied in a similar way as on a road surface. As a result, suspension parameter changes and degradation effects on the vehicle dynamics resemble those on the road. Test set up is easier and fixture costs are lower with tire coupled systems, and they can be configured independent of the particular test vehicle. The same input, once established, can often be used as the simulated road for most vehicles, requiring only compensations for track and wheel base differences [8, 9].

A schematic of one leg of a tire coupled road simulator is shown in Fig 2.1. The test vehicle's wheels are mounted on the wheel plates located at one end of a double acting piston. A servovalve modulates flow to and from the top ($q_t(t)$) and bottom ($q_b(t)$), piston-actuator cylinder chambers, where the necessary pressure force is developed. The

usual controller is a Proportional Integral Derivative (PID) controller acting on piston position error and supplying current to the servovalve. Sometimes differential pressure (ΔP) feedback is included for additional damping [10]. Model based tuning of PID controller parameters for such a road simulation system is detailed by Gore et al. [11]. In the rest of this chapter, the variants of a PID controller are referred to simply as PID control, regardless of whether a P or PD or even PD+ΔP loop is really meant.
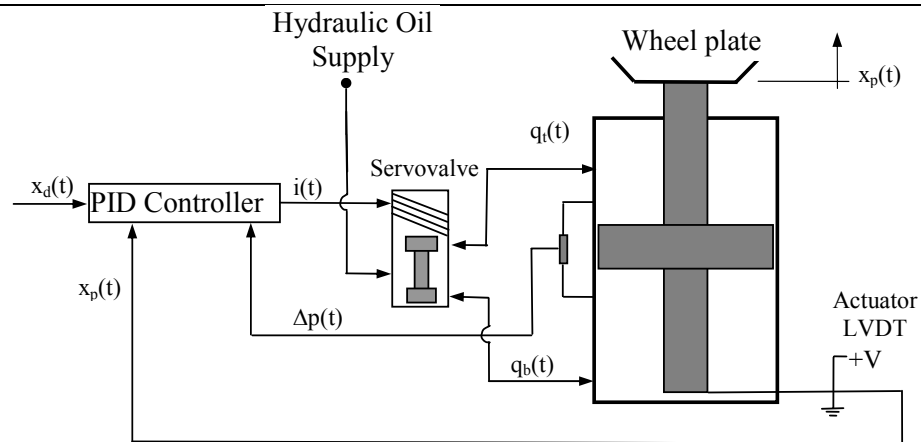
Figure 2.1: Schematic of one leg of a tire coupled road simulator

The study in this thesis focuses on a tire coupled system. However, the control issues to be pointed out are generic and apply to all road simulators whether they are tire-coupled or spindle-coupled.

2.1.2 Control Problem: Drive signal generation

The control problem with road simulators is often posed as the generation of the control reference inputs, labeled $x_d(t)$ in Fig 2.1, hereafter referred to as drive signals in this chapter. This interpretation is a consequence of the practical prevalence of 'outer-loop' control techniques that will be described below.

It is possible to playback road profile measurements from a road profilometer as the drive signals [9, 12]. However, some important limitations have to be recognized. The vehicle response on the simulator using these inputs could be different from that on the

actual profiled road. This is due to mainly the inherent nonlinear dynamics of the electrohydraulic actuators of the road simulator and the differences in rolling tire (on the road) and non-rolling tire (on simulator) properties. Other difficult to monitor issues include the strong possibility that the road profilometer and the test vehicle do not traverse the same on-the-road profile and also that forward velocity effects may not be properly replicated using this approach. However, this approach remains the cheapest and simplest road simulation solution. In terms of minimizing the influence of the dynamics of the actuators on the simulation quality, the approach depends heavily on the performance of the PID controller.

However, conventional PID control loops acting on electrohydraulic hardware have practical difficulties such as stability margins, actuator and test fixture bandwidth limitations and inevitable nonlinearities in the electrohydraulic system. These all have a negative bearing on the effort to match the drive signals ($x_d(t)$) with the actual piston position in a repeatable manner using only PID control loops. The testing community employing electrohydraulic actuators has found it necessary to use the PID controller as an 'inner' control loop and include 'outer' compensation loops to improve control accuracy, stability and repeatability [6]. In Section 2.2, a review is presented for other advanced control techniques that could be considered for improving the 'inner'-loop control. In fact, it is the objective of this thesis to investigate such solutions to enhance the 'inner' loop control.

A common goal of the 'outer' loop compensation methods is to modify the input drive signal in such a way that responses measured during the test on the simulator match those measured on the actual road. These compensation methods are the most common and are referred to as input correction methods. These can be divided into two major groups. The most common ones are referred to here as "response replication" methods to reflect the basic principles of the approach and are discussed in Subsection 2.1.2.1. The other group use compensation filters and are discussed in Subsection 2.1.2.2.

Output correction methods, which post-process the on-road-simulator responses obtained by using profilometer measured road profile inputs, have also been recommended [13, 14]. Typically, the on road simulator responses are multiplied by the

inverse of a linear transfer function model of the road simulator to remove effects of the road simulator dynamics. However, the effectiveness of the approach depends to a great extent on the degree of linearity of the vehicle and road simulator coupled system. Moreover, output correction methods do not address the actual inputs that the test vehicle is exposed to and as such have limited application when the actual on-the-road inputs and corresponding responses need to be replicated. These methods will not be discussed any further in this thesis.

2.1.2.1 Input Correction by Response Replication

One of the earliest versions of the input correction methods is the one suggested by Cripe [7] in 1972. He used an electrical analog circuit model of the vehicle's tire to derive an "effective road profile" for use as drive signals. The approach involved taking measurements of spindle responses and inverting the tire model to derive the inputs that would approximately generate the measured spindle responses. Using the method, he investigated the enveloping effect of the rolling tire that is absent on the road simulator and thus would negatively affect the performance of the simulator. He noted that the non-rolling tire for use on the simulator has higher radial stiffness and damping coefficient than the rolling tire for the same inflation pressure and preload.

Today, Cripe's idea of inverting a model is a subset of more rigorous methods that aim at replicating on-the-road vehicle responses such as stresses and accelerations measured at specific locations on the vehicle and not necessarily at the spindles [15]. The philosophy behind this group of methods is that when the measured responses are replicated with acceptable fidelity on the road simulator, the road is considered to have been simulated satisfactorily [3, 4, 6, 9, 16-18]. In these response replication methods of input correction, the vehicle and the simulator hardware, including the PID controllers are treated as a black-box with the drive signals as inputs (X) and some remote response parameters as outputs (Y). One leg of such a set up is shown in Fig 2.2. The test process involves some distinct steps as outlined in the following paragraphs.
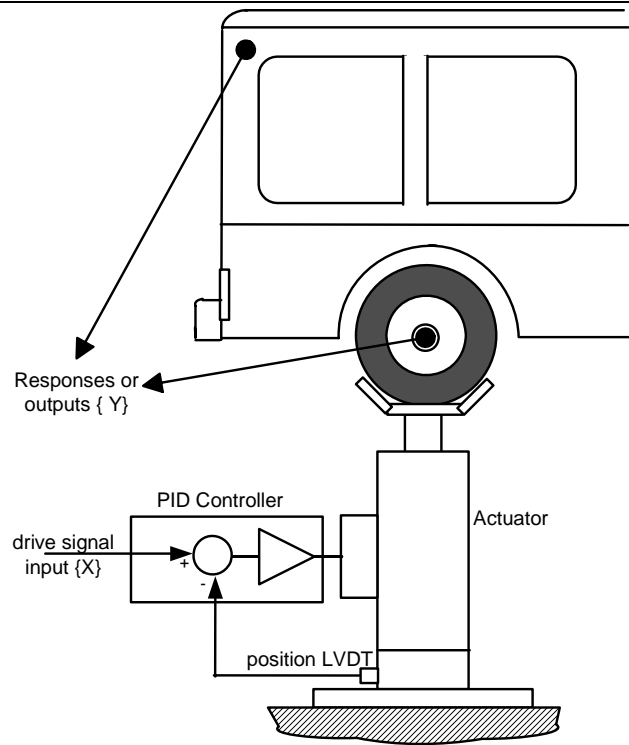
Figure 2.2: Schematic of test setup for Response Replication approach to road simulation

In a first step, the responses to be replicated are measured on a desired road section or test track. These could then be digitally edited to remove non-significant content. Suppose these are designated Y_d for desired output. In a second step, the test vehicle is mounted on the road simulator and experimental model identification is performed on the system. The popular approach for doing this is frequency domain system identification in which a Frequency Response Function (FRF) of the system (H) is determined with white noise broad band signals as inputs and measuring the responses of the vehicles, Y, using the same set of transducers as those used to obtain Y_d. Given the input auto spectral density (G_{XX}) and input-output cross spectral density (G_{XY}), the system FRF model is given by

$$H(j\omega) = G_{XX}^{-1}(j\omega)G_{XY}(j\omega) \tag{2.1}$$

The computation of the spectral densities uses the Fast Fourier Transform (FFT). In a third step, Eq. 2.1 is rearranged and used to derive the inputs X from the known outputs Y_d. Since FRFs are linear estimates of the system model and since the test system

invariably contains nonlinearities, the inputs obtained as a result of using Eq. 2.1 are, at best, estimates. Therefore, in a fourth step, iterations are performed to improve on the drive signals thus obtained. These iterations are generally done offline.

De Pont [3] tried a numerical setup where the inverse FRF is corrected at each step of the iteration by assuming the FRF to be a piecewise linear function of the drive signal. But he also found that this approach suffers numerical difficulties during the computation of the inverse FRF matrices as successive sets of excitations (drive signals) tend to be dependent as the solution is approached, at least for his particular test setup. The practically popular approach for this offline iterative scheme is to compute the inverse FRF only once at the beginning, as described above, and compute corrections to the drive signals iteratively from the errors in the responses [3, 16, 18]. This process, also called iterative de-convolution by Soderling et al. [6] and time waveform replication (TWR) by De Cuyper et al. [18], is summarized as follows:

$$\Delta Y_i = Y_d - Y_i$$
$$G_{\Delta X_i \Delta X_i} = H_i^{-1} G_{\Delta X_i \Delta Y_i} \qquad\qquad (2.2)$$
$$X_{i+1} = X_i + \alpha \Delta X_i, \qquad i = 1,2,3...$$

where, i is an iteration count and α is an iteration gain constant used to control the stability of the iterations and help prevent overdriving the system. For highly linear systems α[1] approaches 1 and fewer iterations are required. For highly nonlinear systems, the iteration gain approaches 0 [6, 17, 18]. The final drive signal is the one with acceptable response matching and it is typically used for subsequent durability testing.

De Cuper, et al. [18] provided a theoretical justification for the offline iterative response replication approach by investigating its convergence properties. They also showed that the introduction of a real time controller within the iterative loop (at each iteration step) helps reduce the number of iterations, and they go on designing an H_∞ controller that does this while keeping the PID as an inner loop.

Conventional test setups involve square models where the number of control input channels and response transducers used are equal and the system FRFs are represented by

---

[1] This iteration gain could be a matrix, with values that may change with the iteration count i.

square matrices. In some cases, non-square models, which use more response transducers than available control channels, can give improved accuracy of response matching by including more information in the simulation that adds to the test fidelity. However, unlike direct conventional matrix inversion for square models, the most direct numerical methods for non-square simulation involve the computation of a pseudo-inverse of the system model, since the system now becomes numerically over-conditioned. The pseudo-inverse approach results in drive signals that minimize error across all response channels in the least squares sense. The success of the non-square models depends, therefore, on the quality of response data across all response channels. By using a mix of spindle accelerometers and wheel to body displacement transducers, Fash et al. [16], showed that the improvement in accuracy using non-square test set-up strongly depends on the dynamic frequency range characteristics of the transducers used. Displacement transducers typically show better fidelity at low frequency and accelerometers are typically more sensitive at high frequency. The non-square model employing this mix of transducers showed improved broadband performance in replicating both responses (acceleration and displacement) over square models employing only one type of transducers (acceleration only or displacement only).

Raath [17] replaced the FRF system model identification step of the response replication effort by parametric dynamic system identification of a state space time domain ARX (autoregressive with exogenous input) model. The rest of the steps involved are detailed by Eksteen and Raath [19] and are similar to the steps summarized above. It is claimed in [19] that this time domain approach needs less data for system identification and leads to faster convergence of iterations to the final drive signals. Another advantage is the elimination of the need for FFT analysis, which also alleviates difficulties of simulating low frequency and high amplitude loading. These include the simulation of a vehicle traveling on long wavelength off-road tracks and of impact loading like that of aircraft take-off and landing cycles with magnified mean load changes [19].

The response replication methods reviewed above also are included in commercial versions. Remote Parameter Control (RPC®) from MTS Corporation and Time Waveform Replication (TWR™) from LMS International use the frequency

domain approach [15, 18, 20]. QanTiM^{TM} from Kelsey Instruments Ltd. uses the time domain approach [6, 19].

2.1.2.2 Input Correction with Compensation Filters

Other basic input correction methods exploit the fact that for a linear system, the product of a transfer function and its inverse is unity. This implies that if the response to be replicated (desired response) is filtered with a 'compensation filter' having a transfer function given by the inverse of the test system (actuators and test vehicle), then the on-simulator response can be expected to match the desired response. Wang [13] and Brauer [21] used additional low pass filters on the compensation filter to keep the inverse transfer function proper and maintain causality. Brauer [21] also formulated Artificial Neural Networks (ANN) as inverse models of the system dynamics for use as compensation filters for input correction.

In Soderling et al. [6], an adaptive inverse control (AIC) method is described in which an inverse FRF model identifier continuously updates the compensation filter characteristics online. The desired response parameter could be a road profile, in which case, the output of the PID control loop is the measured piston position response. Alternatively, a mixed mode or cascade setup could be used, where the inverse identifier (and the compensation filter) could act on some remote parameter like spindle acceleration as the desired response, with the PID loop still acting on the piston position.

Online iteration (OLI) is a method intended to complement the basic AIC described above by providing a way of iteratively compensating for nonlinearities [6]. This is done by combining the basic AIC with the scheme of iterative response replication reviewed in the previous subsection. The scheme is shown in Fig 2.3. In the figure, x(t) is the drive signal, y(t) is a response signal, y_d(t) is the desired field measured response and i is an iteration count. Each time a drive data point is executed for iteration i, a corresponding input of the next iteration, $i+1$, is also computed in real time. This online iteration scheme works faster than the pure (offline) iterative response replication methods since it does not need a separate model identification step.
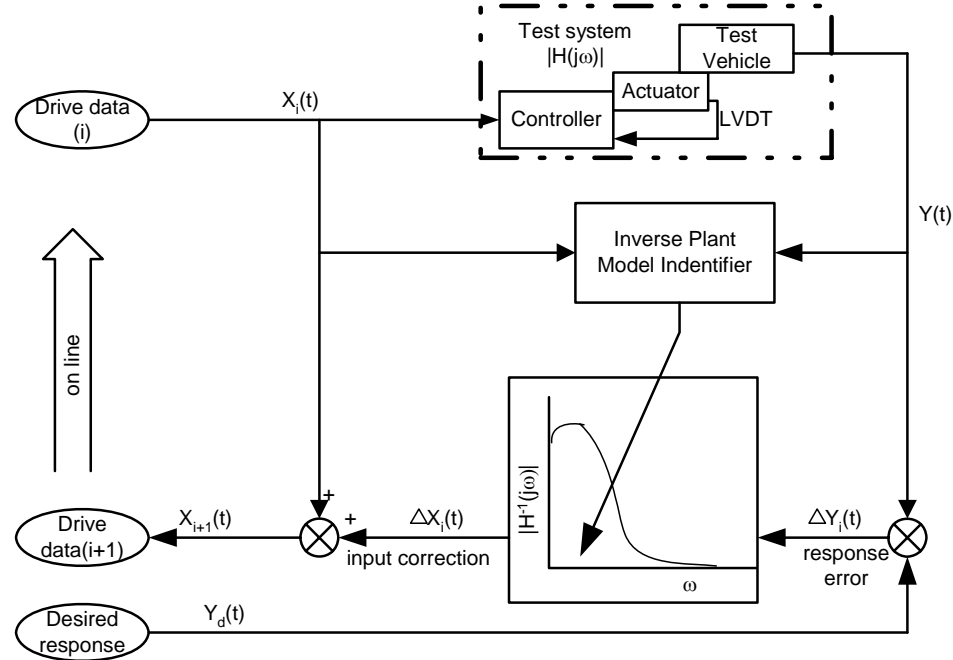
Figure 2.3: Schematic of online iteration method

In the preceding subsections, a detailed review of the available and practical methods for obtaining an acceptable road simulator performance was presented. It was observed that all of the methods use an 'outside' the loop strategy to compensate for the dynamics of the electrohydraulic test system. Most successful applications use iterative schemes to deal with system nonlinearities. The 'inside' loop is almost entirely a PID ($+\Delta p$) controller.

In the following section, 'inside' the loop compensation techniques that deal directly with the control of electrohydraulic hardware are reviewed. It is the focus of this thesis to seek such solutions that would reduce or possibly eliminate the iterations required by the 'outside' the loop techniques.

2.2 Control of Electrohydraulic Systems

As mentioned in the Chapter 1, electrohydraulic systems (EHS) have a wide range of applications. They owe this to their high power density, their ability to apply large

forces without an intermediate transmission, their high stiffness, and their inherent self cooling and lubrication for extended periods of time. However, unlike their rival electric motors, electrohydraulic actuators exhibit significant nonlinearities and hence pose a relative difficulty of control.

The advent of the electrohydraulic servovalve since the 1940's (and recently, of the electrohydraulic proportional valve), and subsequent advances in linear control implementations tailored for EHS have helped overcome most of the difficulty [22]. Today, most high flow servovalves include on-board feedback control electronics [23], and off-the-shelf PID control modules are readily available for most EHS [24].

Even though linear control solutions seem to be generally adequate for most applications, more demanding performance specifications can be met only by controllers that take into account the inherent nonlinearities in the dynamics of the EHS. These nonlinearities include: the pressure/flow gain characteristics of the servovalve, the dependence of system compliance on the fluctuating entrapped fluid volume, Coulomb and static friction in the actuator cylinders, flow forces affecting valve spool position, magnetic hysteresis in the valve torque motor, dead band and saturation [25, 26]. Other nonlinearities are associated with the driven load and may include nonlinear load dynamics, nonlinear friction, inertial coupling, centrifugal and Coriolis forces on a multi-degree of freedom load [27].

To design controllers that take into account at least the dominant nonlinearities, it is customary to linearize a nonlinear model of the system dynamics about a desired operating point (Jacobian linearization) and obtain a linear model that is valid locally. Then, for robustness, it is attempted to approximate as much of the nonlinearities as possible as parametric uncertainties and design a robust controller for the worst case linear plant model. This usually leads to conservative loop gains. Robust control design techniques such as μ-synthesis and H_∞ design are readily available for systematically handling such problems. In most cases, this results in a controller that trades off low frequency performance for high frequency robustness and vice versa [28, 29].

The alternative approach to deal with the nonlinearities is to employ nonlinear controller design techniques. These include feedback linearization, adaptive control and

variable structure control. Combinations of these methods have also been suggested. The following subsections review the applications of some of these techniques to EHS.

2.2.1 Controllers Based on Feedback Linearization

The theory of feedback linearization is detailed in the texts by Khalil [30] and Slotine and Li [31]. The central idea is to use a detailed nonlinear state space model of the system and choose the control input in such a way that the nonlinearities are cancelled globally, covering the whole region of the operating state space. This results in a linear closed loop system. As will be shown later, the dominant nonlinearities in an EHS can be modeled such that feedback linearization of the system model is possible. Of particular interest is Input-Output (IO) linearization, where only partial feedback linearization is achieved by linearizing the input-output relationship of the system [31].

Axleson and Kumar [32] derived a feedback linearizing flow control law considering only the nonlinearity in the valve flow rate vs. pressure relationship. With their limited model they noted the mathematical complexity of the exact feedback linearizing input which required higher order derivatives of differential pressure and flow variables as the order of the actuator model increased. However, they did not present results regarding the performance of their controller.

Vossoughi and Donath [27] presented an application of feedback linearization to the velocity control of an asymmetric electrohydraulic rectilinear actuator for a robot arm. They noted that the feedback linearizing controller derived from their model ensured exact linearization only with exact estimates of the model parameters and exact measurements of the state variables. Notable in Vissoughi and Donath's paper is their attempt to consider uncertainty error bounds on the parameters and the measurements of the (feedback) linearized model and pose the problem as a parametrically uncertain linear dynamic system and suitable for a subsequent design of a robust controller via μ-synthesis and H_∞ based approaches. They presented only results from performance comparisons of the closed loop system with the nominal feedback linearizing controller

versus the open loop system instead of comparisons with a conventional controller such as a PID loop.

Hahn et al. [33] presented computer simulation results showing the promise of a controller derived from an input-output (IO) linearization of the EHS model, with the controlled output being the piston position. By defining a multi-sensor linear controller for comparison, they were able to show that the nonlinear controller from IO linearization performed better in the presence of servovalve dynamics and Coulomb friction in the plant model, which were originally ignored in the plant model used for linearization. In addition, the IO linearizing controller showed better robustness in the presence of uncertainties in the estimated values of the fluid bulk modulus, the piston mass, and Coulomb friction. However, they did not present experimental verifications of their observation.

Sohl and Bobrow [34] derived a feedback linearizing controller for pressure force control from a Lyapunov-like analysis. They also synthesized a position tracking controller by defining a desired pressure force trajectory from feedback of position and velocity and feed forward of an estimate of friction. A comparison of the performance of their proposed controller with a P and PD controller showed that their proposed controller performed better, with as much as a 35% reduction in settling time and a 100% reduction in a full-stroke path tracking error. Their loading model was limited to a simple piston mass with friction.

It is recognized that the success of a feedback linearizing controller depends on the plant model structure. Del Re and Isidori [35] took a closer look at this issue for a hydraulic system in which the actuator piston controls the swash-plate angle of an electrically driven hydraulic pump which in turn drives a hydraulic motor connected to a load. Evenif their plant setup was different from the ones addressed in this work, their use of a bilinear approximation of the otherwise nonlinear square root valve flow rate vs. pressure drop relation for subsequent feedback linearization is noteworthy. They also used a linear state observer in the feedback linearizing law despite the fact that the resulting closed loop system employing estimated states was no longer linear. Using experiments and simulations, they showed that their feedback linearizing controller based

on the bilinear approximation performed better than a controller based on a purely linear model approximation and exhibited a better potential for optimality in terms of reduction of rise time and overshoot.

The success of the works reviewed above, especially those of Hahn, et al. [33] and Sohl and Bobrow [34], are part of the motivation for the decision to further study feedback linearizing controllers in this thesis. In Chapter 4, aspects of Hahn, et al.'s work shall be extended to the force control case with relevant experiments. In addition, it shall be shown in Chapter 4 that Sohl and Bobrow's controllers can be re-formulated to reveal an interesting relationship between IO linearization for force and position control.

For most of the works on feedback linearizing controllers reviewed in this subsection, the valve coefficients, leakage coefficients, the fluid bulk modulus, friction and supply pressure at the servovalve are some of the uncertain controller parameters. These parameters could also be time varying with temperature changes and wear. The next two subsections review the methods suggested in the literature to enhance controller performance in the presence of parameter/model uncertainty.

2.2.2 Adaptive Controllers

According to Kristić et al. [36], handling parameter uncertainty associated with differential-geometric approaches to nonlinear control (to which feedback linearization belongs) was the motivation for the development of the first series of adaptive nonlinear control schemes. The use of adaptive controllers to handle parameter uncertainty and robustness in the control of linear plants, however, has been well established.

Most of the work on the application of adaptive control to electrohydraulic systems (EHS) directly used or implicitly assumed (on-line identified) a locally linearized plant model. Hori et al. [37] tested a model reference adaptive controller (MRAC) assuming a simple integrator model for an EHS with position output. MRAC has also been implemented by Yun and Cho [38] using a simple model that neglects the fluid compressibility (pressure dynamics). Ziaei and Sepheri [39] developed a MRAC with emphasis on dead-band and nonlinear orifice openings which dominate proportional

valve performance near null. They chose a simple model in which static (memory-less) nonlinearity was cascaded with a third order linear discrete time dynamic model.

Plummer and Vaughan [40] proposed a self-tuning indirect adaptive scheme following offline identification tests to choose the linear model structure from comparisons of the prediction error obtained from different models. Then, they coupled a pole placement controller with a least squares on-line estimator. In Bobrow and Lum [41], a more comprehensive nonlinear model was used to suggest the structure of the linear state space model for subsequent online identification of the model parameters via a least squares estimator with data forgetting. They took advantage of the knowledge of the model structure to reduce the control law design to a sum of a feed forward term, that effectively inverted the online identified dynamics, and a feedback regulator term, for which LQR solutions were employed.

While the results from these and other applications of adaptive control to linear EHS models, or identifications thereof, are quite insightful and encouraging, they still suffered the limitations of local validity. Also, convergence of the adaptation schemes is generally dependent on the richness or persistence of excitation for the system.

For a class of nonlinear systems whose models take what is known as a Strict Feedback Form, recursive Lyapunov controller and adaptation law design methods such as backstepping have been developed and are well documented [30, 36]. An application of backstepping control design schemes for a force/pressure tracking control of an EHS has been by presented by Alleyne and Liu [42]. Their model of the EHS considered the orifice flow and Stribeck-Coulomb friction nonlinearity, but not the nonlinear compliance. A first-order valve dynamics model cascaded with the model of the pressure dynamics was easily structured as a Strict Feedback Form system. The choice of a Lyapunov function based on tracking errors and a parameter estimation error led to a controller and a gradient parameter adaptation law, which were then successively simplified by dropping non-dominant terms and ignoring the valve dynamics. Experimental force tracking results presented were quite noisy.

In Sirouspour and Salcudean [43], backstepping was used to design a position tracking controller for a three-way proportional valve coupled to an asymmetric (single

acting) actuator. Their plant model used a second-order valve dynamics including spool underlap in the orifice flow model and the nonlinear compliance. Parameter adaptation laws were also derived using Lyapunov analysis. Simulation results showed good improvements over a PD controller optimized to minimize position tracking errors. But it was reported that in experiments the adaptive nonlinear controller did not show significant improvement over a non-adaptive nonlinear controller (from backstepping) employing only off-line determined parameters.

The work in this thesis does not consider adaptive controllers, but instead uses offline identification of model parameters from grey box identification techniques described in Appendix B. For robustness to parametric uncertainty, a sliding mode controller is considered because of its closeness in structure to the IO linearizing controllers. Sliding mode control is the topic reviewed in the following subsection.

2.2.3 Variable Structure Control

An alternative solution to handling structured (parametric) uncertainty and unstructured uncertainty (unmodeled dynamics) in the control of nonlinear plants is variable structure control (VSC), specifically sliding mode control. It is closely related to feedback linearization. Typically, sliding mode control design involves:

- the choice of a switching function $S(x,t)$ that gives a sliding mode (or switching surface $S(t)=0$) with a fast and stable dynamics (for example, tracking error dynamics in a tracking application) that behaves as desired, and

- the design of the reaching phase, i.e., the choice of a controller that guarantees that the sliding surface is reached in finite time in the presence of model uncertainty

Traditional versions of sliding mode control use relay control represented by the *signum* function ($sgn(S)$), which generally introduces chattering as the control is switched across the sliding surface with finite speed. Control chattering is undesirable as it may excite unmodeled high frequency dynamics. To reduce chattering, boundary layers are introduced around the sliding surface, but robustness is traded off for reduction of

chattering. Details of the VSC theory and its enhancements are described in the monogram by Utkin [44], the text by Slotine and Li [31], and in the survey paper by Hung et al. [45], among others [44-48].

Many researchers have proposed different versions of VSC or sliding mode control to electrohydraulic systems (EHS). Early VSC applications to EHS focused on locally linearized models [49]. But later work emphasized nonlinear models with fixed boundary layers and switching gains [50, 51]. Hwang [46] proposed a VSC with time varying boundary layer and switching gain, and a sliding surface defined as a first order dynamics of a weighed sum of position tracking error, its integral and the integral of differential pressure (force) tracking error. The desired force trajectory is obtained as a second order filtered output of a desired position trajectory with bounded constant friction entering as a disturbance. Computer simulation results demonstrated attenuation of control chattering while achieving satisfactory simultaneous position and force tracking. Nguyen et al. [52] implemented a VSC for a force tracking problem by defining $S = F - F_d$, where the desired force trajectory(F_d) is obtained in the same way as in Hwang [46], but they employed a discontinuous friction observer from extensions of variable structure theory. They used a fixed switching gain and replaced tanh(S) for sgn(S) to reduce chattering. Experimental results demonstrated that position tracking errors increased by a factor of about 10 when friction compensation was removed from the control.

Sliding mode control has also been considered for position control of EHS with a flexible mechanical load, which is the case of interest in this work. Fung and Yang [50] included a nonlinear spring load on the linear EHS model. Liu and Handroos [51] presented a VSC method where the sliding surface is defined as a first order dynamics of the weighted tracking errors of all five states (piston position and velocity, load position and velocity, and differential pressure) in the model. Desired trajectories for the states other than the piston position were obtained using reference filter models with the desired position trajectory as input. Experimental and simulation results suggested strong robustness against structural (load) uncertainty.

Alleyne and Hedrick [53] proposed a two sliding surface approach for a force tracking application of VSC on an active vehicle suspension employing an EHS. The control input ensures tracking of the spool valve displacement on the second sliding surface, while the first surface provides the desired trajectory for the spool position from the desired force tracking error dynamics. This cascaded approach is similar to backstepping. The proposal also included adaptive parameter identification for the VSC.

From this review of literature, it appears that sliding mode control (VSC) solutions have good potential for control of EHS, particularly because of their close relationship with feedback linearization. In this thesis, sliding mode controller are considered as robust versions of the IO linearizing controllers.

2.3 Interaction in Multi-Actuator Systems

As already stated in Chapter 1, road simulation systems are inherently multi-actuator systems, and the test vehicles are dynamic structures which exhibit varying degrees of cross-coupling between actuation locations. Traditional road simulation test setups use decentralized servo (PID) control loops as 'inner-loops' that attempt to drive each actuator separately, as shown in the schematics in Figs 2.1 and 2.2. However, all multi-channel (actuator) systems are known to exhibit interaction due to dynamic load cross-coupling, which, even if linear by itself, can become nonlinear when combined with the nonlinear actuator dynamics.

The practical testing methods reviewed previously deal with cross-coupling effects only implicitly. The solution is included in the input-output 'black-box' approach together with successive iterations on the Multiple Input Multiple Output (MIMO) matrix setup. In this manner, the methods need not make explicit distinction between linear and nonlinear cross-coupling.

In this thesis, it is sought to enhance the "inner"-loop decentralized controllers. For the purpose of quantifying the effectiveness of the decentralized controllers, we define certain interaction/cross-coupling measures. This section reviews literature on the subject of interaction in multi-actuator systems.

Witcher and McAvoy [54] analyzed the issue of quantifying the amount of interaction which exists in a multivariable process control system. They extended the relative gain array (*RGA*), which was initially defined for steady state processes by Bristol [55], to include dynamic interaction measurement via MIMO transfer matrices for the process. They also outlined a time domain procedure for calculating the dynamic relative gain array. For a 2x2 process comprised solely of first-order dead time models with individual PI controllers to close each of two identical isolated (major diagonal) loops, Witcher and McAvoy [54] illustrated that the interaction, which is frequency dependent, deteriorates the respective behavior of the individual loops to the point of instability unless the PI loops are separately tuned taking the interaction into account. Their analysis, even if presented from a process control perspective, highlighted the effect of interaction on the decentralized control loops to a coupled process.

An investigation of interaction in multi-actuator EHSs was done by Ramachandran and Dransfield [56]. They looked into the analysis of the origins and behavior of actuator interaction experienced by one actuator due to other actuators when all were operating on a cantilever beam load under decentralized force tracking control. A proportional controller was used. By varying the location of the actuators individually along the beam during their experiments and simulations, they showed that interaction effects changed the effective damping at one actuator when the relative location of the others changed. They noted that interaction effects are felt more at the actuator connected to the stiffer point for any location combination. In particular, in a two actuator case, interaction increased the tendency of the actuator connected at the stiffer point to be oscillatory, as the other actuator was brought progressively closer to it from its less stiff side. These conclusions were also verified by quantitatively computing a time domain interaction index similar to that of Witcher and McAvoy [54]. The paper by Ramchandran and Dransfield [56], while quite insightful regarding multi-actuator EHS interaction, did not offer control solutions for compensating actuator interaction effects.

Pannala et al. [57] also addressed actuator interaction for a similar two-actuator force control setup as above. They employed graphical multivariable frequency response techniques based on the direct Nyquist array to iteratively design PID controllers for each

loop of their centralized or MIMO setup. Their final optimum design retained only P terms in each loop. Experiments showed that even these simple centralized or MIMO controllers reduced actuator interaction significantly. However, the graphical iterative method is cumbersome to apply to more than 3x3 systems. Their work exemplifies the fact that whenever centralized controllers are easy to design and the system can be considered linear, the potential performance loss (due to interaction) from using decentralized controllers can be avoided [58].

Sun and Chiu [59] presented a controller design for motion synchronization of an EHS with two single-acting actuators. They exploited the particular structure of the system model that resulted when the coupling load is an uncertain rigid mass and with uncertain locations for attaching the actuators to the load. Linear MIMO robust control design was ultimately used to reduce the position synchronization error by an order of magnitude from that of a simple mechanical linkage solution for synchronization, but the tracking error remained significant.

In this thesis, it is proposed to control each channel independently as with the conventional decentralized 'inner' loops, however nonlinear control will be employed to compensate for electrohydraulic system nonlinearities. As shall be shown later, the nonlinear controllers employ more information (namely dynamic tire forces) that refer load cross-coupling to each channel of excitation. We shall quantify the interaction index using a dynamic time domain extension of the *RGA*.

Chapter 3

Modeling and Experiments on a Single Actuator Electrohydraulic System

In this chapter, we present a detailed model of an electrohydraulic system which shall be employed as an experimental test stand and validation system for the development of the nonlinear controllers in the next chapter. During the course of this research, it was found necessary to increase the level of detail in the electrohydraulic system model from the level traditionally considered in control oriented design and analysis of these systems [25, 32, 35, 37, 39, 41-43, 53, 57, 60]. In particular, detailed models of transmission lines and accumulators needed to be considered in order to satisfactorily capture the dynamic behavior of the whole system.

We shall start by describing the layout of the test system and the basic modeling assumptions in Section 3.1. The detailed models of the components upstream and downstream of the servovalve will be discussed in Section 3.2. Modal approximation of the distributed dynamic models of supply and return transmission lines will be detailed in Subsection 3.2.1. The modal approximation of the causality case treated in Subsection 3.2.2 has not been treated before in reviewed literature. The significance of this particular causality case and the resulting model order reduction shall be taken advantage of in the selection of the model interconnection in Subsection 3.2.4 .

Section 3.3 presents the fundamental nonlinear model of the servo-actuator subsystem that forms the basis of controller design in the next chapter. A nonlinear actuator friction model shall also be extracted from simple closed-loop experiments. In Section 3.4, the model of the interconnected electrohydraulic system will be simulated and some open-loop and closed loop experiments will be used to validate the model predictions for select responses. Finally, Section 3.5 presents the chapter summary.

3.1 Description of the Single Actuator System

3.1.1 Introduction

A very common assumption in the development of models for valve-controlled hydraulic actuation systems is that of constant supply and return pressures at the servovalve [25, 32, 34, 35, 39, 41-43, 53, 57, 60]. On the other hand, a survey of research on fluid transmission line dynamics reveals that significant pressure dynamics are introduced in hydraulic systems as a result of the compressibility and inertia of the oil as well as the flexibility of the oil and the walls of pipelines [10, 61-64]. Transmission line dynamics can be significant on the supply and return lines between the hydraulic power unit (pump) and the servovalve as well as between the servovalve and the actuator manifold [10, 26].

Close-coupling (i.e., mounting the servovalve directly on the actuator manifold) is often used as a solution to the problem of minimizing the effects of transmission line dynamics between the servovalve and the ports of short-stroke actuators. In the case of long-stroke actuators, where such close-coupling may not be physically feasible, the effect of transmission line dynamics can be analyzed by explicitly including a transmission line model in the model of the servo-system, as shown by Van Schothorst [26]. However, in the case of the supply and return lines to the servovalve, close-coupling may not be a convenient solution for either short- or long-stroke actuators. This is because usually the Hydraulic Power Supply (HPS) unit, including the hydraulic pump, drive elements, heat exchangers and cooling water pumps, needs to be housed separately, away from the work station of the actuator or the load frame supporting the actuator. In such cases, supply and return lines from the HPS to the servovalve that are of significant length may be unavoidable. In addition, from installation considerations, these supply and return lines are usually flexible hoses rated for the appropriate working pressures.

Aside form the extensive presentation by Viersma [10], not much has been reported on the analysis of an electrohydraulic system including supply and return pressure variations at the servovalve. Viersma's analysis was done in the frequency

domain and the emphasis was to provide design rules for the location and sizing of the components of electrohydraulic systems. For time domain simulations involving nonlinear elements (actuator, accumulator, servovalve, etc), modal approximation of the frequency domain results for transmission lines provide modular and simpler alternatives to direct numerical solutions of the flow equations in time domain.

In the following subsections of this chapter, modal approximation results are used within a model of an electrohydraulic actuation system to include and investigate supply and return pressure variations at the servovalve due to transmission line dynamics. Experimental results that validate the model are also included.

3.1.2 Description of Test System and Basic Modeling Assumptions

The electrohydraulic system shown schematically in Fig 3.1 was designed for fatigue testing applications. The servovalve is a 5 gpm (19 lpm) two-stage servovalve employing a torque motor driven double nozzle-flapper first stage and a main spool output stage. The servovalve is close-coupled with a 10 kN, 102 mm-stroke symmetric actuator, which is mounted on a load frame. Pressure transducers are used for sensing the pressures at the four ports of the servovalve. An LVDT and an accelerometer are mounted on the actuator piston for position and acceleration measurement, respectively.
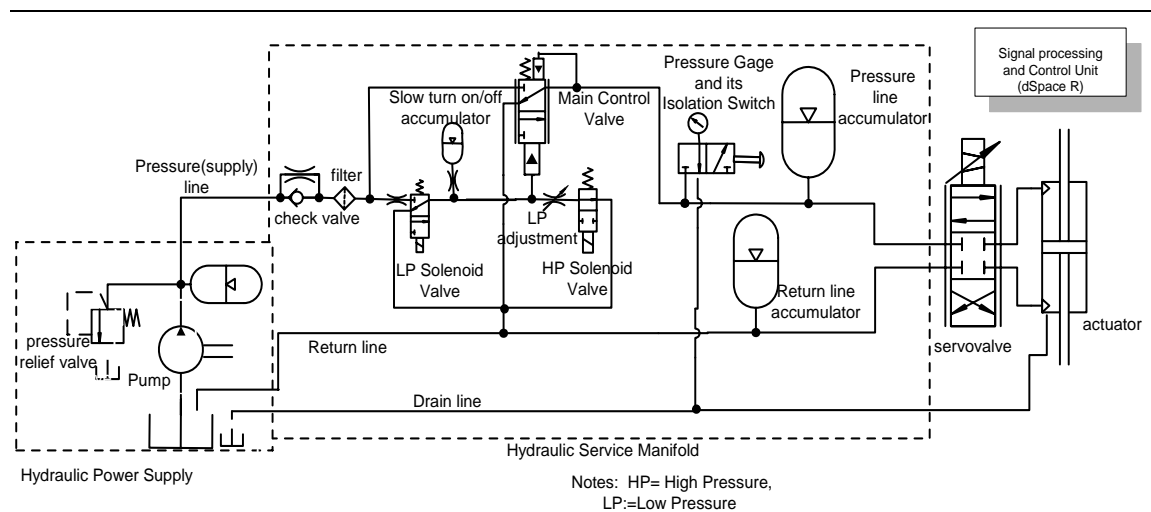
Figure 3.1: Schematic of test system

Control and signal processing is done with a dSpace® 1104 single processor board, which includes onboard A/D and D/A converters and a slave DSP. An amplifier circuit converts a 0-10 V control output from the dSpace® D/A to a high-impedance current input of range -50 to +50mA to the torque motor coils of the servovalve.

The unit labeled Hydraulic Services Manifold (HSM) is connected to the servovalve using 3.048 m-long SAE-100R2 hoses. The Hydraulic Power Supply (HPS) unit, including its heat exchanger and drive units, is housed separately and is connected to the HSM via 3.048 m-long SAE-100R2 hoses. The HSM provides basic supply and return line pressure regulation via the accumulators. In addition, the HSM is equipped with a control manifold circuitry to permit selection of high- and low-pressure operating modes, low-pressure level adjustment, slow pressure turn-on and turn-off, and fast pressure unloading. The drain line provides a path for oil that seeps past the seals in the actuator and also for draining oil from the HSM pressure gage.

During a normal fatigue testing operation, both the low-pressure and high-pressure solenoids (designated in Fig 3.1 as LP and HP solenoids, respectively) are energized, the main control valve is completely wide open, and the circuitry of the HSM allows flow at full system pressure [65]. The HSM is therefore modeled by considering the lumped nonlinear resistance arising from change of flow directions, flow cross-sections, as well as flow in the filter element. The total pressure drop between the pressure inlet and outlet ports of the HSM is given in manufacturer specifications. The available data satisfies a nonlinear expression relating flow rate to pressure drop. While the HSM unit is rated for a wide range of flow rate capacities, the rated flow rate through the servovalve is within 10% of nominal flow rate of the HSM. Hence, we use a local linear approximation to account for losses in the HSM as given by:

$$\Delta p_{HSM} = R_{HSM} \ q \tag{3.1}$$

Here, q is the flow rate, Δp_{HSM} is the pressure drop and R_{HSM} is the equivalent hydraulic resistance of the HSM circuitry. It's assumed that the check valve is an ideal one, so that its own dynamics are fast enough to be neglected and its backflow restriction has a large enough parallel resistance that the permitted backflow is very small. The drain

flow is also considered to be negligible. With these simplifications, the system reduces to the one shown in Fig 3.2. It should be noted that the resistances are lumped in the HSM excluding the gas-charged accumulators.
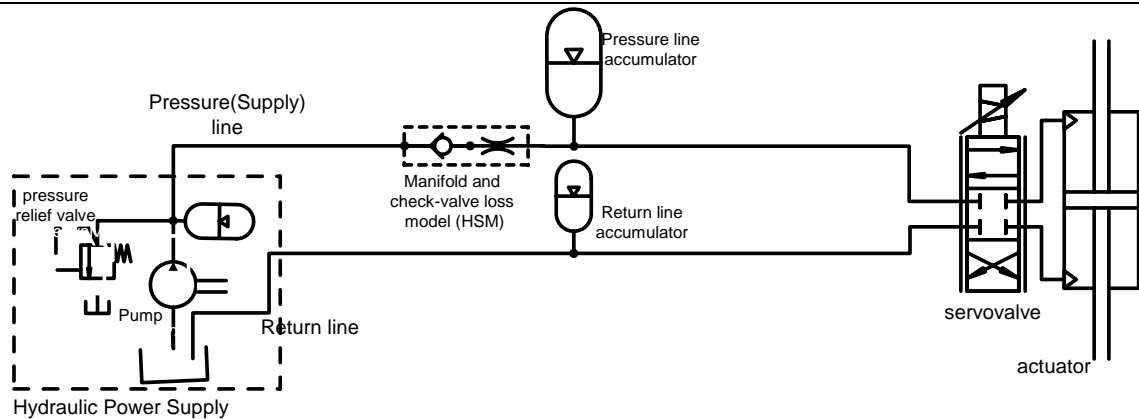
Figure 3.2: Simplified system

One more assumption is needed to further simplify the system for analysis. Through extensive frequency domain analysis, Viersma [10] has shown that, provided the accumulator and the pressure relief valve on the Hydraulic Power Supply(HPS) unit are located sufficiently close to the pump outlet (within 0.3 m, as is the case here), the pump flow pulsation frequencies can be suppressed from the pump output pressure. Therefore, in the following discussion, it is assumed that the output pressure just after the accumulator and pressure relief valve connection points in the HPS unit can be set as a known pressure input to the rest of the system. In fact, this is not a very restrictive assumption, since the modeling approach presented here is modular and models of the components of the whole HPS unit can easily be incorporated if needed.

For the simplified system, two sections of transmission hoses remain to be modeled. The first section is for the supply and return hoses between the HPS and the HSM and the second for the hoses between the HSM and the servovalve. A model applicable for each section is discussed next.

3.2 Model of Transmission Line Components

3.2.1 Transmission Line Modeling

To model the hydraulic hoses for the system described above, a separate literature survey was done. It provided rigorous results on validated solutions of the mass and momentum conservation equations governing flow in one-dimensional fluid transmission lines with a circular cross-section [10, 61-64]. Most of the available analyses have been done in the frequency domain, including extensive results for the lossless, the linear friction and the 'exact' dissipative models [10, 64]. For interconnected system level simulations and analytical studies of hydraulic systems, modular time domain solutions of the governing conservation equations are often desirable. For this purpose, modal approximation of the analytical frequency domain solutions offers an alternative technique to direct numerical solutions.

In general, some assumptions are necessary for the basic results to hold. These assumptions include laminar flow in the lines, negligible gravitational effects, negligible tangential velocity, and negligible variations of pressure and density in the radial and tangential directions. Furthermore, constant and uniform temperature is assumed and by so doing heat transfer effects in the fluid line are ignored. Thereby the discussion is limited to the linear friction model, which does not include distributed viscosity and heat transfer effects [63, 66]. Corrections are applied on the linear friction model to account for the frequency dependence of viscosity, following the work of Yang and Tobler [66].

The flow lines are assumed to have rigid walls in some derivations [10, 67]. However, Blackburn et al.[61], and McCloy and Martin [68] arrive at the same governing equations as the rigid wall case (for a frictionless flow) by allowing for wall flexibility and defining an effective bulk modulus combining the flexibility of the wall and that of the oil. Their definition of effective bulk modulus is the same as that derived by Merritt [25], where the effective bulk modulus is viewed as a series interconnection of the "stiffness" of the oil, of the container wall and even of entrapped air volume in the oil. Following this approach, flexibility effects are considered here via the effective bulk

modulus, β_e. The model parameters required for any section of the transmission line reduce to the ones shown in Fig 3.3. For the hydraulic hoses in this work, nominal values of the bulk modulus were taken from charts in [68].

p_u $\qquad$ p_d

q_u $\qquad$ $r_h, l, A_r, \nu, \rho, \beta_e$ $\qquad$ q_d
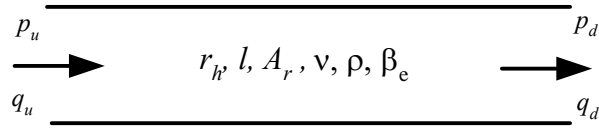
Figure 3.3: One dimensional fluid transmission line

Using the above assumptions for the single transmission line, the conservation laws can be integrated in the Laplace domain to yield a well-known distributed parameter model commonly expressed as a two-port matrix equation and sometimes known as the four-pole equations [10, 67]. The four-pole equations can take four physically realizable causal forms [26, 61, 63]. Two of these four forms are readily relevant to the problem at hand: one for the supply line hoses and another for the return line hoses. The third form was addressed by Van Schothorst [26] for modeling distributed pressure dynamics in cylinder chambers. The fourth form finds use with accumulator connection lines and is discussed in the next subsection and also the publication by the thesis author[69].

The mathematical derivation of the modal approximation for the four pole equations for three of the four causal cases have directly or indirectly been addressed by other researchers, notably, Yang and Tobler [66] and Van Schothorst [26]. A derivation of the fourth causal case is presented in detail in Subsection 3.2.2, and also in author's paper [69]. For continuity of discussion in this subsection, however, we focus on the first two forms for the supply and return line dynamics for which we adopt results from Ref [66].

Taking the supply line case first, we notice that in most hydraulic servo-system applications, a control signal modulates the servovalve consumption flow rate downstream of the supply line, $q_d(t)$, following the excursions of the (loaded) actuator piston. Then $q_d(t)$ is a preferred input to the transmission line model, and a realizable causality form requires that either $p_u(t)$ or $q_u(t)$ should be the other input [61]. Since we have already assumed the pressure just after the connection point of the pressure relief

valve and first accumulator (at the HPS) to be taken as an input to the system, the desired causal form of the four-pole equations for the supply line is the so-called pressure-input/pressure-output causality form [70]. It takes the form of Eq. 3.2 and can be derived by defining the boundary conditions for the distributed parameter model as the upstream pressure and flow rate (p_u, q_d) and the downstream pressure and flow rate (p_d, q_u) at the opposite ends of the line.

$$\begin{bmatrix} P_d(s) \\ Q_u(s) \end{bmatrix} = \begin{bmatrix} \dfrac{1}{\cosh\Gamma(s)} & -\dfrac{Z_c(s)\sinh\Gamma(s)}{\cosh\Gamma(s)} \\ \dfrac{\sinh\Gamma(s)}{Z_c(s)\cosh\Gamma(s)} & \dfrac{1}{\cosh\Gamma(s)} \end{bmatrix} \begin{bmatrix} P_u(s) \\ Q_d(s) \end{bmatrix} \tag{3.2}$$

The definitions of the propagation operator $\Gamma(s)$ and the line characteristic impedance $Z_c(s)$ depend on the friction model chosen [26, 63]. In this work, the linear friction model is adopted and the approach of Yang and Tobler [66] for incorporating frequency-dependent damping and natural frequency modification factors into analytically derived modal representations of the four-pole equations is used. For this case, $\Gamma(s)$ and $Z_c(s)$ are defined by Eqs. 3.3 an. 3.4, respectively as:

$$\Gamma(s) = D_n \frac{d^2 s}{4v}\sqrt{\alpha^2 + \frac{32\alpha\beta v}{sd^2}} \tag{3.3}$$

$$Z_c(s) = Z_0\sqrt{\frac{32\alpha\beta v}{sd^2} + \alpha^2} \tag{3.4}$$

Here, d is the line cross sectional diameter. The frequency-dependent correction factors α and β are obtained by comparing the modal undamped natural frequencies and damping coefficients of the modal approximations of the dissipative ("exact") model, which was described in detail in [71], against the modal representation of the linear friction model [66]. Corrected kinematic viscosity (v) values were suggested in [64]. The dimensionless numbers D_n and Z_o are the dissipation number and the line impedance constant, respectively, and are given by Eqs. 3.5 and 3.6. These parameters depend on the line geometry via the line cross sectional diameter, d, and length, l, and the oil properties via the density, ρ, and kinematic viscosity, v.

$$D_n = \frac{4l\nu}{cd^2} \tag{3.5}$$

$$Z_0 = \frac{4\rho c}{\pi d^2} \tag{3.6}$$

where c is the speed of sound in the hydraulic oil and is computed using:

$$c = \sqrt{\frac{\beta_e}{\rho}} \tag{3.7}$$

Here, the effective bulk modulus of the fluid β_e takes into account the flexibility of the wall of the transmission line, compressibility of the fluid and also of any entrapped air.

The three causal functions $1/\cosh\Gamma(s)$, $Z_c(s)\sinh\Gamma(s)/\cosh\Gamma(s)$, and $\sinh\Gamma(s)/Z_c(s)\cosh\Gamma(s)$ can be represented as infinite sums of quadratic modal transfer functions. The goal is to use a finite number of modes to approximate the otherwise infinite sum of the modal contributions for the outputs[1]. Of particular interest for the time domain description sought in this section is the state space formulation derived in [66, 70] and given here by:

$$\begin{bmatrix} \dot{p}_{di} \\ \dot{q}_{ui} \end{bmatrix} = \begin{bmatrix} 0 & (-1)^{i+1}Z_0\omega_{ci} \\ -\dfrac{(-1)^{i+1}\omega_{ci}}{Z_o\alpha^2} & -\dfrac{32\nu\beta}{d^2\alpha} \end{bmatrix} \begin{bmatrix} p_{di} \\ q_{ui} \end{bmatrix} + $$

$$\begin{bmatrix} 0 & -\dfrac{8\nu Z_o}{d^2 D_n} \\ \dfrac{8\nu}{d^2 Z_o D_n \alpha^2} & 0 \end{bmatrix} \begin{bmatrix} p_u \\ q_d \end{bmatrix} \qquad i=1,2,3...n \tag{3.8}$$

Here, the ω_{ci} are the modal undamped natural frequencies of blocked line for the linear friction model and are given by:

$$\omega_{ci} = \frac{4\nu\pi(i-\frac{1}{2})}{d^2 D_n} \qquad i=1,2,3,...n \tag{3.9}$$

---

[1] The derivation is similar to the case treated in the following subsection, Subsection 3.2.2. The reader is referred to that subsection (and Appendix A) for details on the modal approximation procedure.

The modification factors α and β are given as functions of the dimensionless modal frequencies $d^2 \omega_{ci}/4\nu$ [66]. The output is the sum of the modal contributions and is expressed as:

$$\begin{bmatrix} p_d \\ q_u \end{bmatrix} = \begin{bmatrix} \sum_{i=1}^{n} p_{di} \\ \sum_{i=1}^{n} q_{ui} \end{bmatrix} = \begin{bmatrix} I_2 & I_2 \cdots I_2 \end{bmatrix} \begin{bmatrix} p_{d1} & q_{u1} & p_{d2} & q_{u2} \cdots p_{dn} & q_{un} \end{bmatrix} \tag{3.10}$$

It should be noted that the truncation to a finite number of modes introduces steady-state errors. Some methods have been suggested to recover the steady-state output based on the fact that at steady-state the original four-pole equation, Eq. 3.2, reduces to:

$$\begin{bmatrix} p_d \\ q_u \end{bmatrix}_{ss} = \begin{bmatrix} 1 & -8D_n \\ 0 & 1 \end{bmatrix} \begin{bmatrix} p_u \\ q_d \end{bmatrix}_{ss} \tag{3.11}$$

Hsue and Hullender [71] discussed rescaling the truncated sum of the modal approximation for the dissipative model by its zero-frequency magnitude to bring about Eq. 3.11. Van Schothorst [26] and Hullender et al [70] described an additive approach where the steady-state error is eliminated by adding a corrective feed-through term on the output equation, Eq. 3.10. However, the transfer functions so implemented will no longer be strictly proper. This may entail the need for off-line algebraic manipulations when the transmission line is connected to static source and/or load linear resistances or other transmission line models with their own direct feed-through gains. The eigen values of the coupled system may then be altered by the steady-state correction [70].

Yang and Tobler [66] introduced methods that modify the input-matrix or use a state similarity transformation matrix to affect the steady-state correction while preserving the modal eigen values of the truncated model. Since comparable results were obtained by the use of either method, the input-matrix modification method was adopted for this work. Suppose matrices A_i and B_i represent, respectively, the feedback and input matrices in the modal equation, Eq. 3.8. Introducing the input-matrix modifier G,

$$\begin{bmatrix} \dot{p}_{di} \\ \dot{q}_{ui} \end{bmatrix} = A_i \begin{bmatrix} p_{di} \\ q_{ui} \end{bmatrix} + B_i G \begin{bmatrix} p_u \\ q_d \end{bmatrix} \tag{3.12}$$

The steady-state value of the *n*-mode approximation is then:

$$\begin{bmatrix} p_d \\ q_u \end{bmatrix}_{ss} = \sum_{i=1}^{n} \begin{bmatrix} p_{di} \\ q_{ui} \end{bmatrix}_{ss} = -\sum_{i=1}^{n}(A_i^{-1}B_i)G\begin{bmatrix} p_u \\ q_d \end{bmatrix}_{ss} \qquad (3.13)$$

Comparing with the desired steady-state value given by Eq. 3.11 and solving for G:

$$G = -\left(\sum_{i=1}^{n} A_i^{-1}B_i\right)^{-1}\begin{bmatrix} 1 & -8Z_oD_n \\ 0 & 1 \end{bmatrix} \qquad (3.14)$$

The number of modes *n* to be chosen depends on the frequency range of interest for the application.

Similarly, for the return line from the servovalve, we can define the flow rate at the servovalve end and the pressure at the downstream (toward the tank) end as inputs to the model of the return line based on the other four-pole equation of causality dual to Eq. 3.2 (see Ref[63]). Equally, we can use the observation that switching the sign convention of the flow direction for just the return line and using the four-pole equation dual to Eq. 3.2 yields the same set of four-pole equations as Eq. 3.2, provided the inputs to the model remain flow rate toward the servovalve end and pressure at the other end. This fact can easily be shown mathematically, but we omit it here for brevity and state that, for the return line model all of the derivations presented above for modeling the supply line hold. The caveat is to exercise care in using the proper signs for the input and output flow rates at both ends of the return line when forming interconnections with other system components.

For step response simulations, it is desirable to have good estimates of the initial conditions of the modal states, especially when the interconnected system model contains nonlinearities. Usually, for a single pipeline section, the derivative of the modal output can be assumed to be zero just before the application of the step change in the input, and modal initial conditions can be computed from:

$$\begin{bmatrix} p_{di}(0^-) \\ q_{ui}(0^-) \end{bmatrix} = -A_i^{-1}B_iG\begin{bmatrix} p_u(0^-) \\ q_d(0^-) \end{bmatrix} \qquad (3.15)$$

where the $[p_u(0^-), q_d(0^-)]^T$ are the inputs just before the step change. For an interconnected pipeline system, the inputs to one pipeline section may be outputs of another section, in which case the determination of proper initial values for the modal states of each section can be done by trial and error. The step disturbances can also be applied after initial transients have died down. In general "steady" simulations, like those involving sinusoidal fatigue test waveforms, the modal initial conditions of the interconnected system are less important.

Note that the model described in this section requires few parameters, mainly those listed in Fig 3.3, to describe the dynamics of each transmission line section using linear state space models in the time domain. This is particularly more convenient for control design and analysis than finite difference-based time domain solutions, which generally require rigorous discretization methods.

3.2.2 Modal Approximation for the Pressures Input-Flow Rates Output Causality Case

As noted above, the four pole equations can take one of four causal forms. This section deals with the modal approximation for the fourth causality case with upstream and downstream pressures $[P_d(s)\ P_u(s)]^T$ as input and upstream and downstream flow rates $[Q_u(s)\ Q_d(s)]^T$ as output for hydraulic transmission lines for which the linear friction model is considered applicable (typically those with small dissipation number).

A typical application of this fourth causality case, given by Eq. 3.16 below, is for modeling short connection lines to accumulators, which have been shown to be very important for hydraulic system dynamics by Veirsma [10]. Figure 3.4 shows the schematic of such a system, where a preferred integration causality assignment for the accumulator model (as will be detailed in Subsection 3.2.4) and the use of the first causality case for the sections of the main line (as already discussed in Subsection 3.2.1), leaves the fourth causality case for the short connection line to the accumulator. The double headed arrows in the figure indicate the input-output causality assigned to each line element.

The causal four-pole equation with $[P_d(s)\ P_u(s)]^T$ as inputs and $[Q_u(s)\ Q_d(s)]^T$ as outputs is given by:

$$\begin{bmatrix} Q_u(s) \\ Q_d(s) \end{bmatrix} = \begin{bmatrix} \dfrac{\cosh \Gamma(s)}{Z_c(s)\sinh \Gamma(s)} & -\dfrac{1}{Z_c(s)\sinh \Gamma(s)} \\ \dfrac{1}{Z_c(s)\sinh \Gamma(s)} & -\dfrac{\cosh \Gamma(s)}{Z_c(s)\sinh \Gamma(s)} \end{bmatrix} \begin{bmatrix} P_u(s) \\ P_d(s) \end{bmatrix}$$

(3.16)
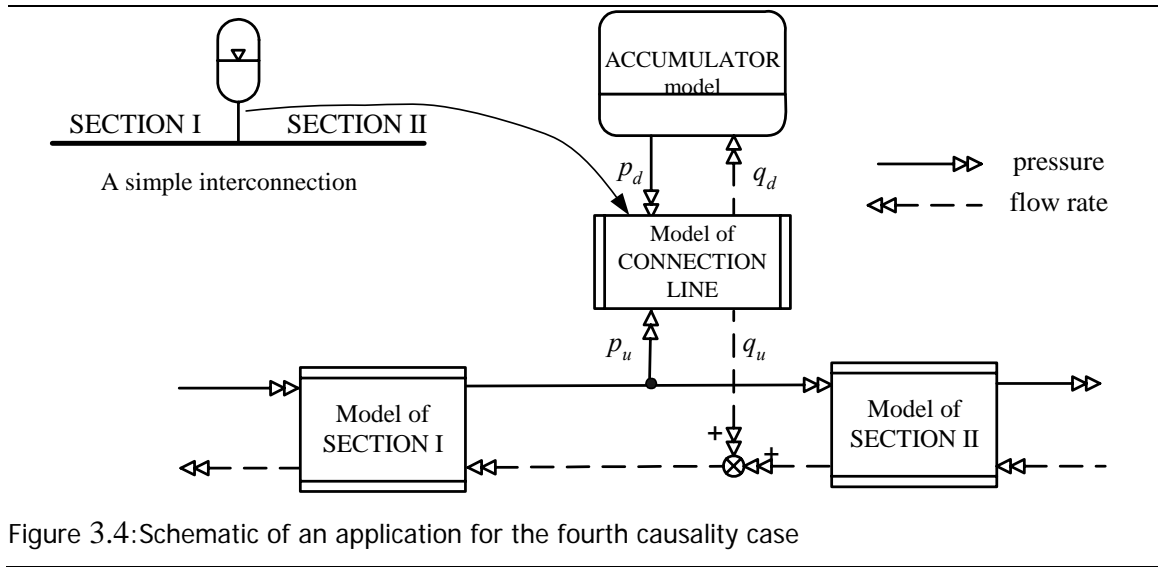
Figure 3.4:Schematic of an application for the fourth causality case

The expressions for the line characteristic impedance $Z_c(s)$ and the propagation operator $\Gamma(s)$ depend on whether the basic model chosen is the lossless model, the linear friction model or the dissipative model [63]. The linear friction case is considered here since the dissipation number, D_n, computed by Eq. 3.5, is of the order of 10^{-3} in the present application and linear friction works well for such cases [63, 66]. Using the normalized Laplace operator $\bar{s} = s/\omega_c$, where $\omega_c = \nu/r_h^2$ is the viscosity frequency, the propagation operator $\Gamma(\bar{s})$, and the line characteristic impedance $Z_c(\bar{s})$ for the linear friction model are given, respectively, by:

$$\Gamma(\bar{s}) = D_n \bar{s}\sqrt{1+\frac{8}{\bar{s}}}$$

(3.17)

$$Z_c(\bar{s}) = Z_0\sqrt{1+\frac{8}{\bar{s}}}$$

(3.18)

As in Subsection 3.2.1, the dissipation number, D_n, and the line impedance constant, Z_o, are given by Eqs. 3.5 and 3.6, respectively.

The modal approximation of Eq. 3.16 is derived by representing each of the transcendental transfer functions in the equation as finite sum approximations of low-order polynomial transfer functions. To this end, the following result from Oldenburger and Goodson [72] is used:

$$\sinh \Gamma(\bar{s}) = \Gamma(\bar{s}) \sum_{i=1}^{\infty} (1 + \frac{\Gamma^2(\bar{s})}{D_n^2 \lambda_{si}^2})$$

(3.19)

where,

$$\lambda_{si} = \frac{i\pi}{D_n}, \qquad i = 1,2,3,...$$

(3.20)

The approach is to use the result in Eq. 3.19 to find the poles of the individual transcendental transfer functions in Eq. 3.16 and then apply partial fraction expansions to obtain the modal approximations. Appendix A details this derivation of the modal representation of the functions $1/Z_c(\bar{s}) \sinh \Gamma(\bar{s})$ and $\cosh \Gamma(\bar{s})/Z_c(\bar{s}) \sinh \Gamma(\bar{s})$. Using the results from Appendix A, the four-pole equation, Eq. 3.16, can be re-written as:

$$\begin{bmatrix} Q_u(\bar{s}) \\ Q_d(\bar{s}) \end{bmatrix} = \frac{1}{Z_o D_n (\bar{s}+8)} \begin{bmatrix} 1 & -1 \\ 1 & -1 \end{bmatrix} \begin{bmatrix} P_u(\bar{s}) \\ P_d(\bar{s}) \end{bmatrix} +$$
$$\frac{2\bar{s}}{Z_o D_n (\bar{s}^2 + 8\bar{s} + \lambda_{si}^2)} \sum_{i=1}^{\infty} \begin{bmatrix} 1 & -(-1)^i \\ (-1)^i & -1 \end{bmatrix} \begin{bmatrix} P_u(\bar{s}) \\ P_d(\bar{s}) \end{bmatrix}$$

(3.21)

In the causality case treated by Yang and Tobler [66] only quadratic terms appear in the modal representation and in the causality case treated by Van Schothorst [26] only an integrator and quadratic terms appear in the modal representation. However, as Eq. 3.21 shows, the causality case treated here contains a first-order lag term in addition to the quadratic modes. This will have an implication for the simplification of the final result as shall be shown below.

The modal approximation is obtained by truncating the summation in Eq. 3.21 to a finite number of terms. Figure 3.5 shows the Bode plot for the element (1, 1) of the exact transfer matrix given in Eq. 3.16. The figure also includes the Bode plots for the

modal approximation taken from Eq. 3.21 with the first-order term only, for the approximation with the first-order plus one second-order term, and for the approximation with the first-order plus two second-order terms included in the summation. Figure 3.6 shows the same information for element (2, 1) of the transfer matrix given in Eq. 3.16.
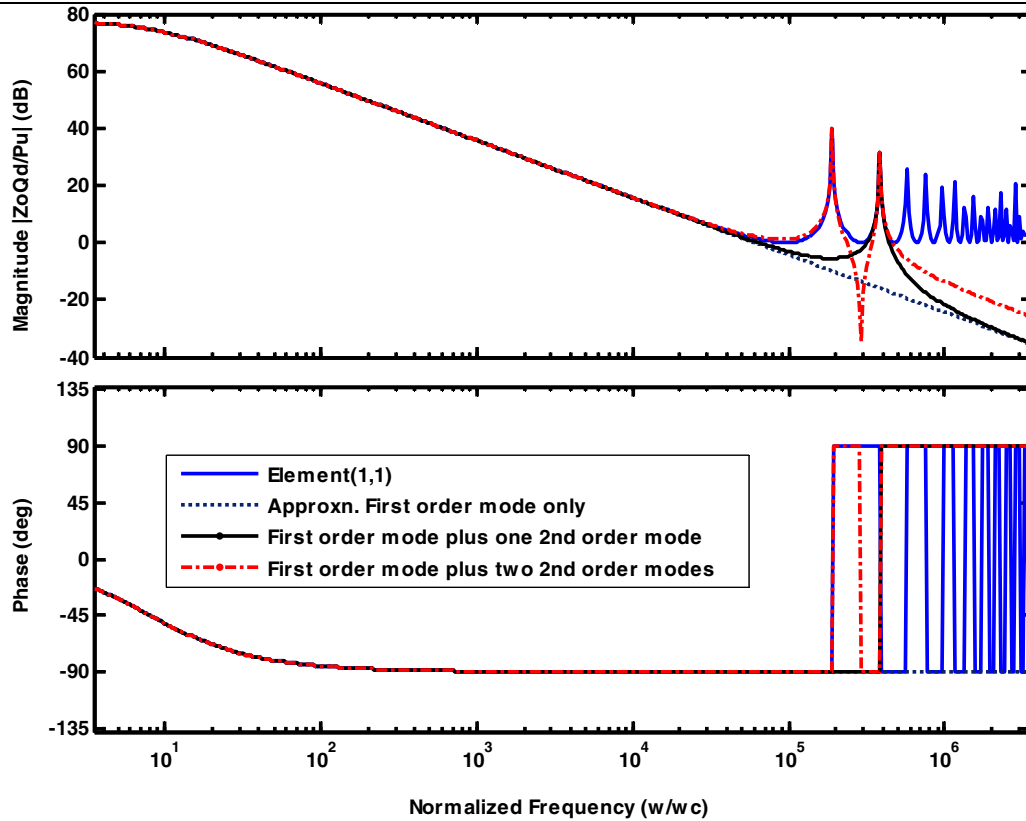
Figure 3.5: Comparison of modal approximations for element (1,1) in Eq. 3.16
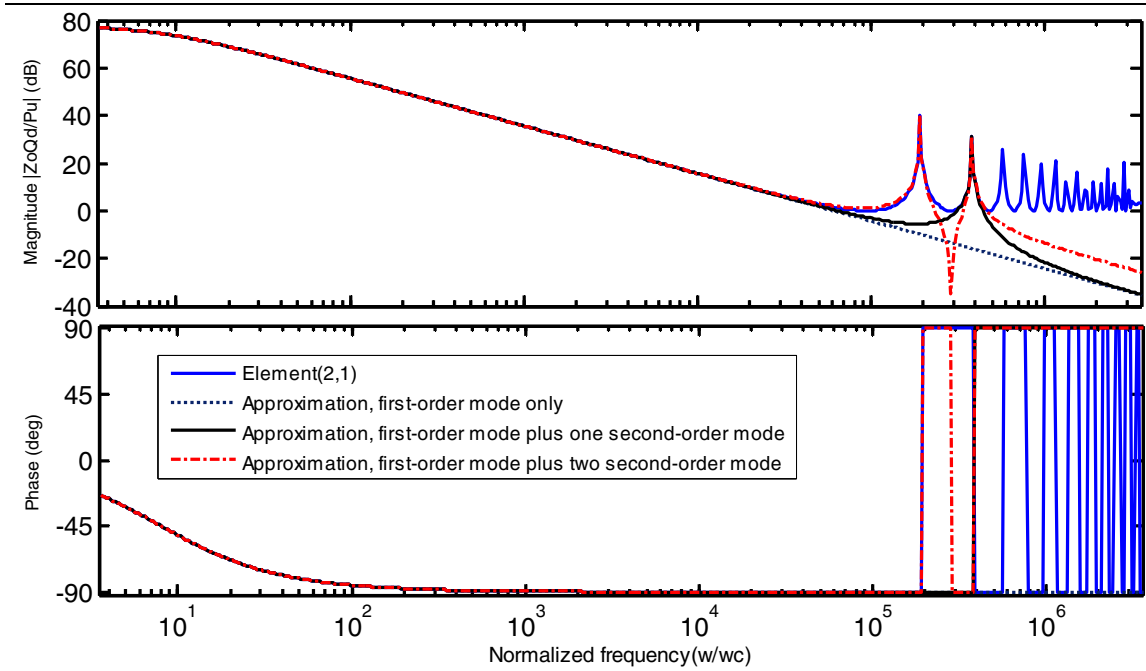
Figure 3.6: Comparison of modal approximations for element (2, 1) in Eq. 3.16.

Note that the overall number of terms to be retained in the approximation depends on the application's frequency regime of interest. It can be seen from Figs 3.5 and 3.6 that for a wide range of normalized frequency (of the order of 10^4) the model given by Eq. 3.16 can be approximated by the first-order lag term (first-order filter) only. This observation implies that for a typical circular sectioned line with a fluid viscosity of 44cSt and a line diameter of 3 cm, the line can be considered as a low-pass filter with a break frequency of about 2 Hz provided the overall frequency regime of interest for the application lies below 311 Hz. In this manner, the order of the system model to which the transmission line model belongs can be reduced significantly.

For time domain simulations, convenient state space forms can be derived for the approximation. Unlike the causality case treated by Van Schothorst [26], the block observer/observability canonical form does not lead to a minimum order realization for the causality case treated here. Instead, the following minimal state space formulation is derived by inspection from the modal transfer functions in Eq. 3.21.

$$\frac{1}{\omega_c}\boldsymbol{x}_i = \boldsymbol{A}_i\boldsymbol{x}_i + \boldsymbol{B}_i\boldsymbol{u} \qquad i = 0,1,2,3,... \tag{3.22}$$

The input and the output vectors are, respectively:

$$u = \begin{bmatrix} p_u \\ p_d \end{bmatrix} \tag{3.23}$$

$$y = \begin{bmatrix} q_u \\ q_d \end{bmatrix} = \sum_{n=1}^{n} y_i = \sum_{n=1}^{n} C_i x_i \tag{3.24}$$

The coefficient matrices are given by:

$$A_0 = \begin{bmatrix} -8 & 0 \\ 0 & -8 \end{bmatrix} \quad B_0 = \frac{1}{Z_o D_n} \begin{bmatrix} 1 & -1 \\ 1 & -1 \end{bmatrix} \quad C_0 = \begin{bmatrix} 1 & 0 \\ 0 & 1 \end{bmatrix} \tag{3.25}$$

for the first-order mode ($i=0$) and,

$$A_i = \begin{bmatrix} 0 & -\lambda_{si}^2 \\ 1 & -8 \end{bmatrix} \quad B_i = \frac{2}{Z_o D_n} \begin{bmatrix} 0 & 0 \\ 1 & -(-1)^i \end{bmatrix} \quad C_i = \begin{bmatrix} 0 & 1 \\ 1 & (-1)^i \end{bmatrix} \tag{3.26}$$

for the second-order modes ($i=1,2,3,\dots$).

For an n-mode approximation, the state and output equations can be augmented diagonally as follows:

$$\frac{1}{\omega_c} \dot{x} = Ax + Bu \tag{3.27}$$

$$y = Cx \tag{3.28}$$

where the augmented state vector and the coefficient matrices are given by the set of equations:

$$\begin{aligned}
x &= [x_1 \quad x_2 \quad x_3 \quad \cdots \quad x_n]^T \\
A &= diag[A_1 \quad A_2 \quad A_3 \quad \cdots \quad A_n] \\
B &= [B_1 \quad B_2 \quad B_3 \quad \cdots \quad B_n]^T \\
C &= [C_1 \quad C_2 \quad C_3 \quad \cdots \quad C_n]
\end{aligned} \tag{3.29}$$

The modal state vectors x_i describing the second-order modes do not have a simple interpretation of partitioned (modal) output like the causality cases treated by Yang and Tobler [66] or Van Schothorst [26] since the modal output matrices, C_i, in Eq. 3.26 are not identity matrices. This should not cause any problems as long as the model is properly interfaced with connecting subsystems with the input and output vectors given above. It should also be noted that as long as the first-order mode is

included in the approximation, the steady-state value of the truncated approximation of Eq. 3.21 with a finite number of modes is the same as that of the exact equation, Eq. 3.21. Unlike the causality cases treated in [66] and [26], there is no need to apply steady-state corrections to the approximation to offset the error of truncation. This implies that in hydraulic system modeling, whenever the causality assignment of the overall system permits it, the causality form given by Eq. 3.21 and the modal approximation given here offers better handling of steady-state response.

As mentioned above, using the first-order mode only is sufficient to approximate the transmission line model over a wide range of low frequencies. In addition, the state space description chosen above for the first-order mode has a simple interpretation: the state variables are the partitioned (modal) outputs. This helps retain physically meaningfull state variables, namely the flowrates (q_u and q_d), for ease of analysis. For a range of normalized low frequency, the inclusion of only the first-order term in the approximation of Eq. 3.21 leads to the following relation for the upstream and downstream flow rates.

$$Q_u(s) = Q_d(s) = \frac{(P_u(s) - P_d(s))}{Ls + R} \tag{3.30}$$

where the L and R are the lumped inertance and resistance of the line given by, respectively:

$$L = \frac{\rho l}{A} \tag{3.31}$$

$$R = \frac{8\rho l v}{A_r r_h^2} \tag{3.32}$$

Therefore, for short connection lines or when $D_n < 0.001$ for which the linear friction model applies [66], the transmission line model given by Eq. 3.16 can be approximated by a simple series combination of the lumped hydraulic inertance and resistance. This result implies that any compressibility effects in the transmission line are neglected for the causality case given by Eq. 3.16 , when only first-order approximation is used. When short connecting lines to gas charged or spring-loaded hydraulic accumulators are modeled with this causality case, as is the application in this chapter,

this result supports the usual assumption that the oil side compressibility is negligible compared to that of the gas/spring side, as is assumed in the following subsection.

3.2.3 Modeling Accumulators

A hydraulic accumulator is an energy storage component in the form of two separable volumes with a movable piston or deformable diaphragm separating the hydraulic fluid from the charge gas (usually nitrogen) or even sometimes a spring. Figure 3.7 shows the design of a typical gas-charged (also called hydro-pneumatic) piston accumulator, which is the only type used in the system under consideration. It is assumed here that the piston mass and seal friction are negligible. With a lumped parameter approach, this assumption implies that the gas pressure and the oil pressure are considered equal. Also the compressibility of the oil in the accumulator is considered negligible compared to the compressibility of the gas side.
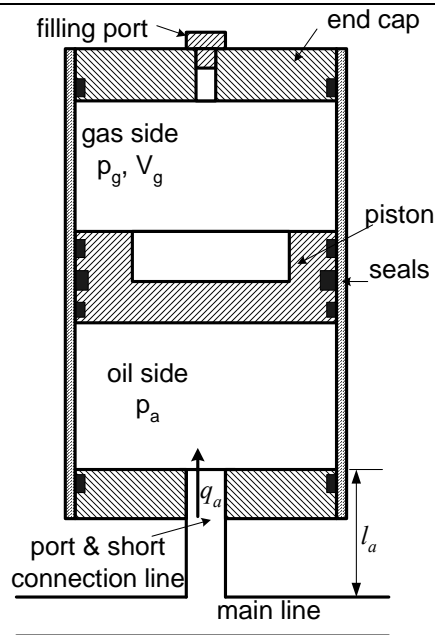
Figure 3.7: Gas-charged piston accumulator

The gas is considered to undergo a polytropic expansion and compression process with polytropic exponent m as given by:

$$p_g V_g^m = constant \tag{3.33}$$

Here V_g is the gas side volume, and p_g is the gas side pressure. The exponent m approaches 1 for a slow (nearly isothermal) process and the specific heat ratio of the gas for a rapid (adiabatic) process on an ideal gas. Given initial gas pressure p_{g0} and gas volume, V_{g0}, the gas pressure is computed from Eq. 3.33 , which is equivalent to:

$$\dot{p}_g = \frac{m\, p_g}{V_{g0} - \int\limits_0^t q_a dt}\, q_a \qquad , p_g(0) = p_{g0} \tag{3.34}$$

where q_a is the flow rate of the hydraulic oil to the accumulator. For simulations involving disturbances applied at the servovalve, it is reasonable to assume that the accumulator already develops an initial gas pressure through a slow isothermal ($m=1$) process[2]. The initial gas volume V_{g0} can be estimated by applying Eq. 3.33 between the pre-charge state (the gas pre-charge pressure at accumulator capacity) and the initial state at the onset of the disturbance. The initial gas pressure p_{g0} can be estimated as the HSM pressure minus the pressure drop in the connection lines.

It should be noted that thermal losses occur in hydro-pneumatic accumulators due to increasing entropy (dissipative heat transfer) during both the compression and the expansion of the gas. These energy losses are usually depicted as hysteresis loops in the pressure vs. volume diagram of the gas. Starting from the lumped parameter energy balance for the gas (represented by a thermal time constant) and using the ideal gas equation of state, Pourmovahed and Otis [73] derived the following transfer function model for a hydro-pneumatic accumulator relating the gas pressure (p_g) to the flow rate of the hydraulic oil into the accumulator (q_a) valid for small perturbations.

$$\frac{P_g(s)}{Q_a(s)} = \frac{p_{g0}}{V_{g0}} \left(\frac{1 + \gamma \tau s}{s(1 + \tau s)} \right) \tag{3.35}$$

---

[2]The present system has an additional slow turn-on/turn-off accumulator that enables the HSM to come to full system pressure from an off state in a slow and controlled manner. The servovalve disturbances considered in this study are applied after the whole system has reached normal operating conditions.

Here, γ is the specific heat ratio of the gas and τ is the thermal time constant. Typical empirically estimated values of the thermal time constant are in the order of 15 sec for a 2.5 liter accumulator [73, 74]. Since, the present system is intended to operate faster (at higher frequencies than relevant for such large thermal time constants), heat transfer effects are considered negligible. Furthermore for the operating pressures, which are generally less than 21 MPa (3000psi) in the present system, the behavior of nitrogen can be described sufficiently accurately using the ideal gas law. The polytropic process assumption leading to Eq. 3.34 is considered sufficient for such cases.

3.2.4 Transmission Line Model Interconnections

Again the supply line (pressure line) case is considered first. The components on the supply line of the simplified model of Fig 3.2 can be interconnected as shown in Fig 3.8 or Fig 3.9. The arrows indicate the input-output causality assigned for each subsystem. Each of the blocks named SECTION I and SECTION II implement Eq. 3.8 through Eq. 3.14 for the corresponding sections of the supply line.
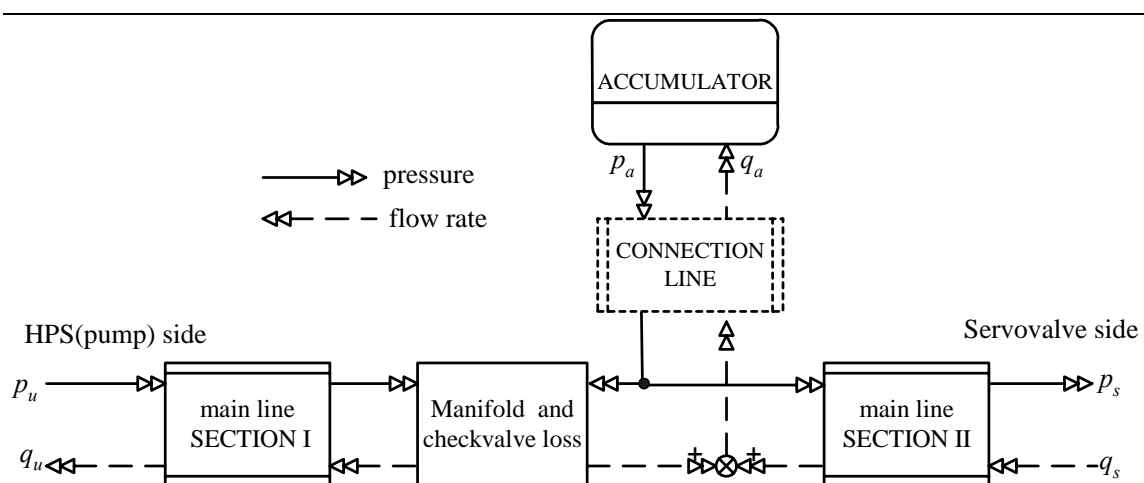
Figure 3.8: Model interconnections for the supply line (Version I)
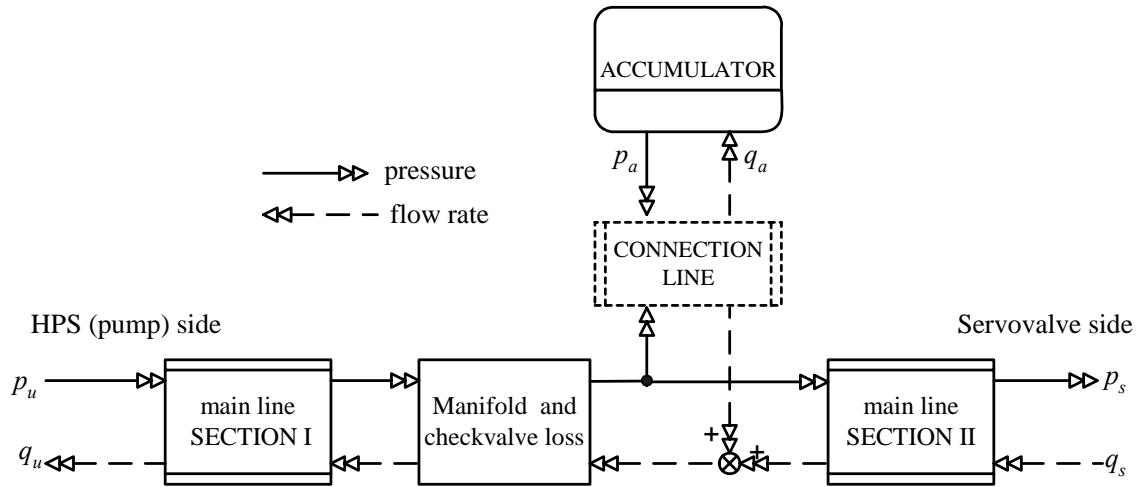
Figure 3.9: Model interconnections for the supply line (Version II)

Integration causality is the desired form for the model of the accumulator, which is given by Eq. 3.34. It was pointed out by Viersma [10] that the flow dynamics in the short branch-away connection lines to the accumulators are significant in most cases. Under the linear resistance assumption given by Eq. 3.1, the subsystem "Manifold and check valve loss" can be configured either as a pressure-input/flow rate-output subsystem (in Version I, Fig 3.8) or as a pressure-input/pressure-output subsystem (in Version II, Fig 3.9). As a consequence, the model of the short accumulator connection line changes between Version I and Version II. The model of the short connection line in Version I has the same structure as the one described above for the sections of the main supply line. The model for the short connection line in Version II is derived using the modal approximation for the relevant four-pole equations with (p_u, p_d) as input and (q_u, q_d) as output, as described in Subsection 3.2.2 and the paper by the author [69]. It was shown there that the dynamics of the short connection line can be approximated by a first-order term that reduces to a series interconnection of hydraulic resistance and inertance. This result goes along with the convenient assumption that the oil side compressibility in the accumulator is negligible compared to that of the gas side. This result also makes interconnection Version II preferable to Version I, since it reduces the dynamic order of the overall system and verifies a physically argued model order reduction for the system.

The model for the return line is developed in a similar way noting the reverse direction of the flow, as mentioned earlier in Subsection 3.2.1. It should be noted that the modularity of the subsystem model interconnections allows changes to be made to the overall system model with ease. The paper [75] by the author shows an application of the interconnected system model where the supply and return line pressure fluctuations are investigated by changing the lengths of SECTION II of the transmission hoses. It's shown there that the shorter the lengths of SECTION II of the hoses, the more effective the accumulators become in filtering out pressure fluctuations introduced by the lengths of SECTION I of the hoses.

As an example, and for future reference, consider the case where the accumulators are close-coupled with the servovalve (whose detailed model is presented in the next section).In this case, the subsystems labeled SECTION II are removed from both the supply line and return line interconnection models. Figure 3.10 shows the simulated open loop response of the pressure at the supply and return ports of the servovalve following a 50mA step current input (corresponding to full spool travel) to the servovalve. It can be seen that supply and return pressure fluctuations are eliminated in this configuration by the filtering action of the accumulators. The static pressure drop levels are attained after a short period of time. We can therefore assume that the supply and return pressures at the servovalve can be assigned average constant values for normal operation.
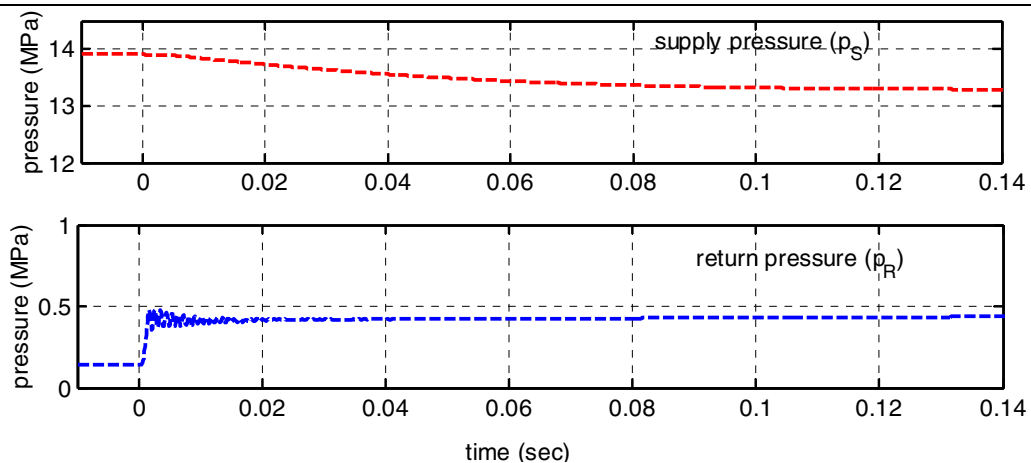
Figure 3.10: Supply and return pressure at the servovalve with close-coupled accumulators

3.3 Model for Servovalve and Actuator

3.3.1 Basic Servo-Actuator Model

Now that the components upstream (and downstream) of the servovalve, as well the possible and preferable interconnection structures have been discussed, it remains to investigate models of the servovalve and the actuator. Physical models of electrohydraulic servo-actuators are quite widely available in the literature [10, 25, 26, 34, 60, 67, 76, 77]. The model presented here is adapted to apply to a four-way servovalve close-coupled with a double-ended piston actuator.

Figure 3.11 shows a double-ended translational piston actuator with hydraulic flow rates q_t from the top chamber and q_b to the bottom chamber of the cylinder. Leakage flow between the two chambers is either internal (q_i) or external from the top chamber ($q_{e,t}$) and from the bottom chamber ($q_{e,b}$). A_t and A_b represent the effective piston areas of the top and bottom face, respectively. V_t and V_b are the volumes of oil in the top and bottom chamber of the cylinder, respectively, corresponding to the center position ($x_p=0$) of the piston. These volumes are also considered to include the respective volumes of oil in the pipelines between the close-coupled servovalve and actuator as well as the small volumes in the servovalve itself.
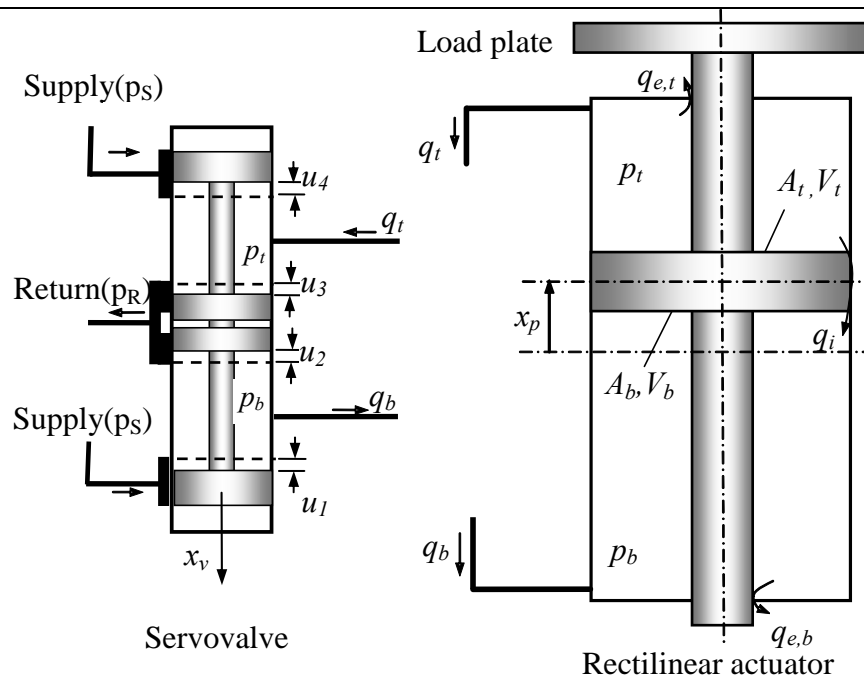
Figure 3.11:Schematic of a rectilinear actuator and servovalve

It is assumed that the pressure dynamics in the lines between the servovalve and the actuator are negligible due to the close-coupling[3]. Furthermore, even for a long-stroke actuator used in a flight simulator application, where close-coupled mounting is not feasible, Van Schothorst [26] has shown that the pressure dynamics in the actuator chambers need not be modeled using distributed parameter models. It is, therefore, assumed that the pressure is uniform in each cylinder chamber and is the same as the pressure at the respective port of the servovalve.

Starting with the continuity equation and introducing the state equation with the effective oil bulk modulus for the cylinder chambers, it can be shown that the pressure dynamics are given by (see, for example [60]):

---

[3] This is to say that any resonances introduced by the short-length lines are well above the frequency range of interest for the system. In fact, this can be verified using the model presented earlier and the causality case treated by Van Schothorst.

$$\frac{dp_b}{dt} = \frac{\beta_e}{V_b + A_b x_p}(q_b - A_b \dot{x}_p + q_i - q_{e,b}) \tag{3.36}$$

$$\frac{dp_t}{dt} = \frac{\beta_e}{V_t - A_t x_p}(-q_t + A_t \dot{x}_p - q_i - q_{e,t}) \tag{3.37}$$

These equations show that the hydraulic capacitance depends on the piston position, and is, therefore, variable. The external leakage flows $q_{e,b}$, and $q_{e,t}$ are considered negligible. The internal leakage past the piston seals is assumed here to be laminar with a leakage coefficient C_L.

$$q_i = C_L(p_t - p_b) \tag{3.38}$$

The predominantly turbulent flows through the sharp-edged control orifices of a spool valve, to and from the two sides of the cylinder chambers, are modeled by nonlinear expressions [25, 60, 67]. Assuming positive flow directions as shown in Fig 3.11, these flows are given by:

$$
\begin{aligned}
q_b = K_{v,1} sg(x_v + u_1) \operatorname{sgn}(p_S - p_b)\sqrt{|p_S - p_b|} - \\
K_{v,2} sg(-x_v + u_2) \operatorname{sgn}(p_b - p_R)\sqrt{|p_b - p_R|}
\end{aligned}
\tag{3.39}
$$

$$
\begin{aligned}
q_t = K_{v,3} sg(x_v + u_3) \operatorname{sgn}(p_t - p_R)\sqrt{|p_t - p_R|} - \\
K_{v,4} sg(-x_v + u_4) \operatorname{sgn}(p_S - p_t)\sqrt{|p_S - p_t|}
\end{aligned}
\tag{3.40}
$$

where the $sg(x)$ function is defined by:

$$sg(x) = \begin{cases} x, & x \geq 0 \\ 0, & x < 0 \end{cases} \tag{3.41}$$

The parameters u_1, u_2, u_3, u_4 are included to account for valve spool lap conditions as shown in Fig 3.11. Negative values represent overlap while positive values represent underlap. The valve coefficients $K_{v,i}$ are given by:

$$K_{v,i} = c_{d,i} w_i \sqrt{2/\rho}, \qquad i = 1,2,3,4 \tag{3.42}$$

These coefficients could be computed from data for the discharge coefficients, $c_{d,i}$, port widths, w_i, and oil density, ρ. If we assume that all orifices are identical with the same coefficient K_v, then the value of K_v can also be estimated from manufacturer data

for the rated valve pressure drop (Δp_N), rated flow (Q_N) and maximum valve stroke (x_{vmax}) using the following equation [25, 67]:

$$K_{v,i} = K_v = \frac{Q_N}{x_{v\,max}\sqrt{\frac{1}{2}\Delta p_N}}, \qquad i = 1,2,3,4 \tag{3.43}$$

As an approximation of the servovalve spool dynamics, a second-order transfer function or equivalently a second-order state space model are extracted from manufacturer specifications.

$$\frac{X_v(s)}{I_v(s)} = \frac{G_v\omega_{n,v}^2}{s^2 + 2\zeta_v\omega_{n,v}s + \omega_{n,v}^2} \tag{3.44}$$

The state equations governing piston motion are derived considering the loading model for the actuator. For the test system, the actuator cylinder is rigidly mounted on a load frame as shown in Fig 3.12. The load fame can be used as an inertial frame.
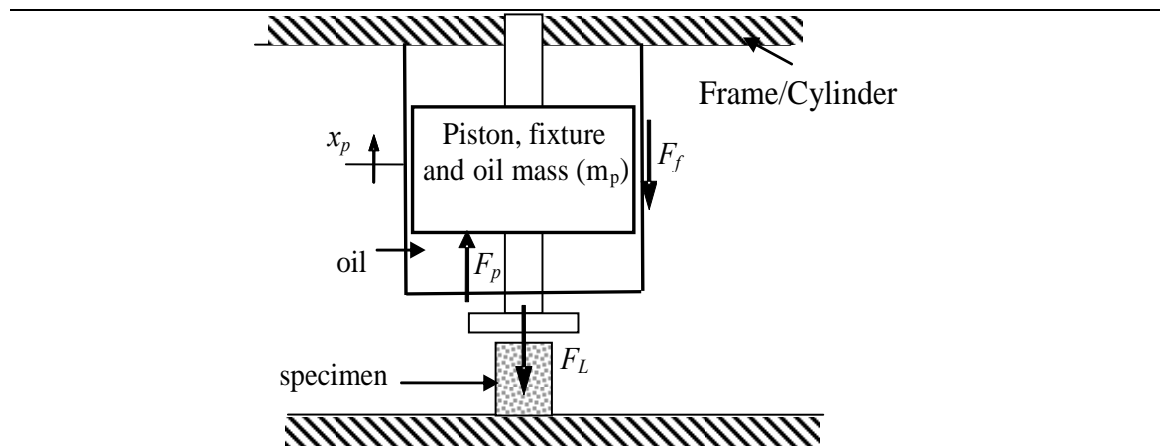
Figure 3.12: Forces on the actuator piston

The upward force on the actuator piston due to the oil pressure in the two cylinder chambers is given by:

$$F_p = A_b p_b - A_t p_t \tag{3.45}$$

The friction force on the piston in the cylinder is denoted by F_f and the external loading including specimen stiffness and damping forces are lumped together in F_L. The equations of motion are easily derived by applying Newton's Second Law as follows:

$$\dot{x}_p = v_p \tag{3.46}$$

$$\dot{v}_p = \frac{1}{m_p}[A_b p_b - A_t p_t - F_L - F_f - m_p g] \tag{3.47}$$

Equations 3.36, 3.37, 3.46 and 3.47, with q_b and q_t given by Eqs. 3.39 and 3.40, respectively, constitute the state space model for the servovalve and loaded actuator subsystem under consideration. These equations also contain the major nonlinearities in the system: the variable capacitance and the square root flow rate versus pressure drop relations. Nonlinearity is also introduced in Eq. 3.47 by the nonlinear friction force, which is discussed next.

3.3.2 Friction Estimation Experiment and Modeling

Friction affects the dynamics of the electrohydraulic servovalve as well as the dynamics of the actuator piston. Friction in the servovalve is generally considered to be predominantly of Coulomb type, acting on the spool of the valve, and can in practice be sufficiently eliminated by using dither signals [26]. The particular friction effect of interest in this section is the friction force that appears in the equations of motion of the actuator piston. The literature offers various empirical models applied to specific hydraulic actuators [34, 42, 67, 78]. In the most general case, friction in the actuator cylinder is considered to be a function of the position and velocity of the piston, the chamber pressures (the differential pressures when the piston is sticking near zero velocity), the local oil temperature and also running time.

In a previous work [75], open-loop and closed-loop tests were performed to identify the friction force on the actuator piston by assuming it to be a function of velocity. The open-loop tests involved changing the set current input to the servovalve while measuring the steady-state cylinder chamber pressure responses as well as

estimates of the steady-state velocity estimated by differentiating piston position responses.[4] The friction force is then estimated from Eq. 3.47, assuming the acceleration and the external force to be zero. Strong scatter was observed in the friction estimated from such open loop tests.

Improved and more realistic friction force estimates, including hysteresis effects, were obtained by performing friction estimation with closed loop position control tests after warm up periods to stabilize oil temperatures. The tests involved tracking a 2 Hz 35 mm sine wave position command under P-control while measuring acceleration, piston position and chamber pressures. Newton's second law (Eq. 3.47) was again used to estimate the friction force without having to assume zero acceleration. The velocity is computed by taking the finite difference derivate of the position response. Fig 3.13 shows the result form one such closed loop test. It shows that the hysteretic behavior of friction is especially strong in the upward (positive velocity) motion. It can also be observed that the friction force is slightly asymmetric with respect to direction of motion.
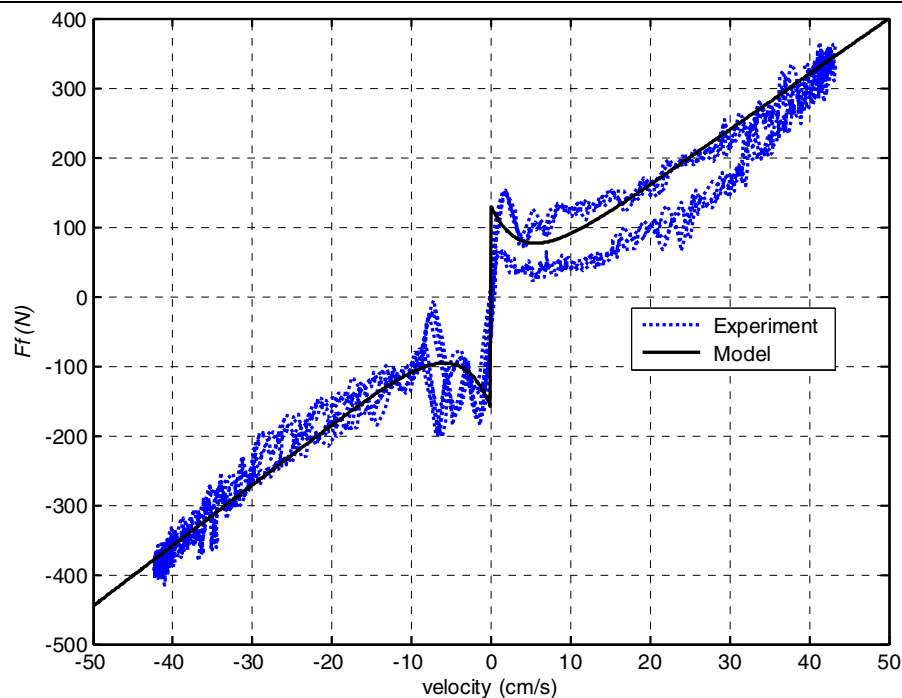
Figure 3.13: Piston friction force

---

[4] It should be recalled that the actuator approximates a velocity source in the open-loop.

For simplicity, the common memory-less analytical model of friction force (without hysteresis) as a function of velocity, given by Eq. 3.48, is adopted.

$$F_f = F_v^\pm \dot{x}_p + sign(\dot{x}_p)(F_c^\pm + (F_S^\pm - F_c^\pm)e^{-|\frac{\dot{x}_p}{C_s^\pm}|}) \tag{3.48}$$

It is a combination of the so called Stribeck, Coulomb and Viscous terms. The coefficients are computed by fitting this equation to the experimental data shown in Fig 3.13. The observed asymmetry of the experimentally determined friction force with respect to the sign of the velocity is taken into account by taking different coefficients for the up and down motions(denoted by $\pm$ superscripts in Eq. 3.48). In Subsection 4.1.4.2, it will be shown that this equation can further be smoothened by using some approximations.

3.4 Experimental Validation of the Overall System Model

The models described in the previous sections were simulated in MATLAB/Simulink and baseline open-loop and closed-loop experiments were conducted to validate the overall system model. In the experiments, a simple load mass is rigidly attached to the piston rod, and so the external load force is set to zero. For the models of each of the sections of the supply and return line hoses, only six modes were retained in the modal approximation. This was decided considering the actuator hydraulic natural frequency of 172 Hz computed using formulae from linear models (see Ref [24, 25]) and selecting the natural frequency of the highest mode of the approximation for each section to be close to twice this value. From frequency response data, the natural frequency for the servovalve was estimated to be 140 Hz with a damping ratio of 1.1 with the pump supply pressure set independently at 14 MPa.

3.4.1 Open-Loop Responses

Open-loop tests were conducted by step changing the current input to the servovalve, which otherwise is the control input in closed-loop feedback control. In these tests, a step change in the current input was supplied to the servovalve in the open-loop. Fig 3.14 shows a comparison of the supply and return pressure at the servovalve from measurement and simulation for a 50 mA step change in the current input. To measure these supply and return pressure fluctuations, pressure transducers were mounted on the supply and return ports of the servovalve.

Two observations can be made from the data in Fig 3.14. First, the supply and return pressure fluctuations contain the fundamental periods of 25 ms and 32 ms, respectively. These correspond to fundamental frequencies of about 40 Hz and 31 Hz, respectively. The implication of these fluctuations is that the bandwidth of the actuation system is limited by the dynamics of the supply and return hoses, since the other dynamic elements including the servovalve and the actuator have higher corner frequencies. Second, the model follows the measurement well, particularly in frequency content. Remaining discrepancies are attributed to errors in the estimation of effective bulk moduli for the different hose sections, truncations in the modal approximation of the transmission line models, the estimation of manifold pressure drop coefficients as well as the estimated parameters in the adopted simplified model of the servo-actuator.
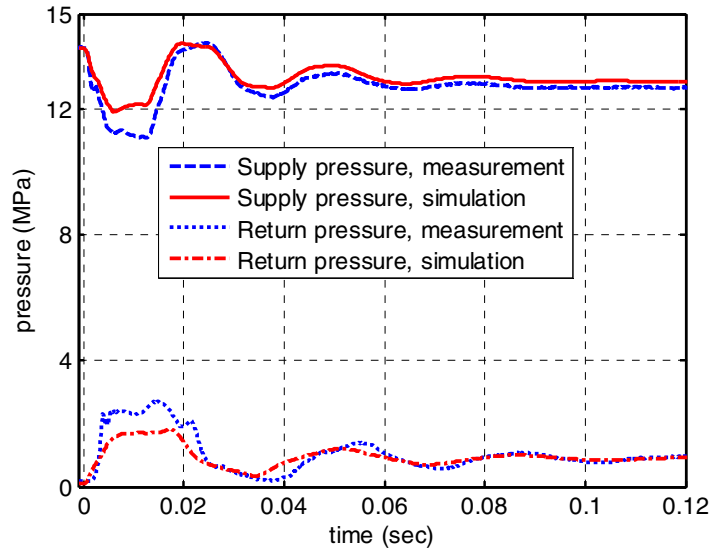
Figure 3.14: Supply and return pressures at the servovalve, model vs. experiment

The open-loop response of the system can be investigated further by looking at the cylinder chamber pressures shown in Fig 3.15 for the same rated step change in the current input as above. It can be seen that the simulation predictions of chamber pressures follow the measurements and that the supply and return pressure dynamics introduced by the long sections of hoses are reflected in the individual cylinder chamber pressures. The oscillation due to the actuator and servovalve dynamics happens on a faster time scale but is dominated by slower line dynamics effects. In this particular test, the fast oscillation happens at about 150 Hz, but this frequency is subject to change with actuator position.
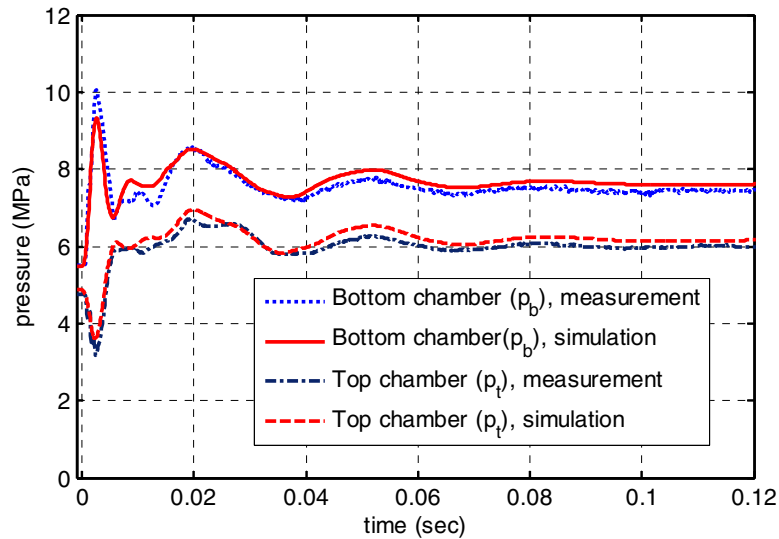
Figure 3.15: Cylinder chamber pressures, model vs. experiment

The open-loop piston velocity responses to various magnitude step changes in the current input are shown in Fig 3.16. The velocity signal was obtained by low-pass filtering (to 400 Hz) and then differentiating the LVDT position signal. In all cases, the step change in current is applied by first bringing the piston to approximately x_p=-30 mm for the positive step current changes (upward motion) and to x_p=30 mm for the negative changes (downward motion). It can be seen that the velocity responses to higher magnitudes of the step current change are different from those to lower magnitudes of current. In particular, the responses to higher magnitude current step changes exhibit more damping. This demonstrates the nonlinear behavior of the servo-actuator as an open-loop velocity source.

Fig 3.16 shows that the model does a good job of predicting the piston velocity responses for different magnitudes of the step current input. Differences are again attributed to uncertainties in the servo-actuator model parameters, limitation of the measured velocity estimation, and also errors in friction estimation, which has a considerable scatter as shown in Fig 3.13 .
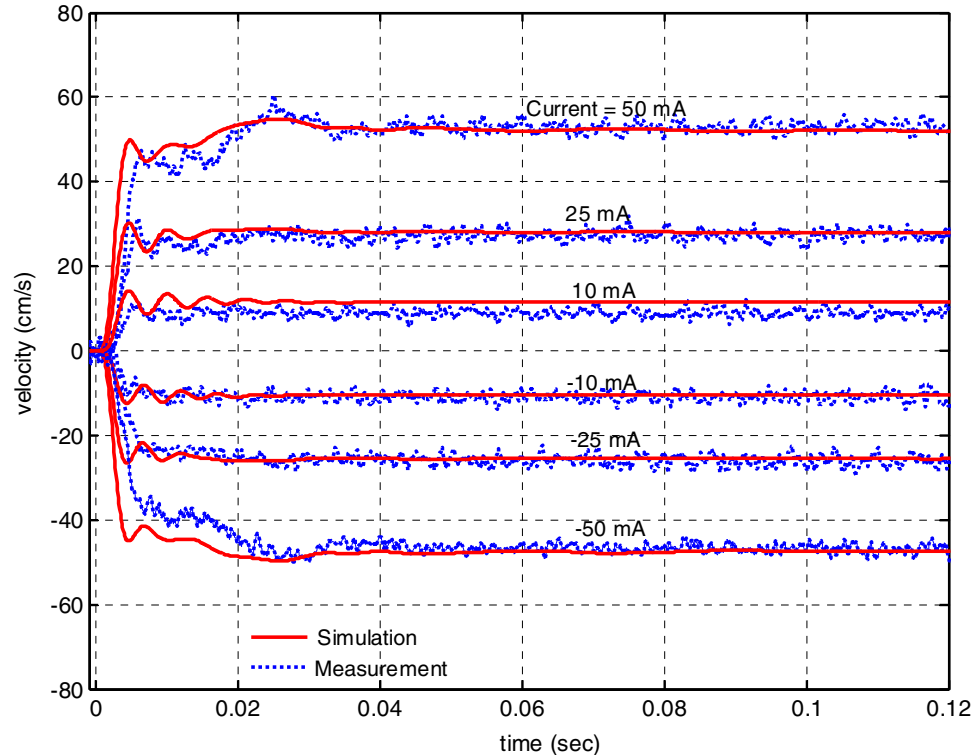
Figure 3.16: Piston velocity at various step changes in current, model vs. experiment

3.4.2 Closed-Loop Responses

Further comparisons were performed between simulations and experiments under closed-loop tests. Linear proportional position controllers (P-controllers) with identical gains were used in both the simulations and the experiments. Sampling rates were set at 1000 Hz for the experiments.

Fig 3.17 shows the simulated and measured position and velocity of the actuator when tracking a 25 mm, 1 Hz square wave reference position. The prediction matches the measurement very well. However, some deterioration is observed in the prediction of the upward motion. This can be explained by the rather large uncertainty in the friction model adopted for the upward motion as shown in Fig 3.13.
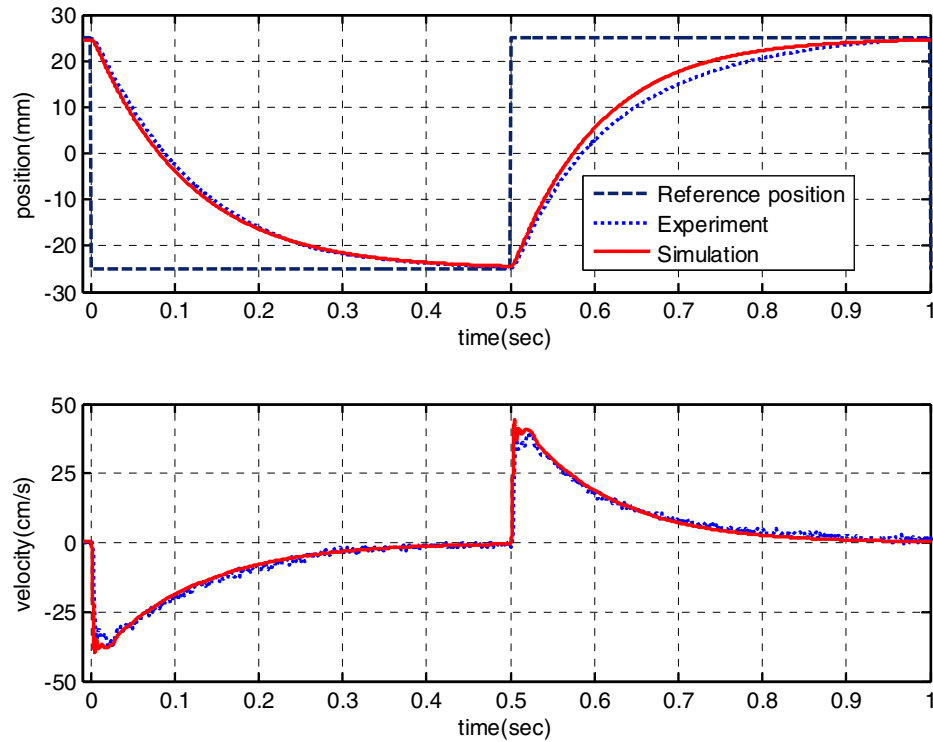
Figure 3.17: Piston position and velocity, model vs. experiment

As can be seen with the lower plot in Fig 3.17, the velocity approaches zero as the piston reaches the commanded position. As could be expected from the velocity source analogy of the servo-actuator, the velocity response also roughly corresponds to the control current input which is shown in Fig 3.18. Recall that the current input, in turn, corresponds to the servovalve spool position response with the dynamics given by Eq. 3.44. The valve spool, therefore, returns to the null position ($x_v = 0$) as the commanded piston position is approached.
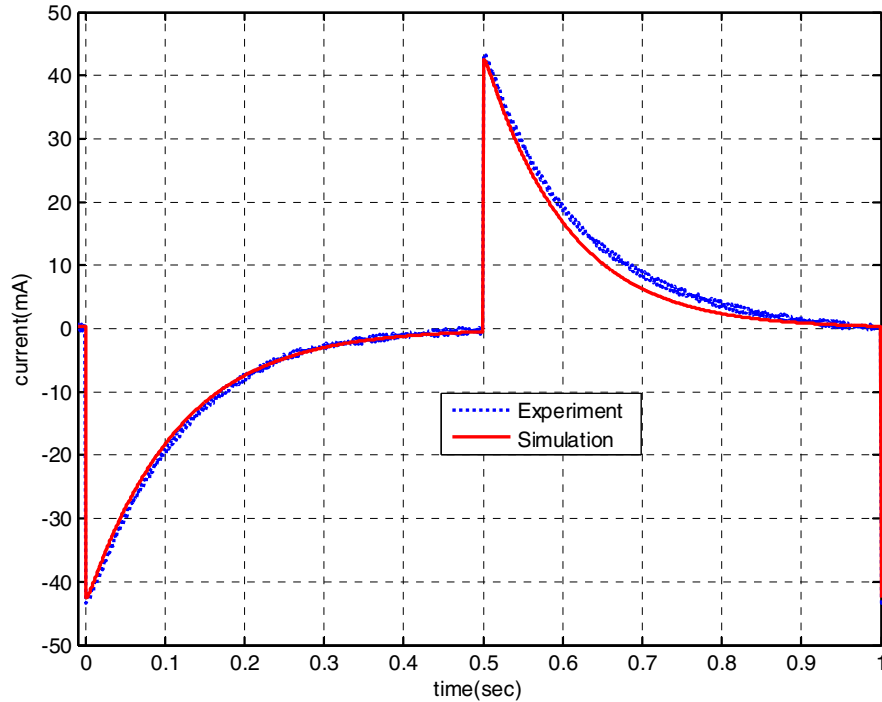
Figure 3.18: Control current input, model vs. experiment

During the same closed-loop test described above, the response of the chamber pressures, which were expected to depend on the supply and return pressure fluctuation based on the previous observation of the open-loop response, shows some interesting features. When valve lap lengths were ignored and a critical center valve was assumed for the model ($u_1=u_2=u_3=u_4=0$ in Eqs. 3.39 and 3.40), the chamber pressures stay at a higher steady-state value after the transients die down as shown in Fig 3.19. The model works well in the fast time transient duration and shows that, just like in the experiment, the line dynamics effects reflect onto the dynamics of the chamber pressures, but it fails to follow the measurements at steady-state.
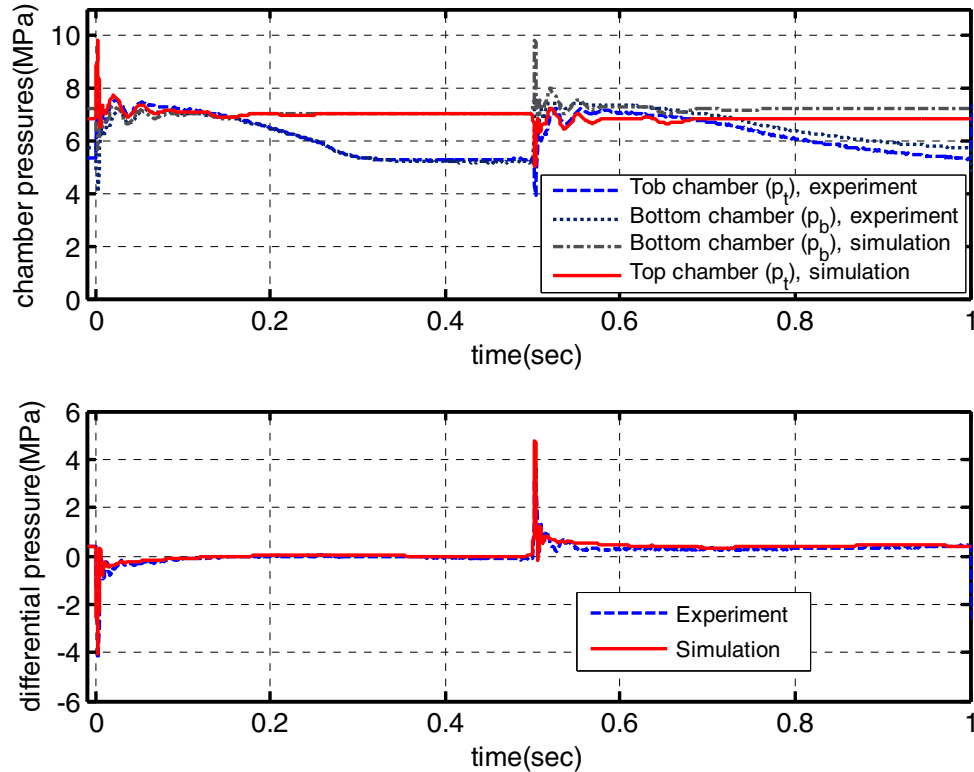
Figure 3.19: Pressure responses under closed loop position control, model vs. experiment

The source of the discrepancy on the steady-state chamber pressures can be explained by referring to the statement made above that in closed-loop position control, the valve spool approaches its null position as the desired piston position is approached. In a real and worn valve, the null region is dominated by valve spool lap conditions and associated leakage [79, 80]. The model adopted above allows for including lap effects only through (u_1, u_2, u_3, u_4), while there were no direct provisions to measure the lap geometry of the worn valve used in the experiments. Therefore, a heuristic approach was used to see if, in fact, the discrepancy between model and experiments can be attributed to lap conditions and undue simplifications in the valve model. Figure 3.20 shows results obtained for one set of lap parameters where the lap values are assumed such that the lands on the supply port (u_1, u_4) are slightly overlapped (order of -10^{-5}cm) and those on the return port (u_2, u_3) are slightly underlapped (order of 10^{-6}cm). The remaining discrepancy that still exists with lap conditions included could perhaps be explained by a more detailed valve model, with the complete leakage geometry accounting also for the

contribution of radial clearance between the valve spool and its sleeve [26]. The latter was completely ignored in the model adopted here in order to simplify the viability of the model for the derivation of the nonlinear control laws detailed in the next chapter.
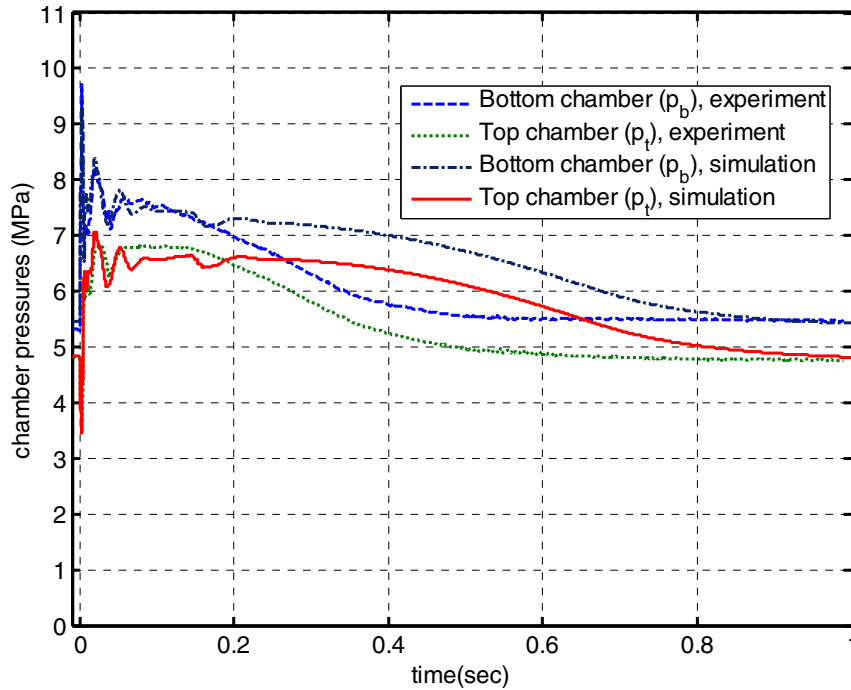
Figure 3.20: Chamber pressures during the upward motion, with port leakage

It should be remarked that the measured differential or load pressure ($p_L=\Delta p=p_b-p_t$) is predicted well with the simulation as shown on Fig 3.19. This will allow us to consider a reduced order system model in terms of load pressure in Subsection 4.1.2.3. For a nearly symmetric servo-actuator with nearly symmetric cylinder volumes and nearly symmetric and matched port flows, only the differential pressure (p_L) can be controlled by modulating flows. The mean of the chamber pressures is hardly controllable, as the dynamics of the individual chamber pressures are governed by nearly anti-symmetric equations. As a result, as one chamber pressure rises, the other can fall by an amount that changes the differential pressure (p_L) and yet keeps the mean pressure constant. This can be shown by linearizing the system equations (Eqs. 3.36, 3.37, 3.46, and 3.47) around operating points [26].

3.5 Chapter Summary

In this chapter, dynamic models were developed for an electrohydraulic system that shall be used as an experimental test stand for the design and analysis of nonlinear controllers in the next chapter. Causality assignments were selected for the different component models and a system interconnection model was chosen for the test system.

The following points summarize the main contributions of this chapter.

- A modular time domain modeling approach, suitable for use with nonlinear actuator models, was developed to incorporate supply and return pressure variations at the servovalve of electrohydraulic systems. This approach enables the analysis of distributed dynamics in fluid transmission lines in the time domain via state space LTI (linear time-invariant) formulations that offer modular and simpler alternatives to finite difference-based time domain solutions of the flow equations.

- The modal approximation adopted for the model of the main supply and return transmission lines fits the causality form treated by others [26, 66]. The mathematical derivation of the modal approximation for the fourth causality case with upstream and downstream pressures as input and upstream and downstream flow rates as output, however, was developed in this work. It applies to hydraulic transmission lines for which the linear friction model is good, i.e., where the line dissipation number, D_n, is of the order of 10^{-3}. Both transfer function and state space forms were presented.

- It was shown that the modal approximation for the latter causality case (treated in this work) offers at least two conveniences over the other forms: namely, better handing of steady-state response, and the possibly of model order reduction since the modal approximation reduces to a first-order filter comprised of a series interconnection of hydraulic resistance and inertance over a wide range of low frequency regimes.

- For controller development, the complete nonlinear servo-actuator state space model described in Section 3.3 is highly relevant. The modeled dominant nonlinearities are highlighted to include: the variable hydraulic capacitance in the cylinder chambers, the square root flow rate versus pressure drop relations, and nonlinear friction force on the piston, which includes Coulomb, static and viscous components. A rather

extensive model-based experimental analysis of the nonlinearities in an electrohydraulic actuator (including those in the servovalve) has already been detailed by other researchers, most notably by Van Schothorst [26].

- The overall system model was validated with experiments. Except for the effects of valve leakage on the chamber pressures, the model captured measured responses well. It is anticipated that the model could work even better for systems with a newer and well adjusted servovalve with somewhat easier to estimate leakage characteristics than the present one (which has unknown wear levels).

Finally, we point out that while the discussion in this chapter was focused on the test system under consideration, most of the results are quite typical for many electrohydraulic systems.

Chapter 4

Nonlinear Control Based on Feedback Linearization

The system model detailed in the previous chapter shall be used to derive nonlinear controllers in this chapter. The chapter is organized in three major sections. In Section 4.1, the analytical derivation of nonlinear force and position tracking controllers will be detailed from a feedback linearization framework. Different versions of force and/or piston position tracking controllers will be presented and analyzed. We will summarize the common characteristics of the nonlinear controllers and discuss robust versions that incorporate sliding mode control. In Section 4.2, the performance of the nonlinear controllers will be discussed at length. Extensive experimental and simulation results will be presented and discussed. Section 4.3 presents the summary for the chapter.

4.1 Derivation of Nonlinear Controllers Based on Feedback Linearization

In this section, nonlinear controllers are derived for an electrohydraulic system under some simplifying assumptions. First, these assumptions will be itemized in Subsection 4.1.1. As shall be evident from the discussion in this chapter, the nonlinear model-based force control problem forms a natural pre-cursor to the position control problem. So, we discuss the force controllers in Subsection 4.1.2, followed by the position controllers in Subsection 4.1.3. The nonlinear force and position controllers exhibit certain common characteristics that will be summarized in Subsection 4.1.4. Since model uncertainties are almost inevitable, it is necessary to seek robust nonlinear controllers. This is the topic of Subsection 4.1.5. Finally, in Subsection 4.1.6, simulations of the validated system model discussed in Chapter 3 will be used to investigate the effect of the basic assumptions made for the derivation of the nonlinear controllers.

4.1.1 Basic Assumptions

For the purpose of control design, it is common practice to simplify the system model to allow the derivation and analysis of suitable control laws. In this section, some simplifications are introduced while retaining the dominant nonlinearities in the model of the electrohydraulic system. Recall that these nonlinearities include the square-root port flow rate vs. pressure drop relation, the position dependence of the hydraulic compliance in the cylinder chambers, and the nonlinear friction force on the piston. It will be shown, in this chapter that, the controllers from feedback linearization attempt to cancel these nonlinearities so that the closed loop system model becomes linear under some simplifying assumptions.

The first set of assumptions made here for the purpose of control law derivation is regarding the servovalve. The servovalve is assumed to be critically centered with symmetric and matched orifices. That is, the underlap/overlap lengths are neglected. Instead, an offset value of the valve position can be estimated during calibration to take into account abrasion-induced null offsets [60]. Also, the valve spool dynamics are neglected on the basis that the natural frequency should be higher than the relevant bandwidth of the position and/or force control system. This implies that the valve spool position is assumed to be related to the servovalve current with a static gain as given by:

$$\bar{i}_v = G_v \bar{x}_v \tag{4.1}$$

where, $\bar{i}_v = i_v - i_{voff}$ and $\bar{x}_v = x_v - x_{voff}$, with i_{voff} and x_{voff} representing the current offset and valve spool position offset, respectively. Under these assumptions, either the servovalve current or the valve spool position can be considered as the control variable for analysis. Since the valve spool position is not measurable for the test system under consideration, and also for the convenience of working with the actual physical control input, only the servovalve current is used as the control variable in this work. The flow rates to and from the cylinder chambers are then rewritten as:

$$q_b = C_{v,1} sg(\bar{i}_v) \operatorname{sgn}(p_S - p_b) \sqrt{|p_S - p_b|} - C_{v,2} sg(-\bar{i}_v) \operatorname{sgn}(p_b - p_R) \sqrt{|p_b - p_R|} \qquad (4.2)$$

$$q_t = C_{v,3} sg(\bar{i}_v) \operatorname{sgn}(p_t - p_R) \sqrt{|p_t - p_R|} - C_{v,4} sg(-\bar{i}_v) \operatorname{sgn}(p_S - p_t) \sqrt{|p_S - p_t|} \qquad (4.3)$$

where sgn(x) is the *signum* (sign(x)) function, and the new valve coefficients $C_{v,i}$ referenced to the current are given by:

$$C_{v,i} = G_v(K_{v,i}) \qquad i = 1,2,3,4 \qquad\qquad (4.4)$$

The form of the flow rate equations given by Eqs. 4.2 and 4.3 make it possible to estimate the actual valve coefficients from experimental data, as described in Appendix B.

The second set of assumptions, made here for the purpose of control law derivation, regards the transmission lines upstream and downstream of the servovalve. It is assumed the supply and return line pressure fluctuations are minimal and that the two pressures can be considered constant at the servovalve. In practice, this is approached by close-coupling the supply and return accumulators with the servovalve.

The third assumption is more of a requirement for the application of the particular control laws discussed in this work. We assume that, in all cases, the desired trajectory or profile for the output to be tracked (position, pressure or force) is bounded and differentiable, with bounded derivatives to the relevant order. The order is usually evident with the particular tracking problem.

The fourth assumption regards whether or not the electrohydraulic system model can be considered truly feedback linearizable. Feedback linearization can be applied directly to a class of nonlinear systems called affine input systems, where the control input appears explicitly and linearly in the state equations. A formal theory of feedback linearization is detailed in the texts by Slotine and Li [31] and Khalil [30]. For some systems, exact (full state or input-state) linearization may not be feasible. However, based on the output definition chosen or called for by the physical application, input-output linearization (which is partial feedback linearization) can be performed.

In the strict sense, as will be detailed in the following subsections, the nonlinear electrohydraulic system model is not an affine input system. However, the system model

lends itself to piecewise input-output (IO) linearization that comes very close to a true feedback linearization and is shown to work satisfactorily well under a simple practical consideration. It is assumed that for the systems under study, the control current does not change signs infinitely fast or at least no faster than the base sample rate of the digital implementation. In this thesis, the controllers relying on this assumption are referred to as Near Input-Output (or Near IO) linearizing controllers.

4.1.2 Force Tracking Control

4.1.2.1 Pressure Force Tracking Control

Taking the derivative of the pressure force defined by Eq 3.45 and using Eqs 3.36 and 3.37 it can be shown that:

$$\dot{F}_p = -\dot{x}_p \beta_e \left(\frac{A_b^2}{V_b + A_b x_p} + \frac{A_t^2}{V_t - A_t x_p} \right) + \frac{A_b \beta_e}{V_b + A_b x_p}(q_b + q_i) + \frac{A_t \beta_e}{V_t - A_t x_p}(q_t + q_i) \quad (4.5)$$

where the external leakages, $q_{b,e}$ and $q_{t,e}$, are neglected assuming a well sealed actuator.

Using Eqs. 4.2 and 4.3 for q_b and q_t respectively, and regrouping variables, Eq. 4.5 can be rewritten as follows:

$$\dot{F}_p = f_F(x_p, \dot{x}_p, p_b, p_t) + g_F(x_p, p_b, p_t, \text{sgn}(\bar{i}_v))\bar{i}_v \quad (4.6)$$

where the nonlinear functions f_F and g_F are, respectively:

$$f_F(x_p, \dot{x}_p, p_b, p_t) = -\dot{x}_p \beta_e \left(\frac{A_b^2}{V_b + A_b x_p} + \frac{A_t^2}{V_t - A_t x_p} \right) + \frac{A_b \beta_e C_L(p_t - p_b)}{V_b + A_b x_p} + \frac{A_t \beta_e C_L(p_t - p_b)}{V_t - A_t x_p} \quad (4.7)$$

$$g_F(x_p, p_b, p_t, \text{sgn}(i_v)) = \begin{cases} \dfrac{A_b \beta_e C_v}{V_b + A_b x_p} \text{sgn}(p_S - p_b) \sqrt{|p_S - p_b|} \, + \\[2mm] \dfrac{A_t \beta_e C_v}{V_t - A_t x_p} \text{sgn}(p_t - p_R) \sqrt{|p_t - p_R|} \qquad for\, \bar{i}_v \geq 0 \\[2mm] \dfrac{A_b \beta_e C_v}{V_b + A_b x_p} \text{sgn}(p_b - p_R) \sqrt{|p_b - p_R|} \, + \\[2mm] \dfrac{A_t \beta_e C_v}{V_t - A_t x_p} \text{sgn}(p_S - p_t) \sqrt{|p_S - p_t|} \qquad for\, \bar{i}_v < 0 \end{cases} \qquad (4.8)$$

Equation 4.6 with f_F and g_F defined, respectively, by Eqs. 4.7 and 4.8, contains all the major modeled nonlinearities in the hydraulic system that arise from fluid compliance and turbulent orifice flow. Also, the derivative of the output pressure force F_p can be seen to be only piecewise linear in the control input ($\bar{i}_v$). This suggests that an input-output (IO) linearization with a relative degree of one can be performed in the respective domains ($\bar{i}_v \geq 0$ and $\bar{i}_v < 0$) [30, 31]. In particular, we can cancel the nonlinearities in the pressure force dynamics (Eq. 4.6) by choosing the piecewise IO linearizing control input:

$$\bar{i}_v = \frac{1}{g_F(x_p, p_b, p_t, \text{sgn}(\bar{i}_v))}(v - f_F(x_p, \dot{x}_p, p_b, p_t)) \qquad (4.9)$$

where v is a new (transformed) control input. The pressure force dynamics (Eq. 4.6) reduce to:

$$\dot{F}_p = v \qquad (4.10)$$

This is a simple linear integrator which can easily be stabilized by state feedback. Exponentially convergent tracking of a desired differentiable pressure force profile ($F_{p,d}$) can be achieved by choosing v as:

$$v = \dot{F}_{p,d} - k_o(F_p - F_{p,d}) \qquad (4.11)$$

The force tracking error dynamics is given by:

$$\dot{e}_F + k_o e_F = 0 \qquad (4.12)$$

where e_F is the force tracking error, $e_F = F_p - F_{p,d}$.

In summary, the control input of Eq. 4.9 with *v* given by Eq. 4.11 and a proper choice of $k_o > 0$ can give a desired degree of exponential force tracking performance regardless of the nonlinearities in Eq. 4.6 provided the internal dynamics are stable. In terms of the force tracking error, the control current is given by:

$$\bar{i}_v = \frac{1}{g_F(x_p, p_b, p_t, \mathrm{sgn}(\bar{i}_v))} (\dot{F}_{p,d} - k_o e_F - f_F(x_p, \dot{x}_p, p_b, p_t)) \tag{4.13}$$

It is important to note that Eq. 4.9 (or equivalently Eq. 4.13) cannot be solved "as is", since it contains the control variable, $\bar{i}_v$, on both sides of an equation involving the sgn function. A practical solution to this problem becomes evident when considering the digital implementation of the piecewise IO linearizing controller. The sign of the value of $\bar{i}_v$ at the previous time step can be used to compute the value of $\bar{i}_v$ at the current time step, if it can be supposed that the current does not change signs at a rate faster than the control sampling rate. It is difficult to prove that this approach does not lead to control chatter, even though this problem has been not reported previously in the literature that discusses IO linearization for hydraulic drives [27, 33, 35]. In addition, chattering problems traceable to this assumption have not been experienced during any of the experiments conducted for this thesis. Another solution is to use approximations of the sgn(*x*) function, like the one given by Eq. 4.47 in Subsection 4.1.4.2, so that Eq. 4.13 can be solved (fast enough) in the real time implementation. This is possible with the load pressure description of g_F given in Subsection 4.1.3.2. We chose the former approach of relying on a fast sampling rate for its simplicity.

The above assumption that the sign of the value of $\bar{i}_v$ at the previous time step can be used to compute the value of $\bar{i}_v$ at the current time step is needed in order to be able to solve Eq. 4.13. It is conjectured that this approach gives an IO linearizing controller that comes very close to a true IO linearizing controller if there were one. To make the explicit distinction between a true IO linearizing controller and the one obtained under the above assumption, the term Near IO linearizing controller is suggested and used in this work.

Note that the piecewise IO linearization resulted in a system of relative degree one in each domain ($\bar{i}_v \geq 0$ and $\bar{i}_v < 0$). That is, only one differentiation of the output was needed before the input appeared. The external dynamics are given by Eq. 4.10. It remains to evaluate the stability of the internal dynamics of degree 3, which involves system states that are rendered "unobservable" during the feedback linearization. An investigation of the stability of the internal dynamics is better handled using the concept of load pressure to be introduced in Subsection 4.1.2.3. The stability analysis is included in Appendix C.

Figure 4.1 shows the schematic for the implementation of the Near IO linearizing pressure force tracking controller. Note that this implementation assumes that the two chamber pressures as well as the position and velocity of the piston are available by measurement. Note also that the pressure force control loop does not explicitly depend on the load force (F_L) or on the friction force (F_f) on the piston. Implicitly, however, these forces determine the position and velocity of the piston (or its internal dynamics as shown in Appendix C).

An important consequence of the nonlinearity cancellation with the Near IO linearizing pressure force tracking controller is that a decoupling of the pressure dynamics from the piston motion is obtained by the positive (nonlinear) velocity feedback. This can be seen by looking at the first term of the nonlinear function, f_F, given by Eq. 4.7, and the expression for the controller given by Eq. 4.13. This observation will be exploited in the discussion of piston position control in Subsection 4.1.3.2.
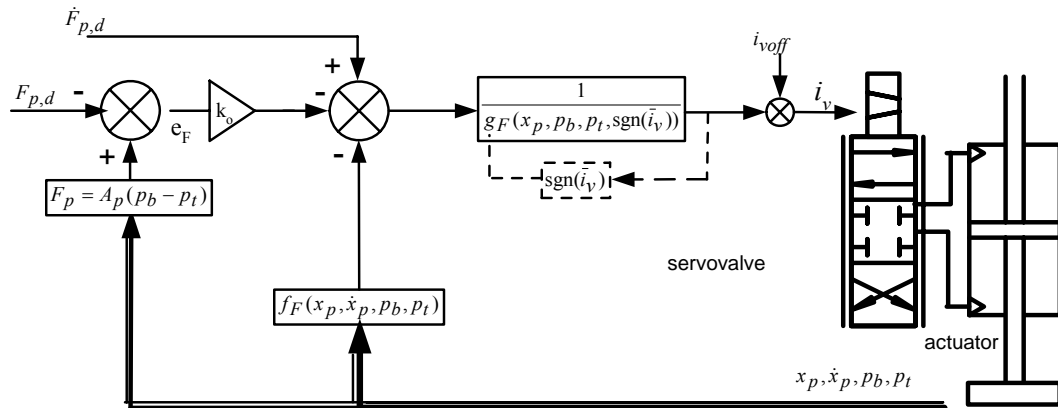
Figure 4.1:Schematic for Near IO linearizing pressure force tracking controller

4.1.2.2 Load Force Tracking Control

This section is included to highlight the application of the IO linearization approach to the control of the net force applied to the load (such as the stiffness and damping forces on a fatigue specimen), which is referred to in this work as the load force (F_L). For the system shown in Fig 3.12, this force is given by:

$$F_L = F_p - F_f - m_p(g + \ddot{x}_p) \qquad (4.14)$$

Differentiating Eq. 4.14 and using Eq. 4.6 , we obtain:

$$\dot{F}_L = f_F(x_p, \dot{x}_p, p_b, p_t) - \dot{F}_f - m_p(\dddot{x}_p) + g_F(x_p, p_b, p_t, \text{sgn}(\bar{i}_v))\dot{\bar{i}}_v \qquad (4.15)$$

Proceeding as above, the Near IO linearizing controller for this definition of system output can be shown to be:

$$\dot{\bar{i}}_v = \frac{1}{g_F(x_p, p_b, p_t, \text{sgn}(\bar{i}_v))}(\dot{F}_{L,d} - k_L(F_L - F_{L,d}) - f_F(x_p, \dot{x}_p, p_b, p_t) - \dot{F}_f - m_p(\dddot{x}_p)) \qquad (4.16)$$

Here, the gain $k_L > 0$ is chosen to stabilize the dynamics of the closed-loop load force tracking error, which is given by:

$$(F_L - \dot{F}_{L,d}) + k_L(F_L - F_{L,d}) = 0 \tag{4.17}$$

It can be seen that the load force tracking controller given by Eq. 4.15 needs additional variables for feedback, compared to the pressure force controller given by Eq. 4.13. Namely, the controller requires feedback of the derivatives of the friction and inertia forces and feedback of the load force. The load force can be measured directly by placing a load cell between the actuator piston and the specimen (or on the load plate) or it can be indirectly estimated from the variables in Eq. 4.14. It is particularly important that a good and differentiable approximation of the friction force be found. This issue is pursued in Subsection 4.1.4.2. While the above load force controller may indeed be studied further, this is not pursued in this thesis. As will be revealed shortly, the pressure force controller of the previous subsection has a convenient theoretical and practical connection to the position control problem, which is the target problem to be pursued for the road simulation application in the next chapter. We, therefore, focus on the pressure force controller in this chapter when referring to force control.

4.1.2.3 Descriptions Using the Load Pressure

The expression for the pressure force controller can be re-written by introducing the so-called load pressure or differential pressure ($p_L = \Delta p$), defined by:

$$p_L = p_b - p_t \tag{4.18}$$

And assuming further that the valve ports are matched and symmetrical ($C_{v,1} = C_{v,2} = C_{v,3} = C_{v,4}$), it can be shown that [25]:

$$p_b = \frac{1}{2}(p_S + p_R + p_L) \tag{4.19}$$

$$p_t = \frac{1}{2}(p_S + p_R - p_L) \tag{4.20}$$

The state equations for the chamber pressures can then be replaced with a single state equation for the load pressure (p_L), thereby reducing the order of the modeled servo-actuator system from four to three. This new state equation is given by:

$$\dot{P}_L = f_{p_L}(x_p, \dot{x}_p, p_L) + g_{p_L}(x_p, p_L, \mathrm{sgn}(\bar{i}_v))\bar{i}_v \tag{4.21}$$

where ,

$$f_{p_L}(x_p, \dot{x}_p, p_L) = -\beta_e \dot{x}_p \left(\frac{A_b}{V_b + A_b x_p} + \frac{A_t}{V_t - A_t x_p} \right) - \beta_e C_L p_L \left(\frac{1}{V_b + A_b x_p} + \frac{1}{V_t - A_t x_p} \right) \tag{4.22}$$

$$g_{p_L}(x_p, p_L, \mathrm{sgn}(\bar{i}v)) = \beta_e C_v \sqrt{\left(\frac{p_S - p_R}{2} \right)} \sqrt{1 - \frac{p_L}{pS - pR} \mathrm{sgn}(\bar{i}_v)} \times \left(\frac{1}{V_b + A_b x_p} + \frac{1}{V_t - A_t x_p} \right) \tag{4.23}$$

Recall that the other two state equations are given by Eqs. 3.46 and 3.47.

For a symmetric actuator ($A_b = A_t = A_p$), the pressure force dynamics are given by slightly simpler expressions, namely:

$$\dot{F}_p = A_p \dot{p}_L = f_F(x_p, \dot{x}_p, p_L) + g_F(x_p, p_L, \mathrm{sgn}(\bar{i}_v))\bar{i}_v \tag{4.24}$$

where,

$$f_F(x_p, \dot{x}_p, p_L) = A_p f_{p_L}(x_p, \dot{x}_p, p_L) \tag{4.25}$$

$$g_F(x_p, p_L, \mathrm{sgn}(\bar{i}_v)) = A_p g_{p_L}(x_p, p_L, \mathrm{sgn}(\bar{i}_v)) \tag{4.26}$$

The rest of the expressions leading to the Near IO linearizing controller are the same as the general case given in Subsection 4.1.2.1. Only the expressions for the nonlinear functions f_F and g_F need to be replaced with those given in Eqs. 4.25 and 4.26. It should be recognized that the piecewise IO linearization achieved is of relative degree one, in this case as well. Second-order internal dynamics remain, the stability of which is

discussed in Appendix C. The implementation of this reduced form of this Near IO linearizing force controller is shown schematically in Fig 4.2.
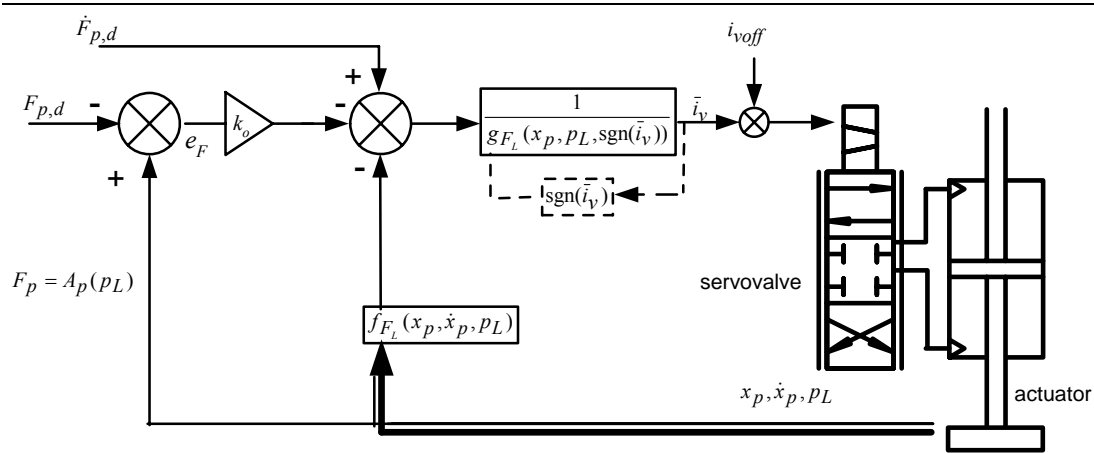
Figure 4.2: Schematic for Near IO linearizing pressure force controller using load pressure

It should be noted that the pressure force control problem and the load (differential) pressure control problem differ only by a factor of the piston area. Therefore, the pressure force control conclusions discussed in this work apply equally well to the differential or load pressure control case. The load force case, however, is significantly different as shown in the previous subsection.

4.1.3 Piston Position Tracking Control

The piston position tracking control problem can be solved using two approaches within the framework of feedback linearization. The first approach is direct Near IO linearization by defining the piston position as the desired system output. The second is to use a cascade control where the position control problem is considered an outer-loop to the pressure force control problem. It is a major observation of this work that the controllers from the two approaches are equivalent. Each approach is detailed in the following subsections.

4.1.3.1 Near IO Linearization with Position Output

In this subsection, direct piecewise IO linearization is performed with piston position, x_p, as the system output and a similar control law to the force tracking case is derived. The first and second derivatives of the output x_p as given by Eqs. 3.36 and 3.37, do not contain the control input, $\bar{i}_v$. However, a second differentiation of Eq. 3.36 gives:

$$\dddot{x}_p = f_p(x_p, \dot{x}_p, p_b, p_t, \dot{F}_f, \dot{F}_L) + g_p(x_p, p_b, p_t, \text{sgn}(\bar{i}_v))\bar{i}_v \tag{4.27}$$

where f_p and g_p are given, respectively, by:

$$f_p(x_p, \dot{x}_p, p_b, p_t, \dot{F}_f, \dot{F}_L) = \frac{1}{m_p}[f_F(x_p, \dot{x}_p, p_b, p_t) - \dot{F}_f - \dot{F}_L] \tag{4.28}$$

$$g_p(x_p, p_b, p_t, \text{sgn}(\bar{i}_v)) = \frac{1}{m_p} g_F(x_p, p_b, p_t, \text{sgn}(\bar{i}_v)) \tag{4.29}$$

Here, for compactness, the expressions for the nonlinear functions, f_F and g_F, from Eqs. 4.7 and 4.8 have been retained. Proceeding as in the pressure force output case of Subsection 4.1.2.1, Eq. 4.27 leads to a piecewise IO linearization with a relative degree of 3, and suggesting the control law:

$$\bar{i}_v = \frac{1}{g_p(x_p, p_b, p_t, \text{sgn}(\bar{i}_v))}(v - f_p(x_p, \dot{x}_p, p_b, p_t, \dot{F}_f, \dot{F}_L)) \tag{4.30}$$

The closed loop position dynamics reduces to the triple integrator:

$$\dddot{x}_p = v \tag{4.31}$$

which can easily be stabilized by state feedback. It also leads to an exponentially convergent tracking (provided the internal dynamics are stable) when the new input v is chosen as

$$v = \dddot{x}_d - k_3(\ddot{x}_p - \ddot{x}_d) - k_2(\dot{x}_p - \dot{x}_d) - k_1(x_p - x_d) \tag{4.32}$$

where x_d is the desired position profile. With Eqs. 4.31 and 4.32, the dynamics of the closed loop tracking error, $e=x_p-x_d$, reduce to:

$$\dddot{e} + k_3\ddot{e} + k_2\dot{e} + k_1 e = 0 \qquad (4.33)$$

The three gains k_1, k_2, and k_3 can be chosen to place the poles of the closed loop tracking error dynamics strictly in the left half s-plane. This could be done by using direct pole placement or posing the problem as a linear optimal control problem [81]. Direct pole placement involves deciding on the location of the three poles for the closed loop error dynamics given by Eq. 4.33 and invoking pole placement routines to compute the gains.

To include some optimality, the gains could be chosen using an LQR (Linear Quadratic Regulator) approach from linear optimal control theory. To this end, Eq. 4.33 is rewritten as Eq. 4.34 with u given by Eq. 4.35 below:

$$\dot{\mathbf{e}} = \mathbf{A}\mathbf{e} + \mathbf{b}u \qquad (4.34)$$

$$u = \mathbf{K}\mathbf{e} \qquad (4.35)$$

where,

$$\mathbf{e} = \begin{bmatrix} e \\ \dot{e} \\ \ddot{e} \end{bmatrix} = \begin{bmatrix} x_p - x_d \\ \dot{x}_p - \dot{x}_d \\ \ddot{x}_p - \ddot{x}_d \end{bmatrix}, \quad \mathbf{A} = \begin{bmatrix} 0 & 1 & 0 \\ 0 & 0 & 1 \\ 0 & 0 & 0 \end{bmatrix}, \quad \mathbf{b} = \begin{bmatrix} 0 \\ 0 \\ 1 \end{bmatrix} \quad \text{and } \mathbf{K} = \begin{bmatrix} k_1 & k_2 & k_3 \end{bmatrix}.$$

It can be shown that the system in Eq. 4.34 is fully controllable with the dummy intermediate control signal, u. Standard solutions of the Algebraic Riccati Equation (ARE) give the optimal gains that minimize the quadratic cost function given by:

$$J = \frac{1}{2}\int_0^\infty (\mathbf{e}^T\mathbf{Q}\mathbf{e} + Ru^2)dt \qquad (4.36)$$

where $\mathbf{Q}$ is a symmetric positive semi-definite weighing matrix and R is a positive scalar weight. By using $\mathbf{Q}$ and R, optimization trade-offs can be performed between the size and

speed of decay of the tracking error **e** and the linear dummy control action, *u*. However, *u* makes only part of the true control action, $\bar{i}_v$. This can be seen by using Eq. 4.32 and the notation following Eq. 4.35 and rewriting Eq. 4.30 as follows:

$$\bar{i}_v = \frac{1}{g_p(x_p, p_b, p_t, \mathrm{sgn}(\bar{i}_v))}(\ddot{x}_d - \mathbf{K}\mathbf{e} - f_p(x_p, \dot{x}_p, p_b, p_t, \dot{F}_f, \dot{F}_L)) \tag{4.37}$$

The choice of the elements of the weight matrix **Q** and R involves at least as much trial and error as the direct pole placement techniques. This is because the number of weight variables to be specified as elements of the **Q** and R matrices is more than the maximum of 3 pole locations necessary for the direct pole placement approach. In this thesis, the choice of these gains was initially done by an interactive combination of direct pole placement and LQR methods. A more useful interpretation that helps with the choice of the gains is revealed in Subsection 4.1.3.2.

It should be noted again that the piecewise IO linearization performed is only a Near IO linearization since Eq. 4.30 cannot be solved explicitly across the null valve current ($\bar{i}_v = 0$) boundary. In practice, this is overcome by invoking the previous assumption that the sign of the value of $\bar{i}_v$ at the previous time step can be used to compute the value of $\bar{i}_v$ at the current time step.

It should also be noted that, by reducing the system to the third order tracking dynamics of Eq. 4.33, the control law of Eq. 4.30 renders one of the four original states (p_b, p_t, x_p, v_p) of the system "unobservable". This leaves a first order internal dynamics. The description of this internal dynamics is not straightforward. However, using the load pressure description from Subsection 4.1.2.3, the original system becomes of order three, with the three states: p_L, x_p, v_p. No internal dynamics remain in this case, and the piecewise IO linearization achieved is a full-state feedback linearization.

Figure 4.3 shows the schematic of the implementation for the Near IO linearizing position tracking controller. The load force is considered to comprise of specimen reaction forces for the application shown in the schematic of Fig 3.12.
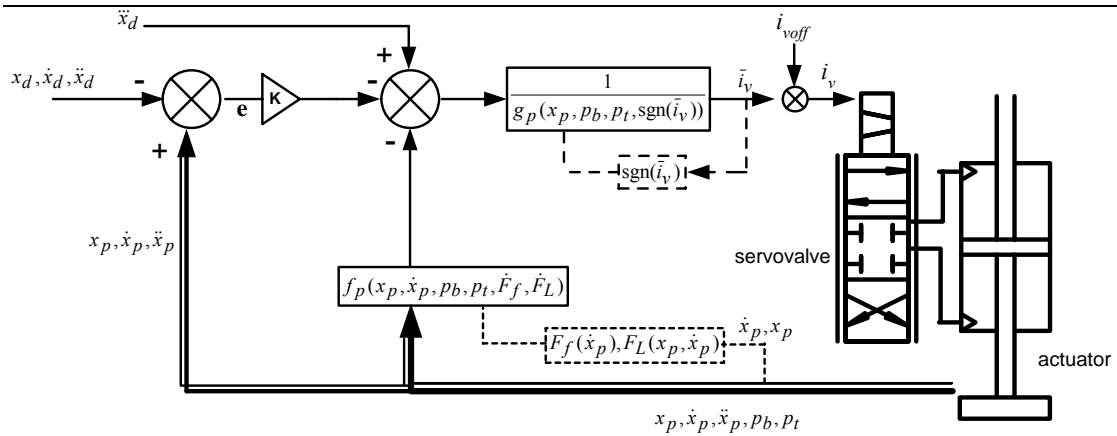
Figure 4.3:Schematic for the Near IO linearizing position tracking controller

4.1.3.2 Cascading with Pressure Force Tracking

The cascade control of hydraulic actuator piston position employing classical and linear state feedback was described in Ref [26, 82, 83]. The central idea of the method lies in treating the actuator as a force generator with an inner-loop force (or differential pressure, P_L) tracking controller, and a feedback plus feed forward outer-loop position controller that computes the desired force profile for the inner-loop. The inner-loop p_L (or F_p) controller generally comprises of a high-gain p_L (or F_p) feedback term in addition to positive velocity feedback. The latter is intended to cancel the velocity coupling of the piston motion and the pressure dynamics. This expectation is reasonable, if flow-pressure and variable compliance nonlinearities could be ignored, as can easily be seen in the expression of the pressure dynamics, Eq. 4.21 (or its local linearization about operating points). Then, with the piston motion decoupled from the pressure dynamics by velocity feedback, the outer-loop control would provide compensation for external loads and friction, and enable tracking of the desired piston motion (position, velocity and acceleration). The outer-loop solves a standard motion control problem and may even include adaptive algorithms to compensate for load and parameter changes [83].

The same basic idea of cascading was extended to the realm of nonlinear control in the work of Heintze and Van der Welden [82], who compared an inner-loop controller based on dynamic inversion with a cascade controller which includes nonlinearity compensation in the original constant gain cascade form of Sepehri, et al [83]. Starting with a Lyapunov-like analysis, Sohl and Bobrow [34] also presented a cascade position tracking controller, with a nonlinear pressure force controller as an inner-loop. The proposals in Ref [82] and [34] are similar in structure to the discussion presented below which exposes certain interesting facts about the nonlinear cascade control from a feedback linearization framework. Eryilmaz and Wilson [84] arrive at a slightly different cascade control structure from a singular perturbation point of view.

It is to be recalled that the Near IO linearizing pressure force tracking control law of Subsection 4.1.2.1 (or equivalently with the results of Subsection 4.1.2.3) cancels the piston velocity feedback on the pressure force dynamics by the first term of the nonlinear function, f_F. This nonlinearity cancellation decouples the dynamics of the piston motion from the hydraulic pressure/force dynamics. The cascade control of piston position discussed in this subsection exploits this result.

We proceed by constructing a desired pressure force profile ($F_{p,d}$), which will be an input to the pressure force loop, in terms of the desired piston position profile in such a manner that when the pressure force output is driven to the desired force profile, the output piston position approaches the desired position. Therefore, we define $F_{p,d}$ as:

$$F_{p,d} = m_p \ddot{x}_d - k_v(\dot{x}_p - \dot{x}_d) - k_p(x_p - x_d) + F_L + F_f + m_p g \qquad (4.38)$$

To understand the reason for this form of $F_{p,d}$, recall that the equation of motion of the piston is given by:

$$m_p \ddot{x}_p = F_p - F_L - F_f - m_p g \qquad (4.39)$$

Here, initially, it is assumed that accurate estimates of the friction force and the load force are available to be included (as feed forward) in the computation of $F_{p,d}$. The piston

mass is assumed to be known. The question of uncertainty and the choice of the gains of k_v and k_p is discussed below.

Combining Eq. 4.38 and 4.39, the closed loop dynamics can be expressed in terms of the closed loop position error, $e = x_p\text{-}x_d$:

$$m_p \ddot{e} + k_v \dot{e} + k_p e = F_p - F_{p,d} = e_F \tag{4.40}$$

where $e_F = F_p\text{-}F_{p,d}$ is the pressure force tracking error. It has already been argued that an exponentially convergent tracking of the pressure force can be obtained using the Near IO linearizing controller of Eq. 4.13. Equation 4.40 shows that the position error dynamics are given by a second-order linear differential equation driven by the pressure force error provided there are no estimation errors for the load and friction forces. The gains k_v and k_p can be easily be chosen to obtain a desired position error dynamics and ensure that the closed loop system so obtained is stable. Figure 4.4 shows a schematic for the implementation of this cascade control structure.
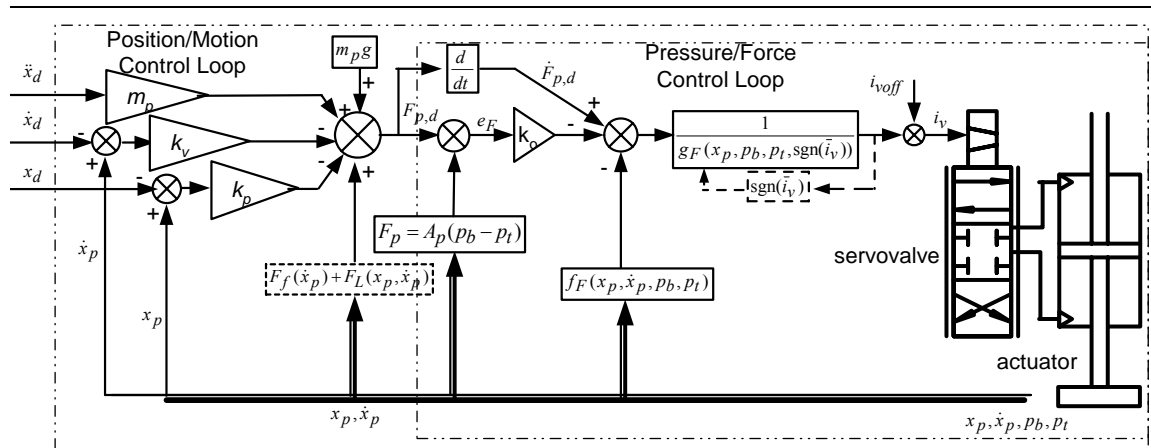
Figure 4.4 Schematic of the cascade controller (no uncertainty in friction and load)

Unless otherwise stated, hereafter in this thesis, we shall use the name <u>cascade controller</u> to refer to the controller structure with the feed forward plus feedback position controller outer-loop and the Near IO linearizing pressure force controller inner-loop.

Note that the closed loop system of the cascade control is of order three, as is the result of the Near IO linearizing position controller of Subsection 4.1.3.1. This can easily

be shown by observing that the inner-loop of the cascade controller requires the derivative of the desired pressure force as shown in Fig 4.4. In fact, taking the derivative of the desired pressure force given by Eq. 4.38, using the result together with Eq. 4.40 in the Near IO linearizing pressure force tracking controller of Eq. 4.13, it can be shown that the control current is given by:

$$
\bar{i}_v = \frac{\ddot{x}_d - (k_o + \frac{k_v}{m_p})\ddot{e} - \frac{(k_p + k_o k_v)}{m_p}\dot{e} - \frac{k_o k_p}{m_p}e - \frac{(f_F - \dot{F}_f - \dot{F}_L)}{m_p}}{\frac{g_F}{m_p}}
\tag{4.41}
$$

where f_F and g_F are given by Eq. 4.7 and 4.8, respectively. Note that Eq. 4.41 has the same form as the Near IO linearizing position tracking controller given by Eq. 4.37. The two controllers will be exactly the same when the gains k_1, k_2, k_3 in Eq. 4.37 are chosen such that:

$$
k_1 = \frac{k_o k_p}{m_p}, \quad k_2 = \frac{k_p + k_o k_v}{m_p}, \quad k_3 = k_o + \frac{k_v}{m_p}
\tag{4.42}
$$

Note that both the cascade controller leading to Eq. 4.41 and the Near IO linearizing position controller given by Eq. 4.37 have three linear gains to be set. The question that can be posed at this point may be: Which structure is better?

It is apparent that even if the control current expressions are the same, the cascade controller has certain advantages over the Near IO linearizing controller. First, it gives a simpler physical insight and interpretation that can aid the choice of the linear gains and judge the performance of the resulting closed loop system. The inner-loop pressure force (load pressure) dynamics can be made as fast as desired by the choice of k_o via pole placement (s=- k_o) of a first order linear dynamics (Eq. 4.12). The other gains, k_p and k_v, are simply coefficients of a second-order linear dynamics (Eq. 4.40), which have straight forward interpretation as factors in the natural frequency and damping coefficient of the position loop. A second advantage is that the cascade form does not need feedback of piston acceleration measurement if Eq. 4.38 is used to compute the desired pressure force, $F_{p,d}$. It also does not require a third derivative of the desired position trajectory to

be available, even though it is implicit that the third derivative must be bounded due to the fact that the derivative of $F_{p,d}$ is used by the inner-loop force control. A third advantage of the cascade control structure regards theoretical robustness analysis, which is detailed in Subsection 4.1.5.2.

However, the cascade control structure has a serious disadvantage in that it computes the derivative of the desired force online. The desired force, $F_{p,d}$, itself is computed in real time from measurements in the position, velocity, and pressure, as well as the estimates of friction and load forces. Since these measurements are susceptible to noise, high quality signal processing may be necessary. Differentiating noise could cause unstable responses with the cascade controller. The Near IO linearizing position tracking controller does not suffer from this problem of differentiation of potentially noisy signals.

It should also be remarked that the gain relations given in Eq. 4.42 can be used in a reverse argument (solving for k_1, k_2, k_3) to guide the choice of the gains for the controller of Eq. 4.37. This provides a much better and (physically) easy to interpret alternative to the LQR based method outlined in Subsection 4.1.3.1 or a direct pole placement technique for choosing the gains k_1, k_2, k_3 based on pole locations for the third order error dynamics given by Eq. 4.33. However, closed form inversion of Eq. 4.42 results in very complicated and unwieldy expressions for the general case, and as such numerical solutions are recommended.

For the special case where all three closed-loop poles of Eq. 4.33 are placed at the same location on the real axis, say $s=-a$, $a>0$, a simple, yet, very useful closed form result can be derived. By expanding the characteristic polynomial $(s+a)^3$ of the dynamics given by Eq. 4.33 and using the equivalence in Eq. 4.42, one can arrive at:

$$k_o = a, \qquad k_p = a^2 m_p, \qquad k_v = 2am_p \qquad\qquad (4.43)$$

In fact, using this result in Eq. 4.40, it is easy to see that, in this case, the second-order position error dynamics has a natural frequency of a (rad/s) and a damping ratio of 1. Most often, a critically damped response is among well behaved responses that can be considered for the design of the position tracking outer-loop. Since $k_o = a$, the first-order force tracking inner-loop also has a break frequency of a (rad/s). This observation will be

used in the interpretation of simulation and experimental results in Subsection 4.2.2, for both the cascade controller and the Near IO linearizing position controller.

4.1.4 Characteristics of the Nonlinear Controllers

In this subsection, we summarize the common characteristics and implementation issues of the nonlinear controllers derived in Subsections 4.1.2 and 4.1.3. Then, a discussion is presented on the estimation of friction forces which appear in the nonlinear position tracking and the load force tracking controllers.

4.1.4.1 Summary of Main Results and Limitations

Each of the control laws in Eqs. 4.9, 4.16, and 4.30 has linear and nonlinear state feedback components. The linear state feedback component comes from the choices of the dummy intermediate part v, and the nonlinear state feedback from the form of the nonlinear functions (f_F, f_p) in the numerators and (g_F, g_p) in the denominators. The nonlinear terms f_p, f_F, g_p, and g_F can be seen to contain the dominant nonlinearities in the electrohydraulic system. The valve flow rate vs. pressure drop nonlinear relation, which appears as in input-nonlinearity, is canceled via the denominators (g_F, g_p). The variable cylinder chamber capacitances are canceled term by term with the both additive and multiplicative terms (f_p, f_F, g_p, and g_F).

A significant observation regarding the additive cancellation of the nonlinearities is in the (nonlinear and positive) feedback of piston velocity via the first term of the nonlinear function f_F (or of f_p) given by Eq. 4.7 (or Eq. 4.28). This velocity feedback leads to the cancellation of the natural feedback of piston velocity in the open loop chamber pressure dynamics of Eqs. 3.36 and 3.37, which describe conservation of mass. With the load pressure description of Subsection 4.1.2.3, this natural velocity feedback appears as a negative feedback in the pressure dynamics, or equivalently, in the pressure force dynamics. Canceling this negative velocity feedback amounts to decoupling the

piston motion (which is governed by loading) from the pressure dynamics of the hydraulic system. This decoupling helps separate the load pressure/pressure force control from the piston motion control. In fact, this is what is exploited by the cascade controller to reduce the closed-loop system to a linear second-order position error dynamics driven by the output of a first-order load pressure/pressure force tracking error dynamics.

Another component of the additive nonlinearity cancellation is the position-dependent cancellation of the effects of the leakage flow inside the actuator via the second term of function f_F (or of f_p) given by Eq. 4.7 (or Eq. 4.28). By design, it is attempted to reduce leakage and hence this term may naturally be small. Nevertheless, in the likely scenario that the leakage is not correctly modeled or estimated, this nonlinearity cancellation appears as a shift in a (position-dependent) pole location for the load pressure/pressure force dynamics. The pole placement after the linearization of the load pressure/pressure force dynamics can be tuned to offset consequences of canceling leakage on the pressure/pressure force dynamics.

The choices for the structure of the linear parts of the feedback linearizing controllers, which are designated by v in Eq. 4.11 and Eq. 4.32, have systematically been done to guarantee exponentially convergent tracking control of the respective outputs. A consequence of these choices was that the derivatives of the desired force profiles and position trajectories are required to be available online (or as some functions of time)[30]. This also limits the application of the nonlinear controllers so derived to tracking applications of only smooth trajectories. This is not a serious limitation whenever desired trajectories can be generated by filtering a given reference with filters of appropriate order and cut-off frequencies. It is also possible that these trajectories are limited to naturally smooth ones depending on the application for the actuator.

Alternative choices of v to those given in Eq. 4.11 and Eq. 4.32 which do not need derivatives of the reference trajectory may sometimes be desirable. One such form employing simple output feedback is given in Jelali and Kroll [67]. However, these choices may mean accepting steady state error and a phase lag or even making the system unstable. Consider the pressure force/load pressure tracking control case with the following choice of v:

$$v = -k_o(F_p - F_{p,d})$$ (4.44)

where $k_o > 0$. The pressure force/load pressure external dynamics, Eq. 4.10, reduces to:

$$\dot{F}p + k_o F_p = k_o F_{p,d}$$ (4.45)

The output pressure force will be a first-order filter on the desired force profile. Exponential tracking is not guaranteed. For sinusoidal desired force profiles, for example, there will always be a phase lag that grows to 90° at high frequencies. If the same output feedback similar to Eq. 4.44 is used on the position output case, Eq. 4.31, the result is:

$$\ddot{x}_p + k_1 x_p = k_1 x_d$$ (4.46)

where $k_1 > 0$. Application of the Routh-Hurwitz criteria shows that this system is unstable. In fact, adding a second term involving derivative of the position error to the form of Eq. 4.44 still leads to an unstable closed loop system. Therefore, we conclude that simpler choices of the linear component v of the feedback linearizing controllers, than those already used in the developments of the previous sections, do not necessarily lead to better closed loop performance.

Examination of the nonlinear denominator functions g_F and g_p in the control laws of Eqs. 4.9, 4.16, and 4.30, suggests the possibility of division by zero during online computations of the control current. In reality, one set of the possible zero conditions, $p_b = p_S$ and $p_t = p_R$ (for $\bar{i}_v \geq 0$) are not likely to happen simultaneously. With the load pressure descriptions given by Eqs. 4.19 and 4.20, it is easy to see that these conditions would imply $p_L = -p_R = p_S$ which is not possible since the supply pressure is normally set at a much higher positive value than the return pressure which is near atmospheric. Another likely zero condition for g_F and g_p is when $p_L = p_S - p_R$ (see Eq. 4.23). This is conceivable, but also not likely to happen in practice since it would imply having the whole pressure drop in the servo-actuator transferred to the load. In any case, a switch can be included to set g_p and g_F to small non-zero numbers to guarantee division by zero does not occur.

The derivation of the nonlinear controllers in the previous subsections did not take into account the possibility that the control current computed could exceed the allowed range (of ± 50mA for the test system in this work). As is evident from the expressions for the controllers, the controller current magnitude depends on the properties of the desired trajectory. If the trajectory has large derivatives, especially of the third position derivative, $\dddot{x}_d$, the control current could exceed these ranges. The issue of trajectory selection is revisited again in later sections. As a safeguard on implementation, the magnitude of the current is limited by a saturation function to be within allowed range (± 50mA) corresponding to the rated characteristics of the servovalve.

An important feature of the nonlinear control laws under discussion is that state measurements are assumed to be available online. This assumption does not cause significant problems since the particular physical modeling adopted uses physically meaningful state variables, each of which can be measured, or in the case of velocity, it can be obtained by stable numerical differentiation of position LVDT output.

As was shown in the implementation schematics of Fig 4.1 for pressure force, Fig 4.2 for load pressure and Fig 4.3 for piston position control, the major structural element of the piston position controller that is absent in the other cases is the fact that the position controller requires the derivatives of the friction and load forces. The load force could be measured directly by using a load cell for the test unit used in this work. The friction force is not directly measurable online but it is estimated from the experimentally identified model of the friction force already detailed in Subsection 3.3.2. The method adopted in this thesis for obtaining a differentiable estimate of friction is discussed further in the following subsection. However, in general, the combined load and friction forces are at best estimates and may not be known without error. This brings up the issue of uncertainty and robustness which is the subject of Subsection 4.1.5.

4.1.4.2 Differentiable Friction Estimation Model

As discussed in Subsection 3.3.2 , the friction force acting on the piston is estimated by fitting the analytical expression given by Eq. 3.48 to the experimental data. The expression accounts for the Stribeck (declining friction at low velocity), Coulomb and viscous components. However, the expression also has a strong discontinuity and sharp corners near zero velocity. Since the implementations of the nonlinear control laws for position tracking use the time derivative of the friction force (directly as in Eq. 4.28 or indirectly in the cascade controller implementation of Fig 4.6), it is necessary to make the nominal expression smooth with respect to velocity before the derivative can be taken.

The following approximations of the sign function (sgn(x)) and the absolute value function ($|x|$) are taken [67]:

$$\text{sgn}(x) = \frac{2}{\pi}\arctan(\gamma x) \qquad\qquad (4.47)$$

$$|x| \approx \frac{2x}{\pi}\arctan(\gamma x) \qquad\qquad (4.48)$$

The parameter γ is used to adjust the degree of smoothening applied to the friction estimation of Eq. 3.48. Fig 4.5 shows typical results from applying these approximations. Note that the higher the value of the parameter γ the better the approximation, but the sharper the corners at zero velocity (i.e, when the piston motion changes direction). A compromise value of γ=5 is selected for the remainder of the results presented in this work, unless otherwise stated. If the asymmetry with the sign of velocity is to be considered, there still remains some corner at exactly zero velocity, but the severity of the discontinuity is reduced when the approximations are applied.
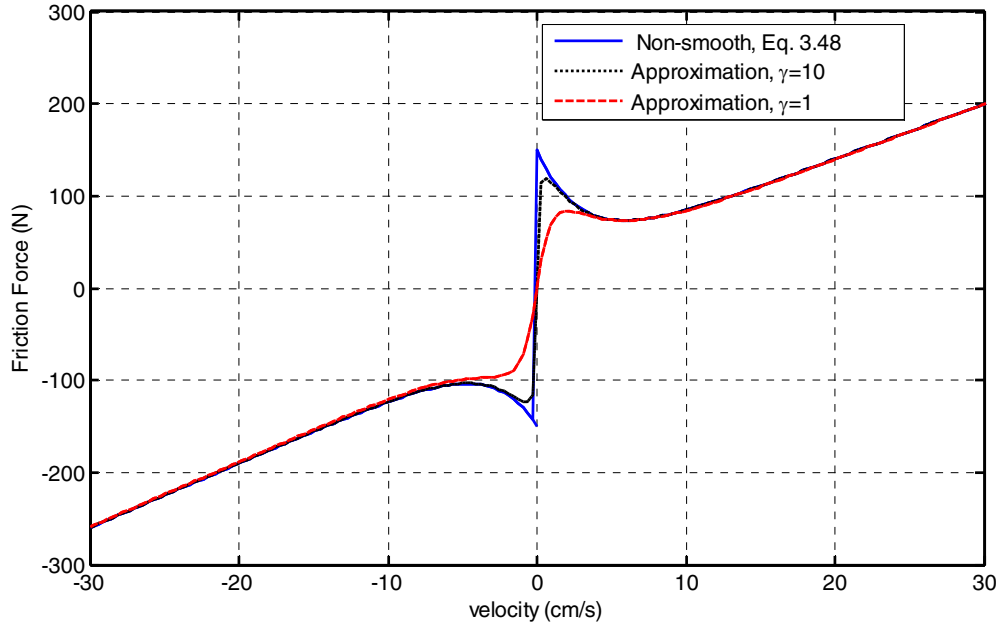
Figure 4.5: Smooth approximations of the friction force

4.1.5 Robustness Considerations

Robustness to parameter variation is a well-known concern when using model based controllers such as the ones derived in the previous subsections of this chapter. These controllers are dependent on possibly uncertain model parameters as well as estimates of load and friction forces. Some of the model parameters can be calculated or measured fairly accurately. This is particularly true of geometric parameters like volumes V_b, V_t, areas A_b, A_t, A_p and the piston mass m_p. The fluid bulk modulus β_e, the valve coefficient C_v and the leakage coefficient C_L, however, are highly uncertain since they can change with oil temperature, air entrapment and the working life of the servovalve and actuator. Nominal values for these uncertain model parameters β_e, C_v, and C_L can be estimated using offline, so called, grey-box identification techniques which are detailed in Appendix B. In coming sessions, experimental and simulation results outlining the effects of these parameters are presented.

In this subsection, a formal treatment of robustness is presented. The nonlinear controllers of the previous sections are modified to account for parameter and measurement uncertainty as well as errors in the load force and friction force estimation. For compactness, we shall consider the system description using the load pressure state variable.

4.1.5.1 Robust Pressure Force Tracking: Sliding Control

It turns out that the form of the Near IO linearizing controller for pressure force tracking can be easily re-considered from a sliding control point of view and thereby formally address the issue of robustness. A detail exposition of the topic of variable structure systems and sliding control is outlined in [30, 31, 44] and a literature review of applications to electrohydraulic system control has already been given in Subsection 2.2.3 of Chapter 2. The main results relevant to the discussion at hand are outlined here.

For the pressure force tracking problem, the system is of relative degree 1 giving the pressure force dynamics of Eq. 4.6, repeated here, after dropping the arguments of the functions f_F and g_F:

$$\dot{F}p = f_F + g_F \bar{i}_v \tag{4.49}$$

Define the sliding manifold parameter S to be:

$$S = Fp - Fp,d \tag{4.50}$$

The desirable sliding manifold (of zero tracking error) is given by *S(t)=0*. If the nonlinear functions f_F and g_F of Subsection 4.1.2 are replaced by their estimates $\hat{f}_F$ and $\hat{g}_F$ to account for parametric and measurement uncertainties in these functions, then it can be shown that the discontinuous controller:

$$\bar{i}_v = \frac{1}{\hat{g}_F}(\dot{F}_{p,d} - K \operatorname{sgn}(S) - \hat{f}_F) \tag{4.51}$$

would make S satisfy the sliding condition for robustness [31]:

$$\frac{1}{2}\frac{d}{dt}(S^2) \le -\eta|S| \qquad\qquad \eta \in \Re^+ \tag{4.52}$$

Note that, aside from the use of the estimated functions $\hat{f}_F$ and $\hat{g}_F$, the main difference between Eqs. 4.51 and 4.13 is really in the use of the discontinuous (switching) term $K\text{sgn}(S)$ in Eq. 4.51 instead of the proportional term $k_o e_F = k_o S$ in Eq. 4.13.

Indeed, using Eqs. 4.49, 4.50 and 4.51 in Eq. 4.52 the following expression can be derived for the size of the gain K of the discontinuity in terms of model uncertainty:

$$K \ge \delta g_F(\eta + \delta f_F) + |1 - \delta g_F||\dot{F}_{p,d} - \hat{f}_F| \tag{4.53}$$

where δf_F and δg_F are the bounds on the uncertainties(perturbations) in the nonlinear functions f_F and g_F, respectively, and are expressed by:

$$\left|\hat{f}_F - f_F\right| \le \delta f_F \qquad 0 < (\delta g_F)^{-1} \le \frac{\hat{g}_F}{g_F} \le \delta g_F \tag{4.54}$$

Here, g_F is considered to be positive (this is the realistic situation described before and evident in Eq. 4.23). Since g_F is a multiplicative gain, it is convenient to consider the nominal value of g_F, i.e, $\hat{g}_F$, as a geometric mean of the maximum and minimum bounds of g_F.

The discontinuous controller of Eq. 4.51 can force the system to the sliding manifold $S=0$ and keep it there, and thus give perfect tracking in the face of the parametric and state measurement uncertainty. The only requirement is for the gain K to satisfy Eq. 4.53. However, in practical implementations, the discontinuous switching across the sliding manifold leads to control chattering. This is particularly a serious problem when there is a neglected servovalve dynamics in the derivation of the control law. This is equivalent to a parasitic neglected "actuator[1]"dynamics that could lead to instability with infinitely fast switching [30, 48]. Other neglected higher frequency mechanical dynamics could also be excited.

---

[1] The neglected servovalve spool dynamics in this work is equivalent to what is referred to as neglected "parasitic actuator" dynamics in the literature on variable structure control. The reader is advised that, in this thesis, the term actuator refers in general to the main part of the controlled system as opposed to just a means to deliver control action.

In order to take advantage of the robustness properties of the sliding mode controller and eliminate chattering, "continuous" approximations are usually considered [30, 31, 48, 53]. The sign function is replaced by the saturation function, thereby introducing a boundary layer around the sliding manifold. By doing so, some deterioration of tracking performance is tolerated.

Replacing the sign function in Eq. 4.51 with the saturation function defined by

$$sat(S/\Phi) = \begin{cases} S/\Phi & if \ |s| \leq \Phi \\ \text{sgn}(s) & if \ |s| > \Phi \end{cases}$$

(4.55)

results in the control law

$$\bar{i}_v = \frac{1}{\hat{g}_F}(\dot{F}_{p,d} - K \, sat(S/\Phi) - \hat{f}_F)$$

(4.56)

where Φ is the boundary layer thickness, which in the present case, translates directly into an acceptable bound on the force tracking error. This controller would still satisfy the reaching condition (Eq. 4.52) outside the boundary layer, and therefore, make the boundary layer attractive and invariant. This gives a degree of tracking performance which is bounded by Φ in spite of the parametric uncertainties.

At this point, it should be clear that the Near IO linearizing controller for pressure force tracking given by Eq. 4.13 is almost identical to the "continuous" sliding mode controller. The difference is the former approach did not explicitly place bounds on the guaranteed tracking performance in the presence of parametric uncertainties, but the latter did. Within the boundary layer, the two forms are exactly the same.

When implementing in the experimental system, it may be more desirable to have smooth approximations to the sign switch of Eq. 4.51 or the continuous, yet non-smooth saturation function of Eq. 4.56. The tangent hyperbolic function was one such function tested in this work. The boundary layer is still invariant and attractive in this case as well [30, 47].

$$\bar{i}_v = \frac{1}{\hat{g}_F}(\dot{F}_{p,d} - K \tanh(S/\Phi) - \hat{f}_F)$$

(4.57)

Note also that it is still necessary to obtain good estimates of the parameters for the nonlinear functions $\hat{f}_F$ and $\hat{g}_F$ so that the gain K remains reasonable and the bound on the tracking error (boundary layer thickness) remains small. Mathematical details for this argument are given in Slotine and Li [31]. Here, it suffices to say that, the modeling effort in the previous chapter as well as the parameter estimation described in Appendix B are all intended to increase tracking performance as best as possible. In the case of the Near IO linearizing controller, the gain k_o was adjusted considering it as a closed loop bandwidth (system pole). In the context of the sliding mode controller, however, the equivalent gain K is tuned to provide robustness to parameter uncertainty as well as to reduce tracking error. This distinction between the two gain values is important.

Finally, it should also be pointed out that the sliding control considered here addressed only robustness to the so called matched uncertainties, which enter the (external) state equation of the pressure force dynamics at the same point as the control input. These uncertainties are due typically to the model parameters β_e, C_v, and C_L and state measurement errors. Uncertainties appearing in the other (internal) state equations are not addressed directly. In Appendix C, the second order internal dynamics are shown to be input-to-state-stable with bounded trajectories for practical approximations of load and friction forces. In the next section, we consider these unmatched uncertainties for the force loop with respect to the position tracking objective.

4.1.5.2 Robust Piston Position Tracking: Backstepping

Sliding control can still be applied to the piston position tracking case. It is to be recalled from Subsection 4.1.3.1 that with piston position as the output, the modeled electrohydraulic system becomes of relative degree 3 (with no internal dynamics when the load pressure description is used). A standard sliding mode controller design would start by defining the sliding manifold ($S=0$) to represent a well-behaved position tracking error dynamics. Sometimes the manifold is defined to represent a weighted sum of a

position and force tracking errors and their integrals. Such applications to piston position tracking control of hydraulic actuators are given in [46, 50-52].

In this thesis, instead of this standard sliding mode approach to robust position control, it is desired to take advantage of the exposition in Subsection 4.1.3.2 regarding the equivalence of the Near IO linearizing position tracking controller with the cascade controller. By keeping the robust pressure force tracking control design results of the previous section as the inner-loop, the robustness of the outer-loop and the overall system is investigated.

The desired pressure force profile given by Eq. 4.38 is re-defined here considering uncertainty in the estimation of load and friction forces. Replacing the load and friction forces by their estimates, the desired force profile is computed by:

$$F_{p,d} = m_p \ddot{x}_d - k_v(\dot{x}_p - \dot{x}_d) - k_p(x_p - x_d) + \hat{F}_L + \hat{F}_f + m_p g \tag{4.58}$$

Using Eq. 4.58 in the equation of motion of the piston, Eq. 4.39 , the closed loop position error, $e=x_p-x_d$, is given by:

$$m_p \ddot{e} + k_v \dot{e} + k_p e = e_F + (\hat{F}_f - F_f) + (\hat{F}_L - F_L) \tag{4.59}$$

where $e_F=F_p- F_{p,d}$ is the pressure force tracking error, and $\hat{F}_f$ and $\hat{F}_L$ are the estimates of the friction and load force respectively. It is assumed that the mass of the piston and attachments is known. The friction force is almost always estimated from a model (see Subsection 3.3.2), while the load force can either be measured (with a load cell) or estimated from a relevant model. It should be recalled that the friction force is generally a function of velocity ($\dot{x}_p$), while the load force is considered a damping and stiffness force, and therefore a function of both piston position (x_p) and velocity ($\dot{x}_p$). Bounds are assumed for the uncertainty in friction and load forces as follows:

$$\left|\hat{F}_f - F_f\right| \le \delta F_f \quad and \quad \left|\hat{F}_L - F_L\right| \le \delta F_L \tag{4.60}$$

Unlike the case where there is no uncertainty (Eq. 4.40), Eq. 4.59 shows that the cascade controller cannot guarantee convergence of the position error to zero in the presence of friction and load force uncertainty, even if the force tracking error converges

to zero. The position error dynamics are driven by the uncertainty in friction and load force estimation in addition to the force tracking error. The uncertainty enters as a disturbance to the position loop. Figure 4.6 shows the revised schematic for the cascade controller in the presence of uncertainty in the friction and load forces.
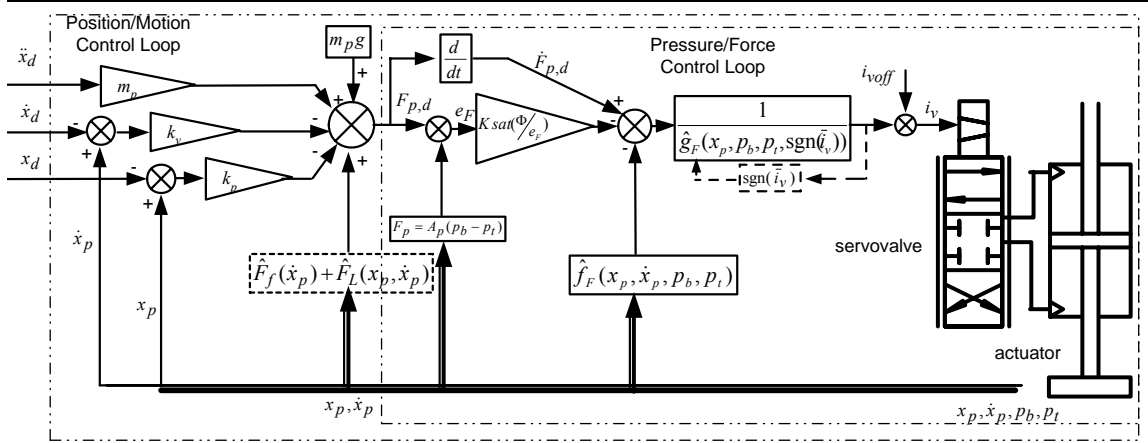
Figure 4.6: Cascade controller with friction and load uncertainty

Even if the force loop has been made robust to the "matched" uncertainty in the functions f_F and g_F , the position loop is still subjected to the effects of uncertainty in friction and load force estimation. The problem of this "unmatched" uncertainty of the force loop (or of the third order system) can be formally addressed by showing that the choice of the desired force output via Eq. 4.58 actually has an interpretation from a Backstepping design point of view. As will be shown shortly, this Lyapunov-based approach also gives bounds of tracking performance in relation to the size of uncertainty.

We start by re-writing the system equations including uncertainty in friction and load force as follows:

$$\dot{x}_p = v_p \tag{4.61}$$

$$\dot{v}_p = \frac{1}{m_p}(Fp - \hat{F}_L + (\hat{F}_L - F_L) - \hat{F}_f + (\hat{F}_f - F_f) - m_p g) \tag{4.62}$$

$$\dot{F}_p = f_F + g_F \bar{i}_v \tag{4.63}$$

This system is in the so called Strict Feedback Form [30, 36]. Starting with the first two equations, the pressure force, F_p, can be considered as the input and the following Lyapunov function candidate can be taken:

$$V_1 = \frac{1}{2}k_p(x_p - x_d)^2 + \frac{1}{2}m_p(v_p - v_d)^2 \tag{4.64}$$

Using the choice of the desired force trajectory given before (Eq. 4.58), the derivative of V_1 reduces to:

$$\dot{V}_1 = -k_v(v_p - v_d)^2 + [e_F + (\hat{F}_L - F_L) + (\hat{F}_f - F_f)](v_p - v_d) \tag{4.65}$$

With the sliding control notation in Subsection 4.1.5.1, a Lyapunov function candidate for the whole system can be written as:

$$V = V_1 + \frac{1}{2}S^2 = V_1 + \frac{1}{2}e_F^2 \tag{4.66}$$

Using Eq. 4.52, the derivative of this function satisfies:

$$\dot{V} \leq -k_v(v_p - v_d)^2 + [e_F + (\hat{F}_L - F_L) + (\hat{F}_f - F_f)](v_p - v_d) - \eta|e_F| \tag{4.67}$$

When the uncertainty is such that the bounds defined by Eq. 4.60 satisfy the condition:

$$\delta F_L + \delta F_f + |e_F| \leq \alpha|v_p - v_d| \qquad \alpha \in \mathfrak{R}^+ \tag{4.68}$$

The inequality given by Eq. 4.67 becomes:

$$\dot{V} \leq -(k_v - \alpha)(v_p - v_d)^2 - \eta|e_F| \tag{4.69}$$

For $k_v \geq \alpha$, $\dot{V}$ is rendered negative semi-definite with the control laws given by Eqs. 4.58 and 4.56 and the uncertainty bounds given by Eqs. 4.53 and 4.68. Recall that, when the matched uncertainty bounds satisfy Eq. 4.53, the pressure force tracking error is driven to the boundary layer $|e_F| \leq \Phi$ in finite time by the "continuous" sliding mode controller. If, in addition, the unmatched uncertainty can be bounded as in Eq. 4.68, i.e., to within a compromise linear growth bound that depends on the (acceptable) velocity tracking error, the derivative of the Lyapunov function $\dot{V}$ is negative semi-definite. Bounded position

velocity and force tracking is achieved provided both the matched and unmatched uncertainty bounds are satisfied.

In summary, in the presence of combined matched and unmatched uncertainty for the cascade controller, some degree of robustness is guaranteed as long as the uncertainties satisfy certain bounds as described. Once again, the results stress the importance of having a good set of parameter estimates and models for friction and load force so that the relevant uncertainties remain small.

4.1.6 System Simulations with Nonlinear Control

In this section, computer simulation results are considered to seek justification for the basic assumptions and idealizations made in Subsection 4.1.1 that allowed the derivation and analysis of the nonlinear controllers in the Subsections 4.1.2 through 4.1.5. For this purpose, we use the validated model of the experimental electrohydraulic system described Chapter 3. The simulation results presented in this section are only intended to highlight the effects of the idealizations. The analysis of the performance of the nonlinear controllers deserves full investigation with real-time experiments and simulations. The latter is the topic of next major section, Section 4.2.

4.1.6.1 Reference Signal Generation

It is to be recalled that the nonlinear controllers described in the preceding sections require differentiable desired or reference trajectories. In this thesis, three types of differentiable signals are used as reference trajectories. These are a sine wave, a chirp signal and an approximation of a step signal (or of a square wave).

A chirp signal is a swept sinusoidal wave with linearly increasing frequency at constant magnitude. Examples are presented shortly (See Fig 4.7). The advantages of using this signal are two fold. First, it can be sufficiently smooth for generating bounded derivatives of the desired position or force trajectory needed by the nonlinear position

and force tracking controllers. Second, it is possible to simultaneously view the performance of the controller with increasing frequency content. The disadvantage is that it is often not straightforward to read and extrapolate conclusions from time response plots from chirp references. For nonlinear systems, the response is dependent on the amplitude of the reference signal, and as such responses to different chirp signals of various amplitudes need to be investigated in order to make conclusive statements.

Relatively easier, and near standard comparison of responses can be obtained by generating approximate "step" responses. The Heaviside step function (which has sharp corners, and hence is non-differentiable) is approximated by the following differentiable function involving the hyperbolic tangent function.

$$x_d = X_d \tanh(\frac{t - t_o}{T})$$
(4.70)

Here X_d is the size of the step, t_o is the time the step is applied and T is a parameter that defines the "sharpness" of the corners of the approximated step. By adjusting T and, of course, X_d, the magnitudes of the derivatives of the desired position or force at the time of the step can be controlled. In the limit as $T \to 0$, the function approaches the Heaviside step function with sharp corners. Examples of the use of this "smooth" step are presented shortly (See Fig 4.10).

4.1.6.2 Effects of Transmission Line and Servovalve Dynamics

This subsection discusses the predicted performance of the nonlinear controllers, derived by neglecting the dynamics of the servovalve as well as the upstream and downstream transmission lines, acting on the all inclusive interconnected model of the electrohydraulic system presented in Chapter 3.

We first remark that in the case where the supply and return line accumulators are close-coupled with the servovalve, the assumption of constant supply and return pressures (as was done for controller derivation) would not be too restrictive. This has already been pointed out in Subsection 3.2.4 and exemplified with Fig 3.10. However, the

accumulators are not close-coupled with the servovalve for the test system under consideration, and so there is a need to evaluate the performance of the controllers in the non-ideal case of the test system. We use simulations for this purpose.

In a similar manner, the effect of neglecting the servovalve dynamics is investigated. Inclusion of the servovalve dynamics in the derivation of the Near IO linearizing control law would have resulted in the appearance of higher order derivatives of the desired and measured trajectories in the control laws. In the position tracking case, including a second order servovalve dynamics, for example, implies that two more differentiations of the third piston position derivative (Eq. 4.27) would be needed before the control signal appears and the Near IO linearization is possible. This in turn would require the availability of the third and fourth order derivatives of the piston position signal as well as further (up to 5th order derivative) smoothness requirements on the desired position trajectory. This undoubtedly would increase the complexity of the resulting controller for implementation. In this work, the nonlinear controllers derived above by ignoring the servovalve dynamics were considered sufficient to deal with the system nonlinearities arising from the turbulent port flow, variable hydraulic compliance and friction. However, to evaluate the effects of the neglected servovalve dynamics on the performance of these nonlinear controllers, extensive system simulations are performed with and without the servovalve dynamics.

In the following simulation results, the case of the Near IO linearizing position controller (of Subsection 4.1.3.1) is considered as it is the most complicated one in terms of involving higher order differentiations. Later sections will present experimental and simulation results for the other position and force tracking nonlinear controllers. The gains k_1, k_2, k_3 were chosen by placing the closed loop poles (roots of Eq. 4.33) at the same location $s=-500$ in the left half s-plane. This location may be too fast, considering model uncertainty, signal processing and control saturation, but it serves the purpose in this subsection. Also, only inertia load ($m_p=12$ kg, $F_L=0$) is considered.
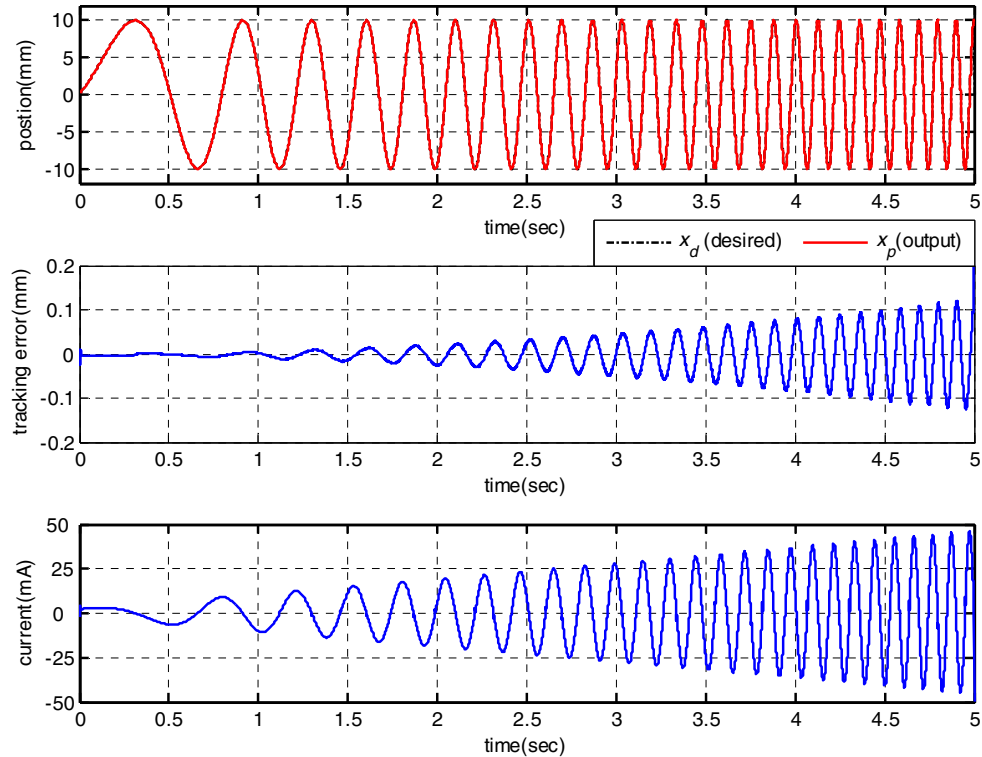
Figure 4.7:Tracking performance neglecting transmission line and servovalve dynamics in the EHS model

Figure 4.7 shows the tracking performance of the position tracking controller when the dynamics of both the transmission line and servovalve are neglected in the model of the electrohydraulic system (EHS) to be consistent with the assumptions for the derivation of the controller. The chirp reference position signal spans frequencies 0.5-10 Hz within the first 5 seconds and has amplitude of 10 mm. It can be seen that for this case, the tracking performance of the Near IO linearizing position tracking controller is near ideal with a maximum tracking error amplitude of about 1.2 % near 10 Hz, without saturation in the control current (to a maximum of ±50 mA).

Figure 4.8 shows the performance of the same controller when the transmission line dynamics are still neglected, but the servovalve dynamics is included in the EHS model. The tracking error increases in this case to a maximum amplitude of about 12 % near 10 Hz. Also the control current saturates at about 4.7 seconds.
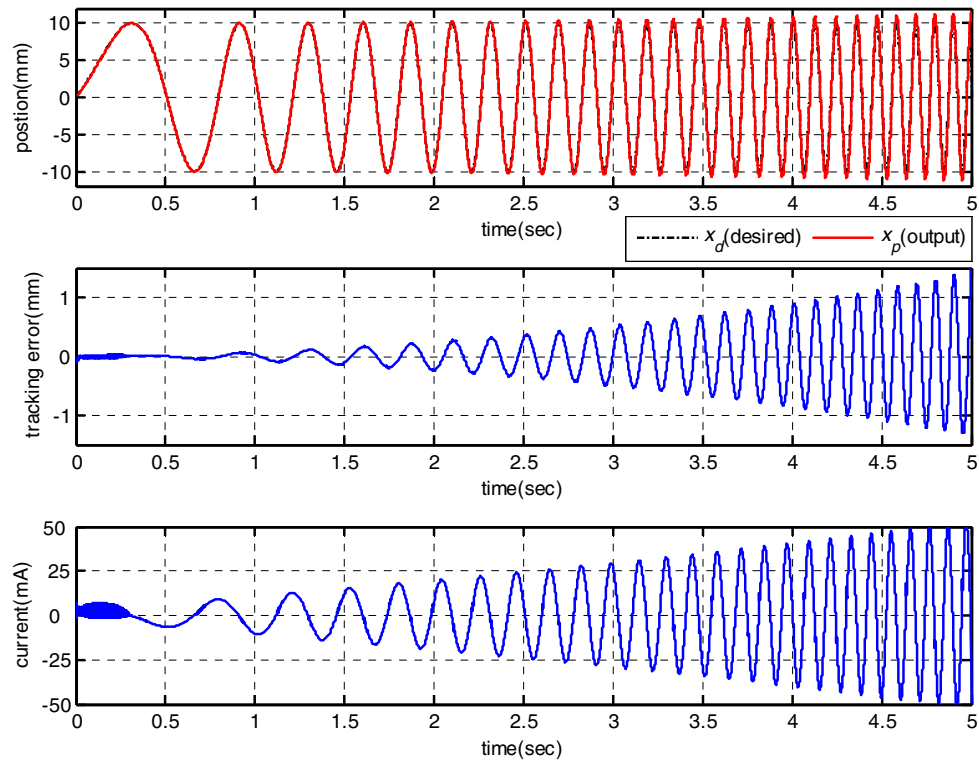
Figure 4.8: Tracking performance with the servovalve dynamics included in the EHS model

From Figs 4.7 and 4.8, it can be observed that the tracking error is higher when the servovalve dynamics is considered in the EHS model. The control current from the nonlinear controller saturates slightly faster as well. The increase in the tracking error at the higher frequencies is in part due to the saturation of the control current, and therefore, the comparisons should focus on the tracking errors before the control current saturated.

Figure 4.9 shows the simulated tracking performance for the same reference trajectory as above but with both the servovalve and transmission line dynamics included in the EHS model, i.e., with the most realistic test system model in which the designed controllers operate in. It can be seen that the tracking error does increase further with the control current saturating faster at about 4.3 seconds.
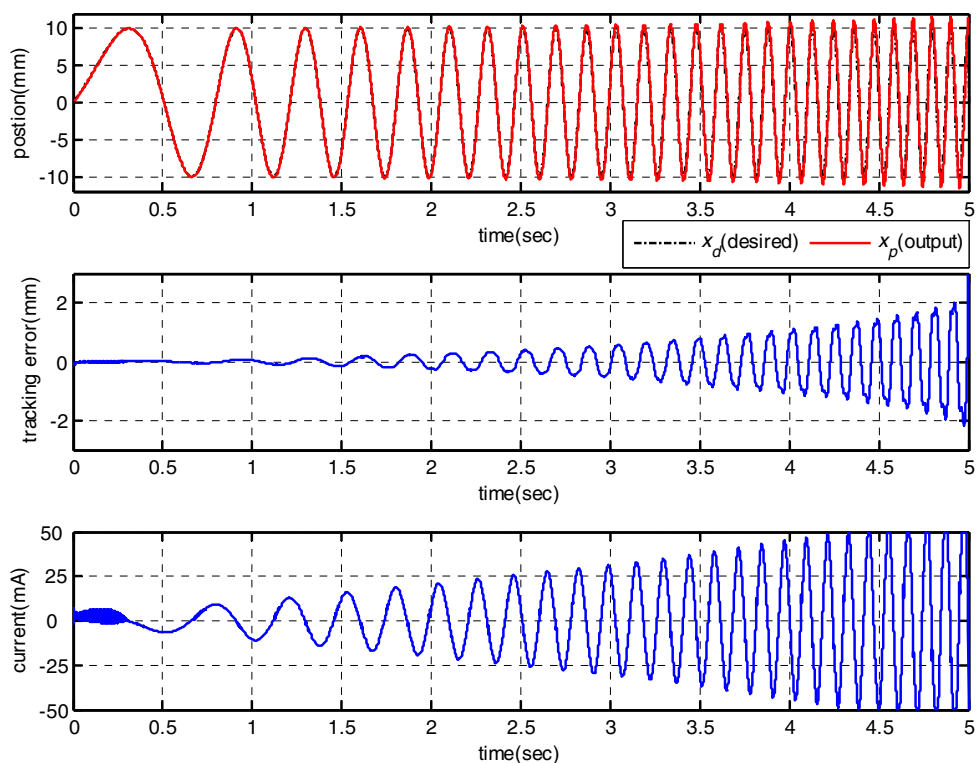
Figure 4.9: Tracking performance with both transmission line and servovalve dynamics included in the EHS model

Further investigations of the effects of neglecting the transmission line and servovalve dynamics can be done using the "smooth" step responses. Using Eq. 4.70 with different combinations of t_o and X_d, the up and down "step" responses can be approximated by a differentiable function. Meaningful comparisons can be made by choosing values of T such that the control current doesn't saturate. Fig 4.10 shows the simulated tracking performance with and without the servovalve and transmission line dynamics included. Large amplitude steps of -30 to 30 to -30 mm are used for this purpose.
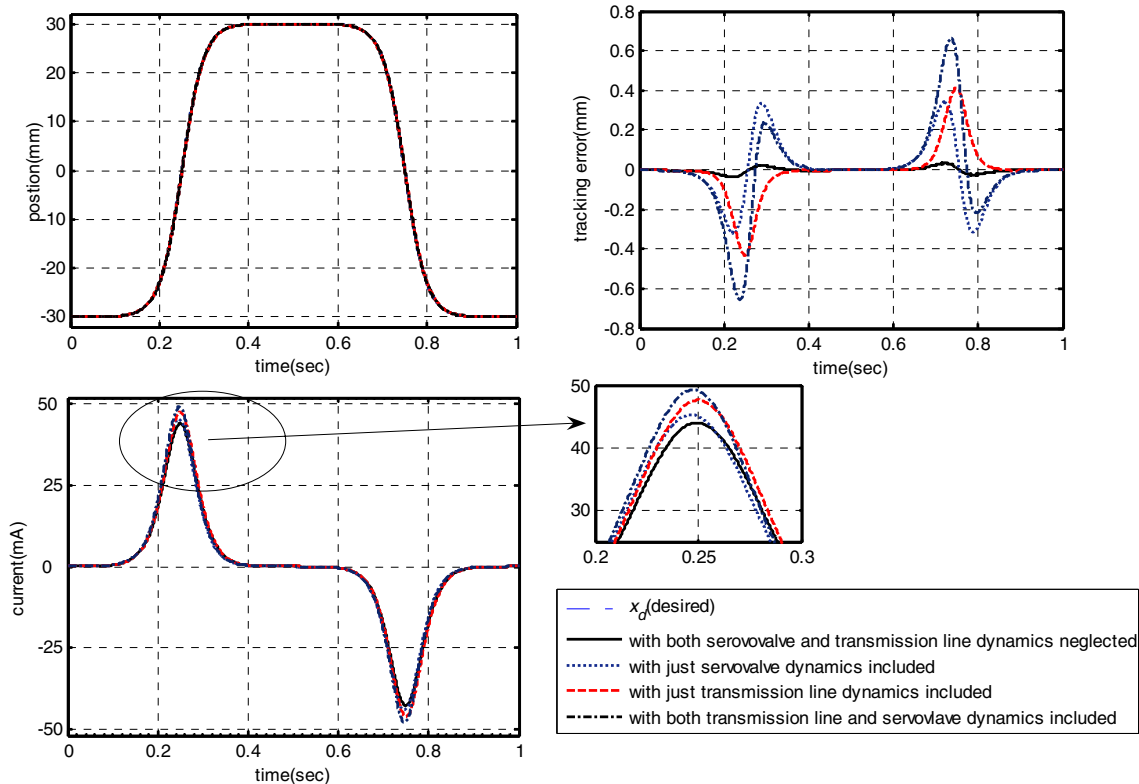
Figure 4.10: Simulated tracking performance using a smooth step reference (T=0.05)

In Fig 4.10 the time histories of the tracking error and the control current are visible indicators of the differences between the four cases. The peak tracking error is higher when just the transmission lines are included than when just the servovalve dynamics are included. This is expected considering the relatively lower bandwidth of the supply and return line dynamics compared to that of the servovalve as discussed in Subsection 3.4.1. Furthermore, the servovalve dynamics increases the oscillation seen in the tracking response before settling.

It should be stressed that using the smooth step trajectory with smaller values of T leads to saturation of the control current even for the case where servovalve and transmission line effects are neglected, provided the three closed-loop poles are still placed at the same location ($s=-500$). Using higher values of T makes the desired trajectory smoother, thereby reducing the magnitudes of the derivatives of the trajectory. The tracking performance is improved in all cases and the control current magnitude is

correspondingly reduced as can be seen by comparing Figs 4.10 and 4.11. On the other hand, lower values of T also mean sluggish demands on the controller and may cover too low frequency regimes.
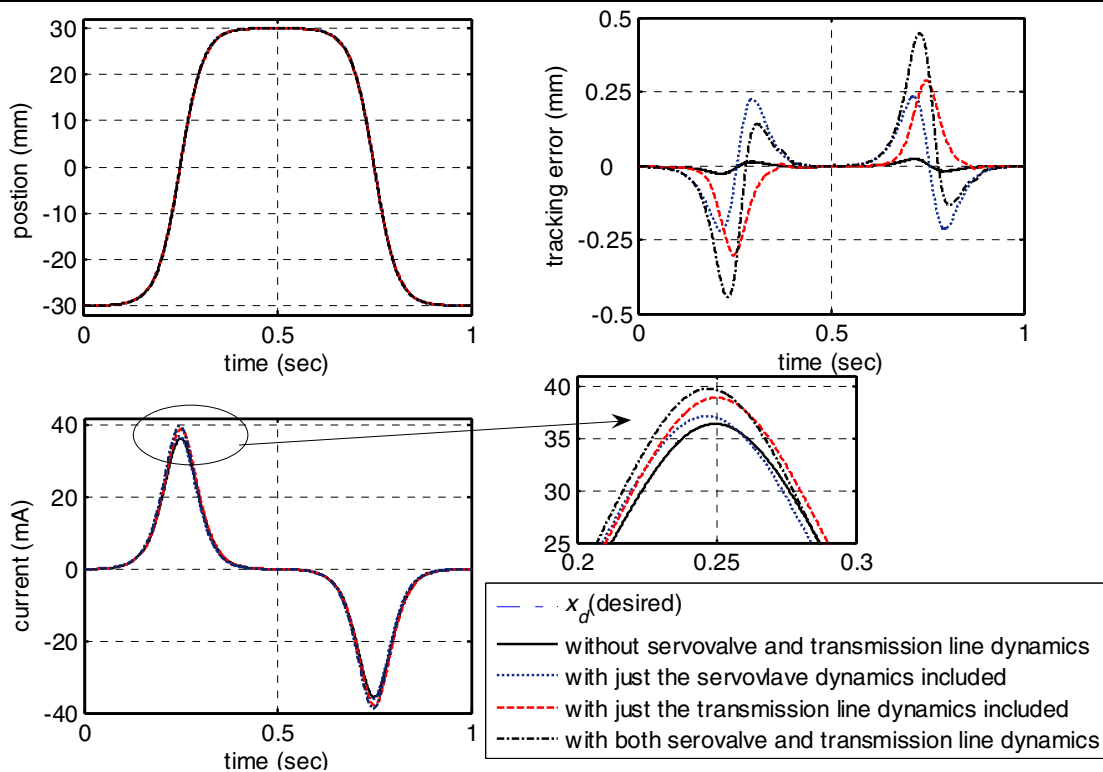
Figure 4.11:Simulated tracking performance using a smooth step reference (T=0.06)

The following points summarize the conclusions from the simulation work:

- For the test system under consideration, there are noticeable differences in performance caused by neglecting the servovalve and transmission line dynamics during the derivation of the nonlinear controllers.

- The fact that the dynamics of the supply and return pressure at the servovalve had to be neglected is more significant than neglecting the servovalve dynamics itself for the derivation of the nonlinear controllers.

- While including a linear servovalve dynamic model can be considered from the point of a Lyapunov based backstepping controller design [43, 85] or using higher-order differentiation for Near IO linearization, such structural convenience of modeling is not available to include the dynamics of the transmission lines (even with the least

order modal approximations in Chapter 3) in controller design. This is because the supply and return pressure variables enter into the valve flow equations as dominant nonlinearities (in the square roots) and without yielding a convenient structure like a strict feedback form.

- The performance of the nonlinear controllers depends strongly on the characteristics of the desired trajectory. This affects the controller performance particularly in the presence of transmission line and servovalve dynamics in the electrohydraulic system model.

- As a consequence of the above points, the high frequency contents of reference signals that can be considered in the simulations and experiments with this test system and with the nonlinear controllers are in the order of 15-20 Hz and well below the influence of the line dynamics (Subsection 3.4.1). This also limits the bandwidth of the experiments considered in this work.

4.2 Performance of the Nonlinear Controllers

In this section, the performance of the nonlinear controllers is investigated with experiments and simulations. In some cases, nominal performance comparisons are made with a traditional PID controller and a Linear State Feedback with Integral (LSFI) controller. The PID controller is chosen for comparison because it is a ubiquitous choice with electrohydraulic actuator control. Any performance improvement over the PID controller will be an interesting contribution. The LSFI controller is chosen among other linear controllers because it uses feedback of the same state variables as the nonlinear controller does, as can be seen by comparing Fig 4.2 and Fig D.1 (in Appendix D). This allows a comparison of linear vs nonlinear state feedback.

The linear PID or LSFI controllers are generally designed using a locally linearized system model. A discussion of the linearized models as well as the equations of the PID and LSFI controllers are given in Appendix D. It will be pointed out in the relevant sections that in experiments with the linear controllers, the gain settings chosen

with the aid of the locally linearized models failed to give a reasonable, if stable, response. Therefore, some trial and error was used to tune the gains and obtain an oscillation free response with these linear controllers.

4.2.1 The Pressure Force Tracking Controllers

The simplest of the nonlinear controllers presented in this chapter is the Near IO linearizing controller given by Eq. 4.13. The modified robust version is given by Eq. 4.56, which is the "continuous" sliding mode pressure force tracking controller. Both controllers are investigated in this subsection.

The experiments for this subsection considered a realistic loading on a fatigue test specimen. The piston was constrained with a neoprene rubber specimen so that large force magnitudes can be absorbed for a better force resolution. The force magnitudes were selected such that the specimen was always in compression purely for convenience with specimen mounting, but there should be no loss of generality for the observations. The experimental setup had an LVDT for position measurement, which was low-pass filtered to 40 Hz before differentiating the signal to obtain the piston velocity. The pressure feedback from two chamber pressure transducers was used to compute the pressure force output.

4.2.1.1 Near IO linearizing Controller

4.2.1.1.1 Nominal Performance Experiments

The nominal nonlinear controller in this subsection is the Near IO linearizing controller given by Eq. 4.13 with the nominal model parameters for the effective bulk modulus (β_e), the valve coefficient (C_v) , the leakage coefficient C_L, and the supply (p_S) and return (p_R) pressures at the servovalve. The first three model parameters were

estimated using simple experiments as outlined in Appendix B. The last two are known to change with the dynamics of the supply and return lines and accumulators as discussed in Subsection 3.4.1. However, constant values were used here, thereby limiting the bandwidth of the experiments considered here.
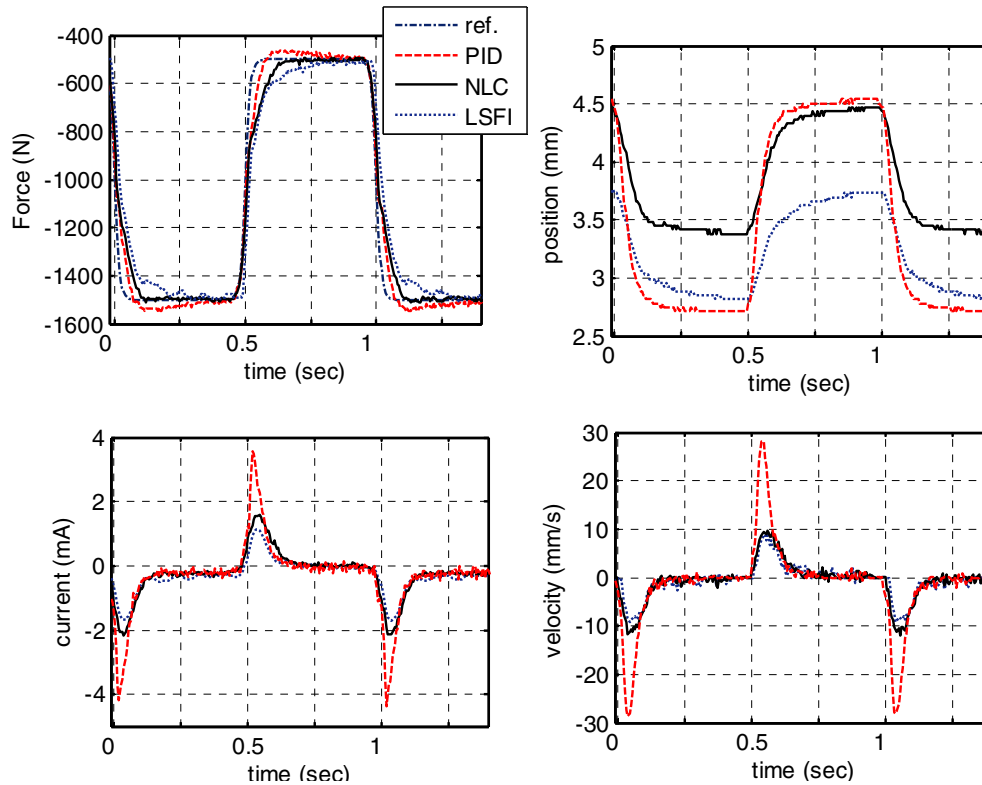
Figure 4.12: Experimental comparison of the tracking performance of the nominal Near IO linearizing controller (NLC) against well-tuned PID and LSFI controllers.

It was difficult to tune the PID controller for no overshoot without oscillations in the force response or a large steady-state error. What is shown for the PID controller is the best compromise performance obtained after many trials. It can be seen from Figs 4.12 that due to the accepted overshoot in the force response with the PID controller, the specimen was compressed the most (piston travel was the highest) and the magnitude of the peak control current required was the highest in the PID control case. The linear state feedback with integral (LSFI) controller case gave a sluggish force response. The performance of the nominal nonlinear controller (with k_o=750 s^{-1}) was the best compromise tracking performance considering the rise time and settling time of the force

response as well as the magnitude of control current. Further comparison can be made between these controllers by looking at the sinusoidal force tracking responses shown in Fig 4.13 with the same gain settings as above. At higher frequencies, the force output with the nominal nonlinear controller starts to show increased phase lag, as with the linear controllers, but the reduction in output force magnitude with the nonlinear controller is not as much as with the linear controllers. In certain applications such as with certain fatigue testing specimen, it may often be necessary to reduce force magnitude errors and tolerate phase lags, in which case the nonlinear controller has a clear advantage. Also, we note that the nonlinear controller uses consistently less current peaks (of the order of 40% lower than the PID controller). However, it should be expected that the performance of the nonlinear controller will eventually deteriorate at higher frequencies (as does that of the linear controllers) due to effects from neglected transmission line and servovalve dynamics.
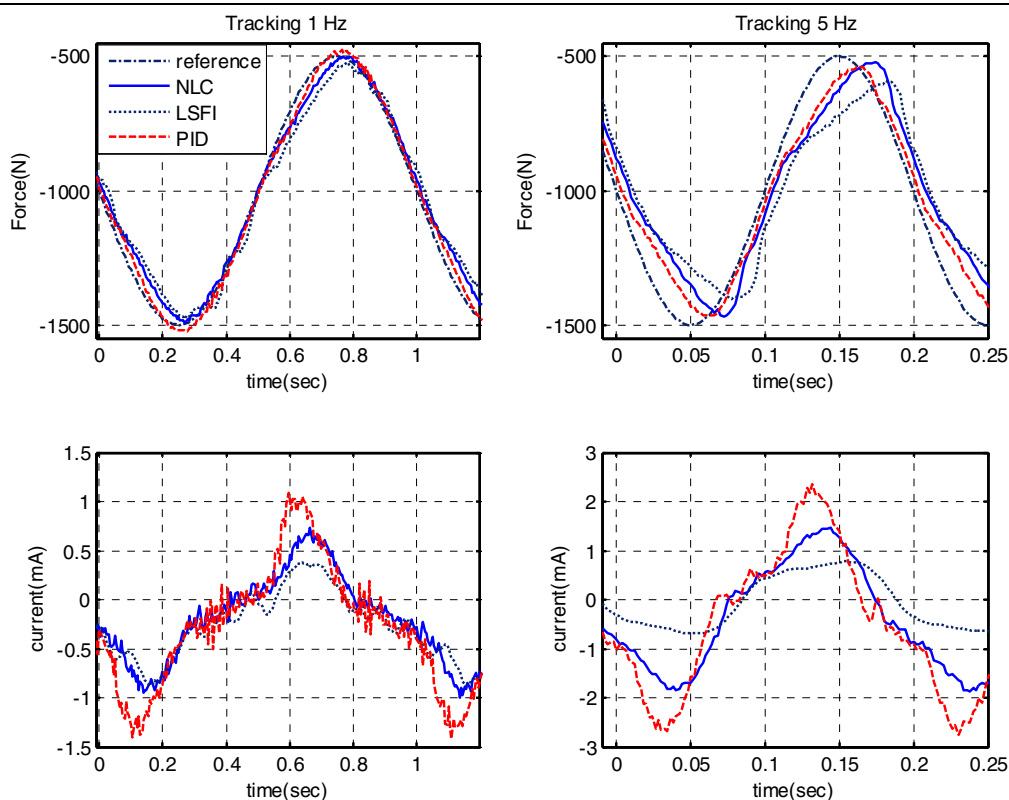
Figure 4.13: Experimental comparison of tracking performance for sinusoidal force trajectories

The main reason for the observed superiority of the nominal nonlinear controller is that with the nonlinearities cancelled by feedback, the nonlinear controller could push the possible closed-loop pole location (s=-k_o) much further in the left half s-plane than it was possible with either the PID or LSFI controllers for these experiments.

Having established a performance comparison of the nominal nonlinear controller against standard linear controllers, it was desired to see how the gain k_o can be used to tune the performance of the nominal nonlinear controller, in Eq. 4.13. Figure 4.14 shows responses as the gain k_o was changed over a range of values.
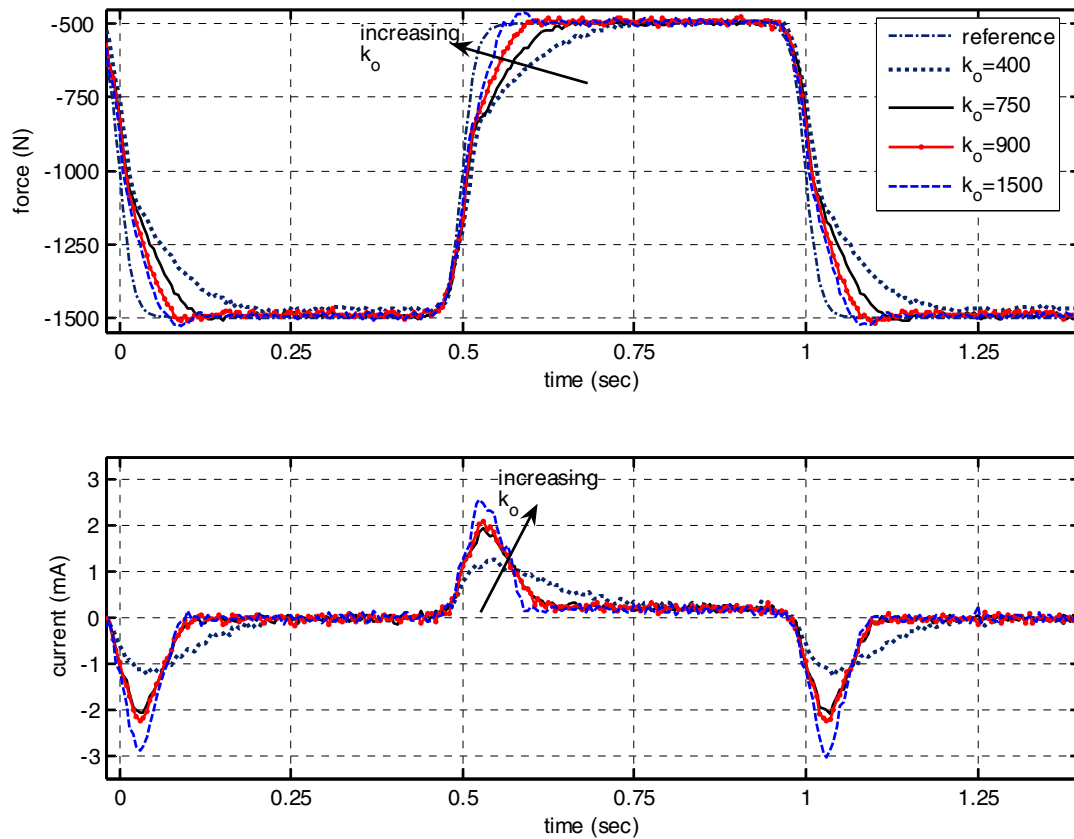
Figure 4.14:Tuning the nominal nonlinear controller with gain k_o

As the gain k_o was increased, the rise time decreased with a corresponding increase in the control current. Above a certain magnitude of the gain k_o (k_o=1500 s^{-1}) the force response showed overshoots and started to include undesirable oscillations from unmodeled dynamics. Lower values of the gain k_o gave sluggish responses. Nevertheless,

it is clear from Fig 4.14 that the single parameter k_o gives a simple way of tuning the controller performance for a desired combination of settling times and rise times.

Steady-state errors were observed to be a function of the null offset (i_{voff}). For these experiments, it was attempted to make the null offset as small as possible by a careful use of the mechanical null adjustment provided with the servovalve.

4.2.1.1.2 Robustness to Parametric Uncertainty

A known concern with the Near IO-linearizing controller under discussion is the potential sensitivity to the model parameters that appear in the controller expression. In this section, experimental results are presented outlining the sensitivity of the performance of the nonlinear controller to changes in the parameters β_e, C_v, and C_L. One of the parameters is changed while the nominal values are kept for the other parameters in the nonlinear controller expression.

Figure 4.15 shows the effect of uncertainty in the effective bulk modulus (β_e). The experiments were conducted by changing the effective bulk modulus by about a factor of more than ±50% of the nominal value of 850MPa. The lower the value of β_e used in the controller, the shorter the rise time, and the higher the tendency to overshoot and show oscillations in the force response. On the other hand, the higher the value of β_e used in the controller, the more sluggish the response became. This also implies that if there were a reduction in the actual value of the effective or working bulk modulus of the oil in the system (from what was set in the controller expression), the controller performance improves or deteriorates in the manner depicted in Fig 4.15. In practice, changes in the effective bulk modulus of the fluid in a hydraulic system could happen due to various reasons including air-entrapment (aeration), changes in mechanical compliance and the effect of temperature on air content.
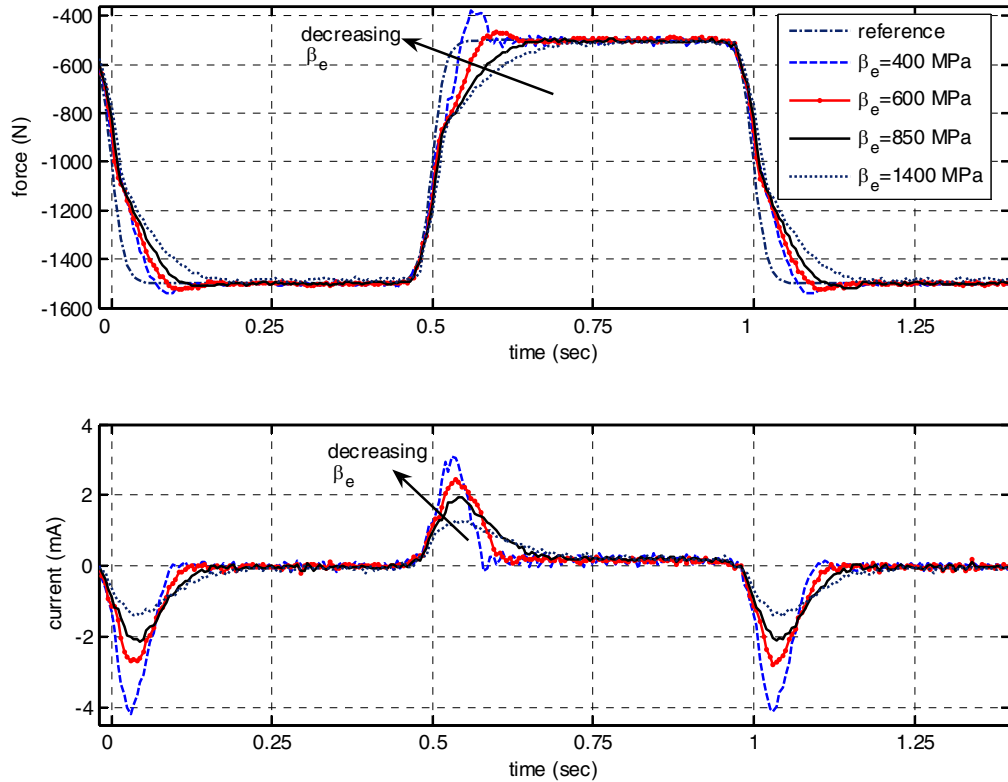
Figure 4.15: Robustness to changes in the bulk modulus parameter of the nonlinear controller (experiment)

It was also observed that the system was more sensitive to changes of β_e settings towards lower values than to changes towards higher values. The response started to overshoot with only a 25% reduction of the value of β_e, while the response remained virtually the same as the nominal case for a 25% increase in the value of β_e. The faster responses corresponding to lower β_e settings also required higher current peak magnitudes as shown in the lower plot of Fig 4.15. For example, for a 25% reduction in the value of β_e the current peak required was as much as 100% higher than the current peak for nominal settings of β_e.

Figure 4.16 shows the effect of uncertainty in the estimation of the valve coefficient parameter (C_v). The experiments were conducted by changing the valve coefficient parameter by as much as ±25% of the nominal value of $2.75\ cm^3/(s.mA.\sqrt{MPa})$ while keeping the other parameters at their respective nominal values. The observed trend

is similar to the effect of β_e. However, the response starts to show overshoot with only a 16% reduction in the value of C_v while it remains less sensitive to increasing the value of C_v by as much as 25% of the nominal value.
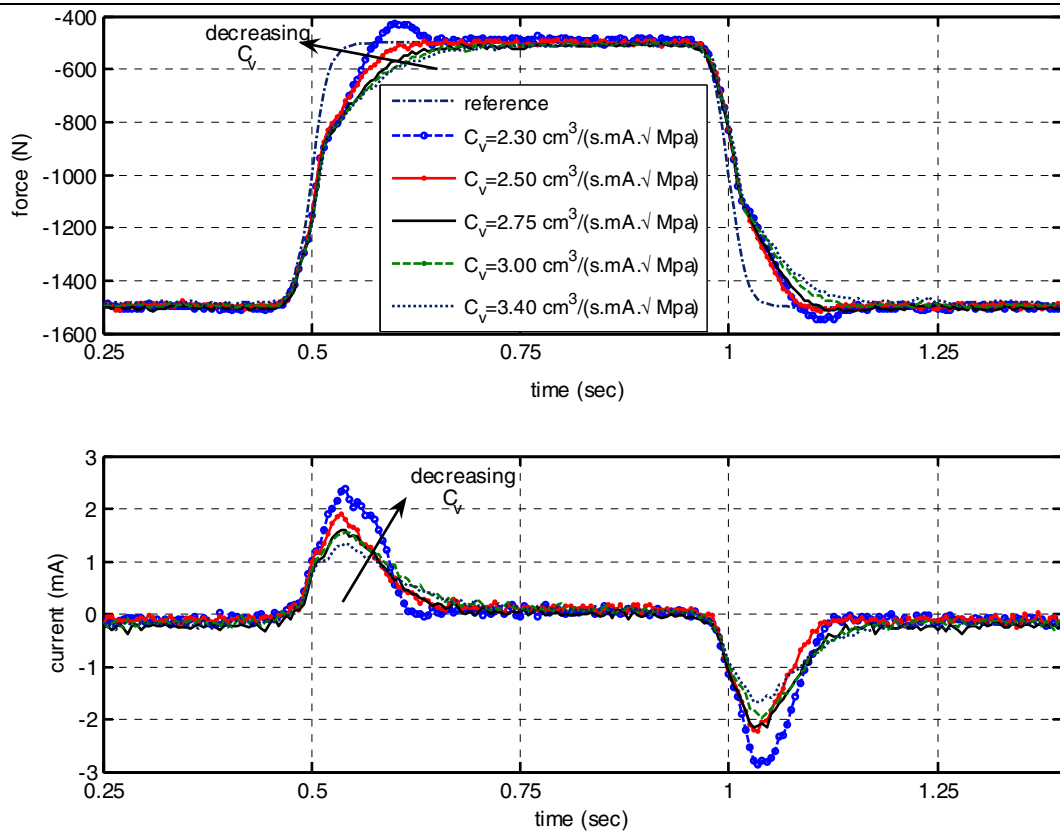
Figure 4.16: Robustness to changes in the valve coefficient parameter of the nonlinear controller(experiment)

It should be remarked that there remains some asymmetry in the responses and control current inputs for the application and removal of the step force reference corresponding to the up and down motions of the piston. These can be explained by the fact that a single value of the valve coefficient was used in the experiments for all valve ports (to simplify the implementation of the nonlinear controller), despite the identification data indicating a slight asymmetry (Appendix B). Furthermore, the motion of the piston (internal dynamics) is influenced by the nonlinear compliance of the neoprene rubber, which is known to exhibit hysteretic behavior.

Finally, Fig 4.17 shows the effect of the settings of the leakage coefficient (C_L) on the performance of the nonlinear controller. In these experiments, the values of the leakage coefficients were changed by as much as 200% of the nominal value of 0.5 cm^3/(s.MPa). This range is exaggerated to magnify the observed response. The effect of the leakage coefficient appears to be causing offset and steady state error when tracking the reference force. The control current does not appear to be affected significantly by changes in the settings for the leakage coefficient (C_L) and it is not repeated here. The asymmetry in the response is again attributed to the averaging adopted for the valve coefficient and the leakage coefficient to simply the implementation of the nonlinear controller (Appendix B).
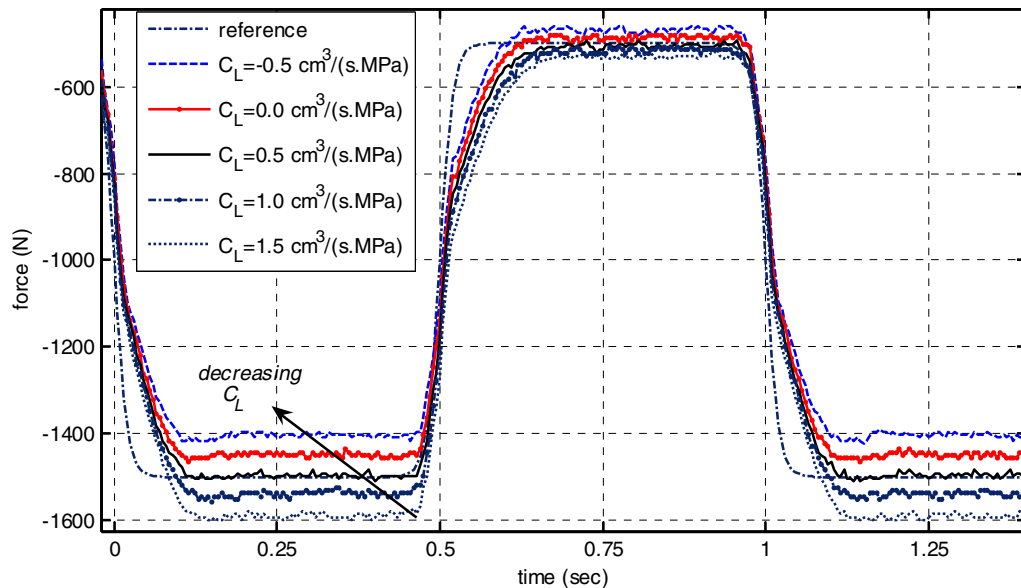
Figure 4.17: Robustness to changes in the leakage coefficient parameter of the nonlinear controller (experiment)

In summary, the above robustness experiments suggest that the nonlinear Near IO linearizing pressure force tracking controller tolerates a measurable shift in the values of the parameters β_e and C_v without sacrificing performance. This is particularly true for the effective bulk modulus parameter β_e whose value is generally considered difficult to predict in a hydraulic system. Finally, the effect of changing the leakage coefficient setting in the nonlinear controller was seen to be an offset and steady-state error.

4.2.1.2 Continuous Sliding Mode Controller

4.2.1.2.1 Basic Performance Experiments

In this section, an experimental study is presented for the modified robust controller given by Eq. 4.56 and the smooth version given by Eq. 4.57. It should be recalled that these controllers are designed to formally address matched parametric uncertainty in contrast to the study of robustness (sensitivity) to individual model parameters presented in the previous subsection.

To implement the controller of Eq. 4.56 or of Eq. 4.57, the gain K (which, in principle, can be made state dependent) should be chosen to satisfy the inequality given by Eq. 4.53 so that the sliding condition is met. For the work in this subsection, the gain K was chosen to be a constant satisfying Eq. 4.53 for the specific smoothened-square desired force trajectory with T=0.02 sec. The constant η is a small positive number formally reflecting the reaching time to the boundary layer. However, this constant was absorbed into the other much larger uncertainty bounds for the present system. The nominal functions $\hat{f}_F$ and $\hat{g}_F$ were computed with the model parameters defined with the nominal Near IO linearizing controller of Subsection 4.2.1.1.1 and given in Appendix B. The bound of the uncertainty (perturbation) in the additive term f_F, designated by $\delta\!f_F$, was taken to be 20% of the nominal value. The bound on the uncertainty in the multiplicative term g_F, designated by $\delta\!g_F$, was taken to deviate from the nominal value of 1 by 20%. These roughly correspond, for example, to a worst case combination of 20% uncertainty in the bulk modulus (β_e) and 15% in the valve coefficient (C_v). The minimum value of the gain K computed with these considerations alone is of the order of 1.5E7 kgcm/s^3. It should be noted that expressing the uncertainty in terms of perturbations of g_F and f_F has the added advantage of incorporating uncertainty in the values of p_S and p_R. It also allows the inclusion of combined parametric uncertainty and measurement errors.

Figure 4.18 shows the experimental tracking performance of the sliding mode controller given by Eq. 4.56. It can be seen that the robust controller with a boundary

layer thickness of Φ=100 N performs similarly to the Near IO linearizing controller with nominal parameters. The boundary layer thickness, which is a bound on the tracking error due to uncertainty, was slowly increased to 100 N until chattering was reduced to a minimum in the observed current and force responses.
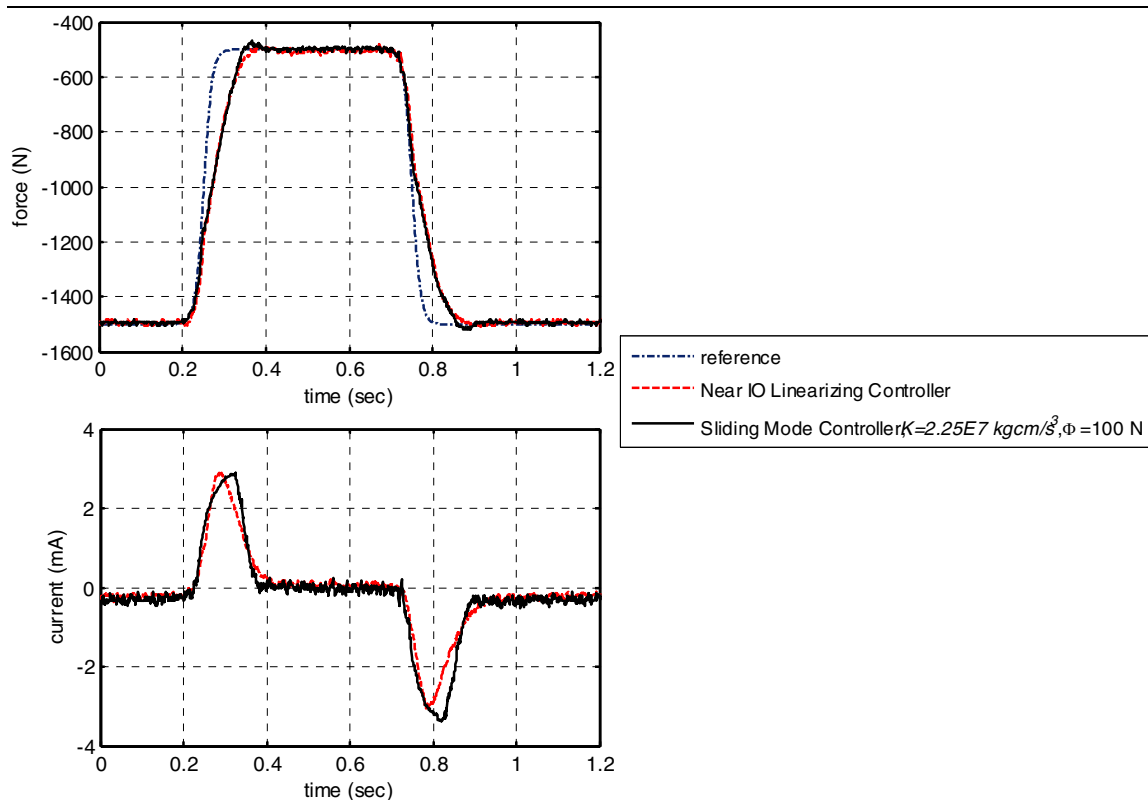
Figure 4.18: Tracking performance of sliding mode controller and the Near IO linearizing controller (experiment)

It is interesting to note that the experiments reported in this section were done after maintenance work (replacing filters and changing oil) was done on the hydraulic system. The value of the bulk modulus (β_e), which is deemed uncertain anyway, is very likely to have changed after such maintenance work. The control current peak is slightly higher (for the Near IO linearizing controller) than what was observed in the previous subsection without much change in tracking performance.

It was desired to see if there is indeed a difference in performance between the smooth version controller given by Eq. 4.57, which uses the tanh function and the version

given by Eq. 4.56, which uses the saturation function. Various combination of gain K and boundary layer thickness Φ were considered. Figure 4.19 shows an example comparison of the responses under the two sliding mode controller versions. In all the cases considered, the differences were negligible; with the smooth version showing slightly less control peaks and correspondingly lower overshoot in the force response. The rest of the experimental work in this thesis uses the smooth version given by Eq. 4.57.
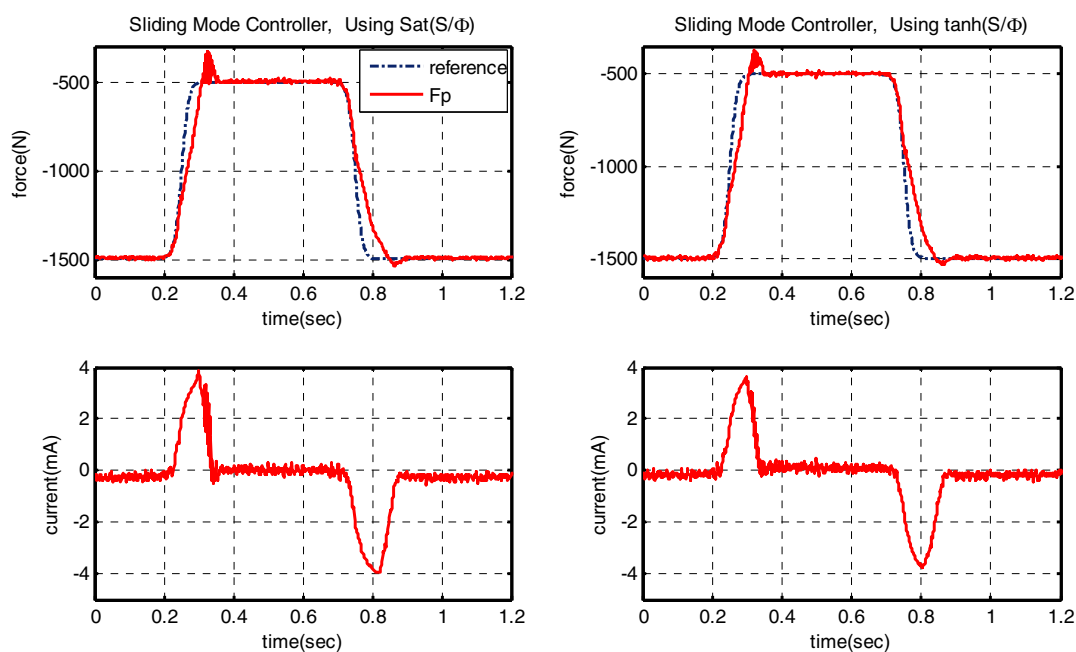
Figure 4.19:Comparison of sliding mode controller versions (Φ=100 N and K=2.75E7 kgcm/s^3) (experiment)

It is to be recalled that Eq. 4.53 gives only a lower bound for the gain K given the modeled part of the system. It should be noted that higher values of the gain K allow for larger uncertainty bounds. Figure 4.20 shows the effect of increasing the gain K. As could be expected, increasing the gain K improves the tracking performance in terms of reducing rise time and tracking error. However, due to the presence of the servovalve and transmission line dynamics in the physical system which were neglected during the

derivation of the controller, the gain K could not be increased arbitrarily[2]. This is evident in the overshoot observed at higher values of K. Further evidence of the problem of using arbitrarily high values of the gain K is given in Fig 4.21.
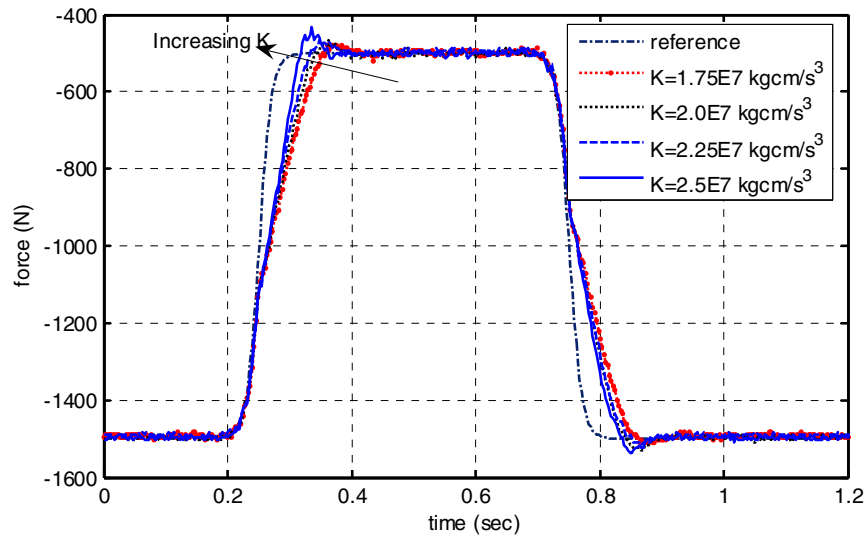
Figure 4.20: Effect of gain K for Φ=100 N (experiment)

Figure 4.21 shows the force tracking response for a high gain setting of K=3.0 E7 kgcm/s^3. Two different settings of the boundary layer thickness are shown; Φ=100 N (left column) plots and Φ=50 N (right column) plots. Clearly, the use of high gain K compounds the problem of chattering with a low boundary layer thickness setting. Chattering excites the dynamics of the servovalve and/or the transmission lines which were ignored for the derivation and design of the controller. During the experiments, audible noise was generated by the chattering in the actuator for the case of small boundary layer setting (Φ=50 N) shown in the figure.

---

[2] Recall that these dynamics are neglected 'parasitic actuator' dynamics for the modeled system for controller design. See footnote in Subsection 4.1.5.1
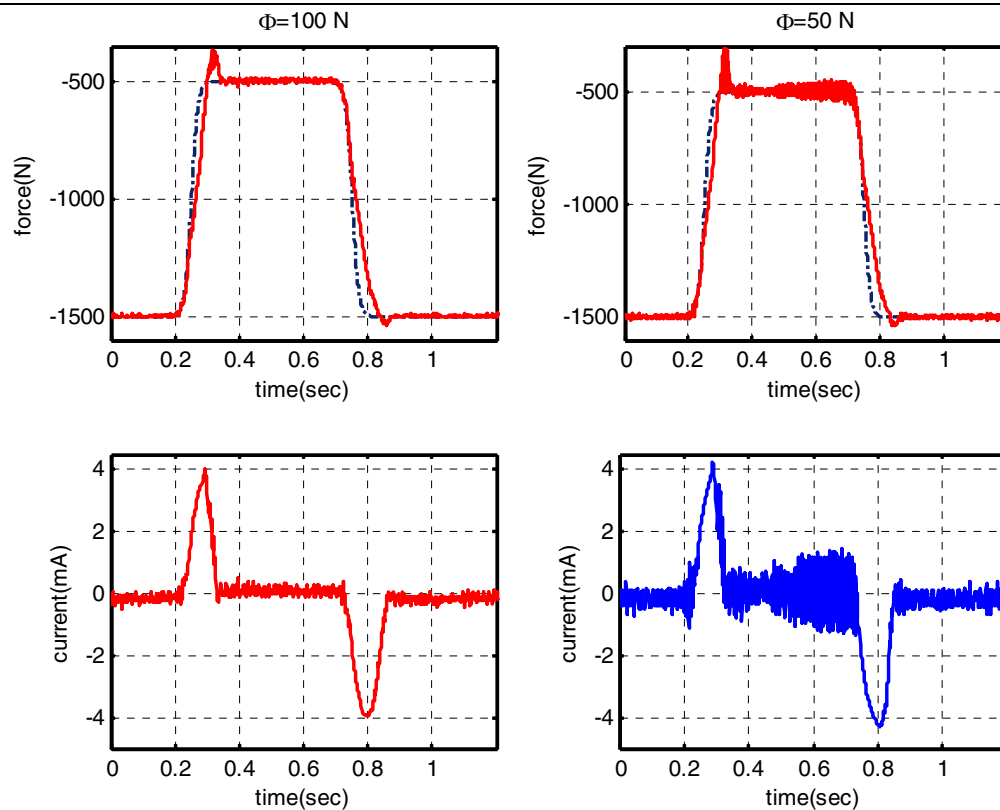
Figure 4.21: Effect of high gain *K* and chattering (experiment)

In summary, in this subsection, experimental results have been presented to show the tracking performance of the continuous sliding mode controllers given by Eqs. 4.57 and 4.56, which were considered as robust versions of the Near IO linearizing controller for pressure force tracking. It is argued mainly that the gain K and the boundary layer thickness Φ should be chosen with care. Too high a value of the gain K induces overshoot and chatter, especially with low boundary layer thicknesses.

4.2.1.2.2 Robustness Tests with Simulations

In the previous subsection, experimental results were presented to show the performance of the sliding mode pressure force tracking controller. This controller was designed with the goal of achieving robustness to matched parametric uncertainty in the basic parameters β_e, C_v, and C_L. To verify the robustness of the sliding mode controller

on the actual system, it is necessary to change the parameters of the plant (the electrohydraulic actuator) in a controlled and quantifiable manner. This is very difficult, if at all possible, to accomplish on the plant itself. Therefore, in this work, it was decided instead to simulate the validated model of the system from Chapter 3, which includes the dynamics of supply and return transmission lines, the accumulators and of the servovalve. In the simulations, the model parameters could be changed while investigating the robustness of the performance of the sliding mode controller to these changes.

For the simulations in this section, the following basic assumptions were made. The specimen reaction, denoted by F_L in modeling discussions, was approximated by a linear spring and damper of coefficients 950 kN/m and 500 Ns/m, respectively. Also, since mounting considerations are absent in computer simulations, larger desired force trajectory steps were considered (± 4 kN) and correspondingly the smoothing parameter T was set higher at T=0.025 sec to limit the derivative of the desired trajectory as described in Subsection 4.1.6.1. The lower bound for gain K was then calculated as in the previous subsection, i.e, assuming the uncertainty bound δf_F to be a minimum of 20% of the nominal value and bound δg_F to deviate from the nominal value of 1 by 20%. In the simulations, K= 3.4E7 kgcm/s^3 and the boundary layer thickness Φ=100 N.

Figure 4.22 shows simulation results comparing the tracking performance of the sliding mode controller when the bulk modulus (β_e) parameter of the electrohydraulic actuator was changed as much as $\pm 40\%$ while the (β_e) parameter of the controller is kept at the nominal value (850 MPa). It can be seen that there is virtually no change in tracking performance of the sliding mode controller for this wide range of variation in the effective bulk modulus of the electrohydraulic actuator.
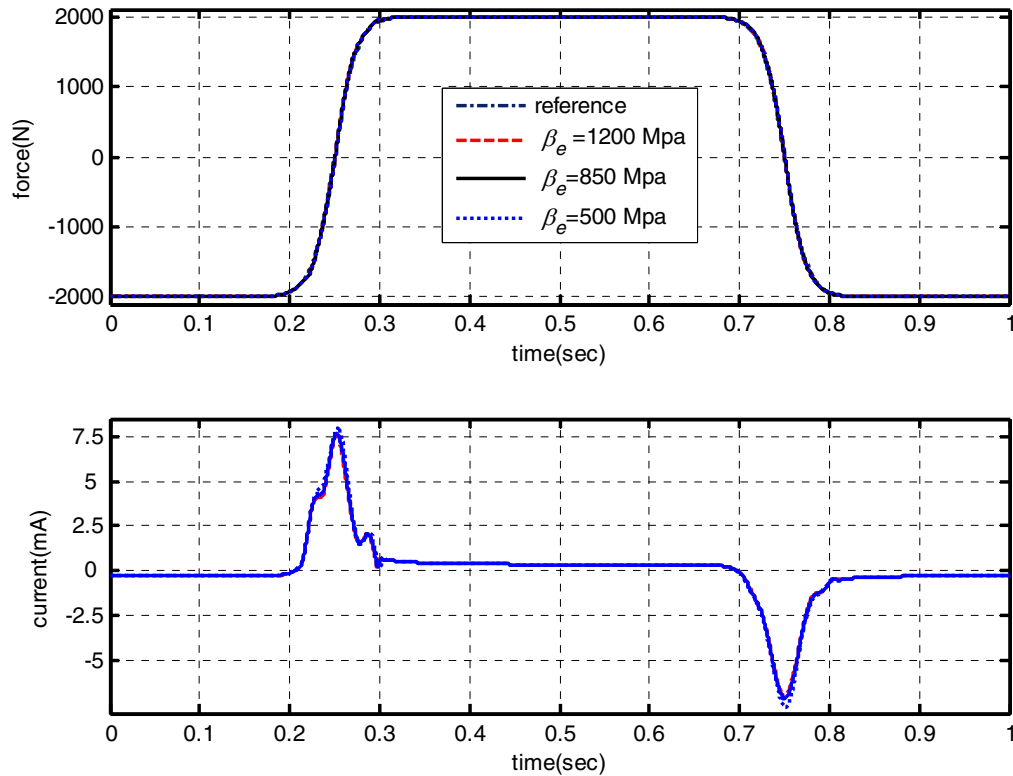
Figure 4.22: Effect of variation in the effective bulk modulus of the electrohydraulic actuator on the sliding mode controller (simulation)

Uncertainty in the controller valve coefficient C_v could come from two uncertain parameters of the electrohydraulic actuator, according to the definition $C_v = G_v K_v$ used in controller derivation where the servovalve dynamics were neglected. Fig 4.23 shows simulation results showing the effects of variations in the valve gain G_v. It can be seen that for as much as $\pm 16\%$ change in the servovalve gain, the tracking performance remains close to the nominal. As the gain deviation from the nominal value increased beyond these bounds, the performance deteriorated in a manner similar to the case of changing K_v discussed below.
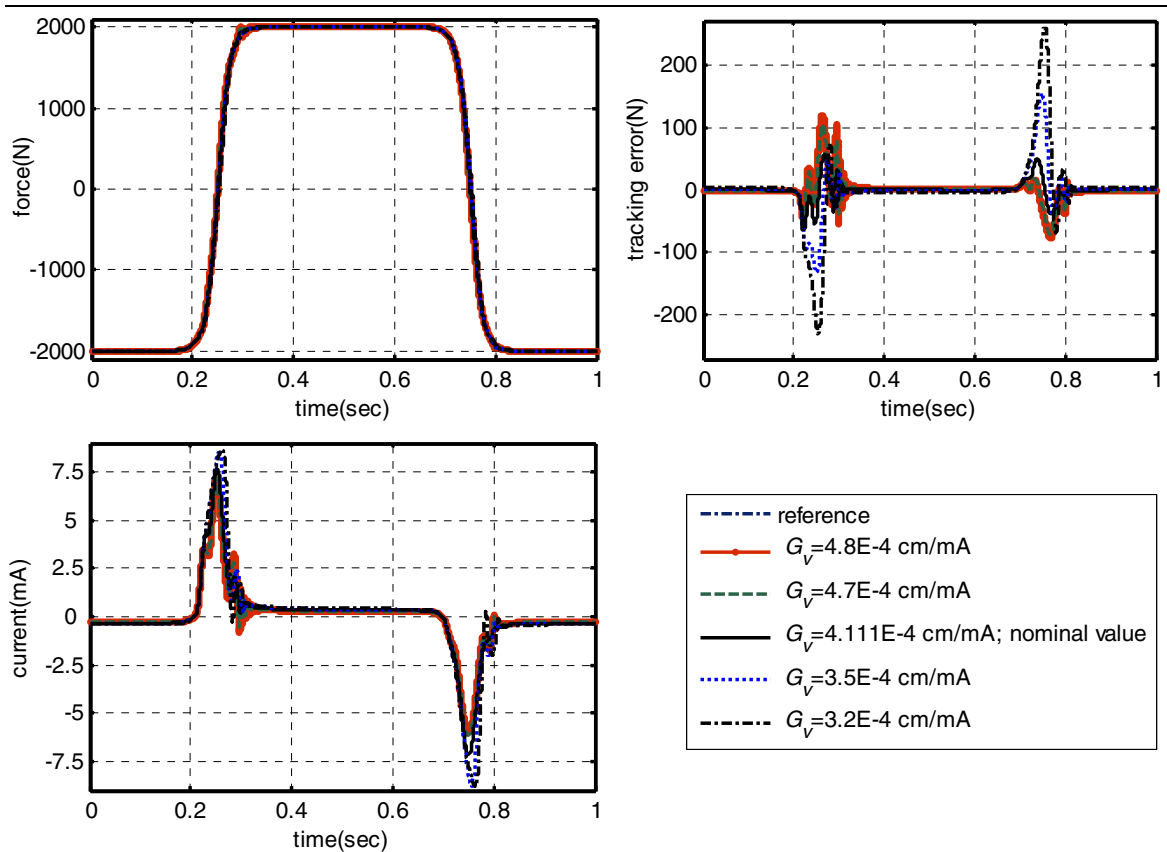
Figure 4.23: Effect of variations in the servovalve gain on sliding controller performance (simulation)

The valve coefficient K_v, which is the coefficient of the nonlinear port flow equations, is defined with respect to the spool position in the servovalve model (see Subsection 3.3.1). As shown Fig 4.24, changing K_v instead of the servovalve gain G_v gave a similar trend in tracking performance as changing G_v within the $\pm16\%$ bound. With increase in K_v (or G_v) to 18% higher than the nominal value, however, the response became oscillatory and ultimately went unstable for only slightly higher values of K_v (or G_v). The figure also shows that lower values of K_v (or G_v) than the nominal did not cause such a stability problem.
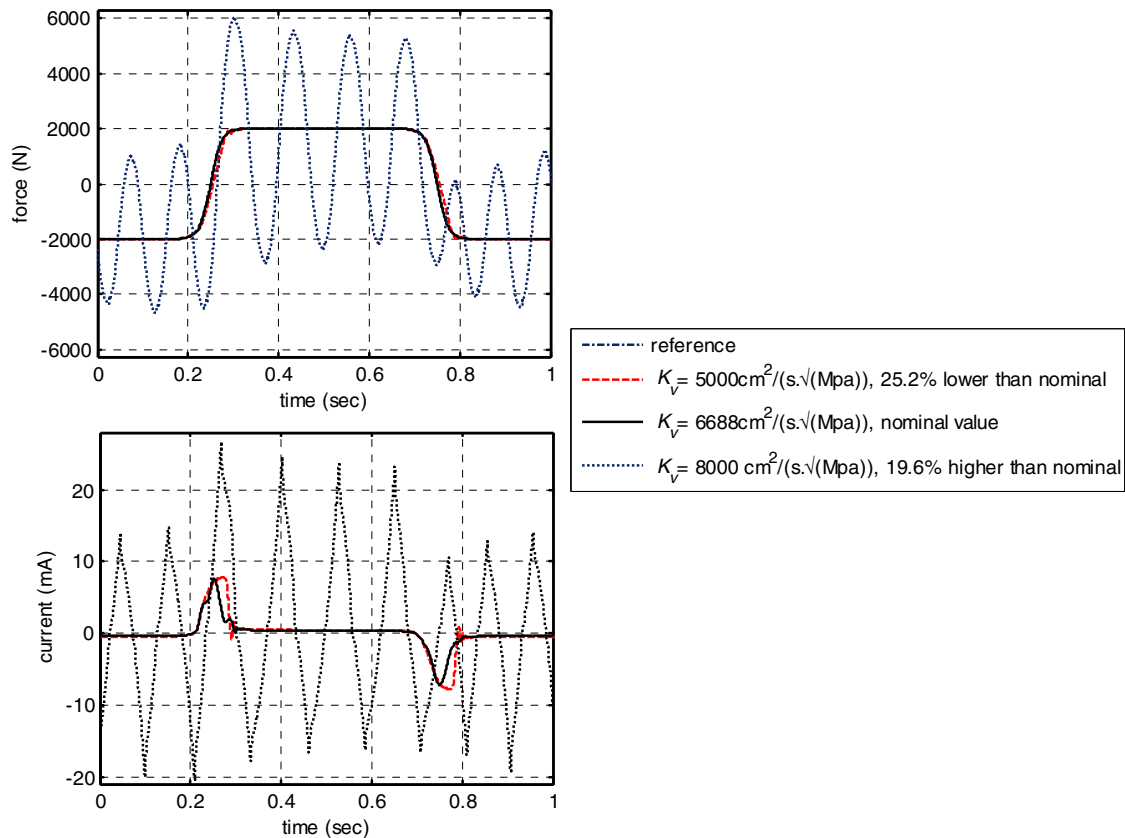
Figure 4.24: Effect of variations in the valve coefficient K_v on the performance of the sliding mode controller (simulation)

It should be recalled that the above observation from simulations with the sliding mode controller parallels the experimental observation made in Subsection 4.2.1.1.2 for the Near IO linearizing controller. The sliding mode controller is more sensitive to uncertainty in the estimate of the valve coefficient than it is to uncertainty in the estimate of the bulk modulus. Furthermore, overestimating the value of the valve coefficient C_v for the controller is better than underestimating it in terms of maintaining bounded or overshoot free response and stability. This is a key observation for both the sliding mode and Near IO linearizing controllers.

Figure 4.25 shows the effect of uncertainty in value of the actuator leakage coefficient C_L. As in the case of the IO-linearizing controller, the effect of mismatch between the leakage coefficient of the actuator and the value used in the controller is to

cause steady-state error in the force tracking response. However, compared to the bulk modulus and valve coefficient parameters, the leakage coefficient has the least effect in terms of altering the transient tracking performance. The negative value of the leakage coefficient is a hypothetical case, to show that for as much as a $\pm$ 200% mismatch in the leakage coefficient, the tracking error was kept within 100 N. When there is perfect knowledge of the leakage coefficient, i.e C_L takes the nominal value, there is no steady-state tracking error.
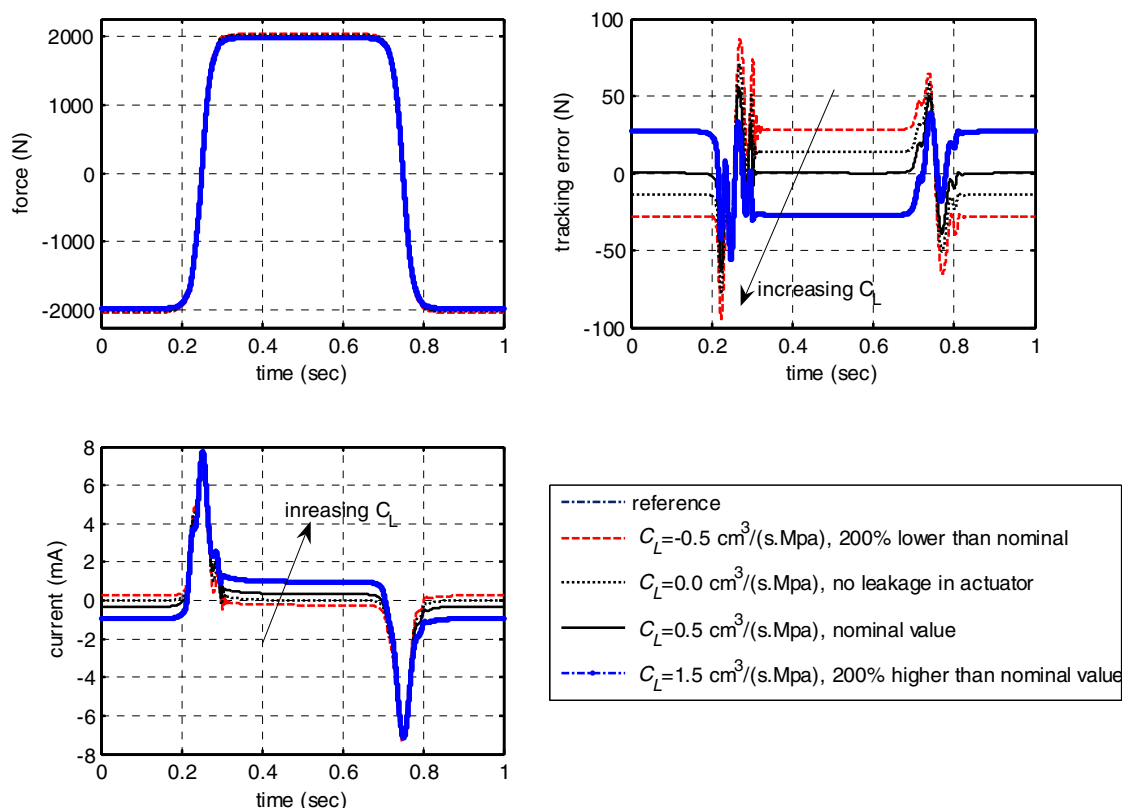
Figure 4.25: Effect of variation in the actuator leakage coefficient C_L on the performance of the sliding mode controller (simulation)

As noted in the previous subsection using experiments with the sliding mode controller, the tracking performance improves, to a limit, with higher gain K settings. However, using too high values of gain K settings, to allow higher modeling uncertainty bounds and increased robustness, leads to chattering particularly with lower boundary layer thickness. This is also demonstrated with system simulations in Fig 4.26. As

discussed before, a good deal of modeling effort (in reducing uncertainty) is necessary to use optimum values of the gain setting K for a desired level of tracking accuracy without exciting the dynamics which are not considered during controller design.
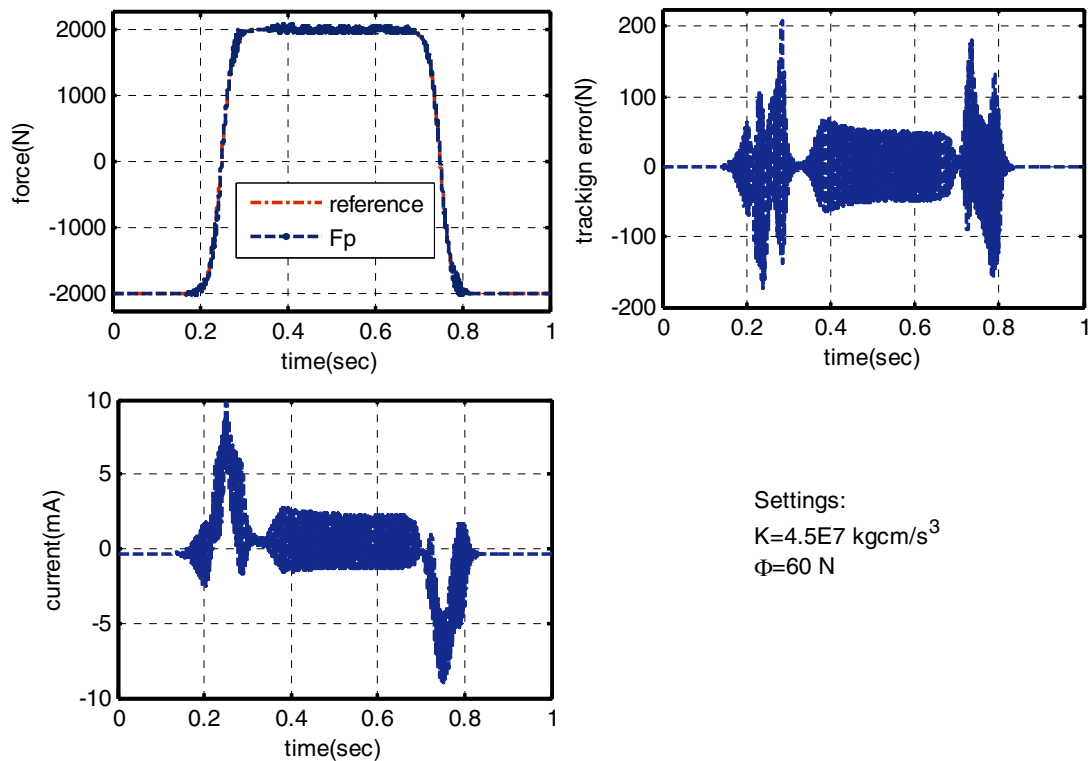
Figure 4.26: Demonstration of chattering at high gain K and low boundary layer thickness settings (simulation)

4.2.1.2.3 Summary of Sliding Mode Force Tracking Results

The following observations summarize the results on the sliding mode controllers:

- It was shown with experiments that the robust sliding mode controller can recover the performance of the nominal Near IO linearizing controller, provided the gain K and the boundary layer thickness Φ are tuned considering allowable uncertainty bounds.

- Both experiments and simulations showed that high values of gain K and/or too low boundary layer thickness Φ values lead to control chatter and excite the servovalve

and transmission line dynamics which were neglected during the derivation of the control laws. High values of K mean allowing larger uncertainty bounds and thereby allowing less emphasis on model accuracy. In the presence of the neglected dynamics for the test system, the allowable increase in gain K before chattering commences is limited. Therefore, it is imperative to get good estimates of the controller model parameters so that the gain K remains reasonable with an acceptable boundary layer thickness that does not lead to control chatter.

- The smooth version of the sliding mode controller using the tangent hyperbolic function given by Eq. 4.57 gives slightly less overshoot and control peaks than the version using the saturation function given by Eq. 4.56.

- Simulation studies were conducted to verify the robustness of the sliding mode controller design to mismatches in controller vs. system (plant) parameters. It is noted that the controller was most sensitive to mismatch in the valve coefficient C_v, which in turn could come from uncertainty in the gain of the servovalve G_v or the valve coefficient K_v defined with respect to valve spool position. It was also observed that it is generally better to overestimate the value of the valve coefficient C_v for use in the controller than to underestimate it. Furthermore, the controller was least sensitive to as much as a ±200% mismatch in the leakage coefficient C_L whose effect was seen to be causing a steady-state error. The sliding mode controller was robust to as much as a ±40% mismatch in the bulk modulus parameter.

4.2.2 The Piston Position Tracking Controllers

As outlined in Subsection 4.1.3, in this thesis, two approaches are described for the problem of piston position tracking control with nonlinear controllers from a feedback linearization framework. The first is Near IO linearization of the system model with piston position as output, giving Eq. 4.30 for the position tracking controller. And the second approach is a cascade controller using the Near IO linearizing pressure force tracking controller given by Eq. 4.13 as an inner-loop to a feedback plus feed forward

position controller outer-loop defining a synthetic desired force profile (by Eq. 4.38 or Eq. 4.58) for the inner-loop. It was shown in Subsection 4.1.3.2 that the two approaches are theoretically equivalent. Using a Lyapunov backstepping interpretation, it was also shown that with the robust sliding mode force controller of Eq. 4.56 (or Eq. 4.57) as the inner-loop, and the desired force profile computed by the outer-loop controller given by Eq. 4.58, the resulting closed-loop system gives bounded tracking errors for bounded uncertainty that meet linear growth conditions.

Furthermore, a quick look at the schematic of the cascade implementation in Fig 4.6 reveals that most of the modeled nonlinear effects and uncertain parameters are confined to the force inner-loop, except for friction and load force estimation. The theoretical equivalence of the Near IO linearizing position controller with the cascade controller implies that the observations on robustness (sensitivity) to parametric variation of the Near IO linearizing pressure force controller apply to the Near IO linearizing position controller case as well. This is also evident from the similarity of the nonlinearity cancellation expressions in the respective controllers; g_p is a scaled version of g_F as given in Eq. 4.29 and f_p includes a scaled version of f_F as given by Eq. 4.28. In this section, the robustness analysis and simulations will be restricted to the uncertainty to unmatched uncertainty of the force loop (to the terms in f_p other than f_F), namely friction.

The experimental setup had an LVDT (for position measurement) and an accelerometer for acceleration measurement. Second-order low-pass Butterworth filters, with cut-off frequency at 40 and 50 Hz, were used within the feedback loop for reducing noise from the position and acceleration signals. The velocity signal was obtained by differentiating the filtered position signal. The pressure transducers for the chamber pressure are good to 400 Hz.

The discussion in this subsection is organized as follows. First, some simulation and experimental results are presented for the basic performance of the nominal Near IO linearizing position tracking controller. This is followed by an analysis of the robustness of the Near IO linearizing controller to uncertainty in friction. We consider load measurement uncertainty to be either less severe than uncertainty in friction estimation or

that it can be lumped with the friction uncertainty. Finally, experimental results and simulations are presented for the cascade controller.

4.2.2.1 Near IO Linearizing Controller

4.2.2.1.1 Basic Performance

In this subsection, experimental and simulation comparisons are presented for the Near IO linearizing controller given by Eq. 4.37, a PID position controller, and a linear state feedback with integral (LSFI) controller. The case $F_L=0$, i.e, where the actuator is loaded with a known inertia load (m_p=12kg) is considered. The same sets of model parameters (from Appendix B) were used in both the simulations and experiments.

For the Near IO linearizing controller, pole placement was used to compute the three gains k_1, k_2, k_3 so that the three closed-loop poles of the position error dynamics (Eq. 4.33) were placed at the same location in the left half s-plane. We used system simulations to evaluate various pole locations and chose the set with satisfactory experimental response (without saturating the current). Similarly, the PID and the LSFI controllers were tuned interactively using nonlinear system simulations and experiments, and finally selecting the gain settings that gave satisfactory experimental response (oscillation free, minimal steady-state error). The tuning of the PID controller was done by increasing the proportional (P) gain until either overshoot commenced in the experimental "smooth" step response or the control current saturated, in which case the other two gains were adjusted. In all of the position control tests performed for this work, the control current saturated with just P control before any overshoot appeared in the response. The derivative (D) gain excited unwelcome oscillations. The steady-state

response error to a step position reference is normally zero and as such the integral (I) gain is not necessary[3], barring valve dead zone effects.

Fig 4.27 shows simulation results when tracking a "smooth" step of -30mm-to-+30mm-to-30mm defined with the smoothening parameter T=0.05. For the Near IO linearizing controller, all three closed-loop poles were set at s=-300. The P-gain of the PID controller was 20 mA/cm. The LSFI controller gains were K_1=65 mA/cm, K_2=-0.005 mA.s/cm, K_3 =0.180 mA/MPa, K_i=-827 mA/s.cm.
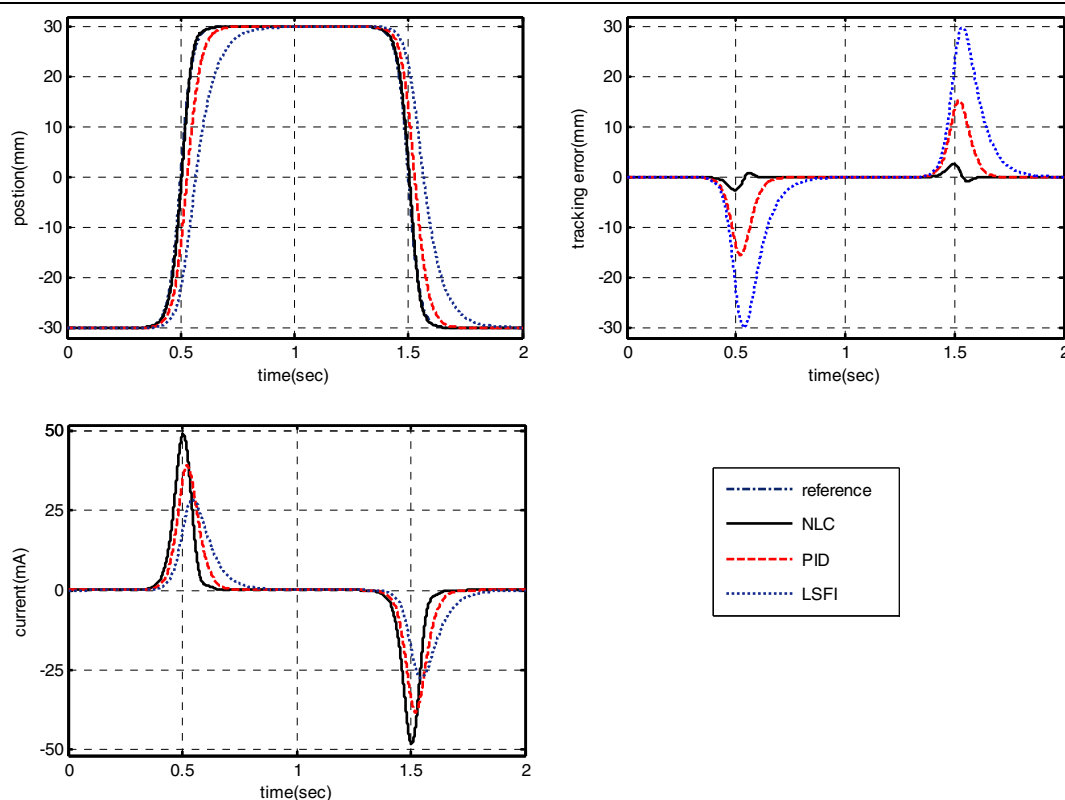
Figure 4.27: Comparison of the basic performance of the Near IO linearizing controller (NLC) against linear PID and LSFI controllers (simulation)

The simulation results in Fig 4.27 show better tracking performance for the Near IO linearizing controller (NLC) than either the PID or the LSFI controller. However, the

---

[3] Recall that the electrohydraulic actuator acts as velocity source and as such is a natural integrator to position. The steady-state response error to a reference position step input is normally zero under closed-loop P-control.

nonlinear controller used larger current peaks than either linear controller. The gains for the simulations of all three controllers were chosen to be the ones that gave well-tuned performance in the experiments without saturating the control current (±50 mA).
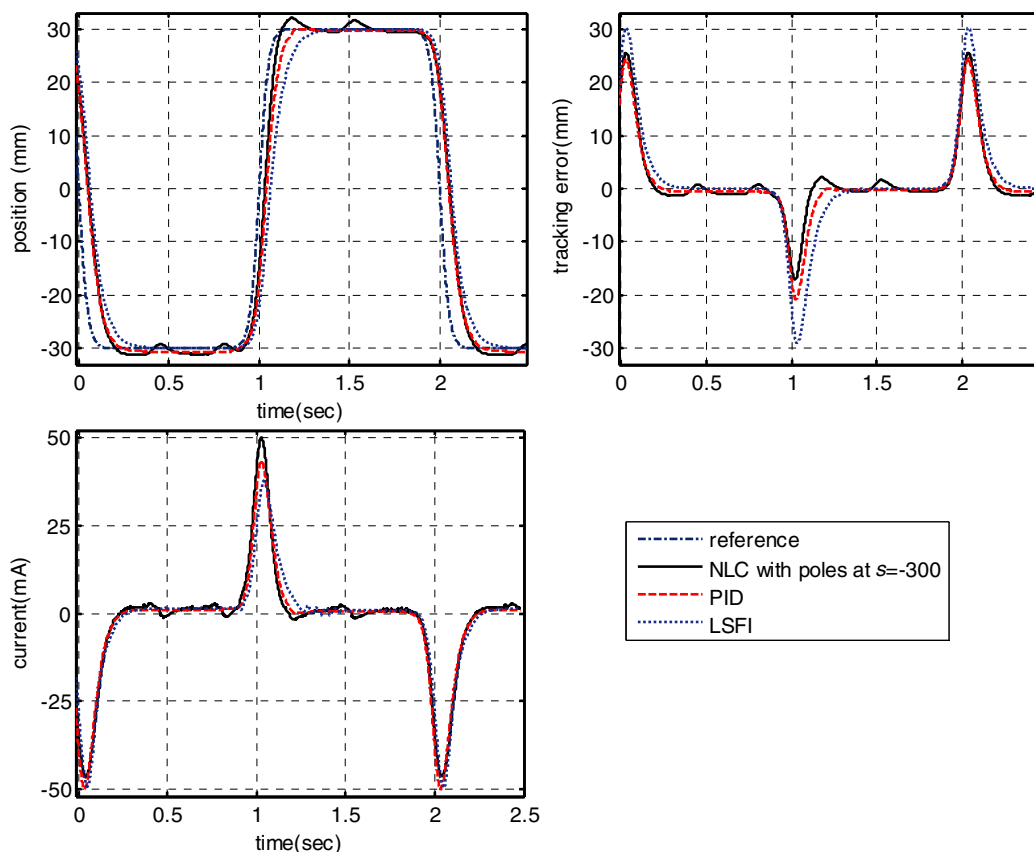
Figure 4.28: Comparison of the basic performance of the Near IO linearizing controller(NLC) with PID and LSFI controllers (experiment)

Fig 4.28 shows results from experiments. The advantage of the Near IO linearizing controller (NLC) over the PID and LSFI controllers did not appear to be significant. The NLC was affected the most from delays and dynamic elements (signal filters) that were relevant in the experiments but absent in the simulated predictions above[4]. Furthermore, there is asymmetry in the experimental response which is attributed mainly to asymmetry in the value of the valve coefficient C_v (see Appendix B) whereas a single nominal value was used in the experiments with the NLC.

---

[4] The effect of this in loop filtering can be included in simulations, but the topic is omitted here for brevity.

Since the LSFI controller turned out to be inferior to the PID controller, the LSFI controller will not be considered any further in this work. It suffices to say here that, nonlinear state feedback (the NLC) performed better than linear state feedback (LSFI) for this particular system. However, the comparison performed here is not claimed to be exhaustive for all possible closed-loop pole locations with the LSFI controller.

Some of the oscillation in the response with the NLC can be removed by moving the three closed-loop poles to the right for a slower response, thereby reducing the effect of the filters. However, it should be recalled from the discussion in Subsection 4.1.6.2 that there still remain the effect of neglected transmission line and servovalve dynamics. Fig 4.29 shows the experimental response comparison of the NLC with the poles placed at $s=-250$ and the PID with the P gain kept the same as before. It can be seen that the NLC does not perform any better than the PID when slower pole locations are chosen.
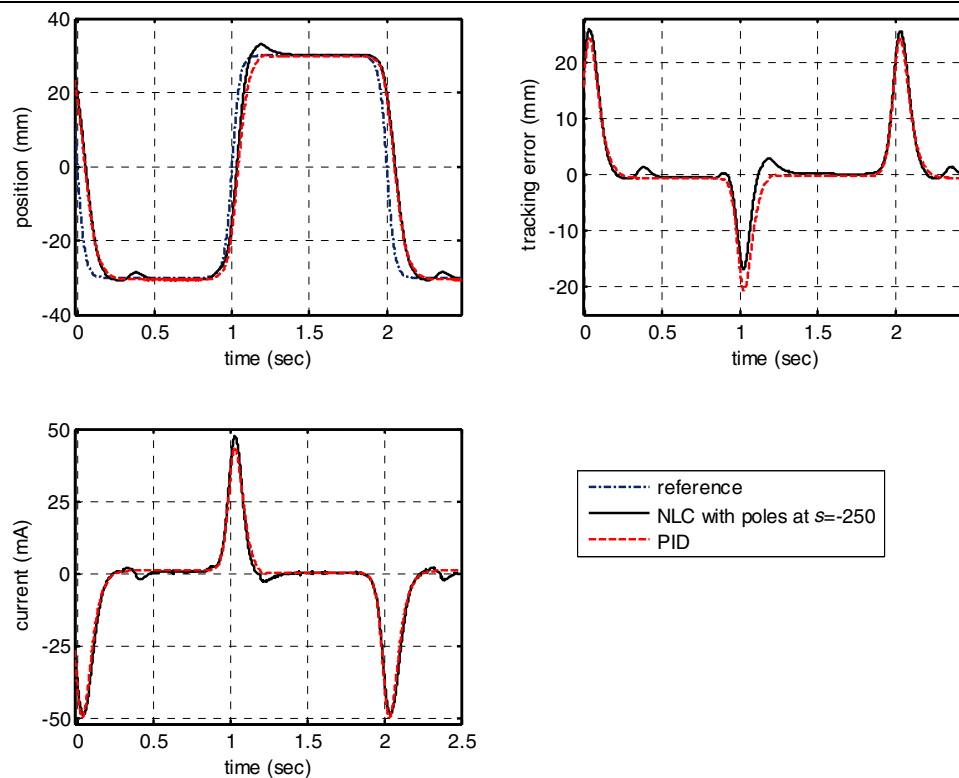
Figure 4.29: The Near IO linearizing controller(NLC) with slower pole location compared with a well tuned PID controller (experiment)

To summarize the results on the basic performance of the Near IO linearizing position tracking controller (NLC), it is noted that the NLC may not perform any better than a well-tuned PID controller in the presence of unmodeled dynamic elements such as signal filters, transmission lines and the servovalve. In practice, high quality sensors can be used and the signal processing limitation can effectively be removed. Also, the effect of the transmission line dynamics can be effectively eliminated by close-coupling the accumulators on the servovalve manifold, as discussed in Subsection 3.2.4.

To make a concluding statement regarding a performance comparison of the Near IO linearizing controller with the PID controller, the effect of the dynamics of the transmission lines and the servovalve need to be investigated further. First, we keep the same parameters for the model of the servovalve dynamics ($\omega_{n,v}$=140 Hz, and ζ_v=1.1) and consider the case where the accumulators are close-coupled with the servovalve, i.e, only SECTIONs II of the supply and return hoses are removed from the system model interconnection shown in Fig 3.9, in Chapter 3. Note that not all of the transmission hoses are removed, unlike the idealized study in Subsection 4.1.6.2. Also, the pump supply pressure is set at 21 MPa, as this is the design supply pressure for all components in the system[5]. Under these conditions, it turns out that even faster closed-loop poles could be considered for the near-IO linearizing controller without saturating the control current. For the simulation result shown in Fig 4.30 , all three closed loop poles are placed at s=-400 for the Near IO linearizing controller. Similarly, for the PID controller, the previous restriction to experimentally useable maximum gain is lifted and the P-gain is tuned to 280 mA/cm, giving the same control peak magnitude as the NLC.

---

[5] During the experiments for this work, the test system was sharing the hydraulic pump with other systems which run at 14 MPa supply pressure. Unless otherwise noted, in all simulations and experiments, 14 MPa was used as the supply pressure at the pump output (see Fig 3.1).
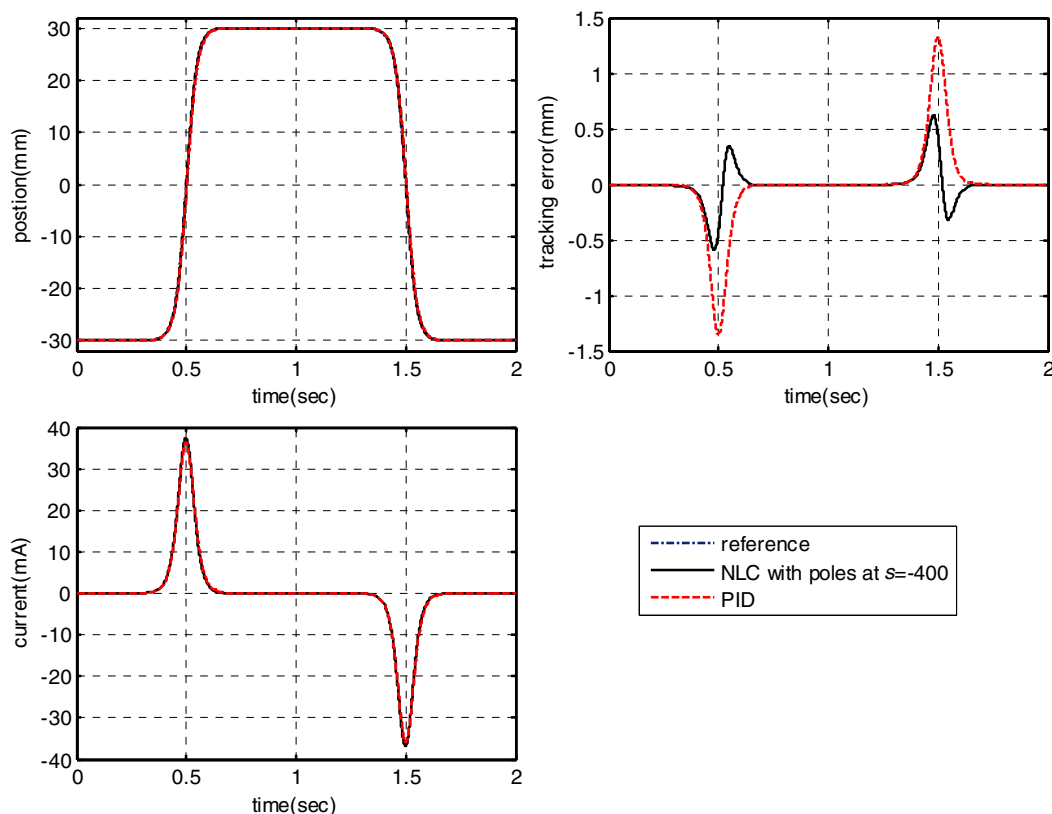
Figure 4.30: Comparison of the Near IO linearizing controller (NLC) with a PID controller considering accumulators close-coupled with the servovalve (simulation)

Figure 4.30 shows that for the same control current peaks for the two controllers, the maximum tracking error is smaller with the NLC (by over a 100%). Furthermore, the NLC gives a response that overshoots before settling as can be seen in the tracking error response. This may be objectionable in some applications.

Second, we consider the accumulator close-coupling and pump supply pressure settings as above, but include the case where the servovalve corner frequency was increased to 240 Hz with the damping ratio of 1.1. This corresponds to the true specifications of the present servovalve with the supply pressure at 21 MPa [86]. Increasing the servovalve natural frequency to 240 Hz approaches the basic assumption of a fast servovalve made for the nonlinear controller derivation. Figure 4.31 shows simulation results with these changes. The two controllers were independently tuned, as above, so that the same control peak was obtained with the two controllers. The P gain of

the PID needed to be reduced to 250 mA/cm since instability occurred when the above gain of 280 mA/cm was used. With the reduced P gain, adding even a small D gain excited instability. On the other hand, with the fast servovalve, the three closed-loop poles for the NLC could be chosen even faster for basically unchanged current peaks.
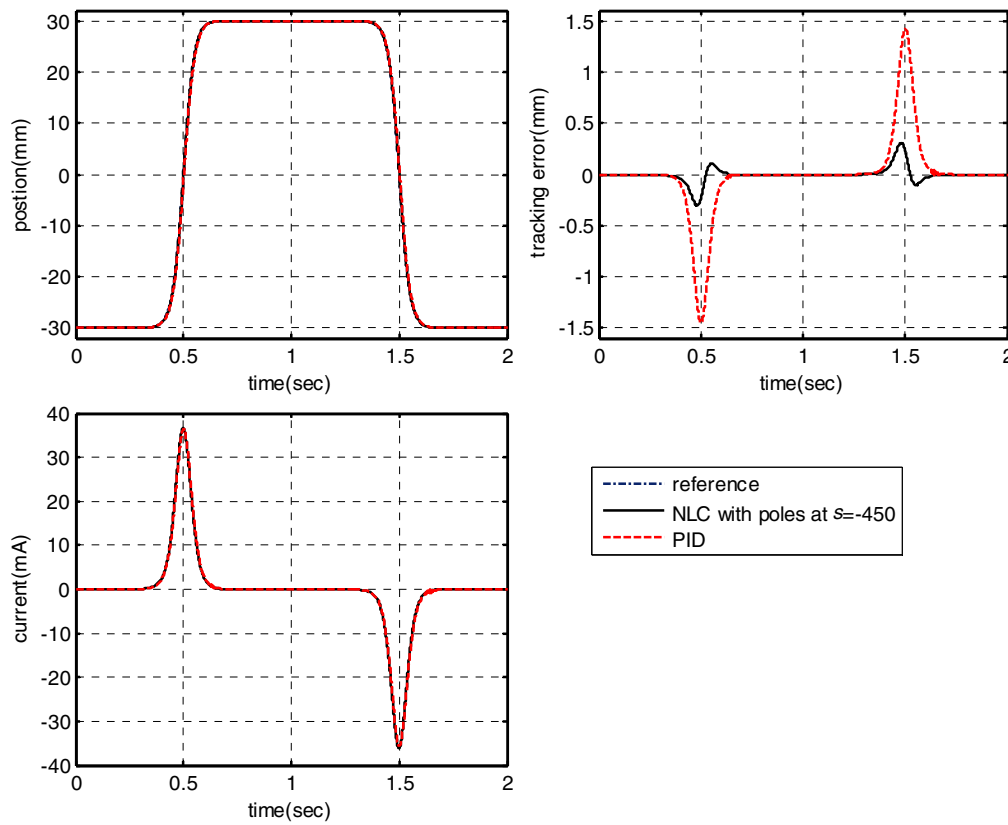
Figure 4.31:Comparison of the Near IO linearizing controller (NLC) with a PID controller considering accumulators close-coupled with a faster servovalve (simulation)

We note from Fig 4.31 that the peak tracking error is lower with the NLC by more than 350% of the peak tracking error obtained with the PID controller. With the faster servovalve operating at the design pressure, and the accumulators close-coupled with the servovalve, we see that the Near IO linearizing controller's performance approaches the ideal conditions where the servovalve dynamics were neglected and the transmission lines were absent (Subsection 4.1.6.2). It is also interesting that with a faster servovalve in the system, the closed-loop poles could be selected further to the left in the *s*-plane for the Near IO linearizing controller, without significantly increasing the control current

peak, and thereby improving the advantage of this controller even more. On the other hand, for the PID controller, a limit of 280 mA/cm was determined for the P gain beyond which instability commenced in the system response. At the end of Subsection 4.2.2.2.1, it will be shown that the Near IO linearizing controller can be tuned for even better performance before the control current saturates.

The following points summarize the main results of this subsection:

- For the experimental test system, the benefits of the Near IO linearizing position tracking controller are greatly influenced by the dynamics of transmission lines and servovalve, hardware delays, and the limited bandwidth of the position and acceleration signal filters. In the experiments where all these effects were present, the Near IO linearizing position tracking controller did not perform much better than a well-tuned PID (or P) controller.

- The response of the Near IO linearizing controller can be tuned by properly selecting the closed-loop poles in the left half s-plane. With the accumulators close-coupled with the servovalve and/or the servovalve operating faster at its design supply pressure, the closed-loop poles could be pushed further to the left in the s-plane for better tracking performance without saturating the control current.

- Assuming the availability of high bandwidth signal processing, and using the validated system interconnection model from chapter 3, it is argued that the Near IO linearizing position tracking controller would be superior to a PID controller in the realizable system including a faster servovalve operating at the design pressure and accumulators close-coupled on the servovalve manifold.

Before closing this subsection, we stress that for the rest of the discussion in this chapter, where we are not concerned with comparing the nonlinear controllers with other controllers, we consider the test system as initially experimented on. That is, neither accumulator close-coupling nor higher supply pressure operation of the servovalve is considered, unless stated otherwise.

4.2.2.1.2 Robustness to Uncertainty in Friction Estimation

In this subsection, we look at the robustness of the Near IO linearizing position tracking controller to uncertainty in the estimation of friction. Recall from the discussions in Subsections 4.1.4.2 that the analytical friction force model, estimated from experiments described in Subsection 3.3.2, was approximated with differentiable functions. This was necessary since the controller expression for the Near IO linearizing position tracking controller (Eq. 4.37) uses the derivative of the friction force estimate to cancel the nonlinear friction force on the piston and result in the linear closed-loop position dynamics.

Again, since it is hardly possible to exactly determine and alter the friction in the actual system in a quantifiable manner, we use system simulations to evaluate the robustness of the Near IO linearizing controller to different representative cases of friction uncertainty. As a first case, we suppose that the nonlinear and smooth friction estimation of Subsection 4.1.4.2 with the smoothening parameter $\gamma=5$ is used as the nominal friction estimate in the controller, and we alter the friction in the actuator model to be higher or lower by 100% (including a hypothetical case of zero friction). In practice, significant variations in friction can happen with changes in temperature, oil viscosity, operating pressure, and also length of running time for the actuator. As a second case, we consider changing the nonlinear friction estimation model used in the controller to a nominal linear viscous case, or to even no friction estimation while we keep the nominal nonlinear estimate of friction in the actuator model. Both of these cases are compared with the case of perfect knowledge of the nonlinear friction in the system by the controller.

For the simulations, we return to the model of the test system from Chapter 3 and nominal controller parameters listed in Appendix B. For the Near IO linearizing controller, all three closed-loop poles are placed at $s=-300$. We consider the performance of the Near IO linearizing controller when tracking a 20 mm-2 Hz sine wave reference trajectory where the velocity is limited to ±25 cm/s. This velocity range is where the nonlinearity due to friction is the strongest as shown in Fig 4.5.

Figure 4.32 shows results for the first case, where the friction estimation used in the controller is mismatched from the actual friction in the actuator by ±100%.
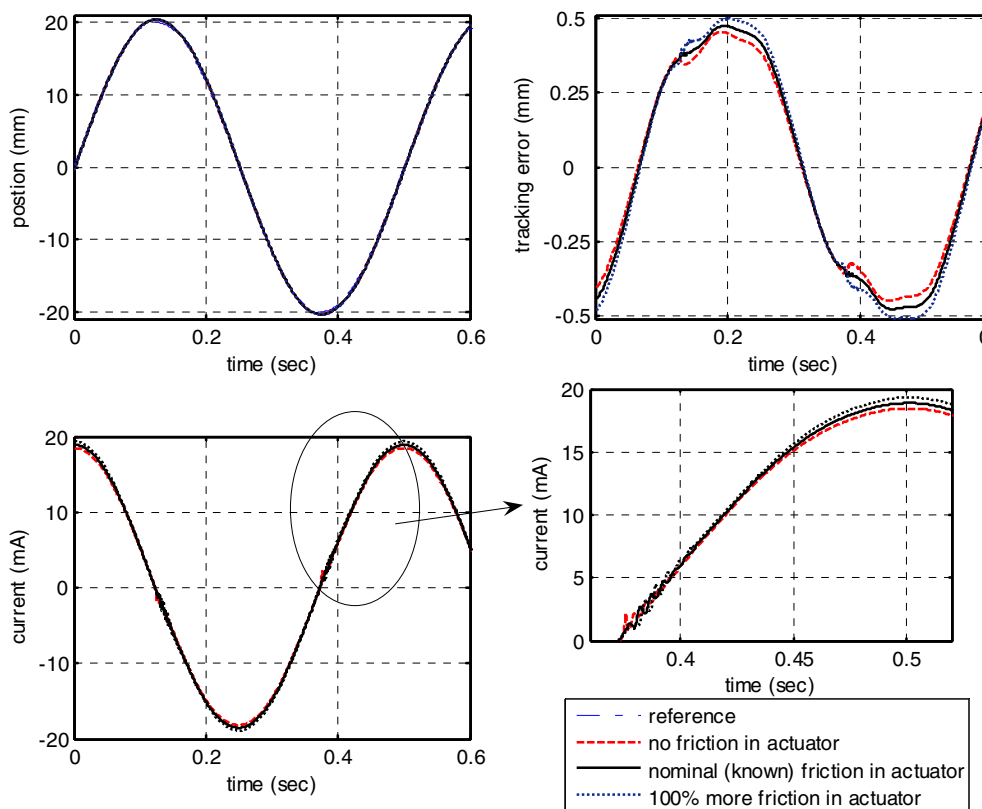
Figure 4.32: Effect of uncertainty in the actuator friction on the tracking performance of the Near IO linearizing controller (simulation)

It can be seen from Fig 4.32 that the effect of uncertainty in the friction estimate is minimal on the tracking error with the Near IO linearizing controller. When there is more friction in the actuator than estimated by the controller, slightly higher control current is required, and the peak tracking error is also correspondingly higher. When there is less friction in the actuator than estimated by the controller, the peak tracking error is lower. The significant deterioration in tracking performance appears mainly near zero velocity, when the piston is coming to rest and changing direction of motion. Also notable from the control current and the tracking error plots is the evidence of the effects of the stick-slip on transition of friction from static to kinetic values near zero velocity.

Now that it is determined that uncertainty in the nonlinear friction estimation does not appear to significantly influence the tracking performance of the Near IO linearizing controller, we look at the possibility of using less accurate friction estimation for the controller on the resulting performance. Fig 4.33 shows a comparison of cases of no-friction estimation, nominal nonlinear estimation and (nominal) viscous estimation in the controller model, while only the nominal nonlinear model is kept in the actuator model.
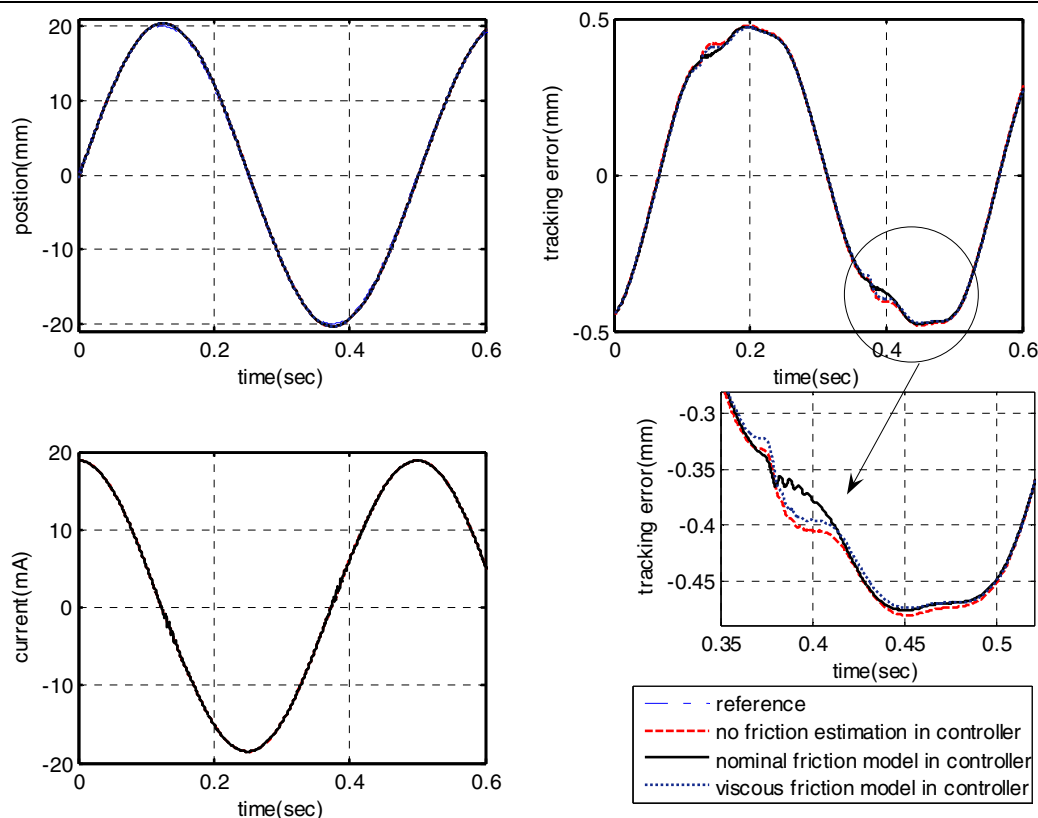
Figure 4.33: Effect of changing the friction estimation model in the Near IO linearizing controller (simulation)

Again, the significant difference in the tracking error from the use of a viscous (linear) friction or nonlinear friction or no friction estimation in the Near IO linearizing controller is mainly near zero velocity, accompanied by the stick-slip phase of the motion, as can be seen in the magnified insert of Fig 4.33. It is slightly better to have an estimate of friction in the controller, even if only viscous, than to ignore it altogether.

In summary, it is observed from the simulation study in this subsection that, for the test system model under study, the tracking performance of the Near IO linearizing

controller does not appear to be significantly affected by uncertainty in friction estimation. A simple viscous estimation may be sufficient for this particular system, depending on whether the observed difference in tracking error is considered critical for a particular application or not.

4.2.2.2 Cascading Position Tracking with Pressure force Tracking

As discussed in detain in Subsection 4.1.3.2, the cascade application of the Near IO linearizing pressure force tracking controller of Eq. 4.13 as an inner-loop and the definition of desired force profile by (Eq. 4.38 or Eq. 4.58) as a synthetic outer-loop position control gives a control current that is equivalent to that of the Near IO linearizing position tracking controller. In this subsection, we first demonstrate this equivalence of the two control approaches with simple experimental results for nominal cases. We then discuss tuning of the cascade controller. And finally, we take a brief look at the performance of the robust cascade controller. Only cases with F_L=0, i.e, where the actuator is loaded with a known inertia load (m_p=12kg), are considered.

4.2.2.2.1 Nominal Performance

Consider that all three closed-loop poles for the Near IO linearizing position tracking controller are set at s=-250. The controller gains k_1, k_2, and k_3 are then computed using pole placement after which Eq. 4.43 can be used to compute the equivalent controller gains k_p, k_v, and k_o. The resulting numerical values are k_p=6.95E5 kg/s^2, k_v= 5560 kg/s, and k_o=250 s^{-1} for m_p=11.12 kg. Figure 4.34 shows the experimental comparison of the two controllers when tracking the smooth step reference from -30-to-30-to-30 mm defined with T=0.05 as in the last subsection. It can be seen that the tracking performance of the two control structures is nearly identical as expected.
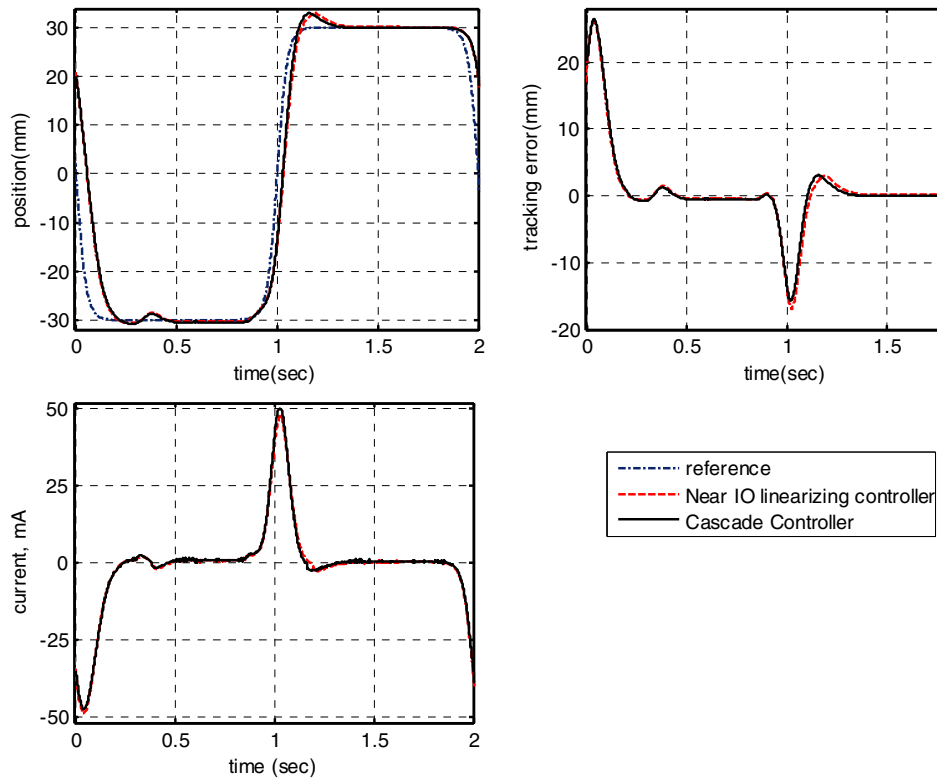
Figure 4.34: Equivalence of the Near IO linearizing position tracking controller and the cascade controller (experiment)

We now consider the tuning of the cascade controller. Recall that, the three gains of the cascade control structure have simple physical interpretations. The gain k_o dictates the speed of response of the force inner-loop as a result of the Near IO linearizing pressure force tracking controller (Eq. 4.13), whereas the gains k_p and k_v determine the natural frequency and damping ratio, respectively, of the second-order outer-loop position error dynamics given by Eq. 4.40. Similar interpretations are not readily evident for the three linear gains of the Near IO linearizing position tracking controller.

With these comments, and using the above numerical values or the discussion following Eq 4.43, we notice that placing all three poles for the Near IO linearizing controller at the same pole location of $s=-250$ is equivalent to setting the natural frequency of the position outer-loop at 40 Hz with a critical damping ratio of 1.0 for the cascade controller. Also $k_o=250$ s^{-1} corresponds to a break frequency of 40 Hz for the first-order force-loop. This is not a problem, since, with the interpretation revealed by the

cascade form, the force error loop is separated from the position error loop and the force tracking error drives the position tracking error.

Figure 4.35 presents experimental results showing the effect of tuning the force inner-loop by changing gain k_o, while keeping the k_p and k_v gain settings as above. The lower the setting for gain k_o, the slower the decay rate of force-tracking error, and correspondingly, the slower the position tracking error decays. The need to avoid control saturation places an upper bound on the gain k_o, and hence, on the speed of the tracking response for given settings for k_p and k_v (specified for the outer-loop).
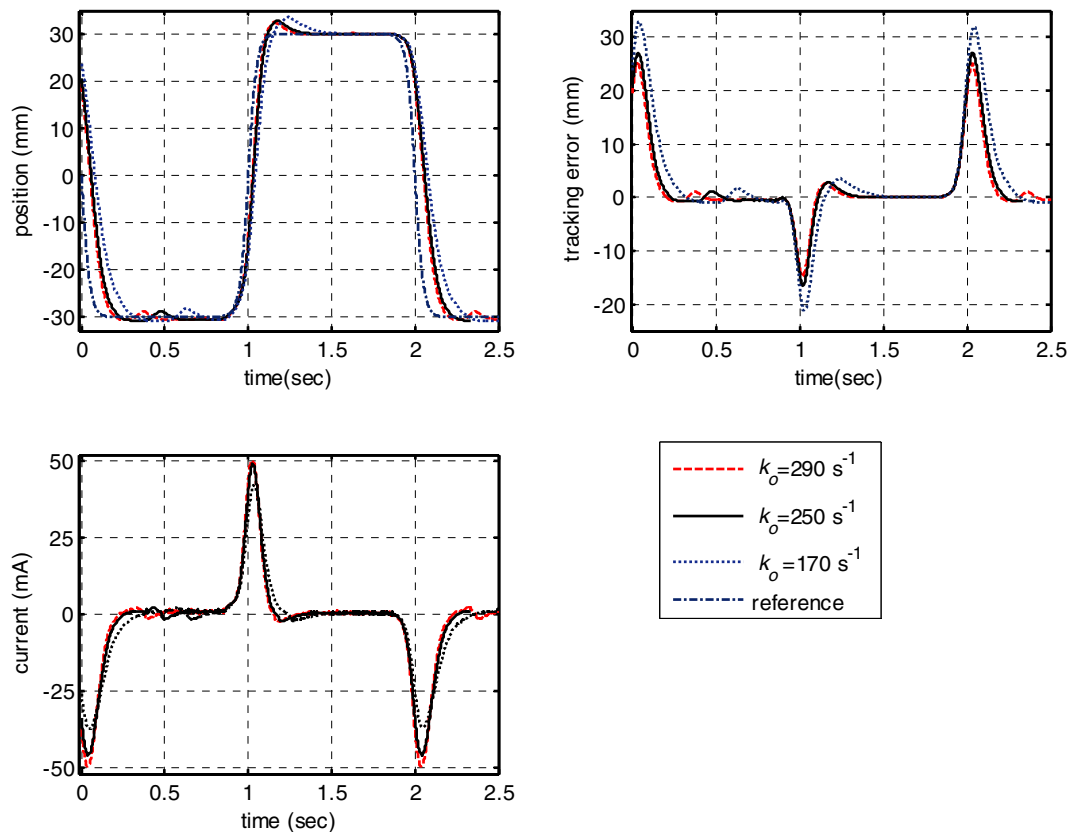
Figure 4.35: Effect of independently tuning the inner force loop with gain k_o (experiments)

To demonstrate the effect of the gain k_o more elaborately, we can start with gain settings corresponding to slower pole location with the Near IO linearizing position controller that do not saturate the control current. For example, for the experimental data in Fig 4.36, the design started by placing all three poles of the closed loop system for the Near IO linearizing controller at $s=-202$. With the cascade control, this corresponds to

settings of k_p=4.45E5 kg/s^2 and k_v=4490 kg/s, such that the natural frequency of the second order position error dynamics is 202 (rad/s) or 32Hz with critical damping. Then the gain k_o, which is the break frequency of the first-order force loop dynamics, can be independently tuned over a wide range without saturating the control current.
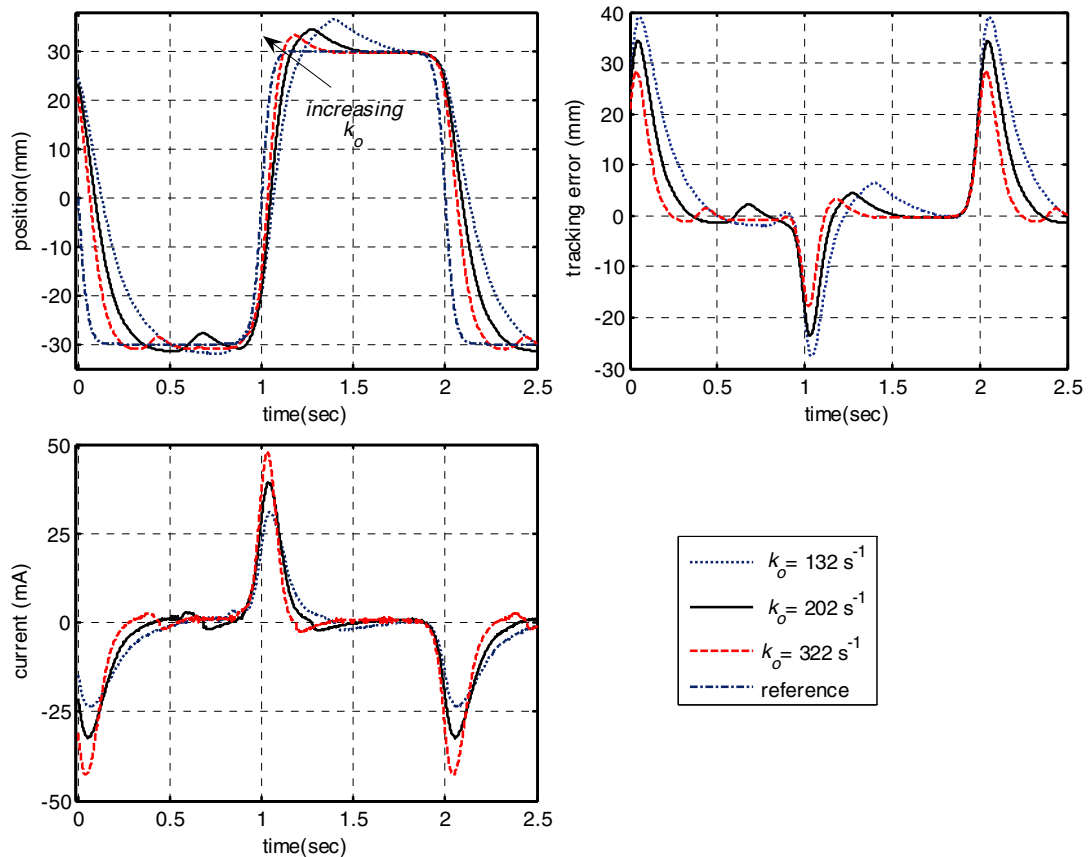
Figure 4.36: Further tuning with gain k_o starting from a slower outer-loop position error dynamics (experiments)

We note from Fig 4.36 that, by increasing only k_o, it was possible to recover the position tracking response previously obtained in Fig 4.35 using higher values for k_p and k_v. This is done without control saturation in this case.

Similar tuning can be performed using the other two gains, k_p and k_v, in the cascade controller. Fig 4.37 shows the effect of tuning k_p while keeping k_o and k_v at values corresponding to three poles at s=-202 as above (i.e, k_o=202 s^{-1} and k_v=4490 kg/s). Since increasing k_p implies increasing the natural frequency of the outer-loop position error dynamics, the position response rises and settles faster with higher values of k_p.
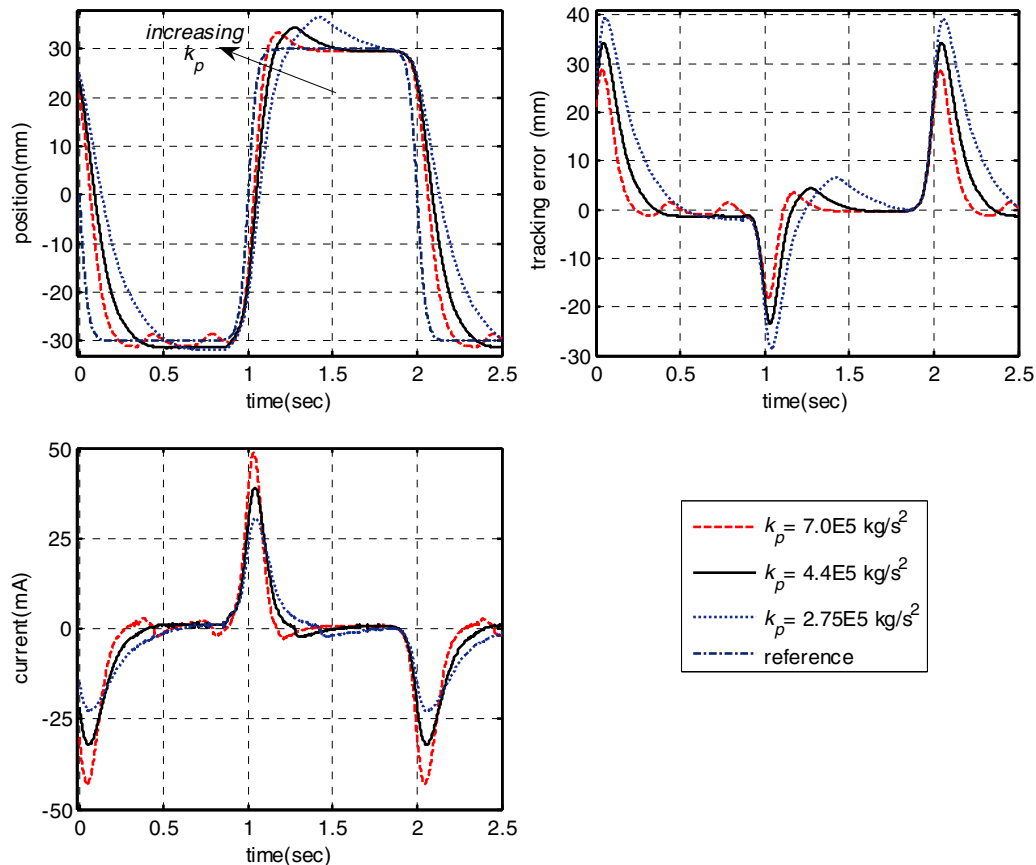
Figure 4.37: Tuning the response with gain k_p (experiments)

Fig 4.38 shows the effect of tuning of gain k_v while keeping the other gains the same, i.e., k_p=4.45E5 kg/s^2 and k_o=202 s^{-1}. It can be seen that for this particular choice of gains, reducing k_v significantly reduces the damping of the response. Some closed-loop response improvement is obtained by increasing k_v (and hence the damping) in reducing oscillations and overshoot.
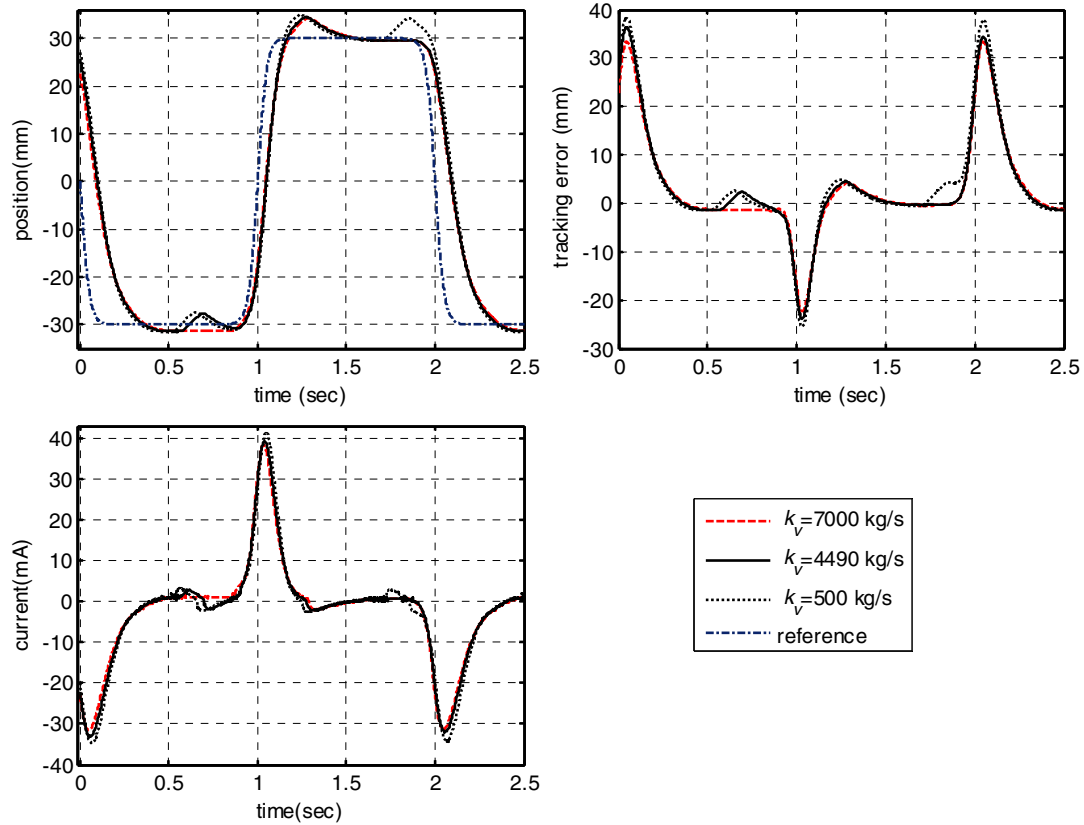
Figure 4.38: Tuning the response with gain k_v (experiments)

Before closing this subsection, a remark is due regarding the tuning of the gains k_1, k_2, k_3 for Near IO linearizing position tracking controller studied in Subsection 4.2.2.1.1. Consider the servovalve to operate at the design supply pressure of 21MPa with natural frequency 240Hz (instead of the 14MPa supply pressure set in the experiments) and also the accumulators to be close-coupled with the servovalve. We also assume the availability of high bandwidth feedback signal filters. Recall that, under these conditions, it was shown in Subsection 4.2.2.1.1 and Fig 4.31, that the Near IO linearizing position controller designed by choosing all three poles at s=-450 performs much better than a well-tuned PID controller for the same control current peak magnitude. We remark here that by exploiting the equivalence of the Near IO linearizing position controller with the cascade controller, it is possible to further tune the Near IO linearizing position controller.

The recommended tuning procedure is summarized as follows:

1. Select three stable pole locations for the Near IO linearizing controller. Placing all three at the same location, $s=-a$, $a>0$, gives simple solutions and convenient interpretations.

2. Invert the equivalence relations in Eq. 4.42 to solve for k_p, k_v and k_o. A numerical solution is recommended for inverting this equation for arbitrary pole locations. If all poles are chosen at $s=-a$, $a>0$, then Eq. 4.43 gives the values $k_p=a^2m_p$, $k_v=2am_p$ and $k_o=a$ (only in terms of the mass m_p, and the pole location a). Furthermore, the second-order position tracking loop has a natural frequency of a (rad/s) and critical damping, and the first-order force loop also has a break frequency of a (rad/s).

3. Tune the gain k_o to make the force loop as fast or slow as desired. Similar interactive tuning can be carried out for the position loop by using k_p and k_v.

4. For the Near IO linearizing position controller, compute the gains k_1, k_2, k_3 from Eq. 4.42 using the tuning results of step 3.

4.2.2.2.2 Robust Cascade Control

As shown in the schematic of Fig 4.6, robust cascade control is achieved by utilizing the continuous sliding mode force controller of Eq. 4.57 as an inner-loop to deal with the "matched" parametric uncertainty. The outer-loop position controller computes the desired force, $F_{p,d}$ from Eq. 4.58. Recall that with the cascade implementation of these two controllers, the unmatched uncertainty in the friction and load force drives the outer-loop position error dynamics as a disturbance (see Eq. 4.59). The robustness of the sliding mode inner-loop force tracking controller has already been investigated in Subsection 4.2.1.2. In this subsection, the robustness of the cascade controller to unmatched uncertainty is considered.

It is to be recalled from the discussion on backstepping in Subsection 4.1.5.2 that when the unmatched uncertainty due to friction and load force estimation can be bounded with a linear growth bound as in Eq 4.68, and the matched uncertainty satisfies a bound as in Eq 4.53, bounded tracking can be guaranteed. Unlike the matched uncertainty bound, which can easily be computed to aid in the selection of the switching gain, K, and

the boundary layer thickness, Φ, the unmatched uncertainty bound of Eq 4.68 is not straightforward to specify or guarantee. This is because it doesn't explicitly involve controller parameters. We may, however, infer from the linear growth bound of Eq 4.68 that one way to approach satisfying the bound is by driving the force error e_F to be as small as possible in spite of the matched uncertainty in the force loop. This entails using very large gain K values with the sliding mode controller.

In this subsection, we briefly present an experimental result that demonstrates that the robust cascade controller can recover the performance of the nominal cascade controller extensively studied in Subsection 4.2.2.2.1. Note that the only major difference between the two controllers is that the robust version uses the continuous sliding mode controller instead of the Near IO linearizing pressure force controller in inner-loop of the cascade. While the nominal cascade controller doesn't consider parametric and modeling uncertainty, the robust cascade controller does (within bounds).

Figure 4.39 shows a comparison of the robust and nominal cascade controllers. During experimentation, it was observed that, in general, rather large magnitudes of K and/or Φ were necessary to accommodate the unmodeled dynamics of the transmission lines, the servovalve and feedback signal filters in addition to the matched and unmatched uncertainty. The gain, K, and the boundary layer thickness, Φ, were heuristically determined to obtain a chatter free response with the robust cascade controller without saturating the control current. For the data in Fig 4.39, the following values were set for the nominal controller (and the outer-loop of the robust controller): $k_p = 3.0E5$ kg/s^2, k_v=2000 kg/s, and k_o=502 s^{-1}.; and for the robust controller K=3.0E8 kgcm/s^3 and Φ=5000 N. The outer loop gains correspond to a natural frequency of 26 Hz and a damping ratio of 0.6. It can be seen that the performance of robust cascade controller is comparable to the nominal one for just these settings, while still using lower control current peaks. Note that even higher values of K, with correspondingly higher settings for Φ, could be used to recover the nominal performance with the robust controller.
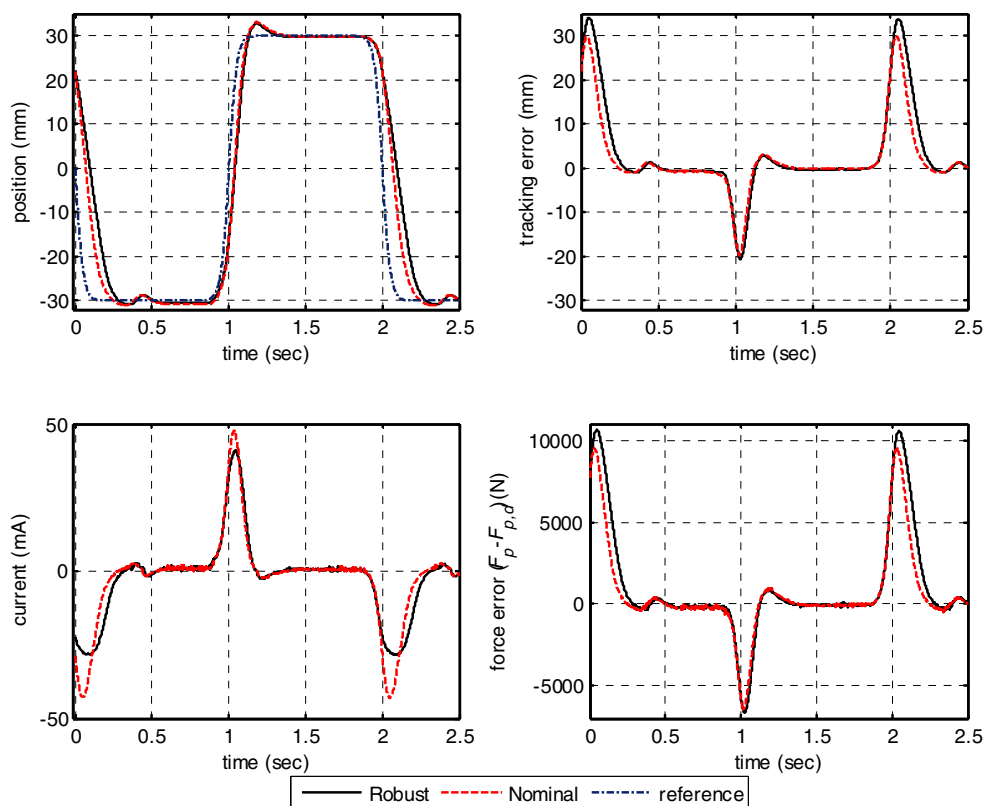
Figure 4.39:Typical comparison of the robust and nominal versions of the cascade controller (experiment)

We now return to the simulation of the system where we consider the desirable configuration of the system in which the accumulators are close-coupled with the servovalve and the servovalve corner frequency is 240Hz with the damping ratio of 1.1, corresponding to the specifications of the present servovalve with the supply pressure at 21 MPa [86]. Recall from the discussion at the end of Subsection 4.2.2.1.1 that under these considerations, the Near IO linearizing piston position tracking controller performed much better than a well-tuned PID controller. It would be interesting to see how the robust version of this Near IO linearizing controller (through its equivalence to the nominal cascade controller) performs.

As examples, we present two typical perturbations in the model of the electrohydraulic system to show the performance of the robust cascade controller in the presence of uncertainty. For the simulations, the outer-loop position controller is designed to have a natural frequency of 50 Hz and a damping ratio of 1.0, corresponding

to k_p=1.1E6 kg/s^2 and k_v= 7000 kg/s. Starting values of the sliding control gain K can be estimated from Eq 4.53 as described in Subsection 4.2.1.2.1 for the force inner-loop, and subsequently tuned, together with the value of Φ, by looking at the tracking error dynamics and the control activity. For the cascade controller considered in this section, the choices are K=3E8 kgcm/s^3 and Φ=3000N.

As a first case, the value of the valve coefficient C_v of the actuator is underestimated by the controller by 10% (through K_v or G_v). That is, the value of C_v in the model of the actuator is increased while a nominal value of C_v is used in the controller. Recall from the discussion in Subsection 4.2.1.2.2 that the sliding mode controller is most sensitive to this parameter. Also, consider at the same time that the friction in the actuator is 100% higher than the estimate used by the controller. Fig 4.40 shows the simulated tracking performance of the robust cascade controller under these perturbations. For comparison, the case of perfect knowledge (no perturbation) by the robust controller is also shown. It can be seen that the robust controller gives bounded tracking errors, unlike the non-robust cascade (or Near IO linearizing) controllers which drive the tracking error to zero. Recall that with the robust cascade controller, bounded-ness of the tracking error is all that is guaranteed. The boundary layer thickness Φ helps tune this bound on the tracking error. It can be seen also that the robust controller uses slightly lower current peak to give a slightly smaller peak position tracking error. This is generally not the case with the other position controllers discussed so far. As will be shown in the next case, neither is this the universal trend with the robust cascade controller.
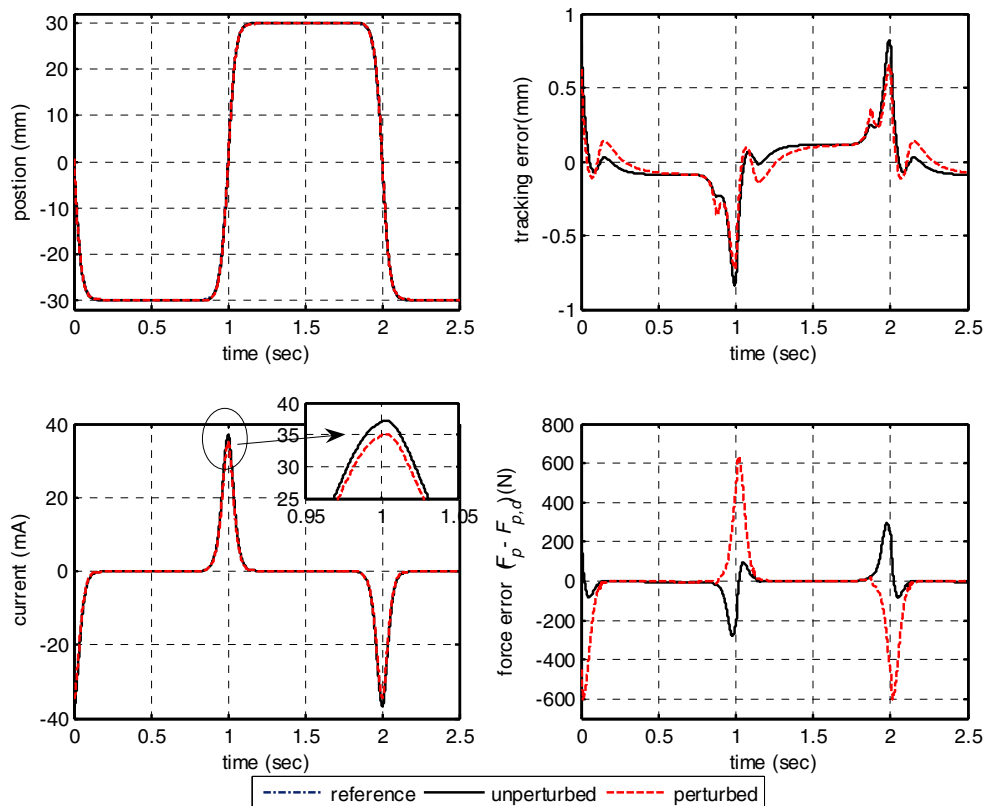
Figure 4.40: Tracking performance of the robust cascade controller with valve coefficient and friction perturbations (simulations)

As a second and special case that involves the transmission lines, consider the supply line pressure at the pump to drop to a level 20% lower than the nominal value of 21MPa set in the cascade controller. Consider also that the servovalve response is slower with corner frequency of 200 Hz. Fig 4.41 shows the simulation results for this case. It can be seen that even for this case of the supply pressure uncertainty (which has not been considered before), the robust cascade controller does a decent job at tracking this particular reference trajectory in the presence of the perturbations. Note also that the current peak and the tracking error are both higher in the perturbed case.
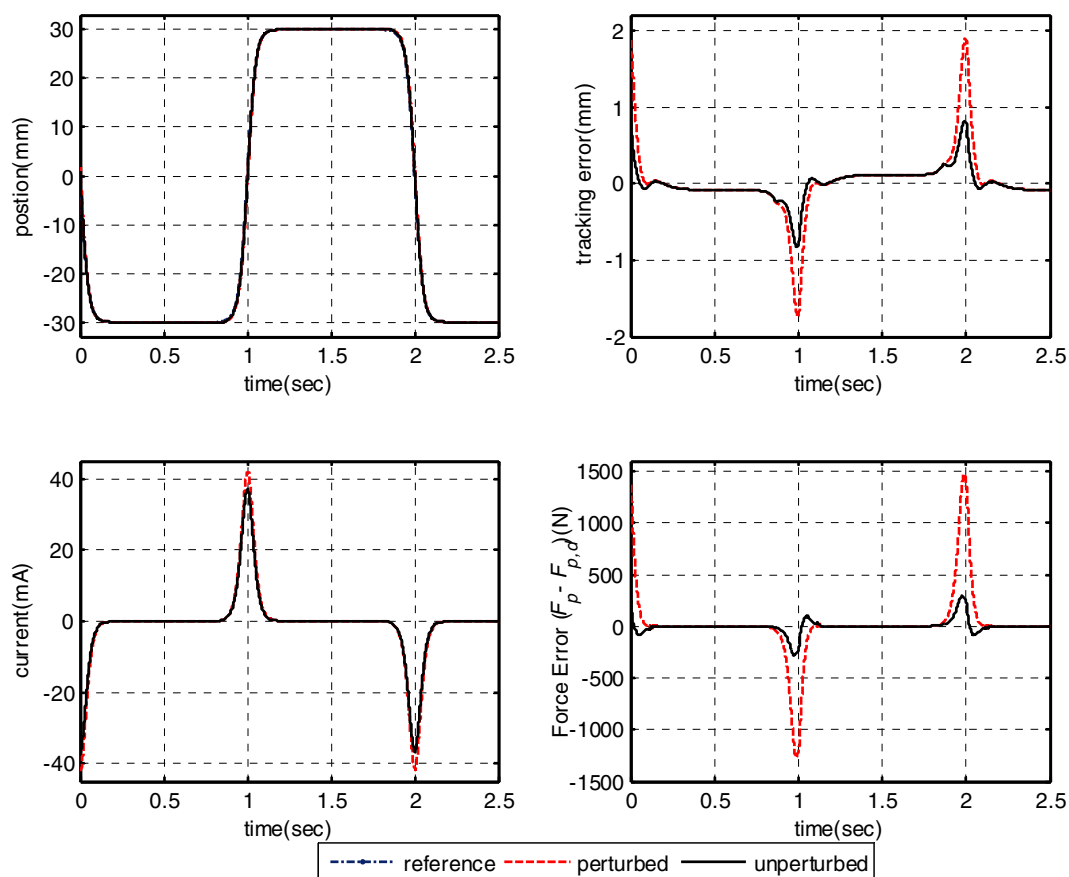
Figure 4.41: Tracking performance of the robust cascade controller with supply pressure perturbation(simulations)

In summary, the robust cascade controller discussed briefly in this subsection implements the sliding mode inner-loop force controller with an outer-loop position controller generating the desired pressure force for the inner-loop. As shown from a backstepping point of view in Subsection 4.1.5.2, when the parametric and modeling uncertainty satisfy certain conditions, the robust cascade controller keeps the tracking error bounded (and not necessarily zero). An experimental result was shown comparing the robust cascade controller with the nominal cascade controller. And two perturbation cases were simulated to show the tracking performance of the robust cascade controller.

4.3 Chapter Summary

In this chapter, nonlinear piston position and force tracking controllers were developed from a feedback linearization framework. Their performance was then analyzed using experiments and simulations on the electrohydraulic test system whose model was discussed in the previous chapter.

For the derivation of the nonlinear controllers, we started by listing basic assumptions in Subsection 4.1.1. The main ones are neglecting servovalve dynamics and assuming that supply and return line pressure fluctuations are minimal. The latter assumption is justified when line accumulators are close-coupled with the servovalve. Furthermore, to be able to proceed with the Near Input-Output (IO) linearization, it was found necessary to assume that the control current does not change signs faster than the base sampling rate of the digital implementation of the resulting controllers.

In Subsection 4.1.2, different versions of Near IO linearizing force tracking controllers were derived for two different force output definitions: the pressure force defined by Eq. 3.45 and the load force defined by Eq. 4.14. It turns out that the pressure force controller has a very convenient connection to the subsequent study of the position control problem. Therefore, it was studied in further detail. The basic Near IO linearizing piston force tracking controller is given by Eq. 4.13. It was pointed out that this controller cancels the dominant nonlinearities in the pressure force dynamics that arise from turbulent valve orifice flow and nonlinear hydraulic compliance, and results in first-order linear pressure force error dynamics. Furthermore, it was remarked that the Near IO linearizing controllers for tracking load pressure (or differential pressure) and pressure force differ only by a factor of the piston area.

The piston position tracking control problem was investigated using two approaches in Subsection 4.1.3. The first approach is Near IO linearization of the system model using piston position as output. It has been shown that the resulting controller, given by Eq. 4.37, cancels the nonlinear contributions of friction and load force as well as that of turbulent valve-orifice flow and hydraulic compliance. The controller reduces the

closed loop position tracking error dynamics to a third-order linear dynamics which can be tuned by its gains k_1, k_2, and k_3.

The second approach is based on a cascade controller implementation of the Near IO linearizing pressure force tracking controller as inner-loop and a feedback plus feed forward piston position tracking controller as outer-loop that computes the desired pressure force trajectory for the inner-loop. It was noted that by canceling the natural velocity feedback in the pressure force dynamics with the Near IO linearizing pressure force tracking controller, a decoupling of the pressure force dynamics from the dynamics of the piston motion is obtained. The cascade controller presented exploits this and allows one to treat the actuator as a linear force generator which applies the desired force for positioning the piston.

It was shown that the cascade controller is theoretically equivalent to the Near IO linearizing position tracking controller. The gains in the two controllers (k_1, k_2 and k_3 for the Near IO linearizing one and k_p, k_v, and k_o for the cascade controller) are related through Eq. 4.42. Furthermore, it was noted that the cascade form reveals useful interpretations for the gains involved: k_p and k_v are coefficients of the second-order position error dynamics and k_o is the break frequency of the first-order force inner-loop. These interpretations can be used to aid in the selection of the gains for the Near IO linearizing controller, which do not have straightforward interpretations in themselves. In particular, placing all three closed-loop poles at the same location gives the simple expressions, given by Eq. 4.43. Experimental and simulation examples and an outline of the recommended procedure for tuning the Near IO linearizing controller were detailed in Subsection 4.2.2.2.1.

A summary of the common characteristics and limitations of the Near IO linearizing pressure force and position tracking controllers was given in Subsection 4.1.4.1. The summary includes interpretations for the nonlinearity cancellation as well as the choice of the possible structures of the linear part for the Near IO linearizing controllers. It is noted that exponentially convergent tracking is achieved only with the original choices given by Eq. 4.11 and Eq. 4.32 despite the requirement of higher-order differentiability on the respective reference trajectories with these choices.

The performance of the basic Near IO linearizing controllers was investigated with experimental results in Subsection 4.2.1.1.1 for the force controller and Subsection 4.2.1.1.1 for the position controller. In the force control case, the Near IO linearizing controller performed better than a PID or a LSFI controller in experiments. In the position control case, the improvement obtained in experiments with the Near IO linearizing controller over the PID or LSFI controller for this particular test setup was not significant. However, using model simulations, it was argued that, given practicable considerations of accumulator-close coupling and high supply pressure operation for the servovalve, significant improvements can be obtained with the Near IO linearizing controller (or the robust versions revised below).

Furthermore, with experiments and simulations, the sensitivity of the Near IO linearizing controllers to the estimated controller parameters, β_e, C_v and C_L, was investigated. For the test system considered, the performance of the controllers is most sensitive to the valve coefficient C_v, and least sensitive to the leakage coefficient, C_L. The controllers tolerate a measurable shift in these parameters (of the order of 15% for the most sensitive one, C_v) when each is changed individually. In Subsection 4.2.2.1.2, simulations were used to show that the position controller, which uses estimates of friction, has good robustness to friction uncertainty.

Robust control versions of the nonlinear controllers were also considered. For the force tracking case, it turned out that the Near IO linearizing pressure force tracking controller can be slightly modified considering continuous sliding mode controllers to formally address robustness to matched uncertainty. This is given by Eq. 4.56 (or Eq. 4.57). Choices of the control gain K and the boundary layer thickness Φ involve trade-offs between the size of tolerable uncertainty as expressed by Eq. 4.53 and the need to avoid chattering due to unmodeled parasitic dynamics. In Subsection 4.2.1.2, these trade-offs and verifications of robustness were demonstrated with experimental and simulation results.

For the position tracking case, robustness to unmatched uncertainty of the force-loop was investigated from a backstepping point of view in Subsection 4.1.5.2. When the uncertainties satisfy certain conditions, bounded tracking is obtained by the cascade

controller employing the sliding mode pressure force tracking controller as an inner-loop to the outer-loop position controller computing the desired force profile for the inner-loop by Eq. 4.58. Experimental and simulation results were given for this robust cascade controller in Subsection 4.2.2.2.2.

In conclusion, each of the nonlinear controllers presented in this chapter has merit provided the following conditions are met.

- The model parameters are carefully identified or estimated from simple experiments as outlined in the Appendix B.

- The accumulators are close-coupled with the servovalve to minimize the dynamic effect of transmission lines.

- The servovalve spool dynamics is fast enough to be neglected justifiably in the controller design. In this work, servovalve natural frequencies about 4 times higher than the desired system bandwidth were found satisfactory.

- High bandwidth, low-pass feed back signal filtering is available.

Under these conditions, each of which is feasible, the Near IO linearizing controller (and the cascade controller) can give improved performance than what is possible with simple linear controllers (PID o LSFI). The robust nonlinear control versions can be used to accommodate the lack of high quality model parameter estimates, within bounds.

Chapter 5

Application to Multi-Actuator Electrohydraulic Systems in Road Simulation

It is to be recalled from the literature review in Section 2.1 that the common use of multi-actuator systems for road simulation employs offline iterative generation of reference signals using MIMO (Multiple Input Multiple Output) model inversion approaches to remove nonlinearities. In general, decentralized linear PID (or PID+Δp) position controllers are maintained as the 'inner-loop' real-time actuator controllers. Here, by decentralized control we mean the control of each actuator independently of the others, in an essentially SISO (Single Input Single Output) configuration. In this chapter, the goal is to study the effect of removing the nonlinearities in each actuator's dynamics using decentralized nonlinear controllers.

To extend the application of the feedback linearizing controllers described in the previous chapter to the case of a multi-actuator electrohydraulic system, a model of a four-post electrohydraulic road simulator (four-poster) is developed. Basic assumptions are itemized in Section 5.1. In addition to the model of the electrohydraulic actuator, which has been detailed in Chapter 3, a nonlinear model of a transit bus is considered as the dynamically coupled structural load on the actuators. Section 5.2 details the full-bus model and the interconnected model of the road simulator adopted for the simulation study in this chapter.

Note that the independent actuators and their respective decentralized controllers are coupled through the dynamics of the load (the test vehicle). In Section 5.3, we define explicit interaction measures to help in quantifying the interaction between different decentralized control loops. In Section 5.4, we shall compare interactions between the respective decentralized loops of Near IO linearizing controllers and PID+Δp controllers.

In Section 5.5, we present an evaluation of the performance of the road simulation system using a typical road profile. Certain performance metrics are defined for this purpose. Finally, we close this chapter by summarizing the main points in Section 5.6.

5.1 Basic Assumptions

For the model based study in this chapter, we make the following assumptions:

- The accumulators upstream and downstream of the servovalve are close-coupled on the servovalve manifold. It is to be recalled from the previous chapter that this allows us to use constant values for the supply and return pressures at the servovalve in the nonlinear control laws.

- As in the previous chapter, the servovalve dynamics is considered to be fast enough to be neglected for the purpose of control design. However, a second-order linear dynamics model with a natural frequency of $\omega_{n,v}= 66$ Hz and $\zeta_v=0.7$ is considered to approximate the valve dynamics in the interconnected model of the road simulator. The servovalve in this application is a three-stage servovalve employing a two-stage servovalve as a pilot and its own output spool position feedback. The maximum control current is estimated to be ±9 mA corresponding to an output spool travel of ± 0.170 cm given in product specifications [87].

- To simplify the analysis, we assume perfect knowledge of the necessary parameters for the nonlinear controller. In other words, the nominal parameters of the electrohydraulic actuators are used in the controller expressions. The robust control versions described in the Chapter 3 will not be considered. Aside from the determination of parametric and measurement uncertainty bounds, we note that there should be no major difficulty in switching to the robust versions of the nonlinear controllers for this application as well.

- For comparisons with PID+Δp controllers, we consider the Near IO linearizing position tracking controller in this chapter. It is to be recalled that, this controller is equivalent to the cascade implementation of the Near IO linearizing pressure force tracking controller as an inner-loop and the feed forward plus feedback position controller as an outer-loop.

- We consider a nonlinear full-bus model of a transit bus to represent the test vehicle on the road simulator. Subsection 5.2.1 lists further assumptions pertinent to this model.

5.2 Description of the Model

5.2.1 Full-Bus Model

We consider a full-bus model of a transit bus with dependent suspensions as shown in Fig 5.1. The air suspensions and shock absorbers are modeled as nonlinear elements. The parameters of the model are extracted from various sources [88-92] and are listed in Appendix E. Yaw motions of the bus are considered irrelevant on the four-poster. Pitch and roll motions of the body (sprung mass) and of the unsprung masses are assumed to be small enough to allow use of small angle approximations for the pitch and roll motions. The resulting model has seven degrees of freedom comprising of the following: bounce of the rear and front unsprung masses (z_{ur}, z_{uf}), roll motion of the rear and front unsprung masses (ϕ_{ur}, ϕ_{uf}), and the pitch (θ), roll (ϕ) and bounce (z_s) motions of the sprung mass.
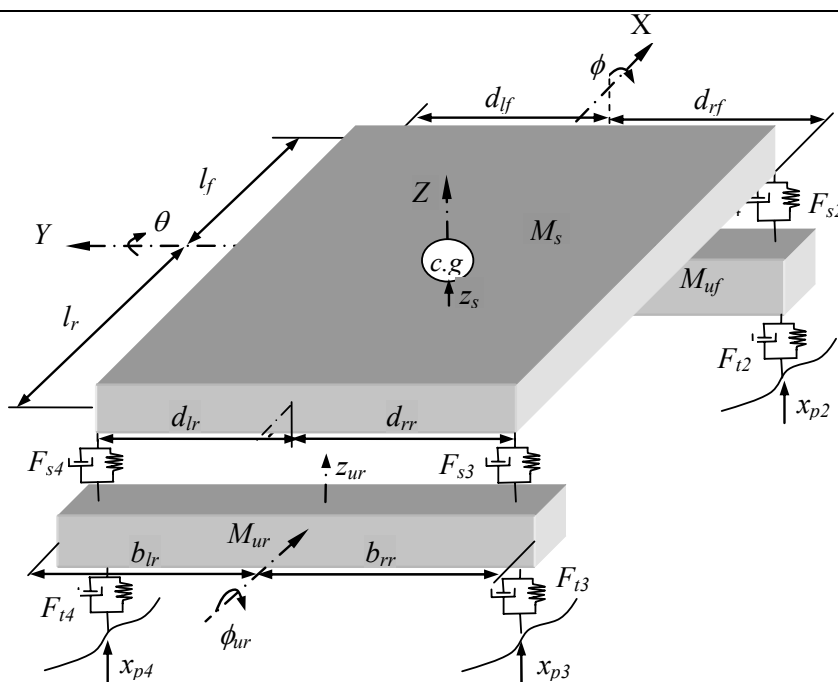
Figure 5.1: A full-bus model with dependent suspensions

The equations of motion for the sprung mass (M_s) and front and rear unsprung masses (M_{uf}, M_{ur}) are:

$$M_{uf}\ddot{z}_{uf} = \sum_{i=1,2} F_{ti} + F_{si} - M_{uf}g$$

$$I_{uf}\ddot{\phi}_{uf} = b_{lf}(F_{t1} + F_{s1}) - b_{rf}(F_{t2} + F_{s2}) - T_{arf}$$

$$M_{ur}\ddot{z}_{ur} = \sum_{i=3,4} F_{ti} + F_{si} - M_{ur}g$$

$$I_{ur}\ddot{\phi}_{ur} = b_{lr}(F_{t4} + F_{s4}) - b_{rr}(F_{t3} + F_{s3}) - T_{arr} \tag{5.1}$$

$$M_s\ddot{z}_s = -\sum_{i=1}^{4} F_{si} - M_s g$$

$$I_p\ddot{\theta} = \sum_{i=1,2} l_f F_{si} - \sum_{i=3,4} l_r F_{si} - T_{ap}$$

$$I_r\ddot{\phi} = -d_{lf}F_{s1} - d_{lr}F_{s4} + d_{rf}F_{s2} + d_{rr}F_{s3} + T_{arf} + T_{arr}$$

Note that in the above equations, we have assumed compressive tire forces to be positive for reasons that will become evident in the next subsection. These tire forces, F_{ti}, are approximated by:

$$F_{ti} = K_{ti}(x_{pi} - z_{ui}) + C_{ti}(\dot{x}_{pi} - \dot{z}_{ui}) \qquad i = 1, 2, 3, 4 \tag{5.2}$$

And the nonlinear suspension and damping forces, F_{si}, are given by:

$$F_{si} = f_{si}(z_{si} - z_{ui}) + f_{di}(\dot{z}_{si} - \dot{z}_{ui}) \qquad i = 1, 2, 34 \tag{5.3}$$

where, f_{si} and f_{di} represent interpolations in tables of air suspension stiffness and shock absorber damping data, respectively. The displacements of the suspension attachment points, z_{si}, i=1, 2, 3, 4, are given by:

$$\begin{aligned}
z_{s1} &= z_s - l_f\theta + d_{lf}\phi \\
z_{s2} &= z_s - l_f\theta - d_{rf}\phi \\
z_{s3} &= z_s + l_r\theta - d_{rr}\phi \\
z_{s4} &= z_s + l_r\theta + d_{lr}\phi
\end{aligned} \tag{5.4}$$

The displacements of the wheel centers, z_{ui}, i=1, 2, 3, 4, are given by:

$$z_{u1} = z_{uf} + b_{lf}\phi_{uf}$$
$$z_{u2} = z_{uf} - b_{rf}\phi_{uf}$$
$$z_{u3} = z_{ur} - b_{rr}\phi_{ur}$$
$$z_{u4} = z_{ur} + b_{lr}\phi_{ur}$$

(5.5)

Not shown in Fig 5.1 are the auxiliary roll stiffness and damping torques (T_{arr}, T_{arf}) and the body pitch stiffness and damping torque (T_p). These are included to account for any additional stiffness and damping provided by elements of the suspension geometry such as torsion bars and radius rods. The defining equations are:

$$T_{arr} = K_{arr}(\phi_{ur} - \phi) + C_{arr}(\dot{\phi}_{ur} - \dot{\phi})$$
$$T_{arf} = K_{arf}(\phi_{uf} - \phi) + C_{arf}(\dot{\phi}_{uf} - \dot{\phi})$$
$$T_{ap} = K_{ap}\theta + C_{ap}\dot{\theta}$$

(5.6)

where, K_{arr}, K_{arf}, K_{ap} are the respective auxiliary torsional stiffnesses, and C_{arr}, C_{arf} and C_{ap} are the auxiliary torsional damping coefficients.

5.2.2 Road Simulator Model Interconnection

Note that for the full-bus model of the previous section, the piston positions, x_{pi}, of the four actuators represent road profile inputs to the test vehicle as a system. On the other hand, the tire forces, F_{ti}, i=1, 2, 3, 4, can be considered as the outputs of the full-bus model and act as the load forces on each of the electrohydraulic actuator load-plates. These compressive-positive tire forces F_{ti}, i=1, 2, 3, 4 acting on the actuator load-plates have an equivalent role as the tensile-positive specimen reaction forces, F_L, in the fatigue testing actuator depicted in Fig 3.12 (Chapter 3). Therefore, we state here that, with this observation and the basic assumptions listed in Section 5.1, the electrohydraulic actuator model developed in Chapter 3 can be used for each of the actuators of the road simulator. Similarly, the nonlinear controllers developed in the Chapter 4 apply equally well to each of the actuators of the road simulator.

Figure 5.2 shows how the input-output interconnection of the road simulation system is implemented. To simplify the presentation, the figure shows the interconnection of a quarter-bus mechanical model to the model of the electrohydraulic actuator including its corresponding controller. The case of the full-bus model has a similar structure.
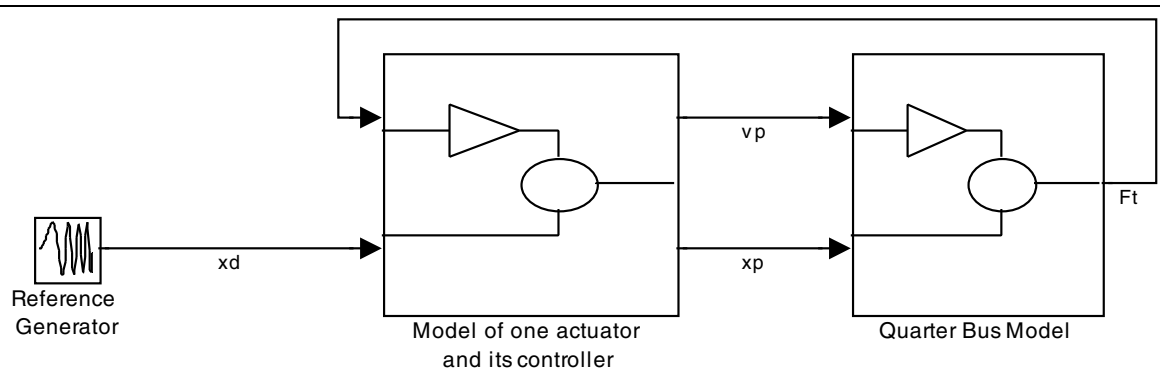
Figure 5.2: Road simulator model interconnection

5.3 Cross-Coupling and Interaction Measures

In the practical 'black-box' approaches reviewed in Section 2.1, the MIMO FRF models' off-diagonal terms represent linear cross-coupling between the respective excitation and response pairs. However, it is desirable to have a more concise measure of actuator interaction arising from the dynamic (and nonlinear) cross-coupling in the fore to aft and side to side motions of the test vehicle. Such a measure could be used to directly evaluate and compare potential decentralized controllers without completing a full (iterative) response replication procedure.

Three main interaction measures are in use in multivariable process control applications. These are the Relative Gain Array (*RGA*), the direct Nyquist array and the μ- or structured singular value interaction measure [58]. The last two can be computed only in the frequency domain. However, frequency domain analysis is not applicable to non-linear systems in a straightforward manner. In this chapter, we seek time domain extensions of the *RGA* for use with the nonlinear model of the road simulation system.

The *RGA* was initially defined for steady-state processes by Bristol [55] and was later extended by Witcher and McAvoy [54] to include dynamic interaction measurement. Ramachandran and Dransfield [56] used the *RGA* to look into the origins and behavior of interaction between electrohydraulic actuators under linear decentralized force tracking controllers operating on a flexible cantilever beam load. In this chapter, we use the RGA to study interaction between the actuators in a road simulator under decentralized linear and nonlinear position tracking controllers.

Consider a linear 2x2 system with transfer matrix G, input vector $\boldsymbol{u} = \begin{bmatrix} u_1 & u_2 \end{bmatrix}^T$ and output vector $\boldsymbol{y} = \begin{bmatrix} y_1 & y_2 \end{bmatrix}^T$ as shown in Fig 5.3.
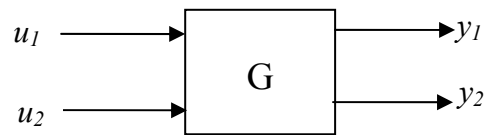
Figure 5.3: A two-input two-output system

The (i,j) element of the *RGA* is defined as:

$$\lambda_{i,j}(s) = \frac{\left(\dfrac{\partial Y_i(s)}{\partial U_j(s)} \right)\bigg|_{U_k}}{\left(\dfrac{\partial Y_i(s)}{\partial U_j(s)} \right)\bigg|_{Y_p}} \qquad k \neq j, p \neq i \tag{5.7}$$

It compares the effect of input u_j on output y_i when all other inputs are zero (or open-loop) against the effect when all other outputs are held constant (by possibly perfect closed-loop control) at any particular frequency ω (s=jω). Note that the notation with the signals U_k and Y_p as subscripts indicates which variables to hold constant when evaluating the derivatives. Given the components of the transfer matrix G, one can show that:

$$\lambda_{1,1}(s) = \frac{1}{1 - \dfrac{G_{12}(s)G_{21}(s)}{G_{11}(s)G_{22}(s)}} \tag{5.8}$$

The closer an element $\lambda_{i,j}$ of the *RGA* is to 1, the stronger is the coupling between that particular input u_j and output y_i. Note that the *RGA* is a matrix of the same size as *G* and that it is invariant under scaling. Therefore, the closer the *RGA* is to the identity matrix, the stronger the diagonal dominance of the system *G*. This implies that in such a case, a decentralized control loop employing a diagonal input-output pairing of u_i with y_i suffers minimal interaction effects from other loops.

Bristol [55] showed that the elements in any row or column of *RGA* sum to one. Due to this property, for an *n* x *n* system, only (n-1) x (n-1) elements need to be computed. Therefore, for a 2x2 system, use of Eq. 5.8 is sufficient. Furthermore, it can be shown that:

$$RGA(s) = G(s).*[G(s)^{-1}]^T \tag{5.9}$$

where the dot-star(.*) product denotes element by element multiplication [93, 94].

As noted above, the closeness of the *RGA* to the identity matrix can be used to measure the diagonal dominance of a system *G* at relevant frequencies. The *RGA number*, defined as the sum norm of the deviation of *RGA* matrix from the identity matrix gives a more compact measure of interaction [94]. It is given by:

$$RGA\ number(\omega) = \|RGA(j\omega) - I\|_{sum} \tag{5.10}$$

where, $s=j\omega$ is substituted to make the distinction that the *RGA number* is a norm and hence a real scalar at each frequency ω. The closer the *RGA number* is to zero at a particular frequency, the more diagonally dominant the system *G* is, and the less a decentralized control employing SISO loops between input u_i and output y_i is affected by interaction with other loops.

For nonlinear systems, such as the system in the present study, time domain extensions of the *RGA* are desirable. To do this, one by one, each input is step changed while the other input is held steady [54] . The integrals of the deviations of the respective responses from the steady state or equilibrium values[11]are computed as:

---

[11] Equally, the responses themselves or the integrals of the squared deviations of the responses can be used.

$$\delta y_i = \int_0^t (y_i - y_{iss})d\tau \qquad i = 1,2,..n \qquad (5.11)$$

Then, a matrix with similar structure as G is assembled. For the 2x2 case, we have:

$$\hat{g}(t) = \begin{bmatrix} \left(\dfrac{\delta y_1}{\delta u_1}\right)\Big|_{u_2} & \left(\dfrac{\delta y_1}{\delta u_2}\right)\Big|_{u_1} \\ \left(\dfrac{\delta y_2}{\delta u_1}\right)\Big|_{u_2} & \left(\dfrac{\delta y_2}{\delta u_2}\right)\Big|_{u_1} \end{bmatrix} \qquad (5.12)$$

where, the $\delta u_i, i = 1,2$, are the step changes in the respective inputs. In the case of smooth steps (as shall be used in this work), similar integrals as Eq. 5.11 can be computed. By analogy with Eq. 5.9 , for n x n system, we compute the time-dependent RGA by:

$$RGA(t) = \hat{g}(t). *[\hat{g}(t)^{-1}]^T \qquad (5.13)$$

Similarly, a time-dependent RGA *number* corresponding to Eq. 5.10 can be computed. It should be noted that, while the RGA elements show actual cross-coupling between respective input-output pairs, the RGA *number* gives a compact measure of the overall interaction between all input-output pairs.

When decentralized control is used in diagonal SISO loops, the RGA can be used to assess the potential or the effectiveness of such control. If the (MIMO or decentralized SISO) controller is included in the system of interest for the RGA computation, then the RGA can be considered as an indicator of control effectiveness in reducing interaction. On the other hand, if the controller is excluded from the system for the RGA computation, the results indicate the degree of interaction that a controller(s) is expected to deal with, and in particular the potential control difficulty facing decentralized SISO control loops. These interpretations will be exploited in the discussion that follows on the decentralized control of the multiple actuators of the road simulator

5.4 Interactions in Decentralized Control of Multiple Actuators

In a previous paper [95], the author used ADAMS simulations of a four-poster to investigate the nature of interaction between the actuators in the open-loop condition as well as under decentralized linear PID control of load plate (piston) positions. It was shown there that the *RGA number* (and interaction) was reduced by a factor of about 200 when the decentralized PID position control loops were included as opposed to the theoretical[12] open-loop condition on all actuators. It was also remarked there that, for a high setting of effective bulk modulus at 1200 MPa and decentralized PID position control gains chosen somewhat arbitrarily, the remaining interactions between the actuators with piston position outputs were minimal and died away quickly. On the other hand, the interactions facing a second cascaded decentralized control loop acting on tire-spindle vertical accelerations, with the decentralized PID piston position loops as inner-loops, were very significant and persistent.

In this section, the emphasis is placed on comparing the interaction effects between decentralized loops of a linear PID+Δp controller against the decentralized loops of the Near IO linearizing position controller. For this comparison, we take advantage of the two interpretations of the *RGA* given above: one for investigating the effectiveness of decentralized linear and nonlinear position control loops and the other for evaluating the potential of a second cascaded decentralized control loop acting on a remote response parameter like tire-spindle vertical acceleration.

5.4.1 Tuning the Decentralized Controllers

As noted before, simulations of the nonlinear system model described in Section 5.2 are employed for the discussion in this chapter. It was first attempted to tune the decentralized controllers for the four actuators by using a nonlinear quarter-bus model

---

[12] Rectilinear electrohydraulic actuators behave as velocity sources and hence as integrators to position. Open-loop use with position output is mainly of theoretical importance.

with parameters corresponding to the nonlinear full-bus model. The equations describing a quarter-bus (often referred to as quarter-car) model can be derived from Eq 5.1 by ignoring all pitch and roll motions and focusing on one corner of the full-bus. Two different quarter-bus models were employed to tune the controllers for the front and rear actuators, since the front quarter-bus model parameters are generally different from those of the rear ones.

However, the best actuator control gains determined using the quarter-bus model led to instability when used on the coupled four-actuator case with the full-bus model. The problem was particularly severe when tuning the P-gains of the PID+Δp controllers. This is to be expected considering the ignored motion cross-coupling in the quarter-bus model that is relevant in the more realistic full-bus model. The gains are, therefore, re-tuned interactively by considering the useable gains on the full-bus four-actuator system as well. The problem of instability (due to coupled load dynamics) with higher gains or faster pole locations is much less acute for the Near IO linearizing controller. This is because the Near IO linearizing controller uses some of the cross-coupling information via feedback of the tire force, which is equivalent to the load force F_L in the controller expressions derived in chapter 4.

Fig 5.4 shows a basic comparison between the tracking performance of the Near IO linearizing position controller and a PID+Δp position controller for one of the rear actuators loaded with a quarter-bus. A large magnitude smooth step reference (from -60 mm to 60 mm) was generated as discussed in Section 4.1.6.1 with T=0.05. Following the procedure in Chapter 4, all three poles of the Near IO linearizing controller were placed at s=-400 for the fastest response that doesn't saturate the control current ($\pm$9mA) for the chosen smooth step reference. As discussed above, the P-gain for the PID+Δp controller is tuned for reducing the peak tracking error for the chosen smooth step-reference without destabilizing the response in the four-actuator full-bus case as well. The Δp-gain introduces artificial leakage, and therefore damping [10, 26], but it could not be arbitrarily increased without increasing steady-state error. For the data in Fig 5.4, P-gain=3 mA/cm, Δp-gain=0.001 mA/MPa.
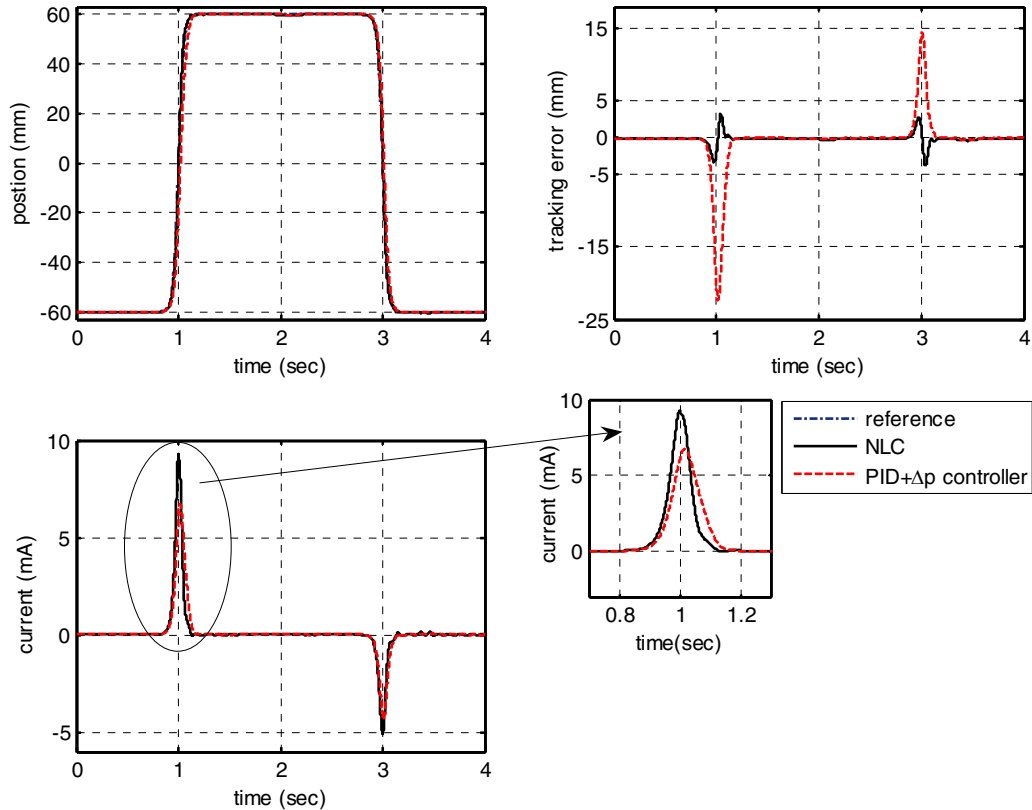
Figure 5.4: Tuning the Near IO linearizing controller (NLC) and a PID+Δp controller using a quarter-bus load model

A similar comparison was obtained for the front actuators. With the lighter masses and softer suspension associated with the front portion of the bus, the closed-loop poles for the Near IO linearizing controller could be pushed further to the left (to $s=-650$) than it was possible with the rear actuators without saturating the control current or inducing instability of the full-bus four-actuator system. The P-gain of the PID+Δp controller could likewise be increased further (to 18mA/cm) without destabilizing the full-bus case. However, the comparative performance of the Near IO linearizing controller with the PID+Δp controller remains similar to that shown in Fig 5.4. It is remarked here that, the decentralized Near IO linearizing controller shows consistently less tracking error peak magnitudes than the decentralized PID+Δp controller, under the assumptions listed in Section 5.1 and the tuning considerations discussed above.

The decentralized controllers tuned using the approach described in this subsection will be used to assess interactions for the four-actuator cases in the following subsections.

5.4.2 Interaction Resulting from Decentralized Piston Position Control

The effect of interaction due to dynamic load cross-coupling on the decentralized control of each of the four-poster's actuator load-plate positions is investigated in this section. Both time responses and the *RGA* interaction measures are used to analyze interactions. To this end, the nonlinear system is first brought to a steady-state and then, one by one, the reference inputs (desired positions) for the position control loops are step changed, while the other actuators are held at zero reference. As remarked in Section 5.3, only the effectiveness of decentralized control is being evaluated with these tests. This is because the controller for each actuator is already included in the system description for the *RGA* analysis (by analogy with plant G in Fig 5.3).

The models for the four actuators in the present study use identical parameters. Unlike the assumption made in the previous paper by the author [95], internal cylinder leakage is not ignored. The effect of internal leakage is seen to be the appearance of a steady state error in the present study (as noted in Chapter 4 as well).

Fig 5.5 shows one set of responses following a step change in the reference input for the rear-left actuator controller from 0 to 80mm (with smoothening parameter T=0.05) while zero reference is given to the controllers of the other actuators. Similar results were obtained when applying the step change at the other actuators.
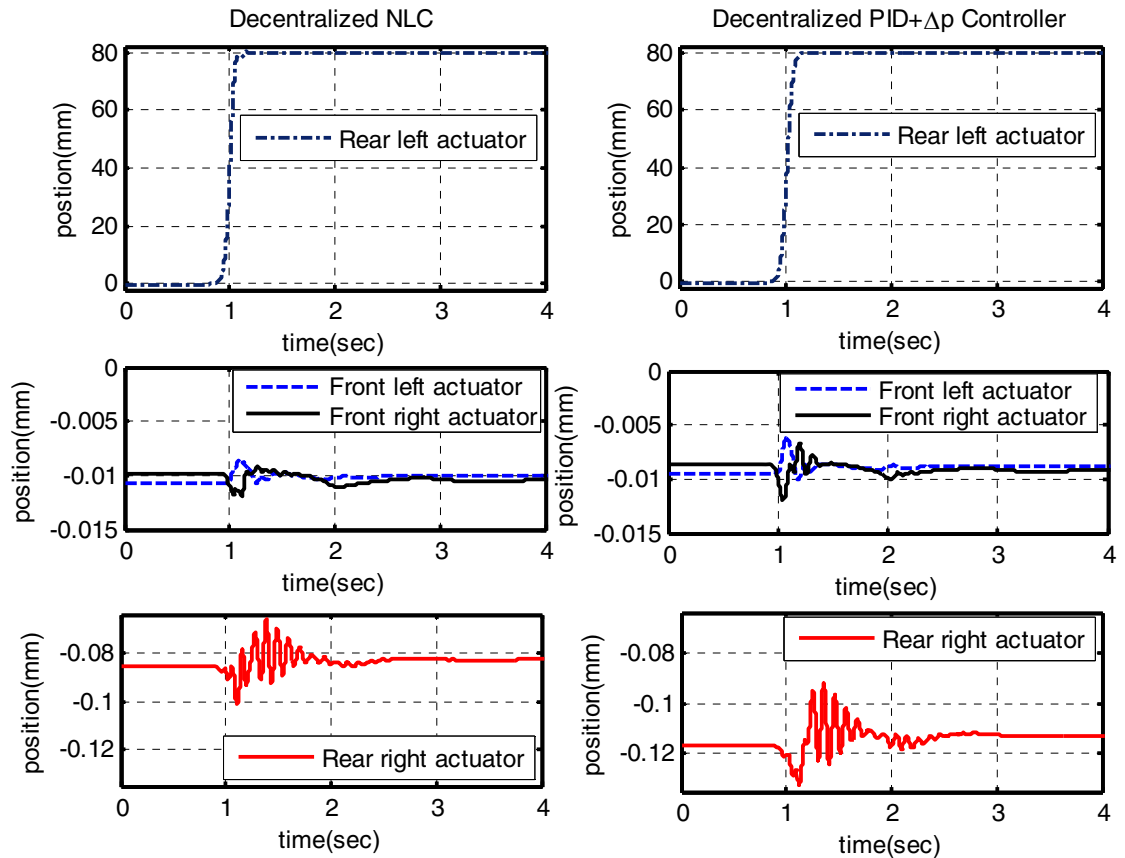
Figure 5.5: Actuator interaction in terms of load-plate positions with decentralized Near IO linearizing controller(NLC) (left column) and decentralized PID+Δp controller(right column)

It can be seen from Fig 5.5 that, following the step disturbance, clearly, interaction is present between the decentralized control loops, but the degree of interaction is very small with either controller. The strongest interaction is side to side. That is, the rear-left actuator interacts the most with the rear-right actuator, and so on. Furthermore, the advantage of the Near IO linearizing controller over the PID+Δp controller does not appear to be significant in terms of minimizing interactions in this application.

The diagonal elements of the *RGA* matrix and the *RGA number* are computed by repeating the tests shown in Fig 5.5 with the other actuators. The results are plotted in Fig 5.6. For the *RGA* elements ($\lambda_{i,j}$), the actuators are indexed as 1, 2, 3, 4 corresponding to front left, front right, rear right , rear left, respectively.
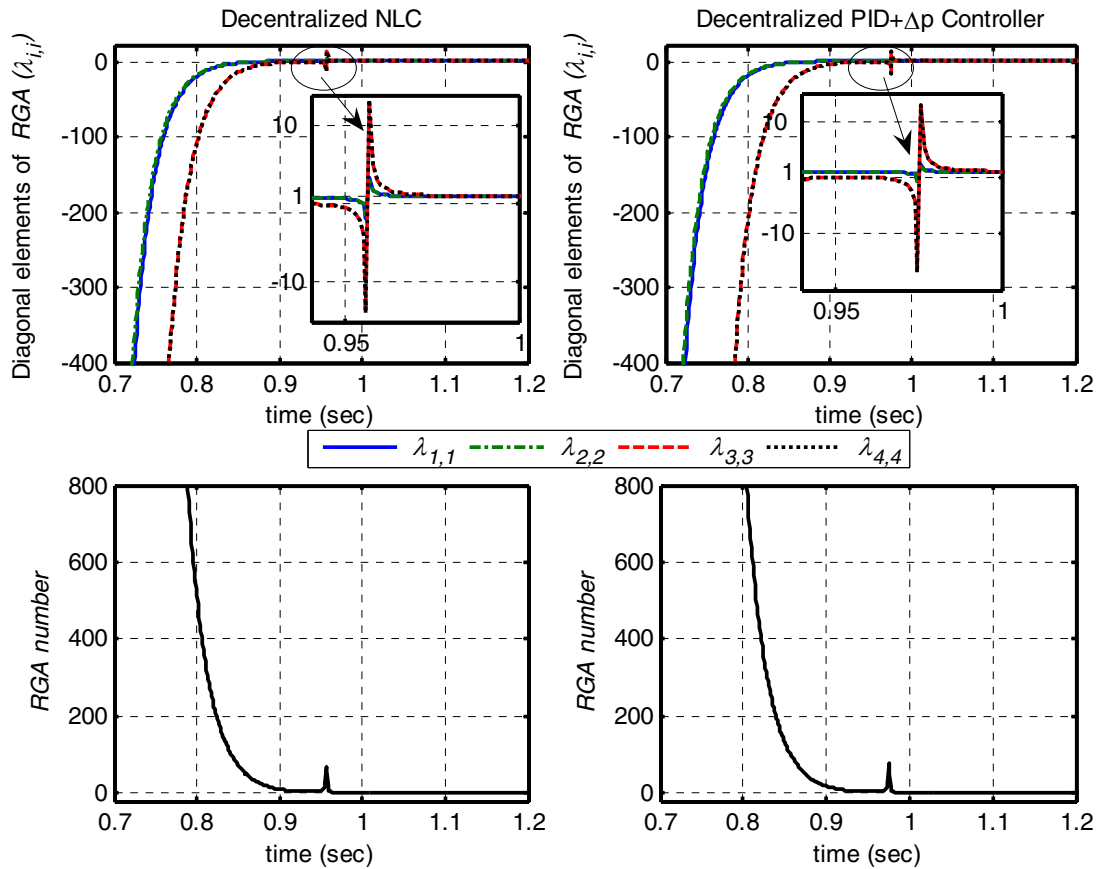
Figure 5.6: Diagonal elements of the *RGA* and the *RGA number* with decentralized Near IO linearizing controller (NLC) (left column) and decentralized PID+Δp controller (right column).

Note that the time scales shown in Fig 5.6 are within the rise-time of the step change in the reference (or the corresponding response at the test actuator at which the step change is applied) shown in Fig 5.5. The diagonal *RGA* elements rapidly approach one and the *RGA number* vanishes to zero very fast, showing the diagonal dominance of the decentralized position control loops. The *RGA number* with the Near IO linearizing controller decays slightly faster than with the PID+Δp controller but overall either controller works well on suppressing interactions. The large initial magnitudes of the diagonal *RGA* elements show that interactions are present in the system, but they die away very quickly. The switch in the sign of the diagonal *RGA* elements magnified in the inserts in Fig 5.6 is typical of systems showing inverse response (related with non-minimum phase plants) [54]. In the present application, Fig 5.5 shows that inverse response is evident in the actuators on the right side (both front and rear), when positive

step reference is applied to the rear left actuator. As Witcher and McAvoy [54] point out, these large and switching *RGA* magnitudes are normally expected to cause control difficulty. In the present application, however, the interactions die away very fast, even faster than the 'smooth' step change (considered reasonable for the application), showing the effectiveness of the present decentralized feedback controllers.

In the paper [95], we used short time-span open-loop tests, without any control on all actuators, to trace the physical cause of this behavior. When one actuator moves in response to current input, cross-coupling in the vehicle's dynamics causes load changes on the other actuators even if they were operating with a closed valve (zero current). However, the actuators do not move much, or any induced motion due to these load changes dies away quickly, similar to the closed-loop case shown in Fig 5.5. This can certainly be attributed to the good stiffness property of the electrohydraulic actuator.

The stiffness (inverse of compliance) of the electrohydraulic actuator is largely determined by the effective bulk modulus, β_e, in the actuator cylinder chambers. It is to be recalled that the Near IO linearizing controller cancels the effects of nonlinear compliance in the hydraulic cylinder. In simulation experiments conducted by assuming perfect knowledge of the value of β_e by the Near IO linearizing controllers, and lowering the value of β_e by as much as 60% from a nominal value of 850 MPa, interactions remained insignificant or died away very quickly. In addition, as pointed out in Chapter 4, the Near IO linearizing controller tolerates a measurable mismatch or uncertainty in the value of β_e without degrading its performance. Fig 5.7 demonstrates the interactions in decentralized loops when the value of β_e in the system is 425 MPa, i.e., 50% lower than the setting in all four Near IO linearizing controllers.
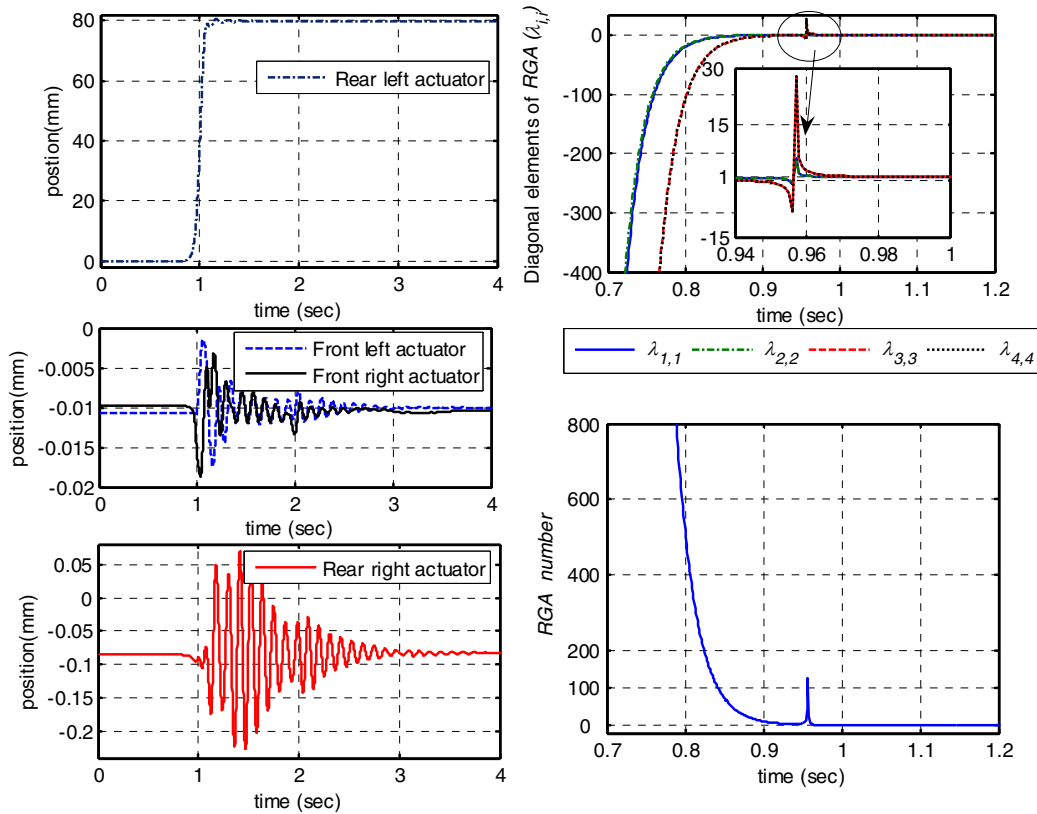
Figure 5.7: Effect of mismatch in the bulk modulus parameter (β_e) on interactions when employing decentralized Near IO linearizing controllers. Time responses (left column), diagonal elements of the *RGA* and the *RGA number* (right column)

Comparing the plots in the left column of Fig 5.7 with those in the left column of Fig 5.5, we see that interaction leads to higher magnitude oscillations for the case in Fig 5.7. However, when compared with the size of the smooth step applied (80 mm), these oscillations are insignificant. This is further confirmed by the little change in the *RGA* magnitude and time history seen between the right column of Fig 5.7 and the left column of Fig 5.6.

We conclude this section by stating that the four-poster with decentralized control of actuator load-plate positions and the transit bus as a test vehicle behaves as an almost diagonal MIMO system. Any interactions exhibited are quickly suppressed by either the decentralized Near IO linearizing position controller or the decentralized PID+Δp position controller. The advantage of the Near IO linearizing controller with respect to interactions appears to be small. The performance of the individual loops, however,

depends of the tuning considerations discussed in the previous subsection; in which case, the Near IO linearizing controller shows better tracking properties.

5.4.3 Interaction Facing Decentralized Cascade Spindle Acceleration Control

It has been discussed in the previous subsection that the interactions in a four-poster, when measured in terms of actuator load-plate positions, disappear very quickly and that, the decentralized control of actuator load-plate positions does a good job of suppressing the interactions. In this section, we suppose that some remote response parameters is to be considered for decentralized feedback control cascaded[13] with the default inner-loop control of load-plate positions. Vertical spindle accelerations are one common set of response parameters employed in response replication approaches to road simulation testing [6, 16].

The goal of the simulation analysis in this subsection is to see if cascaded decentralized control should indeed be considered for tracking desired spindle acceleration responses without resorting to iterative response replication approaches. We make the evaluation based on an interaction analysis of the decentralized control loops with spindle vertical accelerations as outputs. For the model given in Subsection 5.2.1, the relevant outputs are $\ddot{z}_{ui}$, where z_{ui}, i=1, 2, 3, 4, are the displacements of the wheel centers given by Eq. 5.5.

The cascaded control structure for one leg of the four-poster is shown schematically in Fig 5.8. Note that Controller I in the figure represents either the Near IO linearizing position controller or the traditional PID+Δp controller, while Controller II represents the cascaded controller being considered for tracking a desired spindle vertical acceleration signal, $\ddot{z}_{ud}$. Recall that when Controller I is the Near IO linearizing position controller, the feedback signals include, in addition to the position, x_p, shown), chamber

---

[13] The reader should note the distinction between the cascade control of remote parameters, considered in this section, and the cascade control of piston position with pressure force control, outlined in Chapter 4.

or differential pressure(s), velocity and acceleration as well estimates of tire and friction forces.
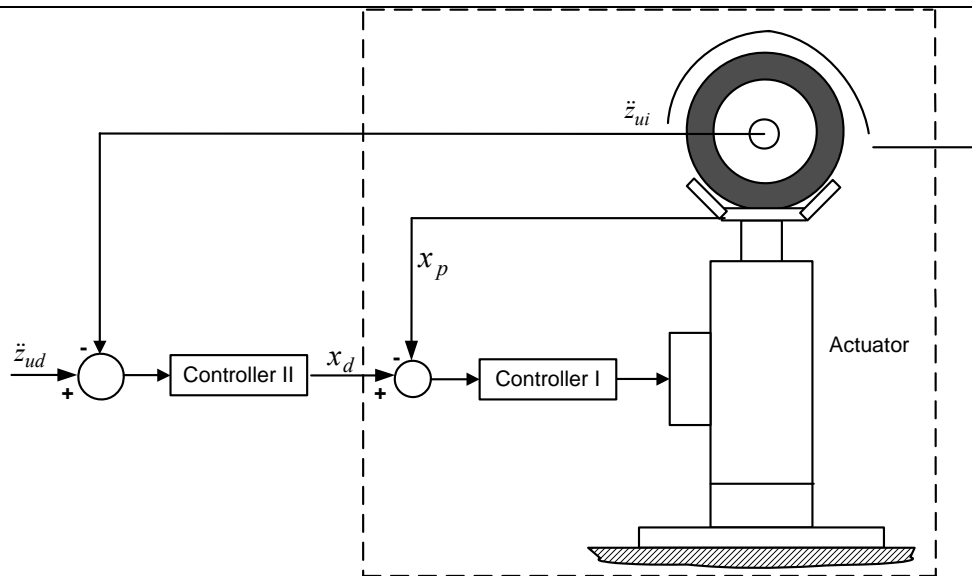
Figure 5.8: Cascaded decentralized control structure for spindle vertical acceleration

For the *RGA* analysis of this subsection, the system of interest is boxed by the dashed lines in Fig 5.8. The reference load-plate positions (x_d) are outputs of the cascaded controller and inputs to the boxed system. We invoke the second use of the *RGA* to evaluate interactions in the proposed decentralized cascade structure, without designing Controller II[14]. We proceed as in the previous subsection by step changing the reference load plate positions one actuator at a time, while the other actuators were given zero reference inputs. The outputs of interest, here, are the spindle vertical accelerations.

Figure 5.9 shows the time history of spindle acceleration responses following smooth step change (of 80mm with smoothening parameter T=0.05) in the reference input to the rear left actuator. The results are qualitatively similar when the reference input is applied to the other actuators. Note the different acceleration scales between the top and bottom row plots.

---

[14] When Controller I is the Near IO linearizing controller (or its cascade equivalent of Chapter 4), Controller II should output the relevant derivatives of the desired position as well.
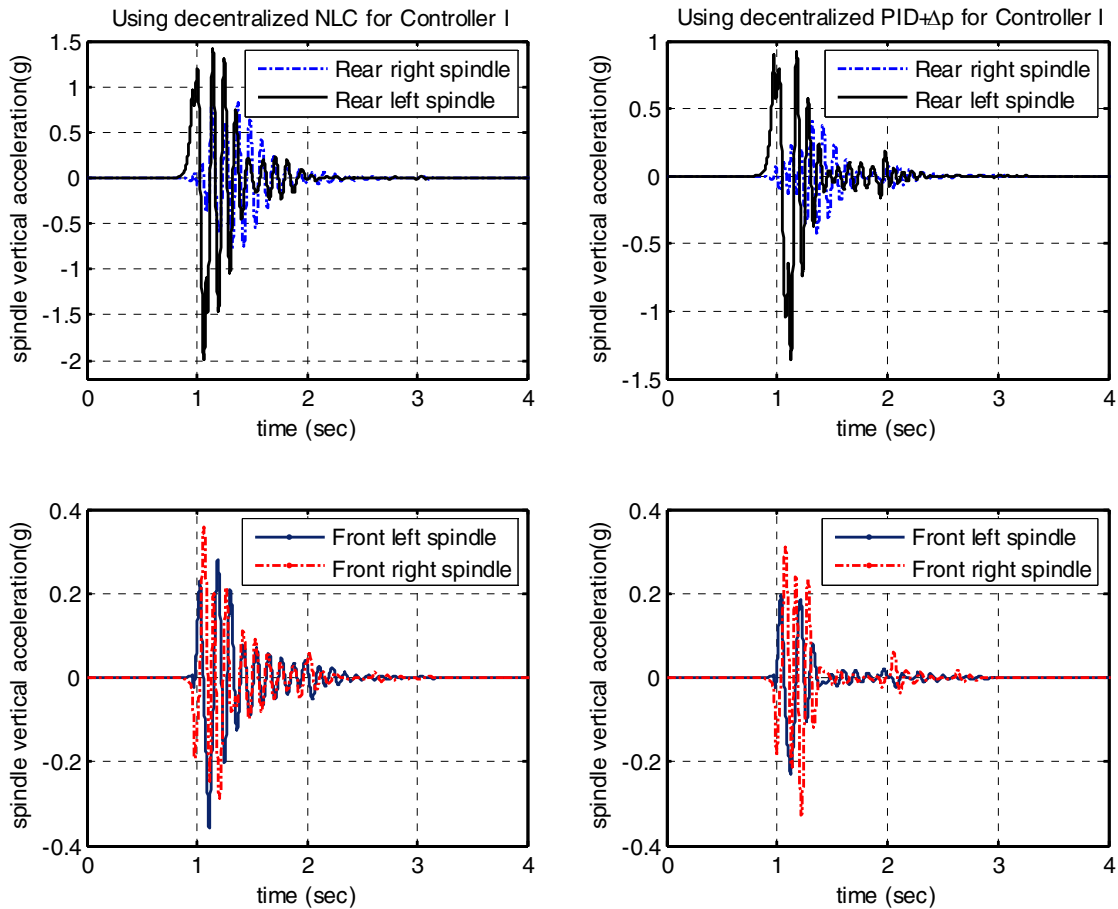
Figure 5.9:Actuator interaction in terms of spindle vertical accelerations with decentralized Near IO linearizing controller(NLC) (left column) and decentralized PID+Δp controller(right column)

It can be seen from Fig 5.9 that, again, the strongest response interaction happens side to side; the spindle accelerations for the front actuators are of the same order of magnitude, as are those of the rear actuators. However, unlike the case of load-plate position control discussed in the previous subsection (see Fig 5.5), the interactions in the present case are much more significant. We also note from the figure that for the controllers tuned specifically as described in Subsection 5.4.1 for the position tracking inner-loops (Controller I), higher spindle accelerations are excited by the Near IO linearizing controller. This is not necessarily a negative on the performance of the Near IO linearizing controller, since at this point, the cascade controller (Controller II), is not designed, nor is the desired spindle acceleration profile specified. However, we note that

response interactions are similar when using either the Near IO linearizing controller or the PID+Δp controller as the inner-loop controller (Controller I).

Further analysis of the interactions can be made by computing the *RGA*. The top rows of Fig 5.10 show element (1, 1) of the *RGA*, $\lambda_{1,1}$, relating front-left spindle vertical acceleration to front-left actuator reference position. The other diagonal *RGA* elements also show similar behavior. The *RGA number*, plotted in the bottom rows of Fig 5.10, gives the interaction information for the whole system in a compact manner.
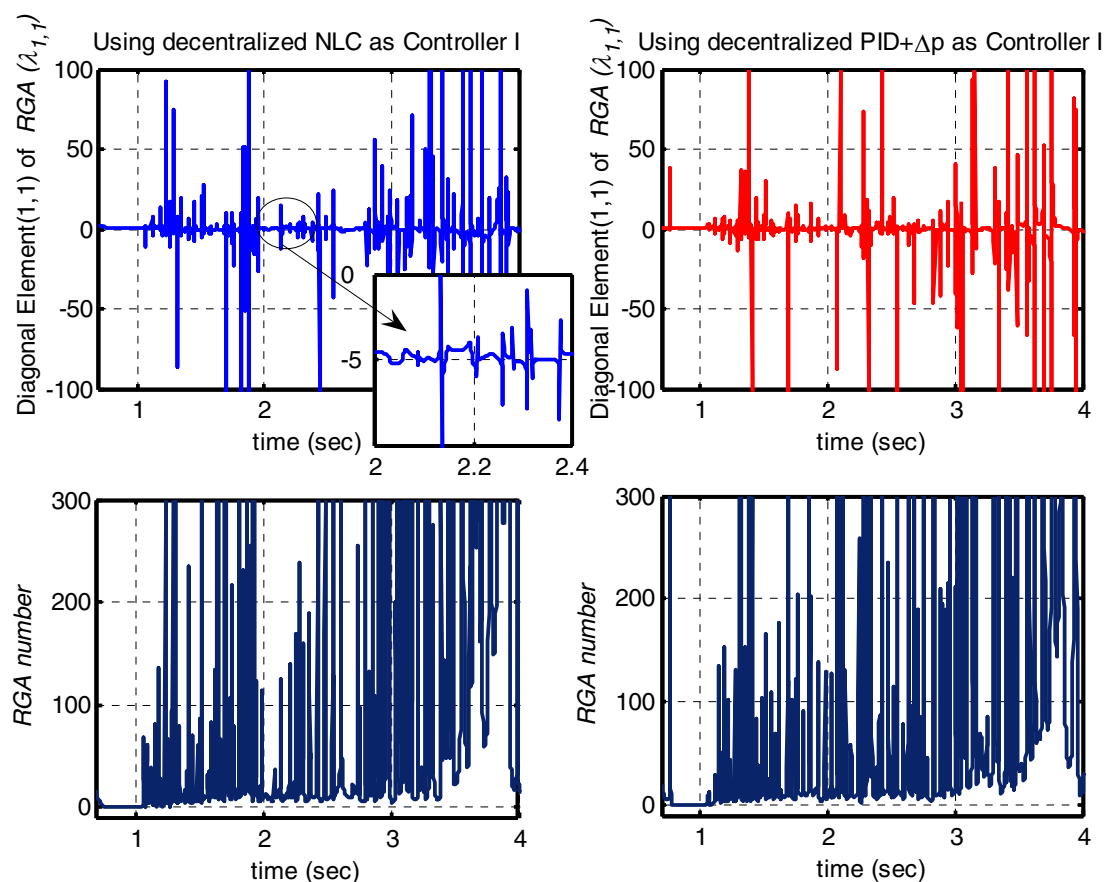
Figure 5.10: Diagonal element (1,1) of the *RGA* and the *RGA number* computed with spindle acceleration response, when Controller I is the decentralized Near IO linearizing controller (NLC) (left column) and the decentralized PID+Δp controller (right column).

The farther the value of a diagonal element of the *RGA* is from 1, the more the decentralized cascade controller (Controller II) at this location gets affected by interaction from the other control channels. As can be seen from Fig 5.10, the diagonal *RGA* element (1, 1) deviates widely and randomly from 1. The magnified insert also

shows that the *RGA* element haphazardly switches signs even when it is momentarily close to 1. Interactions can be seen more clearly by looking at the time history of the *RGA number*, which takes on increasingly nonzero values as time goes by. Again, there is little difference in the interactions exhibited with either the Near IO linearizing controller or the PID+Δp controller as the decentralized inner-loop controller (Controller I).

Recall that in the position control case of the previous subsection, the *RGA* number quickly settles to zero under decentralized position control. The fact that the *RGA number*, in the present case, persistently differs from zero suggests significant control problems (due to interactions) facing a cascaded decentralized control of spindle accelerations employing independently controlled actuators of the four-poster. These interactions can be compounded by the nonlinearity of tire compliance[15] between the actuation inputs and the spindle acceleration measurement points. Given these excessive and persistent interactions, therefore, it is not considered worthwhile to design a decentralized cascade controller of vertical spindle accelerations employing the actuators of the four-poster.

5.5 Performance of the Road Simulator under Decentralized Position Control

In the previous section, we used step test reference profiles to confirm that decentralized load-plate position control leaves minimal interaction between the actuators of the road simulator with a transit bus as a test vehicle. However, not much has been said regarding the performance of the road simulator under these decentralized controllers on actual road profiles. In this section, we define certain metrics to assess the performance of the road simulator with an actual road profile as a reference.

For the discussion in this section, the nonlinear full-bus model described in Section 5.2 shall be used for evaluating the performance of the road simulator under decentralized Near IO linearizing position controllers and decentralized PID+Δp position

---

[15] Note that a linear tire compliance model is considered in this study.

controllers. In this section, we include comparisons of the tracking performance of the two controllers using a typical road profile as the desired load-plate position trajectory.

Recall from the model interconnection described in Subsection 5.2.2 that on the road simulator, the vehicle model can be considered to be driven by the actuator load-plate positions (x_{pi}) as inputs. Here, we shall also consider the case where the vehicle model is driven directly by the actual road profile (replacing x_{pi} by the road). We shall refer to vehicle response obtained under the latter case as the "on-the-road" response. The performance of the road simulator system in replicating road excitation shall be evaluated by comparing on-simulator response to "on-the-road" response. To this end, we first define some performance metrics.

5.5.1 Performance Metrics

Road profiles typically contain such a widely varying excitation that it would be inconvenient to investigate the effectiveness of the road simulator by scrutinizing time responses or power spectral density (PSD) plots obtained with road profile inputs. The performance metrics we shall consider here give single numbers that quantitatively indicate the quality of the road simulation. We shall assume that all relevant responses output from the numerical simulation are discretized with a constant, yet fast enough, sampling rate.

A simple metric is the *rms* value of a response parameter X, which is given by:

$$X_{RMS} = \sqrt{\frac{\sum_{i=1}^{N} X_i^2}{N}} \tag{5.14}$$

where N is the number of data points considered. We shall compare the *rms* values of the sprung and unsprung mass acceleration responses on the road simulator and on-the-road. Brauer [21] suggested the related metric called Euclidean error. It is computed by taking the *rms* value of the difference between two discrete signals X and Y of length N as follows:

$$Eucl = \sqrt{\frac{\sum\limits_{i=1}^{N}(X_i - Y_i)^2}{N}}$$ (5.15)

We shall compare the Euclidean position error for the decentralized Near IO linearizing position controller and the decentralized PID+Δp controller as two cases on the road simulator.

Since vehicle responses are often described in the frequency domain, we also compute the Power Spectral Density (PSD) for the sprung mass vertical acceleration for both on-simulator and "on-the-road" responses. For a compact comparison, the Euclidean sprung mass acceleration error is then computed between the responses with each of the two decentralized control schemes and the "on-the-road" response.

5.5.2 Results for a Rough Road Profile

The International Roughness Index (IRI) is often used to characterize roughness of road surfaces [96]. The typical road profile we consider in this section is of IRI 170 (in/mile), which falls under a mediocre (bad) road classification. The road profile data used here have been taken from ref [96] and they are actual road profiles from field measurements for a total distance of 500 meters. The profiles differentiate between left-side and right-side tracks and are available as tables of horizontal travel vs. vertical deviation. This data are easily converted to time signals for an assumed vehicle speed. We consider speeds of 35 mph (56 km/hr) and 55 mph (88 km/hr) in this section. Note also that the time lag (= *wheel base/vehicle speed*) differentiates the road excitation applied to the front and rear tires.

For the discussion in this section, the two decentralized controllers are tuned as described in Subsection 5.4.1, but this time, for the specific road profile considered here. Recall that for a nonlinear system, the performance of the controller (particularly of the Near IO linearizing one) depends on the reference trajectory. Since the time waveform corresponding to a road profile depends on the vehicle speed, one may consider tuning

the controller gains for each vehicle speed as well. However, for the basic comparison presented in this section, this was not found necessary. The three-closed-loop pole locations for Near IO linearizing controllers of the front actuators are set at s=-1000 and those of the rear ones are set at s=-900; for PID+Δp controllers of the front actuators, P-gain= 18 mA/cm and Δp-gain=0.004 mA/MPa and for the rear ones, P-gain= 3.5 mA/cm and Δp-gain=0.005 mA/MPa. These gains are determined for a well-tuned tracking performance with the vehicle speed at 35 mph and are used for 55 mph as well.
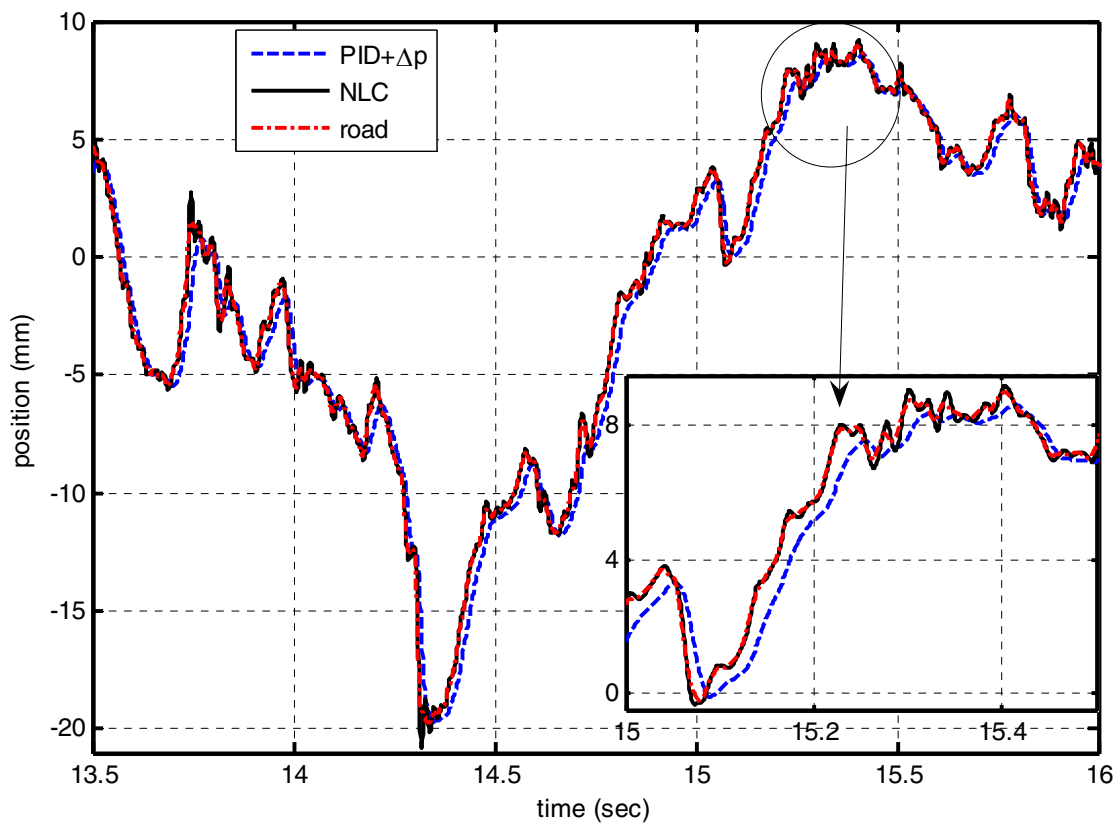
Figure 5.11: Rear left actuator load-plate position for a section of an IRI 170 road at 55mph with the Near IO linearizing position tracking controller (NLC) and the PID+Δp controller.

Figure 5.11 shows a section of the time waveform plots for the load-plate tracking behavior for the rear left actuator. Note that the Near IO linearizing controller gives an almost perfect tracking compared to the PID+Δp controller. Table 5-1 summarizes the tracking performance for all actuators covering the whole 500 m-long profile using the Euclidean position error metric. The position error is computed as the instantaneous error

between the actuator position output and the road-profile reference for the particular actuator, considering time lags and left-side/right-side track differences. As should be expected, for both controllers (which were tuned at 35 mph), the Euclidean error is higher at 55 mph, but in all cases, the Near IO linearizing controller outperforms the PID+Δp controller in terms of matching each load-plate position with the respective desired road profile. The improvement in the tracking performance with the Near IO linearizing controller is more than about 60% at all actuators and at both vehicle speeds.

Table 5-1:Comparison of the tracking performance for the two decentralized controllers

Vehicle Speed (mph)	Decentralized Controller	Euclidean Position Error (mm)			
		Front Left	Front Right	Rear Right	Rear Left
35	PID+Δp	0.166	0.189	0.645	0.640
	NLC	0.060	0.072	0.088	0.072
55	PID+Δp	0.338	0.362	0.897	0.893
	NLC	0.137	0.162	0.211	0.177

Table 5-2 shows a further comparison in terms of vehicle response parameters, namely, the *rms* values of sprung and unsprung mass accelerations for the whole 500 m-long profile. The on-simulator responses using the decentralized Near IO linearizing controller have better matching with the "on-the-road" responses than those using the PID+Δp controller. We also note the improvement with the Near IO linearizing controller is reduced when looking at vehicle responses instead of actuator load-plate tracking errors. This can be attributed to the filtering characteristics of the tire and the suspension.

Table 5-2: Comparison of *rms* values of on-simulator and "on-the-road" responses

Vehicle Speed(mph)	Response Parameter (accelerations (g))	Form of excitation (controlled actuator or direct road profile input)		
		PID+Δp	NLC	road
35	sprung mass	0.0116	0.0120	0.0119
	front unsprung mass	0.3242	0.3201	0.3176
	rear unsprung mass	0.3926	0.4564	0.4377
55	sprung mass	0.0172	0.0187	0.0184
	front unsprung mass	0.5400	0.0538	0.5205
	rear unsprung mass	0.6089	0.7022	0.6700

Finally, we look at a comparison of responses in the frequency domain. Figure 5.12 shows the power spectral density (PSD) of the on-simulator and "on-the-road" sprung mass acceleration responses with the vehicle speed at 55mph. For lower frequencies, there is little difference between the two decentralized controllers. However, at higher frequencies, the on-simulator response with the Near IO linearizing controller matches the "on-the-road" response much better that the on-simulator response with the PID+Δp controller.
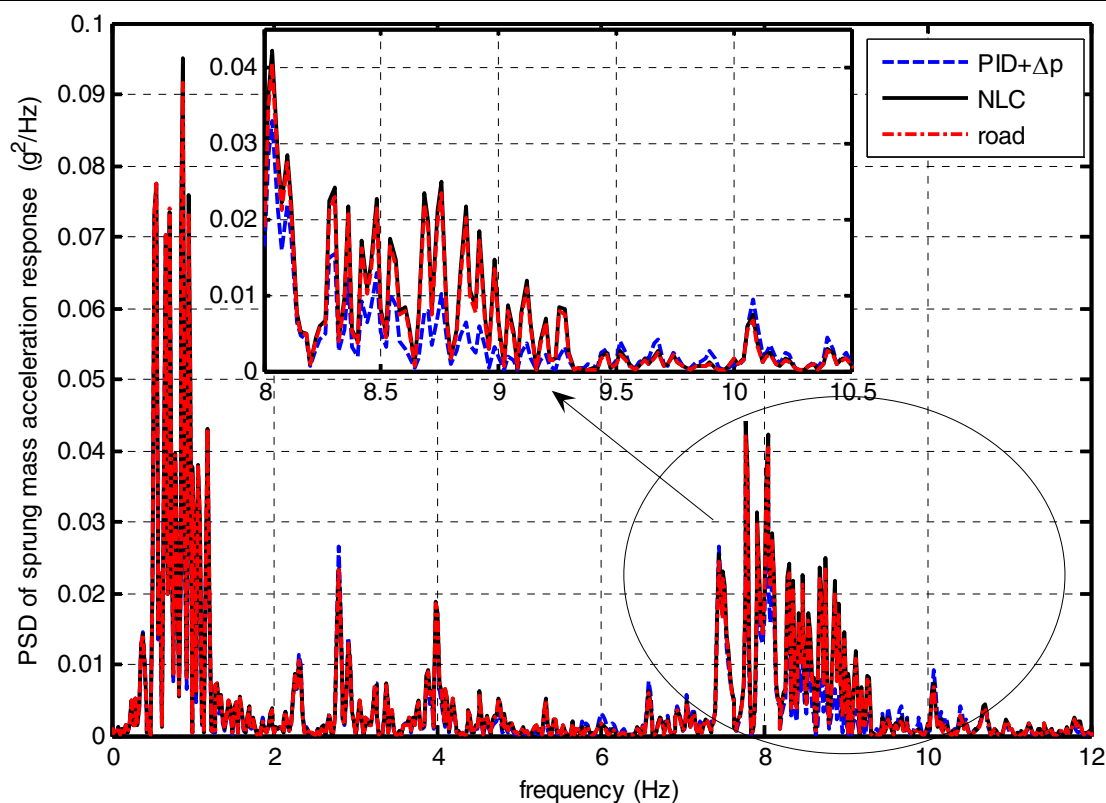
Figure 5.12: PSD of Sprung mass acceleration in the frequency domain for an IRI 170 road at 55mph with the decentralized Near IO linearizing position controller(NLC) and the decentralized PID+Δp controller

Table 5-3 summarizes the differences between the PSDs of the on-simulator and "on-the-road" sprung mass acceleration responses for the whole 500 m-long profile at vehicle speeds of 35 and 55mph. For this table, the Euclidean error is computed as the rms error between the on-simulator response and "on-the-road" response at each discrete frequency point of the FFT (Fast Fourier Transform). For both controllers, it can be seen that the Euclidean PSD error is higher at 55mph than at 35mph (as should be expected, given tuning was done for 35mph), but in all cases, the Near IO linearizing controller(NLC) keeps the error metric smaller than the PID+Δp controller. There is a more than 50% improvement in matching the sprung mass response to the "on-the road response" with the Near IO linearizing controller.

Table 5-3: Comparison of the Euclidean error in the sprung mass acceleration PSD

Vehicle speed (mph)	Decentralized controller	Euclidean error in sprung mass acceleration $((g^2/Hz)x10^{-6})$
35	PID+Δp	8.3967
	NLC	4.0320
55	PID+Δp	16.7080
	NLC	4.5079

5.6 Chapter Summary

In this chapter, the decentralized control of the electrohydraulic actuators of a four-post road simulation system was considered. The Near IO linearizing position tracking controller detailed in Chapter 4 was applied without much modification. Assumptions relevant to this application of the Near IO linearizing controller were detailed in Section 5.1. A full-bus model of a transit bus, employing nonlinear air-suspensions and nonlinear shock-absorbers, was adopted. The road simulator model interconnection used in the simulation studies of this chapter was described in Section 5.2.

In Section 5.3, the Relative Gain Array (*RGA*) was described as a method of determining the level of cross-coupling or interaction in multiple-input multiple-output (MIMO) systems. A feature of the *RGA* interaction measure is that it can be used directly with time history (simulation or experimental) data without the need for frequency response measurements or such identification. The diagonal elements of the *RGA* and the more compact measure, the *RGA number*, were then used for evaluating two decentralized control structures for the four-post road simulator.

The first decentralized control problem considered was the control of actuator load-plate positions. It was shown that in terms of eliminating interaction, decentralized

control of actuator load-plate positions is an effective method. This implies that for the actuator to follow road profile measurements, the decentralized control of the actuator load-plate positions provides a satisfactory solution. It was also highlighted that this arose naturally from the good stiffness property of electrohydraulic actuators. Furthermore, in terms of suppressing interactions, the advantage for the Near IO linearizing controller over the PID+Δp controller appeared to be small.

The second decentralized control problem considered was the decentralized control of a remote response parameter, namely the spindle vertical accelerations, via the four post actuators, which in themselves are independently position controlled. It was shown that significant interactions face such a cascaded decentralized controller structure for tracking vertical spindle accelerations. This was true whether the Near IO linearizing controller or the PID+Δp controller are employed as inner-loop position controllers for each actuator. This decentralized cascade control structure for controlling spindle vertical accelerations (or some similar remote response parameter) did not appear to have a potential in road simulation applications where there may be a desire to use on-road measured spindle vertical accelerations as reference inputs for cascaded decentralized control of the actuators. Iterative response replication approaches, which treat the whole system as a MIMO problem, are suited better for this case.

Finally, some performance metrics were defined in Section 5.5 and used to assess the performance of the road simulation system for an actual road profile of mediocre (bad) roughness. It was shown that the Near IO linearizing controller outperforms the PID+Δp controller in all the cases considered. In particular, there is a more than 60% improvement in matching load-plate positions with reference profile inputs. It was noted that there is a corresponding improvement in terms of response matching as shown by the more than 50% improvement in matching the on-simulator sprung mass acceleration PSD response to the "on-the road response" for the test vehicle, road profile and vehicle speeds considered.

Chapter 6

Conclusions and Recommendations for Further Research

This thesis started by highlighting the applications of service load simulation testing systems and particularly the control challenges with multi-actuator electrohydraulic systems in road simulation. Review of technical literature on the subject indicated that practical difficulties with traditional PID+Δp control loops, such as the nonlinearity of electrohydraulic actuators, stability margins and fixture bandwidth limitations have led to the development of 'outer'-loop MIMO iterative compensation methods. It was noted that the 'inner'-loops still use decentralized PID+Δp loops, and that the original control problem has not been entirely solved by the iterative methods.

In light of the above statements, the main contribution of this thesis is in the development and analysis of nonlinear controllers that cancel the dominant nonlinearities in the electrohydraulic system so that the control loop of an electrohydraulic actuator behaves linearly and the road simulation system performs better. This has been accomplished on two levels; first, via simulations and experiments on a single actuator test system, which brought up further issues with transmission line modeling and interpretations of nonlinear position and force tracking control design, and second, via computer simulations of a multi-actuator road simulation system. Section 6.1 summarizes the conclusions of this thesis from both levels and Section 6.2 gives a brief description of topics identified for possible further research.

6.1 Conclusions

A detailed model was presented for an electrohydraulic system which was eventually employed as an experimental test stand for the design and analysis of the model-based nonlinear controllers. In order to increase the fidelity of the model in capturing measured responses, detailed transmission line modeling work was found

necessary. The following points highlight the main contributions derived from the modeling work in this thesis, particularly on hydraulic transmission line modeling:

- Time domain formulations of transmission line (and related component) models are desirable for interfacing with nonlinear models of actuators. It was shown that the modal approximation of the usual frequency domain solutions (so called four-pole equations) of the distributed dynamics for one-dimensional fluid transmission lines eventually leads to time domain state space formulations. Furthermore, the modularity of the state space models makes them simple alternatives to finite difference-based time domain solutions of the flow equations.

- The modal approximation of the four-pole equations for the causality case with upstream and downstream pressures as input, and upstream and downstream flow rates as output (see Eq.3.16) was developed in this work. Both transfer function and state space forms were presented. It was shown that this causality case has some advantages over causality cases treated elsewhere. It gives better handing of steady-state response. Furthermore, over a wide range of low frequency regimes, a first-term only modal approximation is sufficient, in which case, the model reduces to a series interconnection of hydraulic resistance and inertance. Given these advantages, it is recommended that this causality form be used in hydraulic system modeling, whenever the causality assignment of the overall system permits it. This was demonstrated with the selection of the model interconnection structure for the test system under consideration.

- The dominant nonlinearities of the electrohydraulic actuator included in the nonlinear control design are the variable hydraulic capacitance in the cylinder chambers, the turbulent valve orifice flow rate vs. pressure drop relations, and the nonlinear friction force on the piston. However, an extensive model-based and experimental analysis of the nonlinearities in an electrohydraulic actuator, including those in the servovalve, has already been detailed by many other researchers.

In Chapter 4, nonlinear piston position and force tracking controllers were derived and investigated using experiments and simulations of the nonlinear model of the test system. The basic versions of the controllers were based on a Near input-output (IO)

linearization of the system model by designating either force or position as the system output. This was possible to perform under some assumptions listed in Subsection 4.1.1. These Near IO linearizing controllers cancel the dominant nonlinearities of the system to yield linear closed-loop force and position tracking error dynamics. It turns out that the Near IO linearization with piston force output and the Near IO linearization with piston position output exhibit an interesting inter-relationship. This was revealed from a study of a cascade controller implementing the Near IO linearizing pressure force controller as in inner-loop to a feedback plus feed forward outer-loop position controller that computes the desired force trajectory for the inner-loop. This cascade controller was then shown to be equivalent to the Near IO linearizing position tracking controller. The cascade interpretation exploits the fact that the Near IO linearizing pressure force tracking controller cancels the natural feedback of velocity in the pressure force dynamics thereby decoupling the pressure force dynamics from the piston motion. In essence, the actuator can then be treated as a force generator for piston motion control.

Furthermore, explicit relationships were derived between the respective linear gains of the cascade controller and the Near IO linearizing position controller. This is a major contribution of the analytical work in Chapter 4, since it leads to a design procedure for the choice of the gains for the Near IO linearizing position controller. While the gains for the decoupled loops of the cascade controller have simple interpretations of natural frequency and damping coefficient for the second-order outer position loop and break frequency for the first-order force inner-loop, no such interpretations are evident for the gains of Near IO linearizing position controller. The recommended procedure exploiting the above observations for tuning the Near IO linearizing position controller was summarized at the end of Subsection 4.2.2.2.1.

Performance comparisons were conducted between the Near IO linearizing controllers and PID and linear state feedback with integral (LSFI) controllers. In the force control case, the Near IO linearizing controller performed better than a PID or a LSFI controller in experiments. In the position control case, the improvement obtained in the particular experiments with the Near IO linearizing controller over the PID or LSFI controller for this particular test setup was not significant. It is believed that the effects of

the neglected transmission line and servovalve dynamics (due to operation at non-optimal supply pressure) as well as low bandwidth feedback signal processing contributed to the degraded performance in the experiments. Using system model simulations, it was shown that, under practical assumptions of accumulator close-coupling and design supply pressure operation for the servovalve, significant improvements can be obtained with the Near IO linearizing position controller as well.

Investigations of experimental robustness (sensitivity) investigations revealed that the Near IO linearizing controller tolerates a measurable mismatch between the controller parameter settings and system parameters for the bulk modulus, the valve coefficient and the leakage coefficient, as well as estimation of friction. The issue of robustness was formally addressed by considering a continuous sliding mode force tracking controller for the matched uncertainty. Experiments and simulations were conducted to demonstrate trade-offs between robustness, performance and the need to avoid control chattering (in the presence of neglected servovalve and transmission line dynamics). For the robust position control, a robust cascade controller was considered where the sliding mode force controller acts as an inner-loop to the outer loop position controller subjected to load and friction uncertainty (unmatched uncertainty). Lyapunov backstepping interpretations were invoked to derive linear growth bounds for the tracking errors.

From the simulation and experimental analysis in Chapter 4, we conclude that the Near IO linearizing controllers (or the cascade forms and their robust counter parts) have significant potential in those systems where accumulators are close-coupled with the servovalve and the servovalve dynamics has a natural frequency of about 4 or more times the desired bandwidth. These conditions are met in many electrohydraulic systems.

In Chapter 5, we extended the application of the nominal Near IO linearizing position controller to a decentralized control of a multi-actuator case in a four-post road simulation system. A full-bus model of a transit with nonlinear air-suspensions and nonlinear shock-absorbers was employed as the test vehicle.

Both 'smooth' step time responses and the Relative Gain Array (*RGA*) interaction measure were used to assess interactions in two proposed decentralized control schemes, employing either a PID+Δp controller or a Near IO linearizing position controller.

- The first decentralized control scheme was the control of actuator load-plate positions, and was shown to be very effective in suppressing interactions. It was concluded that this scheme could provide a satisfactory solution if the desire is to match road profiles with load-plate positions with little interaction between the control loops. Both the Near IO linearizing controller and the PID+Δp controller were shown to be nearly equally effective in suppressing interactions for this test vehicle.

- The second decentralized control scheme was a proposed cascaded controller structure for tracking vertical spindle accelerations. This scheme was shown to face strong interactions, with either the Near IO linearizing or the PID+Δp controller as inner-loop actuator position controllers. This approach doesn't appear to have the potential to replace iterative response replication approaches, which treat the whole system as a coupled MIMO problem.

Finally, a comparison was conducted between the decentralized Near IO linearizing position controller and a PID+Δp controller for simulating a vehicle traveling over a typical rough road. Using certain performance metrics, it was shown that the Near IO linearizing controller outperforms the PID+Δp in all the cases considered. In particular, there is more than 60% improvement in the position tracking error metric across all actuators and more than 50% improvement in matching the sprung mass acceleration power spectral density to the "on-the-road" response for the test vehicle and conditions considered.

Recall that practical road simulation approaches generally consider the road simulation system as a MIMO unit, with the decentralized position controllers as 'inner'-loops to the 'outer'-loop iterative drive profile generators that attempt to match on-simulator responses to desired (on-road) responses. The fact that significantly better tracking of actuator load plate positions is obtained with the decentralized Near IO linearizing controller has important implications for response-replication road simulation approaches. It improves the linearity and speed of response of the 'inner'-loop, so that iterative drive profile generation converges faster and outer-loop MIMO controllers work better.

6.2 Recommendations for Further Work

There are certain topics that the author feels deserve further attention. These include the following:

- Complete iterative response replication. In this thesis an extensive review is given for the response replication approaches to road simulation and the work focused on improving the inner'-loops with nonlinear controllers. It remains to implement the nonlinear controllers derived and analyzed in this thesis as 'inner'-loop (replacing the PID $+\Delta p$) controllers in actual iterative response replication algorithms either experimentally or using computer simulations of the system model. Such a study would give further confirmation for the observed improved performance with these controllers.

- Cases of strong cross-coupling. The fact that the observed interactions are the strongest from left side to right side suggests the possibility that different interaction levels (with the decentralized SISO loops) could be possible with other vehicle dimensions. Further study of other vehicles of smaller dimensions than a transit bus would help corroborate the observations regarding the minimal interactions between the actuator position loops.

- MIMO controller design for linearized system. For the general multi-actuator case, once the nonlinearities of the individual electrohydraulic actuators are cancelled by nonlinear feedback, it would be interesting to investigate the possibility of invoking MIMO linear controller design techniques such as H_∞ and μ-synthesis to design robust controllers using the linearized electrohydraulic subsystems. Some work in this direction has been started by Vossoughi and Donath [27] for velocity control in robotic applications. The extension to multi-actuator cases in force and position control with a dynamically coupled-load is largely open.

- Cascade controller in MIMO motion control. It is to be recalled that the cascade interpretation allows one to view the actuator as a force generator by decoupling the actuator force and piston motion dynamics. It would be interesting to investigate the role of this interpretation in a strongly coupled multi-actuator motion system.

Bibliography

1. French, M., 2000, "Introduction to Road Simulation Testing," in *Experimental Techniques*, September/October 2000.

2. White, K. J, 1985, "The Road Simulator- A Practical Laboratory Approach," in Prediction and Simulation of in-Service Conditions, IMechE Conference Publication1985-5, C110/85, London, May 1985.

3. de Pont, J., 1993, "Rating Heavy Vehicle Suspensions for 'road friendliness'," *Heavy Vehicle Systems, Special Series, Int. J. of Vehicle Design*, Vol. **1**(1), pp. 20-33.

4. Hu, Garrick, 1988, "Use of a Road Simulator for Measuring Dynamic Wheel Loads," SAE Paper No. 881194, Warrendale, Pennsylvania.

5. Klinikowski, D.J., Gilmore, B.J, and Kulakowski, B.T., 1999, "Transit bus durability track assessment and validation," Heavy Vehicle Systems, Int. Journal of Vehicle Design, Vol. **6**(1-4), pp. 273-286.

6. Soderling, S., Sharp, M., and Leser, C., 1999, "Servo-Controller Compensation Methods: Selection of the Correct Techniques for Test Applications," in VIII International Mobility Technology Conference and Exhibit, SAE Paper No.1999-01-3000, Sao Paulo, Brazil, Oct 4-6.

7. Cripe, Ronald A., 1972, "Making a Road Simulator Simulate," SAE Paper No. 720095, Warrendale, Pennsylvania.

8. Nolan, Stephen A., and Linden, Nigel A., 1987, "Integrating Simulation Technology into Automotive Design Evaluation and Validation Process," in Passenger Car Meeting and Exposition, SAE Paper No. 871941, Dearborn, Michigan, October 19-22.

9. Cryer, B.W., Nawrocki, P.E., and Lund, R.A, 1976, "A Road Simulation System for Heavy Duty Vehicles," SAE Paper No. 760561, Warrendale, Pennsylvania.

10. Viersma, Taco J., 1980, *Analysis, Synthesis and Design of Hydraulic Servosystems and Pipelines*. Studies in Mechanical Engineering. Vol. I. Elsevier Publishing Co., Amsterdam, The Netherlands.

11. Gore, Sachin A., Kulakowski, Bohdan T., and Gardner, John F., 1999, "Computer Modeling and Analysis of Performance of a Road Simulator," Heavy Vehicle Systems, A Series of Int. J of Vehicle Design, Vol. **6**(1-4), pp. 209-220.

12. Moran, T., Sullivan, M., Menmuir, D., and Mahoney, J., 1995, "Replication of Heavy Truck Dynamic Wheel Loads Using a Road Simulator," in The Fourth International Symposium on Heavy Vehicle Weights and Dimensions, Road Transport Technology-4, pp. 309-315, Ann Arbor, Michigan.

13. Wang, Zhijie, 1996, " An Algorithm for the Correction of Dynamic Wheel Forces Measured on Road Simulators," Masters paper, The Pennsylvania State University, University Park, December 1997.

14. Kulakowski, B.T, Wang, Z., and de Pont, J., 1998, "Correction of Dynamic Wheel Forces Measured on Road Simulators," in The Fifth International Symposium on Heavy Vehicle Weights and Dimensions, Maroochydore, Australia.

15. MTS, Corp., 2001, "RPC Pro: the Intelligent Solution for Laboratory Simulation and Analysis," Eden Prairie, Minnesota.

16. Fash, J.W., Goode, J.G, and Brown, R.G., 1992, "Advanced Simulation Testing Capabilities," SAE Paper No. 921066, Warrendale, Pennsylvania.

17. Raath, Anton D., 1997, "A New Time Domain Parametric Dynamic System Identification Approach to Multiaxial Service Load Simulation Testing in Components," Int. Journal of Fatigue, Vol. **19**(5), pp. 409-414.

18. De Cuyper, Joris, Verhaegen, Michel, and Swevers, Jan, 2003, "Off-Line Feed-Forward and Hinf Feedback Control on a Vibration Rig," Control Engineering Practice, Vol. **11**, pp. 129-140.

19. Eksteen, Jan and Raath, Anton, 2001, "Time-Domain Reconstruction of Dynamic Multi-Axial Responses in Aeronautical Fatigue Testing," Journal of Aircraft, Vol. **38**(1), pp. 147-153, January-February 2001.

20. MTS, Corp., 1999, "Explaining the Six Steps of Remote Parameter Control™," Eden Prairie, Minnesota.

21. Brauer, Matthew, 2000, "Control Algorithms for a Road Simulator in Durability Testing of Transit Buses," Masters Thesis, in Mechanical Engineering, The Pennsylvania State University, University Park, Pennsylvania, May 2000.

22. Maskery, R.H., and, Thayer, W.J., 1978, "A Brief History of Electrohydraulic Servo Systems," Tranactions of the ASME, Journal of Dynamic Systems, Measurement and Control, June 1978.

23. Jones, J.C., 1997, "Developments in Design of Electrohydraulic Control Valves from their Initial Design Concept to their Present Day Design and Application," in

Workshop on Proportional and Servovalves, Monash University, Melbourne, Australia, November 1997.

24.   Norvelle, F.D., 2000, *Electrohydraulic Control Systems*. Prentice Hall, Upper Saddle River, New Jersey.

25.   Merritt, Herbert E., 1967, *Hydraulic Control Systems*. John Wiley and Sons, New York, New York.

26.   Van Schothorst, Gerard, 1997, "Modelling of Long-Stroke Hydraulic Servo-Systems for Flight Simulator Motion Control and System Design," Ph D Dissertation, Delft University of Technology, Delft, The Netherlands.

27.   Vossoughi, Gholamreza and Donath, Max, 1995, "Dynamic Feedback Linearization for Electrohydraulically Actuated Control Systems," Transactions of the ASME, Journal of Dynamic Systems, Measurement, and Control, Vol. **117**, pp. 468-477, December 1995.

28.   Fales, Roger C., and Kelkar, Atul G., 2004, "H_α Loop-Shaping Control Design and Robustness Analysis of a Hydraulic Wheel Loader*,"* in The IMECE2004: 2004 ASME International Mechanical Engineering Congress and Exposition, Anaheim, California, November 13-19, 2004.

29.   Sanĉhez-Peña, Ricardo S., and Sznaier, Mario, 1998, *Robust Systems: Theory and Applications*. John Wiley & Sons, New York, New York.

30.   Khalil, Hassan K., 2002, *Nonlinear Systems*, 3rd ed., Prentice Hall, Upper Saddle River, New Jersey.

31.   Slotine, Jean-Jacques E., and Li, Wieping, 1991, *Applied Nonlinear Control*. Prentice Hall, Englewood Cliffs, New Jersey.

32.   Axelson, Steve, and Kumar, K. S. P., 1988, "Dynamic Feedback Linearization of a Hydraulic Valve-Actuator Combination*,"* in The 1988 American Control Conference, Atlanta, Georgia, June 15-17, 1988.

33.   Hahn, H., Piepenbrink, A., and Leimbach, K.-D., 1994, "Input/Output Linearization Control of an Electro Servo-Hydraulic Actuator*,"* in The 3rd IEEE Conference on Control Applications, pp. 995-1000, Glasgow, UK.

34.   Sohl, Garret A., and Bobrow, James E., 1999, "Experiments and Simulations on the Nonlinear Control of a Hydraulic Servosystem," IEEE Transactions on Control Systems Technology, Vol. **7**(2), March 1999.

35.   Del Re, Luigi, and Isidori, Alberto, 1995, "Performance Enhancement of Nonlinear Drives by Feedback Linearization of Linear-Bilinear Cascade Models,"

IEEE Transactions on Controls Systems Technology, Vol. **3**(3), pp. 299-308, September 1995.

36. Kristić, Miroslav, Kanellakopoulos, Ioannis, and Kokotović, Petar, 1995, *Nonlinear and Adaptive Control Design*. John Wiley & Sons, New York, New York.

37. Hori, N., Ukrainetz, P.R, Nikiforuk, P.N., Bitner, D.V., 1998, "Simplified Adaptive Control of an Electrohydraulic Servo System*,"* in The International Conference on Control, pp. 165-170, Oxford, UK.

38. Yun, J.S., and Cho, H.S, 1991, "Application of an Adaptive Model Following Control Technique to Hydraulic Servo System Subjected to Unknown Disturbances," Transactions of ASME, Journal of Dynamic Systems, Measurement and Control, Vol. **113**, pp. 470-486, September 1991.

39. Ziaei, K., and Sepheri, N., 2001, "Design of a Nonlinear Adaptive Controller for an Electrohydraulic Actuator," Journal of Dynamic Systems, Measurement and Control, Vol. **123**, pp. 449-456, September 2001.

40. Plummer, A.R., and Vaughan, N.D., 1996, "Robust Adaptive Control for Hydraulic Servosystems," Transactions of ASME, Journal of Dynamic Systems, Measurement and Control, Vol. **118**, pp. 237-244, June 1996.

41. Bobrow, J.E, and Lum, K., 1996, " Adaptive, High Bandwidth Control of a Hydraulic Actuator," Transactions of ASME, Journal of Dynamic Systems, Measurement and Control, Vol. **118**, pp. 714-720, December 1996.

42. Alleyne, Andrew, and Liu, Rui, 2000, "A Simplified Approach to Force Control for Electrohydraulic Systems," Control Engineering Practice, Vol. **8**, pp. 1347-1356.

43. Sirouspour, Mohammad R., and Salcudean, S.E., 2000, "On the Nonlinear Control of Hydraulic Servo-systems*,"* in The IEEE International Conference on Robotics and Automation, pp. 1276-1282, San Francisco, California, April 2000.

44. Utkin, Vadim I., 1977, "Variable Structure Systems with Sliding Modes," IEEE Transactions on Automatic Control, Vol. **22**(22), pp. 212-222, April 1977.

45. Hung, John Y., Gao, Weibing, and Hung, James C., 1993, "Variable Structure Control: A Survey," IEEE Transactions in Industrial Electronics, Vol. **40**(1), pp. 2-22, February 1993.

46. Hwang, C.-L., 1996, "Sliding Mode Control Using Time-varying Switching Gain and Boundary Layer for Electrohydraulic Position and Differential Pressure

Control," IEEE Transactions on Control Theory Applications, Vol. **143**(4), July 1996.

47. Kwatny, H.G., Teolis, C., and Mattice, M., 2002, "Variable Structure Control of Systems with Uncertain Nonlinear Friction," Automatica, Vol. **38**, pp. 1251-1256.

48. Young, David, K., Utkin, Vadim I., and Ozguner, Umit, 1999, "A Control Engineer's Guide to Sliding Mode Control," IEEE Transactions in Control Systems Technology, Vol. **7**(3), pp. 328-342, May 1999.

49. Chern, Tzuen-Lih, and Wu, Yung-Chun, 1992, "An Optimal Variable Structure Control with Integral Compensation for Electrohydraulic Position Servo Control Systems," IEEE Transactions on Industrial Electronics, Vol. **39**(5), October 1992.

50. Fung, Rong-Fong, and Yang, Rong-Tai, 1998, "Application of VSC in Position Control of a Nonlinear Electrohydraulic Servo System," Computers & Structures, Vol. **66**(4), pp. 365-372.

51. Liu, Y., and Handroos, H., 1998, "Applications of Sliding Mode Control to an Electrohydraulic Servosystem with Flexible Mechanical Load*,"* in The 4th International Conference on Motion and Vibration Control (MOVIC), Zurich, Switzerland, August 25-28,1998.

52. Nguyen, Q.H., Ha, Q.P., Rye, D.C, and Durrant-Whyte, H.F., 2000, "Force/Position Tracking for Electrohydraulic Systems of a Robotic Excavator*,"* in The 39th IEEE Conference on Decision and Control, Sydney, Australia, December 2000.

53. Alleyne, Andrew, and Hedrick, Karl J., 1995, "Nonlinear Adaptive Control of Active Suspensions," IEEE Transactions on Control Systems Technology, Vol. **3**(1), March 1995.

54. Witcher, M.F., and McAvoy, T.J., 1977, "Interacting Control Systems: Steady State and Dynamic Measurement of Interaction," ISA Transactions, Vol. **16**(3), pp. 35-41.

55. Bristol, Edgar H., 1966, "On a New Measure of Interaction for Multivariable Process Control," IEEE Transactions on Automatic Control, Vol. **11**(1), pp. 133-134, January 1966.

56. Ramachandran, S. and Dransfield, P., 1993, "Interaction between the Actuators in Loaded Multi-Channel Electrohydraulic Drives," Transactions of ASME, Journal of Dynamic Systems, Measurement and Control, Vol. **115**, pp. 291-302, June 1993.

57.   Pannala, A.S., Dransfield, P., Palaniswami, and Anderson, J.H., 1989, "Controller Design for a Multichannel Electrohydraulic System," Transactions of ASME, Journal of Dynamic Systems Measurement and Control, Vol. **111**(2), pp. 299-306, June 1989.

58.   Grosdidier, P., and Morari, M., 1986, "Interaction Measures for Systems Under Decentralized Control," Automatica, Vol. **22**(3), pp. 309-319.

59.   Sun, Hong, and Chiu, George T.-C., 2001, "Motion Synchronization for Multi-Cylinder Electro-Hydraulic System*,"* in the 2001 IEEE/ASME International Conference on Advanced Intelligent Mechatronics, pp. 636-641, Como, Italy, July 8-12, 2001.

60.   Kugi, Andreas, 2001, *Non-linear Control Based on Physical Models*. Springer, London, UK.

61.   Blackburn, J.F., Reethof, G., and Shearer, J.L., 1960, *Fluid Power Control*. The MIT Press, Cambridge, Massachusetts.

62.   D'Souza, A.F., and Oldenburger, R., 1964, "Dynamic Response of Fluid Lines," Transactions of the ASME, Journal of Basic Engineering, Vol. **86**(3), pp. 589-598.

63.   Goodson, R.E. and Leonard, R.G., 1972, "A Survey of Modeling Techniques for Fluid Line Transients," Transactions of ASME, Journal of Basic Engineering, Vol. **94**(2), 474-482.

64.   Woods, R.L., Hsu, C.H., and Chung, C.H.,1983, Comparison of Theoretical and Experimental Fluid Line Responses with Source and Load Impedance, in *Fluid Transmission Line Dynamics*, M. E. Franke and T. M. Drzewiecki, Editor. pp. 1-36, ASME Special Publications, New York, New York.

65.   MTS, Corp., 1985, "Hardware Product Manual, 290.1 X, 290.2X and 290.3X Hydraulic Service Manifolds," Eden Prairie, Minnesota.

66.   Yang, W.C., and Tobler, W.E., 1991, "Dissipative Modal Approximation of Fluid Transmission Lines Using Linear Friction Model," Transactions of ASME, Journal of Dynamic Systems, Measurement and Control, Vol. **113**, pp. 152-162, March 1991.

67.   Jelali, Mohieddine, and Kroll, Andreas, 2003, *Hydraulic Servo-Systems: Modelling, Identification and Control*. -(Advances in Industrial Control). Springer-Verlag, London.

68.   McCloy, D., and Martin, H.R., 1980, *Control of Fluid Power: Analysis and Design*, 2nd ed., John Wiley and Sons, New York, New York.

69. Ayalew, Beshahwired, and Kulakowski, Bohdan T., 2005, "Modal Approximation of Distributed Dynamics for a Hydraulic Transmission Line with Pressure Input - Flow Rate Output Causality," Transactions of the ASME, Journal of Dynamic Systems Measurement and Control, Vol. **127**, September 2005.

70. Hullender, D.A, Woods, R.L, and Hsu, C-H.,1983, Time Domain Simulation of Fluid Transmission Lines Using Minimum Order State Variable Models, in *Fluid Transmission Line Dynamics*, M. E. Franke, and T. M Drzewiecki, Editor. pp. 78-97, ASME Special Publication, New York, New York.

71. Hsue, C.Y-Y, and Hullender, D.A.,1983, Modal Approximations for the Fluid Dynamics of Hydraulic and Pneumatic Transmission Lines, in *Fluid Transmission Line Dynamics*, M. E. Franke and T.M. Drzewiecki, Editor. pp. 51-77, ASME Special Publication.

72. Oldenburger, R., and Goodson, R.E., 1964, "Simplification of Hydraulic Line Dynamics by Use of Infinite Products," Transactions of the ASME, Journal of Basic Engineering, Vol. **86**, pp. 1-10.

73. Pourmovahed, A. and Otis, D.R., 1984, "Effects of Thermal Damping on the Dynamic Response of a Hydraulic Motor-Accumulator System," Transactions of the ASME, Journal of Dynamic Systems, Measurement, and Control, Vol. **106**, pp. 21-26, March 1984.

74. Svoboda, J., Bouchard, G., and Katz, S., 1978, "A Thermal Model for Gas-Charged Accumulators Based on the Heat Conduction Distribution*,"* in ASME Winter Annual Meeting, Fluid Transients and Acoustics in the Power Industry, San Francisco, California.

75. Ayalew, Beshahwired, and Kulakowski, Bohdan T., 2005, "Modeling Supply and Return Line Dynamics for an Electrohydraulic Actuation System," ISA Transactions, Vol. **44**(2), April 2005.

76. Dransfield, Peter, 1981, *Hydraulic Control Systems: Design and Analysis of their Dynamics*. Springer-Verlag.

77. Watton, John, 1989, *Fluid Power Systems: Modelling, Simulation and Microcomputer Control*. Prentice Hall, New York.

78. Manhartsgruber, B., 1999, "Singular Perturbation Analysis of an Electrohydraulic Servo-drive with Discontinuous Reduced Dynamics*,"* in The 1999 ASME Design Engineering Technical Conference, pp. 2001-2011, Las Vegas, Nevada.

79. Eryilmaz, Bora and Wilson, Bruce H., 2000, "Combining Leakage and Orifice Flows in a Hydraulic Servovalve Model," Transactions of ASME, Journal of

Dynamic Systems, Measurement and Control, Vol. **122**, pp. 576-579, September 2000.

80.   Lebrun, M., 1987, "A Model for a Four-Way Spool Valve Applied to a Pressure Control System," The Journal of Fluid Control, Vol. **17**(4), pp. 38-54.

81.   Kailath, Thomas, 1980, *Linear Systems*. Prentice Hall, Englewood Cliffs, New Jersey.

82.   Heintze, J., and Van der Welden, A.J.J., 1995, "Inner-loop Design and Analysis for Hydraulic Actuators with an Application to Impedance Control," Control Engineering Practice, Vol. **3**(9), pp. 1323-1330.

83.   Sepehri, N., Dumont, G.A.M., Lawrence, P.D., and Sassam, F., 1990, "Cascade Control of Hydraulically Actuated Manipulators," Robotica, Vol. **8**(3), July-September 1990.

84.   Eryilmaz, Bora and Wilson, Bruce H., 2001, "Improved Tracking Control of Hydraulic Systems," Transactions of ASME, Journal of Dynamic Systems, Measurement, and Control, Vol. **123**, pp. 457-462, September 2001.

85.   Liu, Rui and Alleyne, Andrew, 2000, "Nonlinear Force/Pressure Tracking of an Electro-Hydraulic Actuator," Tranactions of the ASME, Journal of Dynamic Systems, Measurement and Control, Vol. **122**, pp. 232-237, March 2000.

86.   MTS, Corp., 1994, "Series 252 Servo-valves, Product Specification," Eden Prairie, Minnesota.

87.   Moog, Inc., 2004, "Moog 79 Series Servovalves, Technical Data*,*" Moog Industrial Controls Division, http://www.moog.com

88.   Fancher, Paul S., Ervin, Robert D., Winkler, Christopher B., Gillespie, Thomas D., 1986, "A Fact Book of the Mechanical Properties of the Components for Single-Unit and Articulated Heavy Trucks", The University of Michigan Transportation Research Institute, Ann Arbor, Michigan, December 1986.

89.   Genta, Giancarlo, 1997, *Motor Vehicle Dynamics: Modeling and Simulation*. World Scientific Publishing Co., River Edge, New Jersey.

90.   Nova Bus Inc., Transit Bus Division, 2002, "Low Floor Bus Dimensions and Air Suspension Specifications," David Klinikowski at The Pennsylvania Transportation Institute, University Park, Pennsylvania.

91.   Xiao, Jie, 2002, "System Identificatin for Transit Buses Using a Hybrid Genetic Algorithm," PhD Dissertation, in Mechanical Engineering, The Pennsylvania State University, University Park.

92. Zhang, J., Xinglong, Y., Yi, L., Wangyu, W., Lingzhang, M., Yu, F., and Lin, W., 2002, "Performance Simulation Research on Bus with Air Suspension," SAE Paper No. 2002-01-3093, Warrendale, Pennsylvania.

93. Shinskey, F.G., 1988, *Process Control Systems: Application, Design and Tuning*, 3rd ed., McGraw-Hill Co, New York, New York.

94. Skogestad, Sigurd and Postelthwaite, Ian, 1996, *Multivariable Feedback Control*. John Wiley &Sons, Chichester, UK.

95. Ayalew, Beshahwired and Kulakowski, Bohdan T., 2005, "Decentralized Control of Interacting Electrohydraulic Actuators in Road Simulation," Int. Journal of Heavy Vehicle Systems, Vol. **13**(4).

96. UMTRI, 2005, "International Roughness Index (IRI)," Universtiy of Michigan Transportation Research Institute, http://www.umtri.umich.edu/erd/roughness/index.html

97. Kreyszig, Erwin, 1999, *Advanced Engineering Mathematics*, 8th ed., John Wiley & Sons, New York, New York.

98. Karnopp, Dean, 1985, "Computer Simulations of stick-slip friction in mechanical dynamic systems," Transactions of ASME, Journal of Dynamic Systems, Measurement and Control, Vol. **107**, pp. 100-103, March 1985.

99. Ogata, Katsuhiko, 2002, *Modern Control Engineering*, 4th ed., Prentice Hall, Upper Saddle River, New Jersey.

Appendix A

Modal Representation of $1/Z_c(\bar{s})\sinh\Gamma(\bar{s})$ **and** $\cosh\Gamma(\bar{s})/Z_c(\bar{s})\sinh\Gamma(\bar{s})$

As mentioned in Subsection 3.2.2, to obtain a modal approximation of the distributed system transfer function in Eq. 3.16, we first find the poles of the individual transcendental transfer functions in Eq. 3.16 and then use partial fraction expansions to obtain the modal approximations. This is detailed in this Appendix.

As noted before, we use the following result from Oldenburger and Goodson [72]:

$$\sinh\Gamma(\bar{s}) = \Gamma(\bar{s})\sum_{i=1}^{\infty}(1+\frac{\Gamma^2(\bar{s})}{D_n^2\lambda^2_{si}}) \tag{A.1}$$

where,

$$\lambda_{si} = \frac{i\pi}{D_n}, \qquad i = 1,2,3,... \tag{A.2}$$

First, the zeroes of the transfer function $Z_c(\bar{s})\sinh\Gamma(\bar{s})$ are computed using Eqs. 3.17, 3.18 and A.1 as follows:

$$Z_c(\bar{s})\sinh\Gamma(\bar{s}) = Z_0 D_n(\bar{s}+8)\prod_{i=1}^{\infty}(1+\frac{\Gamma^2}{D_n^2\lambda^2_{si}}) = 0 \quad\Leftrightarrow$$
$$\bar{s} = -8 \quad\vee\quad \bar{s} = -4\pm\sqrt{16-\lambda^2_{si}}, \quad i = 1,2,3,... \tag{A.3}$$

Note that these zeroes are the poles of the original transfer functions in Eq. 3.16. When evaluated at the pole $\bar{s} = -8$, $\Gamma(\bar{s}) = 0$, $\cosh\Gamma(\bar{s}) = 1$ and $\sinh\Gamma(\bar{s}) = 0$. At the pole pairs

$$\bar{s} = a_i \pm b_i = \bar{s} = -4\pm\sqrt{16-\lambda^2_{si}}, \quad \cosh\Gamma(\bar{s}) = \cosh(\pm jD_n\lambda_{si}) = \cosh(\pm j\pi i) = \cos(\pi i) = (-1)^i, i = 1,2,3,... .$$

Note that all of the poles are simple poles [97]. Partial fraction expansion takes the form:

$$f(\bar{s}) = \frac{g(\bar{s})}{h(\bar{s})} = \frac{R_0}{\bar{s}+8} + \sum_{i=1}^{\infty}(\frac{R_i}{\bar{s}-(a_i+b_i)} + \frac{G_i}{\bar{s}-(a_i-b_i)}) \tag{A.4}$$

The coefficient R_o can be computed using:

$$R_0 = \lim_{\bar{s} \to -8} f(\bar{s})(\bar{s}+8) \tag{A.5}$$

The coefficients R_i and G_i are better computed using residues since the numerator and denominator functions are analytic at the respective poles $\bar{s} = a_i \pm b_i$.

$$R_i, G_i = \operatorname{Re} s\{f(\bar{s})\}|_{\bar{s}=a_i \pm b_i} = \frac{g(\bar{s})}{h'(\bar{s})}|_{\bar{s}=a_i \pm b_i} \tag{A.6}$$

Once these residues are computed, the following observation applies:

$$\frac{A_i}{\bar{s}-(a_i+b_i)} + \frac{B_i}{\bar{s}-(a_i-b_i)} = \frac{(A_i+B_i)(\bar{s}-a_i)+(A_i-B_i)b_i}{(\bar{s}-a_i)^2 - b_i^2} \tag{A.7}$$

The denominator in Eq. A.7 simplifies to the quadratic $(\bar{s}^2 + 8\bar{s} + \lambda_{si}^2)$.

The above results will now be used to determine the modal representation for each of the two unique elements of the transfer matrix in Eq. 3.16. First, we consider the element $f(\bar{s}) = 1/Z_c(\bar{s}) \sinh \Gamma(\bar{s})$. Using Eqs. 3.17 and 3.18 in Eq. A.5 together with the comments following Eq. A.3, the coefficient R_o is computed as

$$R_o = \lim_{\bar{s} \to -8} (s+8) \frac{1}{Z_0 D_n (\bar{s}+8) \prod_{i=1}^{\infty} (1 + \frac{\Gamma^2(\bar{s})}{D_n^2 \lambda_{si}^2})} = \frac{1}{Z_o D_n} \tag{A.8}$$

For the other coefficients, note that

$$\operatorname{Re} s\left\{ \frac{1}{Z_c(\bar{s}) \sinh \Gamma(\bar{s})} \right\}_{\bar{s}=a_i \pm b_i} = \left\{ \frac{1}{Z_c'(\bar{s}) \sinh \Gamma(\bar{s}) + Z_c(\bar{s}) \Gamma'(\bar{s}) \cosh \Gamma(\bar{s})} \right\}_{\bar{s}=a_i \pm b} \tag{A.9}$$

where it can be shown that:

$$Z_c'(\bar{s}) = \frac{-4Z_0}{\bar{s}^2 \sqrt{1 + \frac{8}{s}}} \tag{A.10}$$

$$\Gamma'(\bar{s}) = \frac{D_n^2}{\Gamma(\bar{s})}(\bar{s}+4) \tag{A.11}$$

Using Eqs. 3.17, 3.18, A.10, and Eq. A.11 and the notes following Eq. A.3, Eq. A.9 can be evaluated as:

$$R_i, G_i = \text{Re } s \left\{ \frac{1}{Z_c(\bar{s}) \sinh \Gamma(\bar{s})} \right\}_{s=a_i \pm b_i} = \frac{-(1)^i (-4 \pm \sqrt{16 - \lambda_{si}^2})}{\pm Z_0 D_n \sqrt{16 - \lambda_{si}^2}} \tag{A.12}$$

Substituting Eq. A.12 into Eq. A.7 and using the result together with Eq. A.8 in Eq. A.4, and simplifying the expression, the following modal representation results for $1 / Z_c(\bar{s}) \sinh \Gamma(\bar{s})$:

$$\frac{1}{Z_c(\bar{s}) \sinh \Gamma(\bar{s})} = \frac{1}{Z_o D_n} \left(\frac{1}{\bar{s} + 8} + \sum_{i=1}^{\infty} \frac{(-1)^i 2\bar{s}}{\bar{s}^2 + 8\bar{s} + \lambda_{si}^2} \right) \tag{A.13}$$

For the other unique element of the transfer matrix $f(\bar{s}) = \cosh \Gamma(\bar{s}) / Z_c(\bar{s}) \sinh \Gamma(\bar{s})$, R_o is computed as:

$$R_O = \lim_{\bar{s} \to -8} (\bar{s} + 8) \frac{\cosh \Gamma(\bar{s})}{Z_0 D_n (\bar{s} + 8) \prod_{i=1}^{\infty} \left(1 + \frac{\Gamma^2(\bar{s})}{D_n^2 \lambda_{si}^2} \right)} = \frac{1}{Z_o D_n} \tag{A.14}$$

Using Eqs. A.2 and A.10 , and the notes following Eq. A.3, it can be shown that:

$$R_i, G_i = \text{Re } s \left\{ \frac{\cosh \Gamma(\bar{s})}{Z_c(\bar{s}) \sinh \Gamma(\bar{s})} \right\}_{\bar{s}=a_i \pm b_i}$$

$$= \left\{ \frac{\cosh \Gamma(\bar{s})}{Z_c'(\bar{s}) \sinh \Gamma(\bar{s}) + Z_c(\bar{s}) \Gamma'(\bar{s}) \cosh \Gamma(\bar{s})} \right\}_{\bar{s}=a_i \pm b_i} = \frac{-4 \pm \sqrt{16 - \lambda_{si}^2}}{\pm Z_o D_n \sqrt{16 - \lambda_{si}^2}} \tag{A.15}$$

Finally, using Eq. A.7 with R_i and G_i from Eq. A.15 and substituting the result together with Eq. A.14 into Eq. A.4 and simplifying the expression, the modal following representation for $\cosh \Gamma(\bar{s}) / Z_c(\bar{s}) \sinh \Gamma(\bar{s})$ results:

$$\frac{\cosh \Gamma(\bar{s})}{Z_c(\bar{s}) \sinh \Gamma(\bar{s})} = \frac{1}{Z_o D_n} \left(\frac{1}{\bar{s} + 8} + \sum_{i=1}^{\infty} \frac{2\bar{s}}{\bar{s}^2 + 8\bar{s} + \lambda_{si}^2} \right) \tag{A.16}$$

Appendix B

Test Actuator Model Parameters

Some of the geometric parameters in the expression for the controller such as volumes and piston mass could be calculated easily. Table B-1 lists these basic parameters used for the simulations and experiments in Chapters 3 and 4 (unless stated otherwise in specific sections).

Table B-1: Basic actuator model parameters

Symbol	Value	Unit	Comment
$A_t=A_b=A_p$	5.03	cm^2	piston areas
m_p	11.12	kg	piston,fixture, fluid mass
p_R	0.1	MPa	return pressure
p_S	13.89	MPa	supply pressure
$stroke$	11.43	cm	stroke
V_t	34.42	cm^3	volume, top chamber and pipes
V_b	40.48	cm^3	volume, bottom chamber and pipes

For the important, yet unknown parameters such as the effective bulk modulus and the valve coefficients, estimated values from manufacturer specifications and literature could be used. However, these do not necessarily match the present status of the experimental system. Therefore, an offline "grey-box" identification technique is adopted for this thesis [60]. We neglect the lap parameters u_1, u_2, u_3, and u_4 for this purpose. The chamber pressure state equations, Eqs. 3.36 and 3.37, are discretized as follows. At sampling instant k, we have:

$$\frac{V_b + A_b x_p(k)}{\beta_b}\left(\frac{dp_b}{dt}(k)\right) = (q_b(k) + q_i(k) - A_b x_p(k)) \tag{B.1}$$

$$\frac{V_t - A_t x_p(k)}{\beta_t}\left(\frac{dp_t}{dt}(k)\right) = (-q_t(k) - q_i(k) + A_t x_p(k)) \tag{B.2}$$

Discretizing the flow rate equations, Eqs. 3.39 and 3.40, the same way and regrouping variables, the following matrix forms can be written:

$$\left[-(V_b + A_b x_p(k))\left(\frac{dp_b}{dt}(k)\right) \quad D_1(k) \quad D_2(k) \quad (p_t(k) - p_b(k)) \right] \begin{bmatrix} \frac{1}{\beta_b} \\ C_{v,1} \\ C_{v,2} \\ C_{L,b} \end{bmatrix} = \left[A_b \frac{dx_p}{dt}(k) \right] \qquad \text{(B.3)}$$

$$\left[(V_t - A_t x_p(k))\left(\frac{dp_t}{dt}(k)\right) \quad D_3(k) \quad D_4(k) \quad (p_t(k) - p_b(k)) \right] \begin{bmatrix} \frac{1}{\beta_t} \\ C_{v,3} \\ C_{v,4} \\ C_{L,t} \end{bmatrix} = \left[A_t \frac{dx_p}{dt}(k) \right] \qquad \text{(B.4)}$$

where,

$$D_1(k) = sg(i_v(k))\,\mathrm{sgn}(p_S - p_b(k))\sqrt{|\,p_S - p_b(k)\,|} \qquad \text{(B.5)}$$

$$D_2(k) = sg(-i_v(k))\,\mathrm{sgn}(p_b(k) - p_R)\sqrt{|\,p_b(k) - p_R\,|} \qquad \text{(B.6)}$$

$$D_3(k) = sg(i_v(k))\,\mathrm{sgn}(p_t(k) - p_R)\sqrt{|\,p_t(k) - p_R\,|} \qquad \text{(B.7)}$$

$$D_4(k) = sg(-i_v(k))\,\mathrm{sgn}(p_S - p_t(k))\sqrt{|\,p_S - p_t(k)\,|} \qquad \text{(B.8)}$$

For a given length of the sampled (N>4), each of the system of equations, Eqs. B.3 and B.4, is linear in the unknown parameters of bulk modulus (β_t and β_b), valve coefficients ($C_{v,1}$, $C_{v,2}$, $C_{v,3}$ and $C_{v,4}$) and the leakage coefficients ($C_{L,b}$ and $C_{L,t}$). Each of the systems of equations, Eqs. B.3 and B.4, has more equations than unknowns, and is therefore solved in the least squares sense, fitting the best set of parameters for a given data. In this work, several estimates from closed loop position sine sweeps (chirp excitations) were averaged together. Furthermore, the disparate estimates of the fluid bulk modulus for the top and bottom chambers(β_t and β_b) which take on close values anyway, were averaged together to use a single value (for the effective bulk modulus, for example) thereby simplifying the controller. The same was done for the leakage coefficient and the valve coefficient in the various controller expressions derived in

Chapter 4. The following estimates of the parameters, listed in Table B-2, were used as the nominal values for the control experiments in this thesis.

Table B-2: Nominal values of controller parameters

Parameter	Value	Units
β_e	850	MPa
$C_{v,1}$	2.80	$cm^3/(s.mA.\sqrt{MPa})$
$C_{v,2}$	2.73	$cm^3/(s.mA.\sqrt{MPa})$
$C_{v,3}$	2.77	$cm^3/(s.mA.\sqrt{MPa})$
$C_{v,4}$	2.70	$cm^3/(s.mA.\sqrt{MPa})$
C_L	0.5	$cm^3/(s.MPa)$

To further reduce the number of controller parameters required, the valve coefficients values for $C_{v,1}$, $C_{v,2}$, $C_{v,3}$ and $C_{v,4}$ are averaged and represented by a single nominal value of $C_v = 2.75 \, cm^3/(s.mA.\sqrt{MPa})$. It should be noted, however, that most of the nonlinear controllers were observed to be most sensitive to this parameter. And asymmetric response, traceable to this disparity of the valve coefficients for the various ports, was observed. It is therefore recommended that particular attention be made to the consequences of choosing or not choosing disparate estimates for the valve coefficient parameters, even though for the simple experiments in this work, this assumption worked acceptably.

Appendix C

Internal Stability Considerations

The internal stability of the IO linearized system is investigated using the simpler form given in Subsection 4.1.2.3 which uses the load pressure as a state variable. The general case leads to expressions that are mathematically too intricate from which to extract stability proofs. In other words, the discussion in this appendix is limited to the case of a servovalve with symmetric and matched orifices as well as a symmetric actuator.

Recall from Subsection 4.1.2.3 that the output pressure force dynamics is given by (ignoring the offset current, i_{voff}):

$$\dot{F}_p = A_p \dot{p}_L = f_{Fp_L}(x_p, \dot{x}_p) + g_{F_L}(x_p, p_L, \mathrm{sgn}(i_v))i_v \tag{C.1}$$

We choose the Near IO linearizing controller as follows:

$$i_v = \frac{v - f_F}{g_F} \tag{C.2}$$

This results in the closed loop external dynamics:

$$\dot{F}_p = v \tag{C.3}$$

An internal dynamics of order 2 remain, since the system dynamics are of an overall order 3. Two more internal state variables are required to describe this second order internal dynamics. If these are sought in order to complete a normal form description of the system[30, 31], the internal state variables must satisfy the following condition:

$$\boldsymbol{L_g}\eta_k = 0 \qquad k = 1,2 \tag{C.4}$$

where $\boldsymbol{L_g}\eta_k$ is the Lie derivative[30, 31]. Simply put, the new state variables must satisfy:

$$\nabla\eta_k \cdot \boldsymbol{g} = 0 \qquad k = 1,2 \tag{C.5}$$

where the input vector $g = [0 \quad 0 \quad g_{p_L}]^T$. In general, the internal states are of the form $\eta_k = \eta_k(x_p, \dot{x}_p, p_L)$, $k = 1,2$. Choosing, $\eta_1 = x_p$ and $\eta_2 = \dot{x}_p$, the condition of Eq. C.4 is easily satisfied, since the gradients are given by:

$$\nabla \eta_1 = [\frac{\partial \eta_1}{\partial x_p} \quad \frac{\partial \eta_1}{\partial \dot{x}_p} \quad \frac{\partial \eta_1}{\partial p_L}] = [1 \quad 0 \quad 0] \tag{C.6}$$

$$\nabla \eta_2 = [\frac{\partial \eta_2}{\partial x_p} \quad \frac{\partial \eta_2}{\partial \dot{x}_p} \quad \frac{\partial \eta_2}{\partial p_L}] = [0 \quad 1 \quad 0] \tag{C.7}$$

Therefore, the internal dynamics can be described by the piston motion dynamics given in equations Eqs. 3.46 and 3.47 , which are repeated here with the new notation:

$$\dot{\eta}_1 = \eta_2 \tag{C.8}$$

$$\dot{\eta}_2 = \frac{1}{m_p}[A_p p_L - F_L - F_f - m_p g] \tag{C.9}$$

The zero-dynamics is derived by setting the output F_p and hence p_L to zero. For the case of no load force(F_L=0), there will be equilibrium points for the zero dynamics at $\eta_2 = \dot{x}_p = 0$ if and only if a Karnopp-type friction model[98] is adopted such that near zero-velocity, the friction force just balances the weight of the piston. This could be at any piston position within the stroke. In the realistic presence of load force (from specimen reaction, tensile forces being positive), there will be equilibrium points at zero velocity ($\eta_2 = v_p = 0$), and at piston positions obtained by solving:

$$0 = -F_f - F_L - m_p g \tag{C.10}$$

Assuming a specimen with a linear stiffness K_S, there will be equilibrium points at zero velocity ($\eta_2 = v_p = 0$) and

$$\eta_1 = (-F_f - m_p g)/K_s \tag{C.11}$$

In this case, even a viscous only friction model reveals the presence of discrete equilibrium points for the zero dynamics at ($\eta_1 = -m_p g / K_s, \eta_2 = 0$). For more elaborate friction cases, the location of the equilibrium points is still given by Eq. C.11.

The following proof proceeds under viscous friction and linear specimen stiffness assumptions. In this case, the internal dynamics equations, Eqs. C.8 and C.9, reduce to a second order differential equation with constant coefficients. The equilibrium points of the zero dynamics ($p_L=0$) are globally exponentially stable. It can be concluded that the internal dynamics are locally asymptotically stable and the IO linearizing controller ensures convergent local tracking for smooth and bounded reference trajectories F_d with bounded derivatives. To ensure the global stability and global tracking, it is sufficient to prove the input-to-state stability of the system $\dot{\bar{\eta}} = f(\bar{\eta}, p_L)$ where $\bar{\eta} = [\eta_1 \quad \eta_2]$ with p_L as the input[30]. The following Lemma can be used to establish this.

Lemma [30]. *Suppose the function $f(\bar{\eta}, p_L)$ is continuously differentiable and globally Lipschitz in $(\bar{\eta}, p_L)$. If the unforced system $\dot{\bar{\eta}} = f(\bar{\eta}, 0)$ has a globally exponentially stable equilibrium point, then the system $\dot{\bar{\eta}} = f(\bar{\eta}, p_L)$ is input-to-state stable.*

Since the unforced system $\dot{\bar{\eta}} = f(\bar{\eta}, 0)$ is already shown to be globally exponentially stable, it remains to show that the vector function $f(\bar{\eta}, p_L)$ is globally Lipschitz in $(\bar{\eta}, p_L)$. The global Lipschitz condition is also readily satisfied, since:

$$\left\| f(\bar{\eta}, p_L) - f(\bar{\eta}, 0) \right\|_\infty \leq A_p |p_L| \tag{C.12}$$

where A_p is chosen as the Lipschitz constant. This completes the proof for the global stability and global tracking. The caveat is that the Near IO linearization performed by the nonlinear controller discussed in this paper is only assumed (and experimentally implemented) to approach true IO linearization under the practical assumptions made during the controller derivation.

Appendix D

Linearized Models and Linear Feedback Controllers

D.1 Linearized Models

Using the load pressure description, and neglecting the servovalve dynamics, the nonlinear hydraulic actuator model is summarized here by the following state space equations:

$$\dot{x}_p = v_p \tag{D.1}$$

$$\dot{v}_p = \frac{1}{m_p}(A_p p_L - m_p g - F_f - F_L \tag{D.2}$$

$$\dot{p}_L = \Theta(x_p)[-C_L P_L - A_p v_p + C_v i_v \sqrt{\frac{p_S - p_R}{2}}\sqrt{1 - \frac{p_L}{p_S - p_R}\operatorname{sgn}(i_v)}] \tag{D.3}$$

Where,

$$\Theta(x_p) = \beta_e \left(\frac{1}{V_b + A_p x_p} + \frac{1}{V_t - A_t x_p} \right) \tag{D.4}$$

is the inverse of the hydraulic compliance. Here, a symmetric actuator with symmetric valve coefficients is assumed. Furthermore, the friction force, F_f, is assumed to a linear (viscous) force and the load force, F_L, is assumed to be given by:

$$F_L = K_L x_p + B_L v_p \tag{D.5}$$

where K_L and B_L are the stiffness and damping coefficients, respectively of a specimen/load.

Local linearization of the above nonlinear equations about an operating point $(x_{po}, v_{po}, p_{Lo}, i_{vo})$ can be performed by taking the Jacobian of the right hand side of the state equations, Eqs D.1 through D.3. The following linear state space model results :

$$\dot{\mathbf{x}} = \mathbf{A}\mathbf{x} + \mathbf{B}u \tag{D.6}$$

$$y = \mathbf{C}\mathbf{x} \tag{D.7}$$

where u is the input current i_v and the coefficient matrices are given by:

$$\mathbf{A} = \begin{bmatrix} 0 & 1 & 0 \\ -\dfrac{K_s}{m_p} & \dfrac{-(B_v + B_s)}{m_p} & \dfrac{A_p}{m_p} \\ \Theta'(x_{po})f_o(v_{po}, p_{Lo}, i_{vo}) & -\Theta(x_{po})A_p & -\Theta(x_{po})C_L \end{bmatrix} \tag{D.8}$$

$$\mathbf{B} = \begin{bmatrix} 0 & 0 & \Theta(x_{po})C_v\sqrt{\dfrac{p_S - p_R}{2}}\sqrt{1 - \dfrac{P}{p_s - p_R}\text{sgn}(i_{vo})} \end{bmatrix}^T \tag{D.9}$$

with

$$f_o(v_{po}, p_{Lo}, i_{vo}) = -A_p v_{po} - C_L P_{Lo} +$$
$$C_v i_{vo}\sqrt{\dfrac{p_s - p_R}{2}}\sqrt{1 - \dfrac{p_L}{p_S - p_R}\text{sgn}(i_{vo})} \tag{D.10}$$

The output vector C, depends on the output of interest. In this work, the three relevant output cases are: position, pressure force and load force output, for which the C vectors are given, respectively, by:

$$\mathbf{C}_1 = \begin{bmatrix} 1 & 0 & 0 \end{bmatrix} \tag{D.11}$$

$$\mathbf{C}_2 = \begin{bmatrix} 0 & 0 & A_p \end{bmatrix} \tag{D.12}$$

$$\mathbf{C}_2 = \begin{bmatrix} K_L & B_L & 0 \end{bmatrix} \tag{D.13}$$

D.2 Linear State Feedback with Integral Control

For tracking applications, a linear state feedback with integral (LSFI) control is often used. In this thesis, some experimental comparisons were made with this control structure in subsections 4.2.1.1.1 and 4.2.2.1.1. The structure and design of this controller

is briefly discussed here as it applies to the system under study. For a complete exposition of the topic of LSFI control, the reader is referred to textbooks such as [99].

Figure D.1 shows the schematic of implementation of LSFI control for the electrohydraulic actuator. In the figure, y is the output of interest, which could be position, pressure force or load force, and y_d is the desired output ($x_{p,d}$, $F_{p,d}$, or $F_{L,d}$).
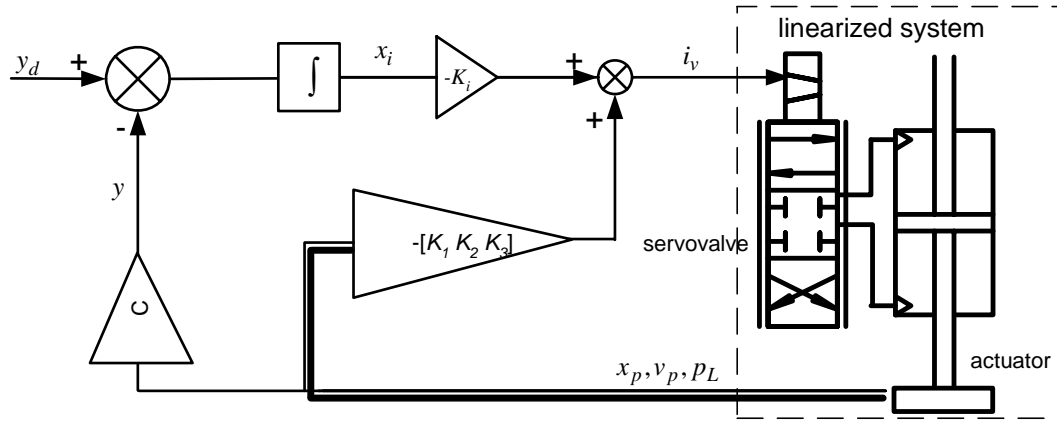

Figure D.1: Schematic for the linear state feedback with integral (LSFI) controller

The controller gains are computed by considering the linearized system with the matrix **A** and vectors **B**, and **C** defined as in the previous section. With the additional integrator output state variable given by:

$$x_i = \int (y_d - \mathbf{C}\mathbf{x})dt \tag{D.14}$$

the system model is augmented as follows:

$$\dot{\mathbf{x}}_\mathbf{a} = \mathbf{A}_\mathbf{a}\mathbf{x}_\mathbf{a} + \mathbf{B}_\mathbf{a}u + \begin{bmatrix} 0 \\ 1 \end{bmatrix} y_d \tag{D.15}$$

$$y = \mathbf{C}_\mathbf{a}\mathbf{x}_\mathbf{a} \tag{D.16}$$

where,

$$\mathbf{A}_\mathbf{a} = \begin{bmatrix} \mathbf{A} & 0 \\ -\mathbf{C} & 0 \end{bmatrix} \quad \mathbf{B}_\mathbf{a} = \begin{bmatrix} \mathbf{B} \\ 0 \end{bmatrix} \quad \mathbf{C}_\mathbf{a} = \begin{bmatrix} \mathbf{C} & 0 \end{bmatrix} \quad \mathbf{x}_\mathbf{a} = \begin{bmatrix} \mathbf{x} \\ x_i \end{bmatrix} \tag{D.17}$$

The linear state feedback controller ($u=i_v$) is given by:

$$u = i_v = -\mathbf{K_a}\mathbf{x_a} = -K_1 x_p - K_2 v_p - K_3 p_L - K_i x_i \tag{D.18}$$

The augmented gain vector $\mathbf{K_a}$ is computed by pole placement. A location of the poles selected and MATLAB's pole placement routines, ACKER and PLACE are used to compute the gain vector $\mathbf{K_a}$, and thereby the individual state feedback gains. As pointed out in Chapter 4, various pole locations were attempted for the present system. And since the gains so computed are based on a simplified and linearized model, often times significant online tuning of these gains is necessary to obtain satisfactory responses when using the LSFI controller with the actual nonlinear system.

D.3 Linear PID+Δp Controller.

The defining expression for this controller is:

$$i_v = K_P e + K_I \int e\, dt + K_D \dot{e} + K_{\Delta p} \Delta p \tag{D.19}$$

Where the K_p, K_I, K_D are the proportional (P), integral (I) and derivative (D) gains, respectively and $K_{\Delta p}$ is a differential pressure (Δp) feedback gain.

Appendix E

Parameters for the Models of Road Simulator Actuators and the Full-Bus Model

The model parameters employed for the simulation study of the multi-actuator road simulator system in Chapter 5 are listed in this Appendix. Servovalve dynamic parameters are as given in Chapter 5.

E.1 Parameters of Actuator and Servovalve

Table E-1: Actuator and servovalve parameters

Symbol	Value	Unit	Comment
$A_t=A_b=A_p$	81.3	cm^2	piston areas
C_L	3.0	cm^3/MPa	leakage coefficient
G_v	0.019	cm/mA	valve gain
K_v	3.4521e4	cm^2/(s.√MPa)	valve coefficient
m_p	63.5	kg	piston and load plate mass
p_R	0.1	MPa	return pressure
p_S	20.7	MPa	supply pressure
stroke	21.6	cm	stroke
$V_t=V_b$	877.5	cm^3	volume
β_e	850	MPa	effective bulk modulus

E.2 Parameters for the Full-Bus Model

Table E-2: Parameters for the full-bus model

Symbol	Value	Unit	Comment
$b_{lf}=b_{rf}$	1.093	m	dimension, see Fig 5.1
$b_{lr}=b_{rr}$	0.971	m	dimension, see Fig 5.1
C_{ap}	5000	Nms/rad	auxiliary pitch damping coef.
C_{arf}	0.0	Nms/rad	auxiliary roll damping coef., front
C_{arr}	0.0	Nms/rad	auxiliary roll damping coef., rear
$C_{t1}=C_{t2}$	75	N.s/m	tire damping coefficient, front
$C_{t3}=C_{t4}$	150	N.s/m	tire damping coefficient, rear
d_{lf}	1.0	m	dimension, see Fig 5.1
d_{lr}	0.942	m	dimension, see Fig 5.1
d_{rf}	1.186	m	dimension, see Fig 5.1
d_{rr}	1.0	m	dimension, see Fig 5.1
I_p	599400	kgm^2	pitch moment of intertia, sprung
I_r	1498	kgm^2	roll moment of inertia, sprung
I_{uf}	1033	kgm^2	roll inertia, front unsprung mass
I_{ur}	1070	kgm^2	roll inertia, front unsprung mass
K_{ap}	1000	Nm/rad	auxiliary pitch stiffness
K_{arf}	500	Nm/rad	auxiliary roll stiffness
K_{arr}	500	Nm/rad	auxiliary roll stiffness
$K_{t1}=K_{t2}$	1155382	N/m	tire stiffness, front
$K_{t3}=K_{t4}$	2310764	N/m	tire stiffness, rear
l_f	4.525	m	dimension, see Fig 5.1
l_r	1.675	m	dimension, see Fig 5.1
M_s	15003	kg	sprung mass
M_{uf}	758	kg	unsprung mass, front
M_{ur}	1571	kg	unsprung mass, rear

The air suspension and shock absorber (damping) forces are interpolated from data given in Fig E.1 for each corner of the bus [90].
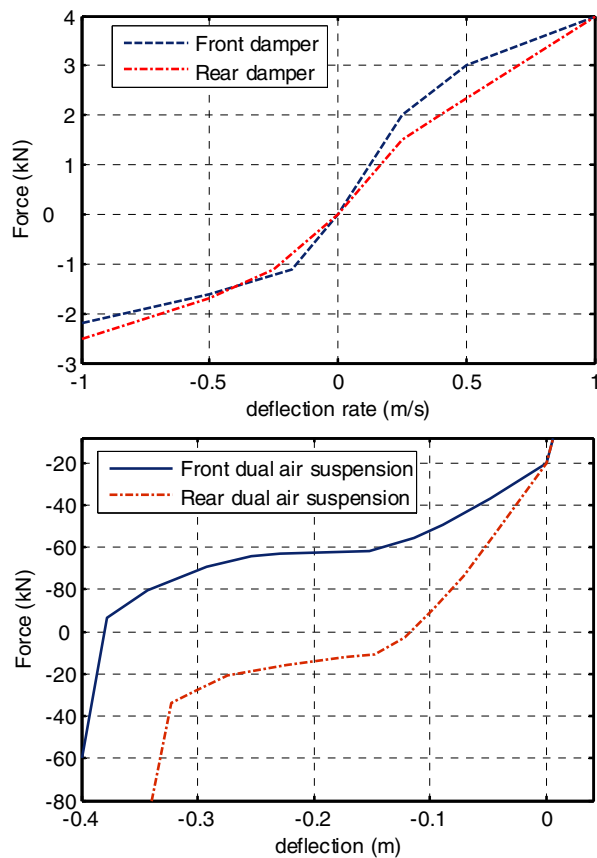

Figure E.1: Nonlinear damping forces (top) and dual air suspension (bottom) forces

VITA

Beshahwired Ayalew

Beshahwired Ayalew was born in Bale Goba, Ethiopia, on September 6, 1975, the son of Birknesh Alemayehu and Ayalew Tafesse. He attended Batu Terrara Comprehensive Secondary School and then Addis Ababa University in Ethiopia and graduated with a Bachelor of Science degree in Mechanical Engineering in July 1997. He was with the faculty of the Mechanical Engineering Department of Addis Ababa University from September 1997 through August 1998 before he joined the Mechanical Engineering graduate program at the Pennsylvania State University (Penn State). He obtained his Master of Science degree in Mechanical Engineering from Penn State in August 2000 and has held various graduate research and teaching assistantship positions at the Pennsylvania Transportation Institute and the Department of Mechanical and Nuclear Engineering at Penn State. He was also a graduate teaching fellow in the fall 2002 and spring 2003 semesters. He just completed his work towards a Doctor of Philosophy degree in Mechanical Engineering at Penn State.